University of Southampton

Faculty of Engineering and Physical Sciences

The national Centre for Advanced Tribology at Southampton (nCATS)

Assessing the Wear and Friction Properties of Self-Lubricating Coatings in Dry-Running Aerospace Actuation Gearboxes

by

Thomas M. H. Finch

BEng (Hons) CEng MIMechE

Thesis for the degree of Doctor of Philosophy in Engineering and the Environment

September 2023

Report Number: TF21022023-01

University of Southampton

Abstract

Faculty of Engineering and Physical Sciences

The national Centre for Advanced Tribology at Southampton (nCATS)

Doctor of Philosophy in Engineering and the Environment

Assessing the Wear and Friction Properties of Self-Lubricating Coatings in Dry-Running Aerospace Actuation Gearboxes

by

Thomas M. H. Finch

Actuation gearboxes used in high-lift systems on commercial airliners suffer from high zero-load losses due to increased fluid viscosity in the low-temperature flight environment. These losses result in an increase in system power consumption and weight, whilst leakage of lubricating fluids reduces reliability. The replacement of fluid lubricants with modern self-lubricating thin films deposited onto the gear teeth provides a potential approach to the reduction in zero-load losses and improvements in reliability. However very little is known of the wear and friction performance of self-lubricating coatings on dry-running gears, and methods to assess their suitability are not yet established.

In this research a power-recirculating test rig is developed to test gears treated with several promising PVD coatings. A wear model is constructed in which the contact between gear teeth is treated as a pair of loaded cylinders of constantly changing diameter and surface velocity in mixed sliding and rolling. Measurements of the pre-test and post-test profiles are used to generate wear maps, which are then compared to model outputs in order derive the wear rate. Detailed inspections and analyses of the worn tooth surfaces are then performed to determine the causes of coating failure. Further tests are performed on a power-absorbing test rig at low temperature to determine the overall power loss, which is then analysed to determine the losses attributable to tooth friction and a coefficient of friction is calculated.

The most successful coating in the wear tests is found to be a sputtered coating consisting of Cr-doped a-C. In efficiency testing the coating's friction coefficient is found to be higher than that obtained with uncoated gears and common fluid lubricants. However, the reduction in low-temperature zero-load losses is found to result in an overall reduction in power loss. Whilst the anticipated efficiency improvement is realised, the coating lacks sufficient durability for the target service life due to high wear on the mid-addenda of the teeth and delamination at the start of active profile. The contact model is then used to propose modifications to the gear design that would improve coating life.

Table of Contents

Table of Tables

Table of Figures

List of Accompanying Materials

The data underpinning this thesis is available under the DOI:

https://doi.org/10.5258/SOTON/D25

Research Thesis: Declaration of Authorship

Print name: Thomas Finch

Title of thesis: Assessing the Wear and Friction Properties of Self-Lubricating Coatings in Dry-Running Aerospace Actuation Gearboxes

I declare that this thesis and the work presented in it are my own and has been generated by me as the result of my own original research.

I confirm that:

1. This work was done wholly or mainly while in candidature for a research degree at this University;
2. Where any part of this thesis has previously been submitted for a degree or any other qualification at this University or any other institution, this has been clearly stated;
3. Where I have consulted the published work of others, this is always clearly attributed;
4. Where I have quoted from the work of others, the source is always given. With the exception of such quotations, this thesis is entirely my own work;
5. I have acknowledged all main sources of help;
6. Where the thesis is based on work done by myself jointly with others, I have made clear exactly what was done by others and what I have contributed myself;
7. Parts of this work have been published as:-

A manuscript discussing the methods developed for this project and the results of efficiency and wear testing on Graphit-iC coated gears have been submitted to the journal “Wear” for consideration.

Signature: ..... Date:.....

Acknowledgements

Firstly, I would like to express my deepest gratitude to my supervisor Professor Tomas Polcar for his support and guidance during the long journey that has led me to this point. Given the time and distances involved, I could not have reached this milestone without the exceptional efforts on his part. I must also thank Dr Tomas Vitu for performing the Raman spectroscopy analysed in my research. Jinlong Yin at Teer Coating, and Todor Vuchkov at Instituto Pedro Nunez, should both be recognised for coordinating the preparation of test samples.

As my research was performed whilst in full-time employment, I'm extremely grateful to my employer Collins Aerospace for providing funding and for their unwavering support. I am very fortunate to be surrounded with colleagues who both took an interest in my work and offered guidance when things were not going according to plan. Special thanks are extended to Joao Passos for his support through a difficult final year, and to John Derry whose encouragement was very influential in my decision to pursue this endeavor. I owe gratitude to Charles de Sainte Marie, Jeremy Kracke, and Bob Holmes for assisting with producing drawings to bring my ideas to fruition and I would also like to mention Dave Bainbridge, Paul Proverbs, and Martin Cresswell for training me in the use of key inspection equipment, without which this research would not have been possible.

Life as a part-time researcher requires significant investment of personal time, and often some of that burden is shared with the people closest to you. Word cannot express my gratitude to my wife, Jo, and my son, Alexander, for supporting me through the many weekend and evening hours I spent in the office. More than anything else I am looking forward to spending more time with each other as a family and taking a well-earned holiday together

Definitions and Abbreviations

AC ..... Alternating Current

a-C ..... Amorphous Carbon

a-C:H ..... Hydrogenated Amorphous Carbon

AGMA ..... American Gear Manufacturers Associations

ASCII ..... American Standard Code for Information Interchange

BNC ..... Bayonet Neill–Concelman

CFUBMS ..... Closed Field Unbalanced Magnetron Sputtering

CMM ..... Coordinate Measuring Machine

CPE ..... Compound Planetary Epicyclic

DC ..... Direct Current

DLC ..... Diamond-Like Carbon

DLCH ..... Diamond-Like a-C:H

EDS ..... Energy Dispersive X-ray Spectroscopy

EHL ..... Elastohydrodynamic Lubrication

EP ..... Extreme Pressure

FFT ..... Fast Fourier Transform

FZG ..... Forschungsstelle fur Zahnrader und Getriebebau (Research centre for gear wheels and gear construction)

GLCH ..... Graphite-Like a-C:H

h-BN ..... Hexagonal Boron Nitride

IFLM ..... Inorganic Fullerene-Like Material

Me-DLC ..... Metal-doped diamond-like carbon

NASA ..... National Aeronautics and Space Administration

PCU/PDU ..... Power Control Unit/Power Drive Unit

PLCH ..... Polymer-Like a-C:H

PTFE ..... Polytetrafluoroethylene

PVD ..... Physical Vapour Deposition

RF ..... Radio Frequency

RMS..... Root Mean Square

SAP..... Start of Active Profile

SEM..... Scanning Electron Microscope

SG..... Spheroidal Graphite

STO..... Safe Torque-On

ta-C ..... Tetrahedral Amorphous Carbon

ta-C:H ..... Hydrogenated Tetrahedral Amorphous Carbon

TEM..... Transmission Electron Microscopy

TMD ..... Transition Metal Dichalcogenide

Chapter 1 Research Aims and Objectives

1.1 Summary of Study Motivations

Large commercial aircraft utilise high lift devices to improve the aerodynamic characteristics of the wing for landing and take-off [1]. These systems operate using translating panels at the leading and trailing edge, the kinematics of which are controlled by complex linkage or track mechanisms [2]. The mechanisms are actuated using high ratio compound epicyclic gearboxes which are driven by a central power drive unit and mechanically synchronised by a system of spanwise shafts, couplings, and gearboxes [3].

Lubrication of the gear meshes is accomplished using a variety of fluid lubricants, including semi-fluid grease and turbine oil. Due to low operating temperatures these lubricants are highly viscous and significant zero-load drag losses are incurred. Drag losses within the system result in a greater power demand and drive additional weight into the design [4]. Sealing of dynamic interfaces is challenging due to the effects of temperature and pressure variations.

Replacing fluid lubricants with solid lubricant coatings could potentially reduce the weight and power consumption of high-lift actuation systems and improve reliability. In many geared applications solid lubrication is not feasible due to the inability to dissipate heat from the working surfaces. However high-lift systems function intermittently and are inactive for long periods at a low temperature, which gives working components time to cool. Therefore, they present an opportunity to explore the feasibility of fluid-free gearboxes lubricated by modern thin hard films.

1.2 Research Aims

This study examines whether modern self-lubricating coatings can replace common fluid lubricants utilised in the actuation gearboxes of civil high-lift systems. As the primary function of the lubricant is to reduce friction and wear, the feasibility of this approach will be determined by a coating's ability to limit wear to an acceptable level and provide sufficiently low friction to ensure that power-losses at low temperature are reduced.

Additionally, methods to assess these characteristics need to be developed, and such methods should provide insights that can allow the optimisation of gear design to suit the use of coatings. The wear processes leading to coating failure must also be understood through detailed examination and analysis of tested components to inform selection of coating composition and structure.

1.3 Objectives

The following objectives were set in order to satisfy the research aims.

- Develop test method for determining the wear life of promising coatings when applied to spur gears.

- Determine the useful life of promising coatings under operating conditions typical of the application.

- Calculate the wear rate of the coatings by comparing test measurement data to a model of the loads and sliding conditions on the gear teeth. Utilise the model to evaluate the impact of different design parameters on predicted coating life.

- Determine the wear mechanisms involved and identify failure modes.

- Develop test method for determining the efficiency of promising coatings when applied to spur gears.

- Compare the efficiency of the coated gears to those operating under conventional fluid lubricants with typical aerospace lubricants.

- Identify the magnitude of load-dependent and zero-load losses in a typical high-lift gearbox under dry and fluid lubrication.

- Calculate the average coefficient friction of the coatings during the mesh cycle.

Chapter 2 Literature Review

2.1 High Lift Systems, their Lubrication and Power Losses

2.1.1 High Lift System Purpose and Functioning Principles

High-lift systems are mechanical devices that temporarily alter the geometry of an aircraft's wing in order to generate additional lift. The primary function of a high-lift system is to reduce required the aircraft speed for approach, landing, and take-off by increasing the maximum lift coefficient and reducing the stall speed, at the expense of creating additional drag. They also reduce the necessary pitch angle of the aircraft during landing, which improves visibility and avoids scraping of the tail. The change in aerofoil geometry increases the usable angle of attack and allows a steeper descent gradient to enable the aircraft to clear obstacles during climb and approach. At high speeds the devices are retracted, allowing the wing to be optimised for its cruise condition whilst maintaining the ability to temporarily obtain satisfactory performance characteristics at lower speeds [1]. On the most advanced modern civil aircraft such as the Airbus A350 and Boeing 787 the flap system can be used to trim the wing camber during flight to compensate for weight losses and improve fuel economy [3].

High-lift systems for large commercial aircraft can be separated into two categories: leading-edge and trailing-edge. These terms refer to the edge of the wing on which they are employed. The most common configuration for large civil aircraft is a slat at the leading edge and a slotted fowler flap at the trailing edge [2]. Both increase the lift coefficient for given angle of attack by increasing the area and camber of the wing, whilst preventing separation of the airflow boundary layer on the upper surface. By allowing flow of high-energy air from the underside of the wing to the boundary layer on top a higher angle of attack can be tolerated without stalling [1].

Figure 2-1 shows an example of an aerofoil with a slat and triple slotted fowler flap. The complexity of flap arrangement shown in this image was typical of aircraft designed in middle of the 20th century, but in more recent years simpler designs with single slots have regained favour [3][2].

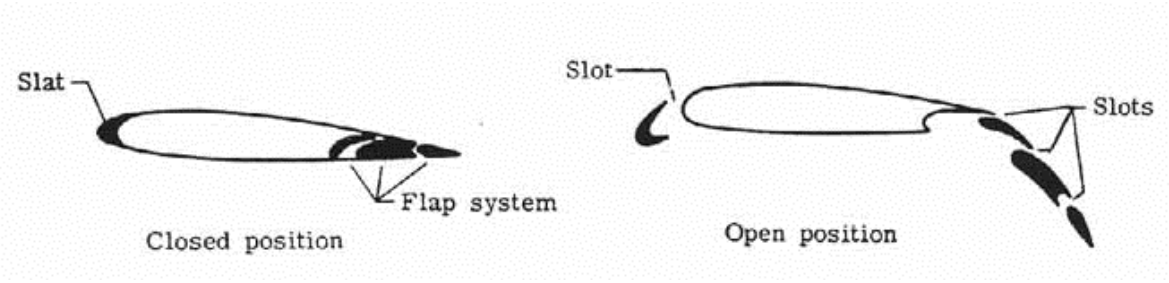

Figure 2-1 Aerofoil Section with Slat and Triple-Slotted Fowler Flap [4]

2.1.2 Actuation Mechanisms

Flap and slat systems are most commonly employed in the form of multiple movable panels. To achieve the necessary schedule of translation and rotation they are guided and supported by either two or three hinge, track, or linkage mechanisms. Figure 2-2 shows several examples of high lift deployment mechanisms from large airliners. As with the aerodynamic aspects, the development trend for deployment mechanisms has been one of reducing complexity in order to eliminate weight and maintenance costs [3][2].

Control and movement of the panel mechanisms on each edge is provided by one or more actuation systems. Each panel is usually controlled by two high reduction-ratio actuators, which are driven by a centrally located power control unit (PCU) and a series of spanwise transmission elements [3]. A typical high-lift system is shown in Figure 2-3. The transmission system ensures symmetrical deployment and prevents panel skew [6].

On modern aircraft the actuators consist of highly loaded geared rotary actuators (GRAs) [6]. Most GRAs utilise compound planet epicyclic (CPE) gear arrangements in order to achieve a large reduction ratio within the small volume of the wing edge [7]. Section views of compound planet flap and slat GRAs are shown in Figure 2-4. Flap actuators are often installed offset to the main transmission and an integrated or separate “down drive” gearbox comprising a simple bevel or spur gear arrangement is used to connect to the input [6]. Actuators also include built-in torque limitation devices, sometimes within the offset gearbox, for overload protection in the event of a panel jam [4].

PCUs consist of one or two electric or hydraulic drive sources [4]. In the case of dual drive their outputs are coupled by either a torque or speed summing gearbox [8]. This redundancy ensures functional reliability [6]. Sensors on the PCU output provide feedback of the system position to the secondary flight control computer (SFCC) [4].

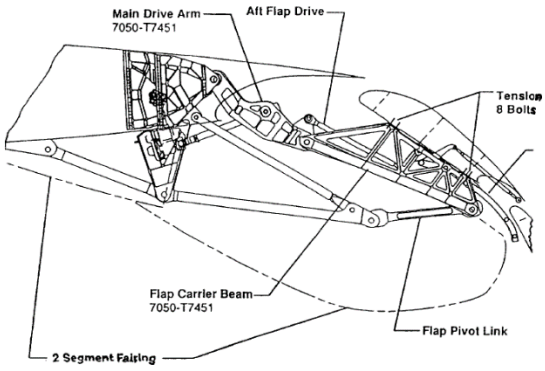

Four-Bar Link, Double-Slotted Flap Mechanism

(Boeing 777 Inboard Flap)

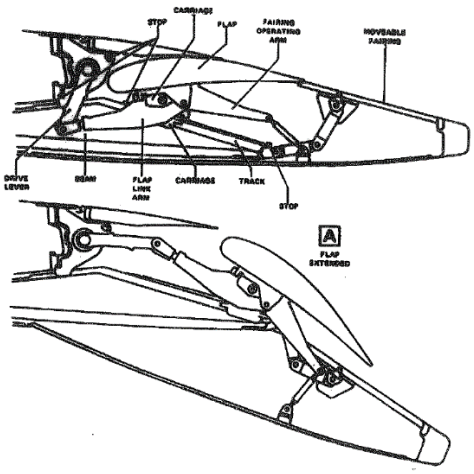

Link-Track, Single-Slotted Flap Mechanism

(Airbus A320 Flap)

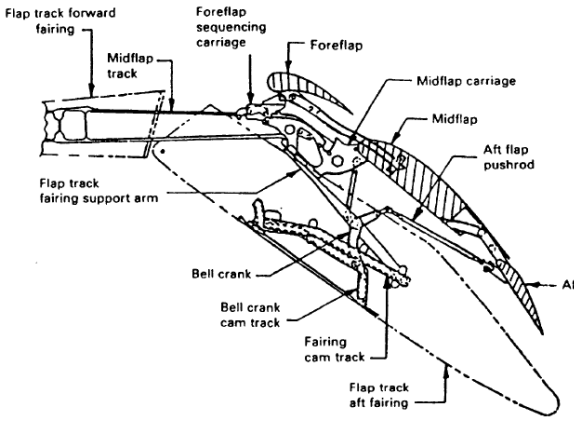

Hooked Track, Triple-Slotted Flap Mechanism

(Boeing 727 Flap)

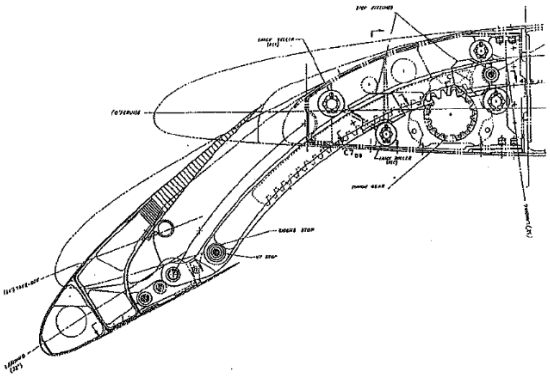

Rack and Pinion Track Mechanism

(Boeing 757 Slat)

Figure 2-2 Example High-Lift Panel Mechanisms [2]

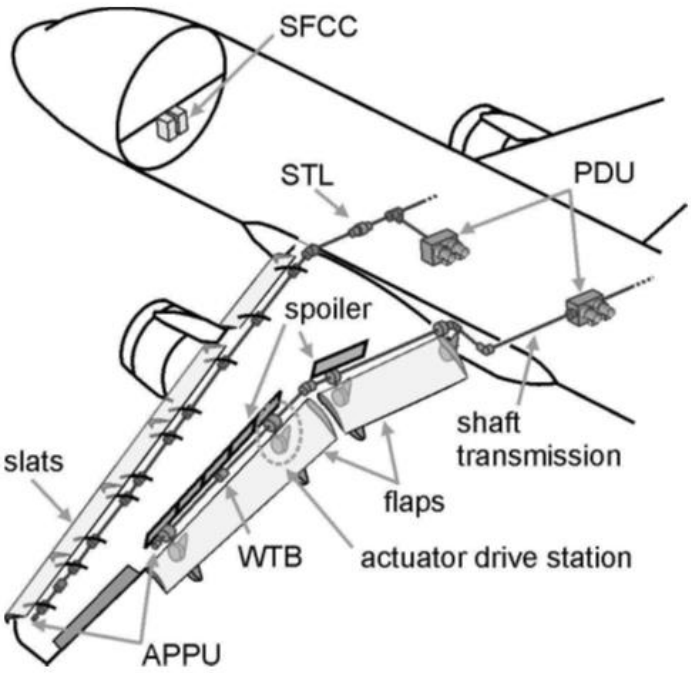

Figure 2-3 – Typical High-Lift System [4]

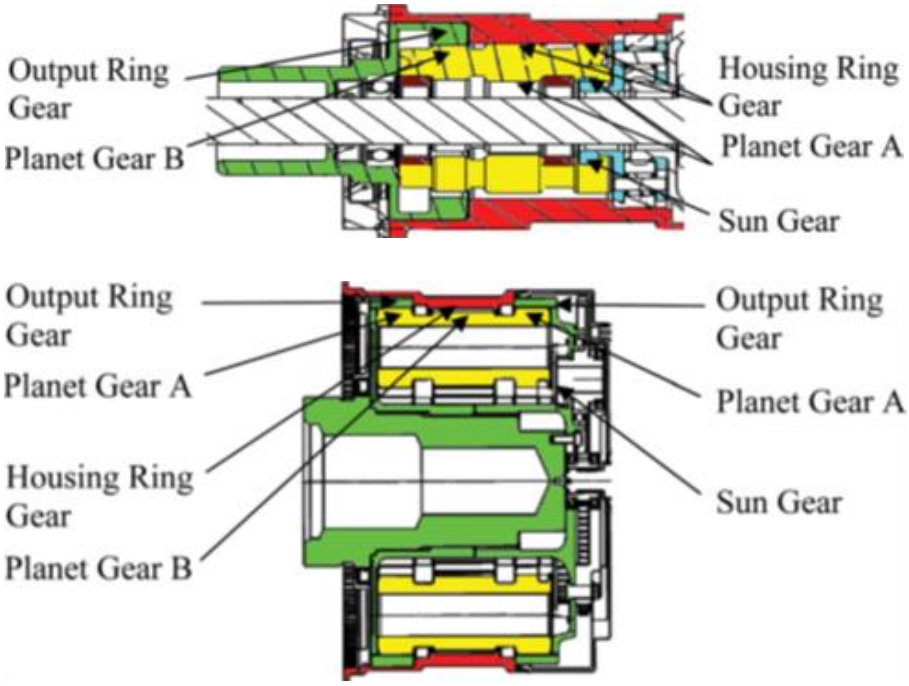

Figure 2-4 Section Views of Slat (top) and Flap (bottom) CPE GRAs [9]

The transmission system connects and synchronises the actuators by a system of thin-walled tubular torque shafts. Directional changes of the shaft routing are achieved with small bevel or spur gearboxes, whilst misalignments and length changes resulting from wing bending and temperature effects are compensated for using universal joints and splined couplings. Tee-gearboxes are used for drive branching where required [10]. Protection must be provided against the possibility of a shaft rupture; a scenario usually addressed by passive irreversibility devices or actively controlled wing-tip brakes [4]. Torque limiting devices may be included in the transmission line in addition to those at the individual actuator stations [10]. A schematic view of the A330/340 flap system is shown in Figure 2-5, and provides an indication of the large number of elements that comprise a typical high-lift actuation system.

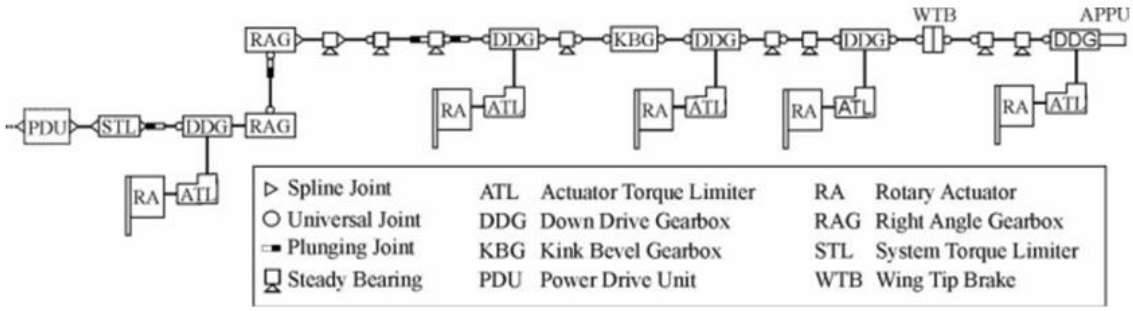

Figure 2-5 Schematic View of Airbus A330/340 Flap System [10]

2.1.3 Operating Environment

High-lift equipment is generally designed for a service life of 20 years [11] and is installed in a relatively environmentally exposed location. During this time the equipment is exposed to cyclic variations in temperature and pressure, exposed to salt-laden and humid air, and subjected to prolonged vibration and low-temperature soak. Environmental resistance is confirmed prior to entry to service by tests in conditioned chambers or on shaker tables, to industry or airframer standards. A common set of test conditions for aerospace equipment is provided by RTCA-DO160 [12]. The commonly applicable test categories for high-lift equipment are shown in Table 2-1 as an indication of worst case in-service operating conditions.

Key amongst these operating parameters is the low temperature that the equipment is exposed to. Following a long flight, the equipment can be deep frozen, resulting in significant increases in lubricant viscosity.

Table 2-1 Environmental Test Categories for High-Lift Equipment per RTCA-DO160 [12]

Section	High-Lift Test Category	Key Parameters
Temperature and Altitude	D2	-55°C to +70°C 50,000ft (11.6kPa)
Humidity	B	95% RH
Waterproofness	R / S	Continuous water stream /spray
Salt Fog	S	48 hour exposure to 5% salt solution mist
Vibration	R (Curves E & E1)	11.33 G_{RMS}

2.1.4 Gear Arrangements and Lubrication

Referring to the descriptions of high-lift devices in previous paragraphs, the types of gear arrangements included in high-lift systems can be summarised as below in Table 2-2. Significant reduction ratios are incorporated within the PCU to reduce the speed from the drive motors to a level that can be transmitted through the torque shafts, and within the RGAs to further reduce the output speed and increase the torque delivered to the linkages of the panel deployment mechanism. Consequently, a typical high-lift system includes gear arrangements with a wide range of torques and speeds: from thousands of revolutions per minute down to less than one.

Table 2-2 Summary of Gear Arrangements in High-Lift Systems

Gear Arrangement	Applications
Spur Gear	GRA downdrives
	Transmission gearboxes
	Sensor “pick-off” drives
	Torque-summing PCUs
Spur Gear Differential	Speed-summing PCUs
Epicyclic	Speed-summing PCUs
	GRA pre-stages
Compound Planet Epicyclic	GRA power stages
Bevel Gear	Transmission gearboxes
	GRA downdrives

Lubrication of the gear meshes is influenced both by environmental and tribological considerations. Lubricants must be selected to keep drag losses to manageable levels at low temperatures and offer protection against corrosion by water ingress, whilst providing load-carrying capability to the working surfaces. Di-ester semi-fluid greases such as those controlled by SAE AMS 3057 having been favoured in modern times, having been specifically designed for use in

Airbus high-lift GRAs [11][13]. These have tended to displace traditional thicker greases as they offer superior corrosion protection, though metallic-soap greases are still employed in many transmission gearboxes. Higher speed meshes such as PDU differentials use more conventional oil lubrication. Synthetic ester turbine oils are common for their low temperature performance and long-term stability.

When employing oil or semi-fluid grease a splash-lubrication approach is followed: each actuator or gearbox is partially filled with fixed quantity of lubricant and the motion of the rotating components is used to distribute the fluid amongst the working surfaces.

2.1.5 Sources and Consequences of Power Loss

As noted by Höhn et al. [14] power losses in a gearbox can be separated into the individual losses of the bearings, gears, seals, and auxiliaries. The losses associated with the bearings and gears can be further divided into zero-load (or "no-load") and load-dependent losses:

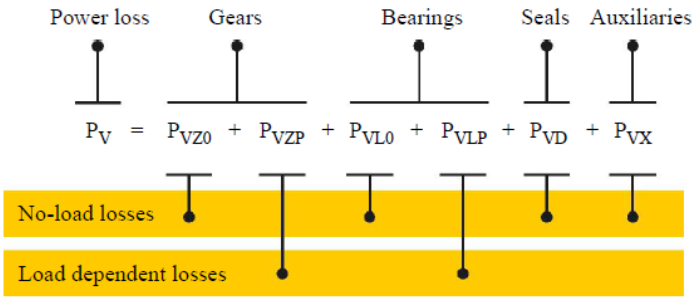

Figure 2-6 Sources of Power Loss in Gearboxes [14]

The load dependent losses stem from frictional forces between the sliding surfaces of the gear teeth and bearings. The zero-load losses include friction from seals or any connected auxiliaries such as sensors but are more strongly influenced by churning losses resulting from interaction between the lubricant and the partially immersed rotating gears and bearings [15]. These losses become more significant with increasing fluid viscosity and shaft speed [16]. When a high-lift system is operating at very low temperatures the viscosity of the lubricant increases significantly, and therefore lubricant churning is a major source of power loss.

The obvious consequence of these losses is that the system PCU must be increased in power output, adding both weight and volume to the system. During various failure scenarios, such as a torque-limiter lockout, the full stall torque of the PCU can be applied to the transmission or RGAs.

These conditions often define the limit torque requirements for downstream components. Such components will require strengthening in order to tolerate the increased torque generating capability of the PCU. Consequently, when zero-load losses are high it leads to an increase in component weight throughout the system. This relationship is illustrated in Figure 2-7, adapted from [4]. Note that although the diagram refers to “friction losses”, this relationship applies equally to zero-load and load-dependent losses.

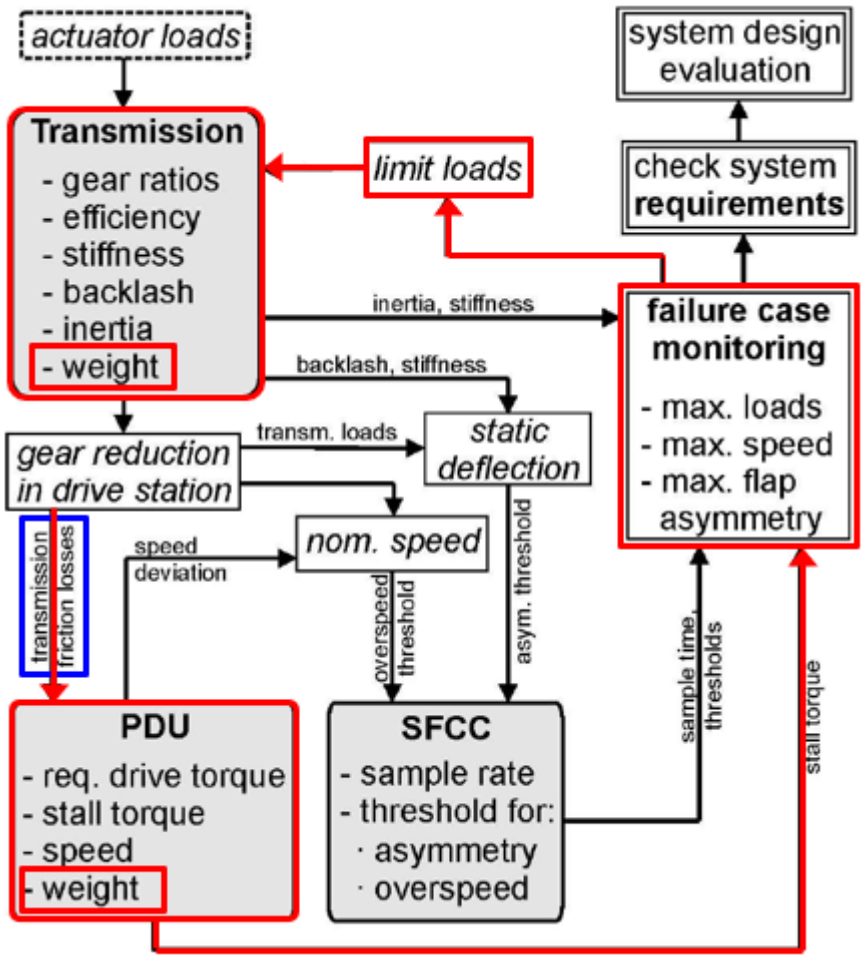

Figure 2-7 Diagram showing Transmission-Loss to System Weight Relationship (adapted from [4])

The temperature dependent nature of the zero-load losses also has implications for system design and strength. System torque limiters are set to trip when the transmitted torque exceeds a predetermined value and reroute any excessive torques to the aircraft structure and protect the RGAs and deployment mechanism. When deriving torque limiter trip settings, a balance must be struck between avoiding nuisance trips and protecting the structure against damaging torques. Consequently, the variation in the system losses effectively narrow the range of acceptable torque limiter settings.

2.1.6 Reducing Zero-load Power Loss in High Lift Systems

Given that the significance of fluid induced zero-load losses at low temperature, a possible approach to reduce overall power loss would be to replace fluid lubricants with solid lubricants: either applying a lubricious, wear resistant coatings to the gears, or constructing them from materials with inherent lubricating or wear resistant properties. Such a coating would need to provide comparable tooth friction, such that the reduction in zero-load loss isn't negated through increased load-dependent loss.

High-lift actuation offers a significant opportunity for the implementation of solidly lubricated gears due to aspects of the operational life and environment that are specific to it. Firstly, the operating life of the system is relatively short. Flaps and Slats are generally only deployed and retracted prior to and after take-off and landing. Typical system deployment or retraction times are less than one minute, sometimes with pauses at intermediary "gated" positions. For a typical single-aisle airliner with a specified life of 60,000 flight cycles, this translates to approximately 1,000 hours of operation. This compares favourably with other geared systems on an aircraft, such as engine accessory gearboxes, which run continuously during flight and whose operating life can be well over 100,000 hours.

Furthermore, this duty is accumulated over a high number of short-duration movements, usually with long rest periods. Consequently, the potential for generating tooth temperatures that may soften materials or aggravate wear modes is reduced. High lift devices are therefore less dependent on the fluid lubricant as a method of dispersing the heat generated at the tooth surfaces.

2.1.7 Secondary Benefits of Adopting Solid Lubrication

Fluid lubricants within a commercial high lift system are often replenished as a scheduled maintenance task to replace any lost due to leakage and to ensure lubricant quality. Lubricant leakage is one of the most common causes of in-service actuator removal, usually occurring at the dynamically sealed interfaces of the rotating shafts. These seals must tolerate large variations in temperature, atmospheric pressure and humidity and achieving completely leak-free sealing often proves problematic. A solidly lubricated system could offer reduced maintenance and improved reliability.

2.2 The Tribology of Involute Spur Gears

2.2.1 Spur Gear Geometry

2.2.1.1 The Involute Tooth Profile

Gears are machine components that transmit rotary mechanical power through the use of meshing teeth. They can be used to change the speed, torque, or axis of a rotating system. The fundamental law of gearing, attributed to Willis (1841) [17], states that in order to transmit rotational mechanical power with uniform ratio the common normal between the mating surfaces of the teeth must at all points of contact pass through a fixed point on the line of centres. This point is known as the pitch point.

In modern times this is almost exclusively achieved with gear teeth profiles based on the involute curve. Involute gears are favoured as the path of contact is a straight line giving smooth operation and constant bearing loads. Additionally, they can tolerate errors in centre distance without affecting the ratio and cutting tools can be cheaply and accurately made [18].

The involute curve can be visualised as the path traced by the end of a piece of string being unwound from a cylinder. The circle from which the involute is generated is referred to as the base circle. Consequently, the radius of curvature of the tooth increases from root to tip and tends to zero when approaching the base circle. See Figure 2-8.

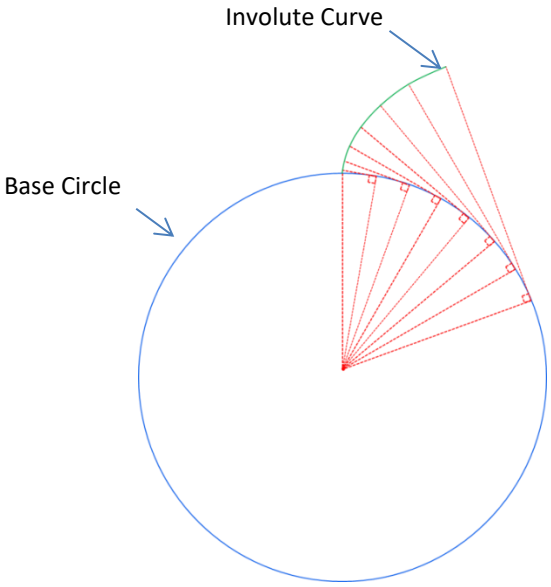

Figure 2-8 Generation of the Involute Curve (Redrawn from [20])

2.2.1.2 Tooth Size, Form, and Proportions

During the meshing action of involute teeth, the path of contact follows a straight line, known as the line of action, which is cotangent to the base circles. The angle between the line of action and a line normal to the line of centres is referred to as the pressure angle α. See Figure 2-9. A high pressure angle implies that the base circles are small relative to the distance between centres. Consequently, the pressure angle has a significant impact on the tooth form. The pressure angle is also the angle through which the forces act upon the supporting bearings. The most common standard pressure angle is currently 20°, though 22.5°, 25°, or other non-standard values also see use [20].

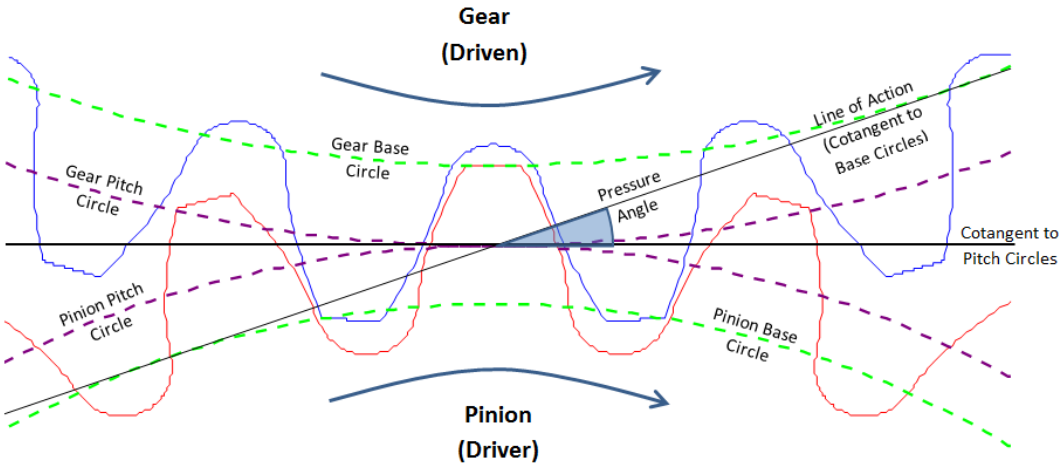

Figure 2-9 Definition of Pressure Angle (Redrawn from [19])

The basic unit for specifying the size of the teeth in European countries is module *m,* which is specified in terms of mm of pitch circle diameter d_p per tooth, the pitch circle being the circle with radius equal to the distance from the gear centre to the pitch point. For a given number of teeth a gear with a higher module will therefore be larger and have bigger teeth.

Whilst the pressure angle defines the form of involute curve, the section of the curve used for the tooth profile, and the tip and root diameters must be specified. This is accomplished by specifying the addendum and dedendum sizes. The addendum *A* and dedendum *D* are the height per unit module above and below the pitch circle respectively. The most common proportions are addendum 1*m*, and dedendum 1.25*m* [20]. The additional dedendum length gives space for a fillet to be added for strength at the root radius. Finally, the face width *b* of the teeth along the axis of rotation must be defined. These parameters complete the basic definition of involute tooth geometry.

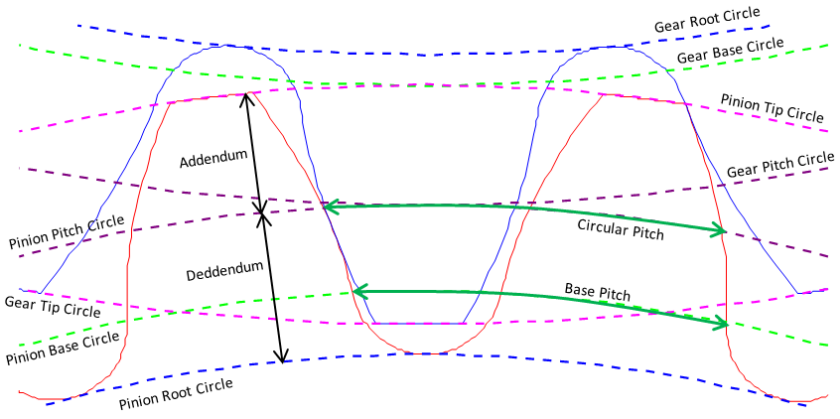

Figure 2-10 Definition of Addendum, Dedendum and Pitch (Redrawn from [19])

2.2.1.3 Tooth Modification

In addition to the basic definition above, the gear tooth geometry may be modified further. Modification, sometimes called “correction”, involves altering the addendum and dedendum proportions. For a given centre distance the addendum of one gear can be lengthened by shortening the addendum of the other gear in mesh. In this situation the inverse must be applied to the dedendum of both gears. These modifications can be used to improve the strength of gears with small numbers of teeth. It also alters the proportion of approach and recess in the gear pair’s action [20]. These refer to the size of the length of action before and after the pitch circle respectively, see Figure 2-11.

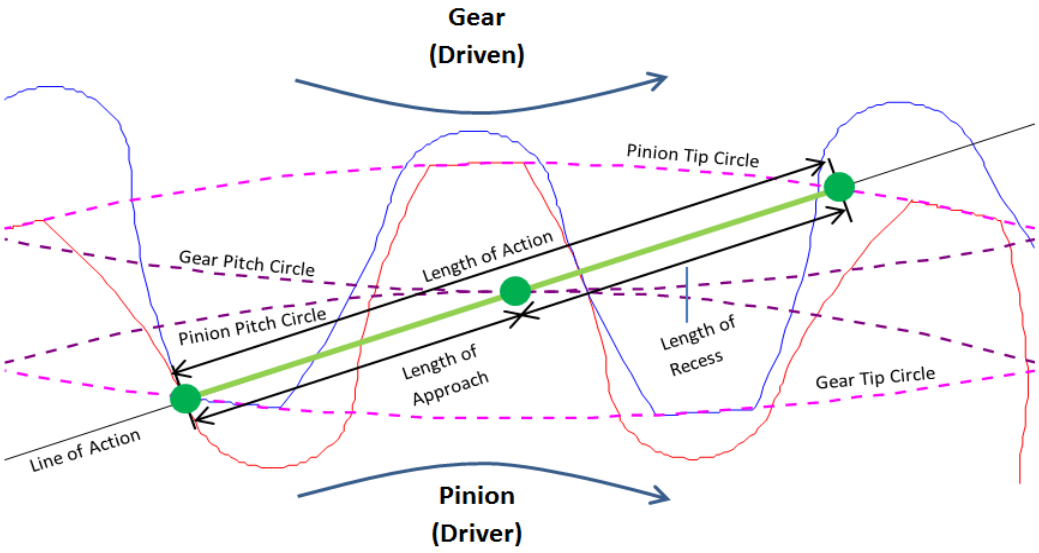

Figure 2-11 Definition of Approach and Recess (Redrawn from [19])

Further modifications come in the form of tip relief, root relief and crowning. Tip and root relief remove a small amount of material from the tips or roots of the teeth to reduce loads at the point of tooth engagement and disengagement. In practice it is more common to apply tip relief to both gears than tip and root relief to one gear as this is easier to control and removing material from the root of the tooth is detrimental to strength. Tip relief is specified in terms of the "amount" of material removed at the tip, and the "extent"; the length over which it tapers back to true involute. See Figure 2-12. The taper may have a linear or parabolic profile [21].

Modifications may also be applied along the face width in the form of lead crowning. Lead crowning removes material from the edges of the tooth face to avoid point contacts occurring due to misalignment. This comes at the expense of raising the nominal contact stresses [20]. It can be specified in terms of the resulting radius of curvature, or the amount of material removed at the edges.

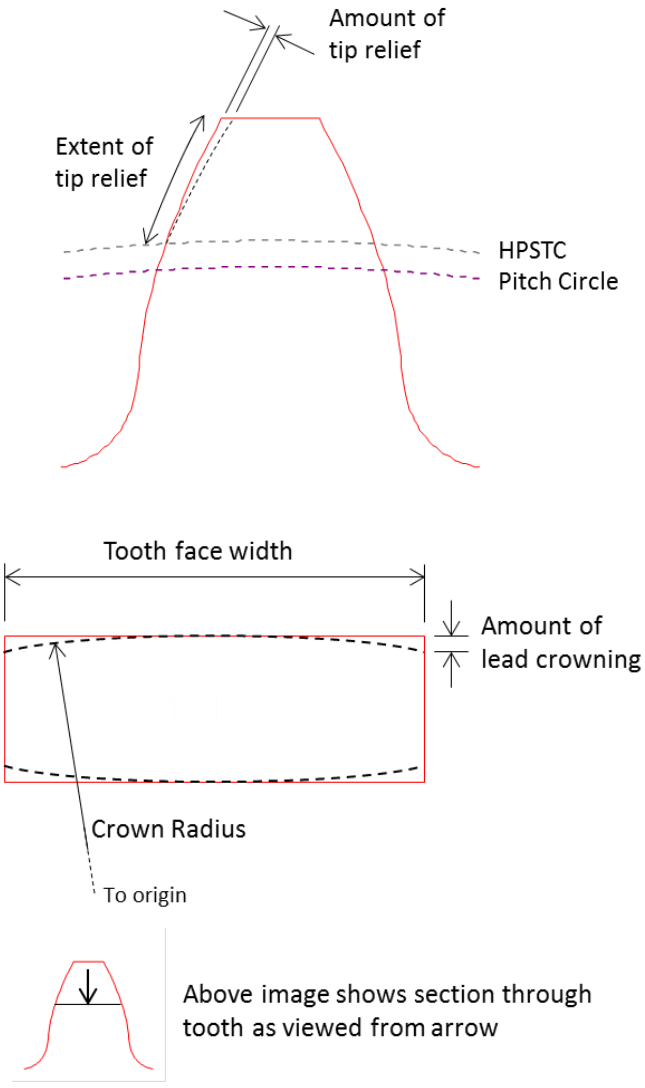

Figure 2-12 Definition of Tip Relief (top) and Lead Crowning (bottom) (Adapted from [22])

2.2.2 Tribological Failure of Conventionally Lubricated Spur Gear Teeth

A multitude of terms are used to define and categorise the various ways in which gear teeth can fail. Some discrepancies exist between the terms used in different industries and on different continents. This study uses the definitions set out by Errichello [23]. As the primary focus is on the use of solid lubricants on gear teeth, the paragraphs below will concentrate on those failure modes that are identified as being lubrication-related, and therefore most likely to be exacerbated by adopting a solid lubrication approach. These are hertzian fatigue, wear, and scuffing.

2.2.2.1 Hertzian Fatigue

When curved surfaces such as gear teeth are loaded against one another, intense shear stresses develop below the surface. These are referred to as Hertzian stresses. Sliding and friction at the contact further increases the stresses and moves the peak stress closer to the surface. See Figure 2-13. As gear teeth repeatedly pass through mesh, they are cyclically subjected to these Hertzian stresses. Eventually the stress cycle leads to the development of a crack either on or below the surface through fatigue. These cracks grow parallel to the surface before branching upwards, causing a particle of material to be ejected [24].

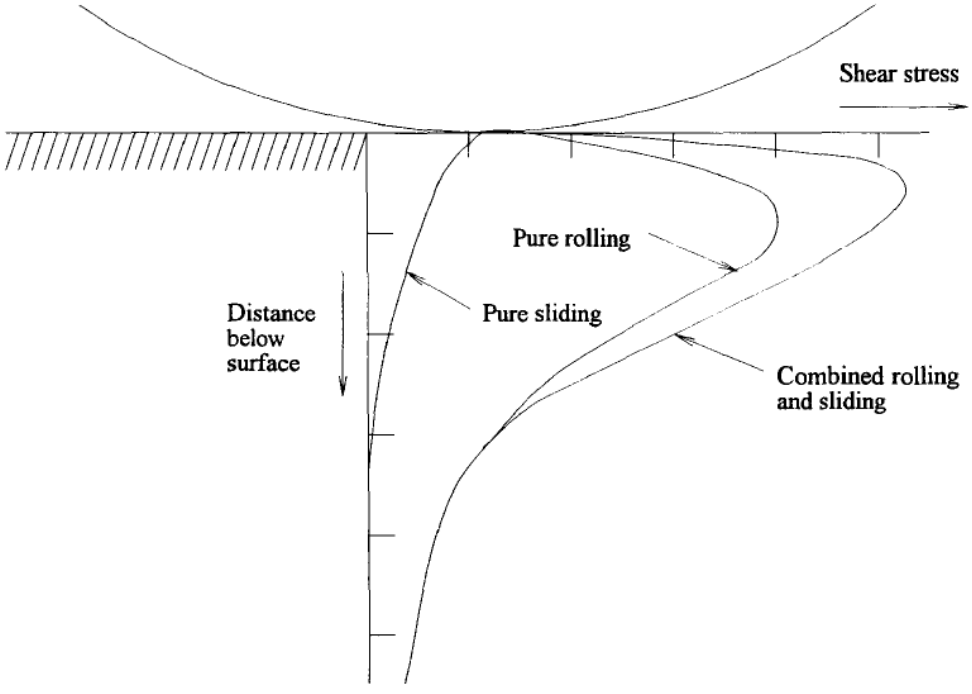

Figure 2-13 Subsurface Shear Stress Distribution for Rolling-Sliding Contacts [24]

Hertzian fatigue is more commonly known as “pitting” and is often subcategorised into macropitting and micropitting. It is visually characterised by the formation of pits on the tooth surface. In macropitting these may be several millimetres across whilst micropitting produces pits typically 10µm in size, giving teeth a “frosted” appearance [23]. Photographs of gear teeth suffering from macro and micropitting are shown in Figure 2-14 and Figure 2-15. Micropitting tends to occur in gears with surface hardened teeth.

Figure 2-14 Macropitting [25] (left) and Micropitting [26] (right) Damage to Tooth

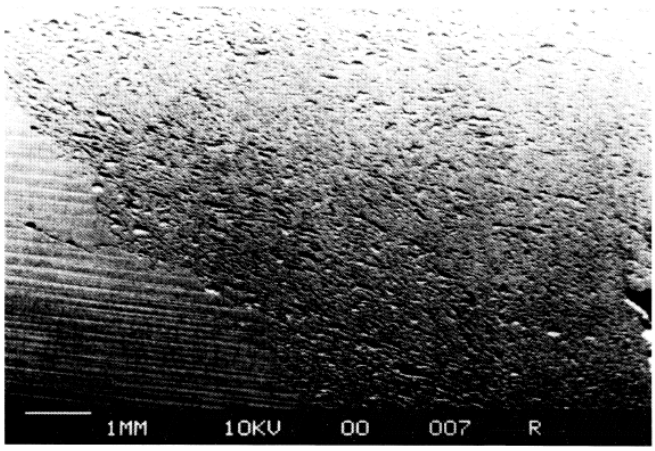

Figure 2-15 Micropitted Tooth at 15x Magnification [27]

For a given gear pair and assuming fixed size and duty, minimising surface roughness [28] and maximising surface hardness [29] both lead to improvements in pitting lives. Pitting often starts at a non-metallic inclusion near the surface, which acts as a stress concentration [30]. Consequently, cleaner steels tend to have longer pitting lives. Processes such as shot peening, which induce compressive stresses into the surface, also help by reducing the subsurface shear stress and slowing crack growth [31]. Pitting lives are also increased by using viscous lubricants to maximise film thickness and prevent asperity contact [32].

2.2.2.2 Wear

Errichello [23] identified three modes of wear between spur gear teeth: adhesive, abrasive, and polishing. Adhesive wear is sometimes referred to as “mild wear” to further distinguish it from scuffing, which also follows an adhesive mechanism but is far more severe. Adhesive wear is caused by sliding in the presence of adhesive forces between the contacting surfaces. Two surfaces bought together under load will form bonds, particularly similar or ductile metals. When the surfaces slide this can cause material to tear away, being either transferred to the other surface or released as a particle [33].

Adhesive wear often results in a slow removal of material and is sometimes referred to as “mild”, “slow-speed”, or “steady-state” wear. It can cause a smoothing of the surfaces, leaving a polished appearance with occasional fine radial grooves [27], see Figure 2-16. The “running-in” of gears at a low power to smooth surfaces though mild wear and prevent subsequent scuffing is common practice among manufacturers [33].

The parameters affecting the rate of mild adhesive wear have received less attention than might be expected as studies instead tend to focus on the prevention of transitioning to the far more destructive scuffing regime. However, many of the prevention strategies are similar. Maintaining a high lubricant specific film thickness prevents contact and bonding between the surface asperities. Consequently, the use of high viscosity oil and pitch line speeds [29], and smooth surfaces [34] are advised. Careful lubricant additive selection is also important. Whilst solid lubricant suspensions such as molybdenum disulphide can reduce the wear rate, phosphor or sulphur-based additives designed to prevent scuffing can actually encourage mild wear at low speeds [29].

Abrasive wear is damage caused by the loaded sliding of hard particles or asperities. In gearboxes hard particles can be a contaminant ingested from the environment, built-in during assembly, or generated internally by wear, scuffing or pitting. These are examples of three-body abrasion and can quickly lead to material loss, indentation, and increased friction [35]. Two-body abrasion can occur where hardened gears with a rough finish are paired with a softer gear like bronze. The harder gear acts like a file and abrades the softer gear to remove material [23].

Abrasive wear is a complex process that removes material through a combination of ploughing, wedging, cutting, microcracking and microfatigue [36]. It is visually characterised by grooves or scratches orientated radially in the direction of sliding, with irregular spacing and length [27]. Three-body abrasive wear is prevented by eliminating or removing the contaminants. This can be achieved by preventing debris generation, lubricant filtration or replenishment, robust sealing, and clean assembly procedures.

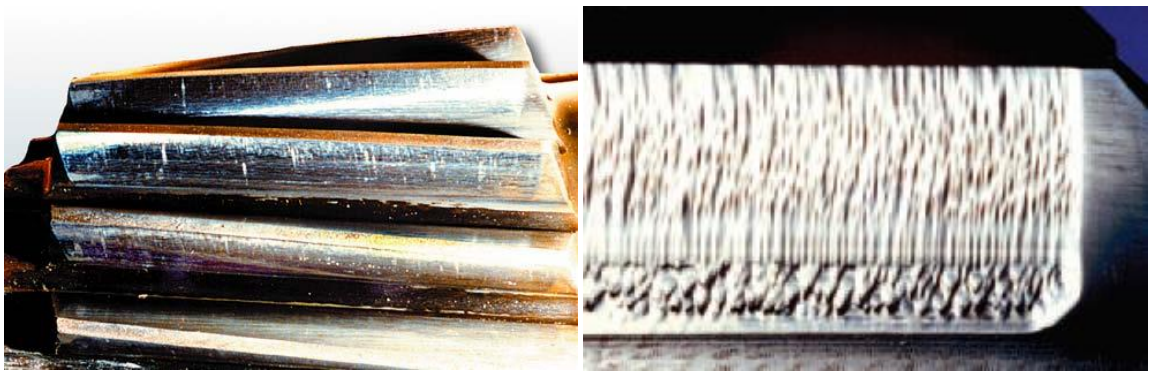

Figure 2-16 Sliding Wear to Tooth Flank due to Adhesion (left) and Abrasion (right) [25]

2.2.2.3 Scuffing

Errichello defined mild wear as being confined to the oxide layer of the material. However, when contact stresses or sliding speeds are very high the protective layer of oxides and adsorbed impurities is worn away. This allows direct contact between clean metals. The high contact pressure at the asperities and sliding motion causes solid phase welding due to frictional heating. The sliding between the teeth then causes tearing and can lead to rapid damage of the surface [23]. Scuffed tooth surfaces have banded areas with a rough, torn appearance running in the direction of sliding. See Figure 2-18 [25].

The transition to scuffing can occur suddenly and causes a rapid increase in wear rate (see Figure 2-17), friction, noise, and heat [37]. As scuffing is generally not tolerable, rather than estimating a life under scuffing conditions, machinery is usually designed to operate in a safe regime that prevents its occurrence [38].

Whilst the precise conditions that lead to scuffing are not completely understood, it is generally accepted that it requires a failure of both the lubricant and surface films in the presence of high contact temperatures [39]. Under high contact pressure the viscosity of the lubricant increases, which in turn leads to an increase in friction. The increased friction leads to an increase in temperatures, and a reduction in viscosity. Dyson [40] proposed that these competing mechanisms form an equilibrium until a critical load is reached, at which point the lubricant film breaks down and scuffing occurs.

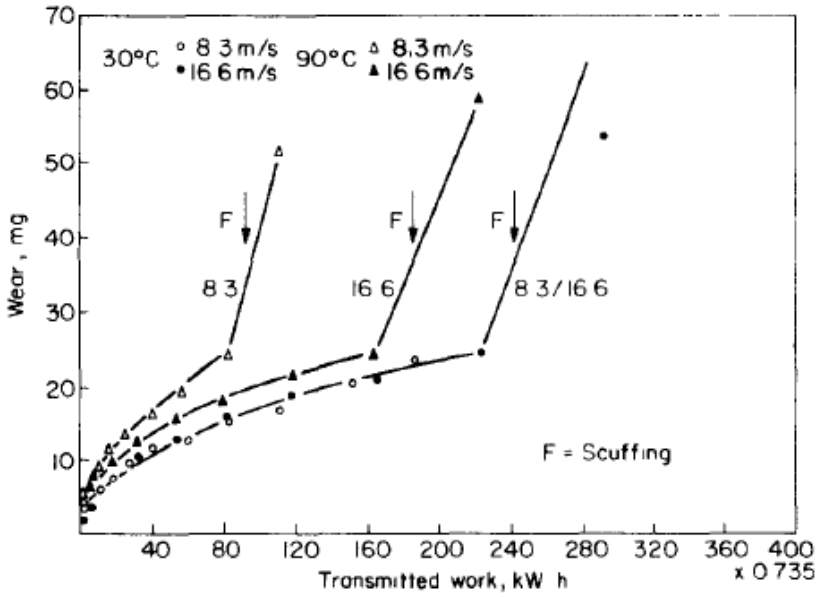

Figure 2-17 Power vs Wear Rate for Oil Lubricated Gear Pair at Different Pitch Line Speeds and Oil Temperatures showing Scuffing Transitions [41]

Figure 2-18 Scuffing Damage to Helical Gear Tooth [25]

For a given gear pair the safe operating range to avoid scuffing can be extended by the use of smooth tooth surfaces [42], whether through manufacturing alone or in conjunction with a controlled running-in process [43]. The use of viscous lubricants to maximise film thickness reduces asperity interactions and further improves resistance to scuffing [44]. Lubricants for gear applications at risk of scuffing frequently make use of phosphor or sulphur based anti-wear or extreme pressure (EP) additives. These react with the surfaces of the metal at areas of high local temperature to produce films that prevent welding [45]. As shown in Figure 2-17, elevated oil

temperatures cause a reduction in the scuffing capacity of the gearset. This is particularly true of non-EP oils as the reduction in viscosity cannot be compensated for by increased chemical activity of the additives [46]. Therefore, cooled circulating lubrication systems incorporating heat exchangers are more effective at preventing scuffing than simple splash-lubricated designs.

The scuffing capacity of a gear set can also be optimised through careful design. Gears with large numbers of small teeth are preferable as sliding velocities are lower, albeit at the expense of strength [37]. Addendum modification can be used to reduce the amount of approach action. This reduces the amount of sliding at the root of the pinion and increases the scuffing load [47]. Further improvements can be made with the addition of tip relief to reduce loads at the extremes of the line of action where sliding is at its highest [48]. For scuffing prevention, tests have shown that nitriding has been shown to be preferable to carburising for surface hardening, provided the compound white layer is removed [49].

For lubricated gears the three regimes of tribological failure are traditionally mapped against the load and speed duty of the gearset as shown in Figure 2-19. With sufficiently high load at low speeds the lubricant film thickness is too low to prevent wear. At high speeds the temperatures cause the lubricant film to fail, and scuffing occurs. If the load causes sufficiently high Hertzian stress, there is a risk of pitting failure. At very high loads strength-based failure occurs.

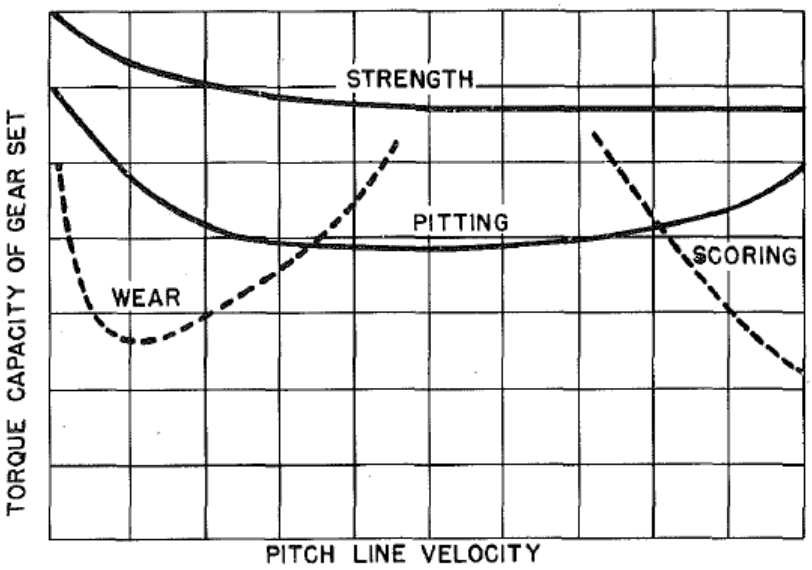

**Note that "scoring" is commonly used by American engineers to describe scuffing*

Figure 2-19 Map of Gear Failure Modes according to Load and Speed [34]

However, although not discussed by Errichello, an uncommon failure mode similar to scuffing is also possible where speeds are very low, and loads are high. Low speed scuffing is usually termed "cold scuffing" to distinguish it from conventional high speed or "hot scuffing". In this instance

whilst the speeds are too low to form a lubricating film, the loads are high enough for welding and tearing to take place. Cold scuffing causes severe damage in the form of deep weld tears and subsequent abrasion and plastic deformation as particles become embedded in the surfaces. See Figure 2-20. It is most common in grease lubricated gearboxes [50].

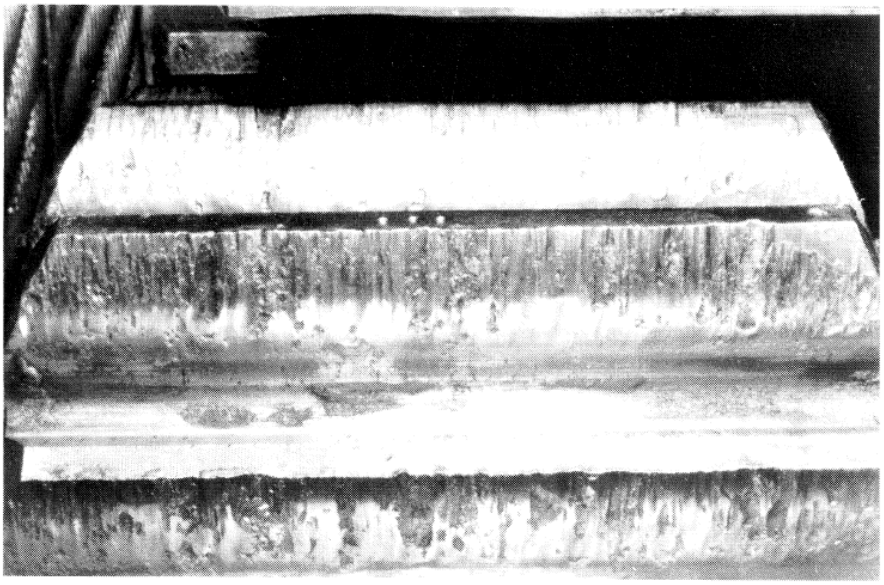

Figure 2-20 Cold Scuffing Damage to Gear Tooth [27]

2.2.2.4 Tribological Failure of Solid-Lubricated or Dry Spur Gear Teeth

Very little evidence is available on the subject of dry-running metallic gears: a testament to the commonly accepted significance of fluid lubricants in the prevention of failure. The most significant work was presented by Walton and Goodwin[51], who reported a series of tests on dry uncoated and coated gears under several load-speed combinations and tooth designs. However, the underlying surface degradation mechanisms were not discussed in detail and therefore some interpretation of the evidence presented is required.

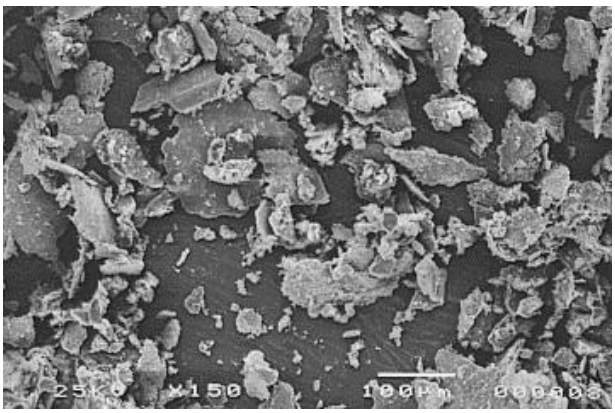

Figure 2-21 Wear Debris from Normalised EN8 Gear following Dry-Running Operation [51]

For uncoated gear pairs the primary failure model was described as “gross wear”. SEM inspection of debris particles from a worn unhardened EN8 gear found they consisted of large thin flakes of the type commonly found in dry adhesive wear [52]. The test results included significant nonlinearity of wear with regards to load, which may indicate that a wear mode transition had occurred over the test range. Additionally, it was noted that each combination of pinion and gear material exhibited a critical speed, above and below which the wear rate increased.

Walton and Goodwin proposed that this type of behaviour could be explained by the interaction of temperature and oxidation of the surface. This theory would appear to have merit as raising the running speed for a given torque both increases the rate of surface oxidation due to increased frictional heating, whilst reducing the available time between tooth engagements for oxide layer repair to take place. Lancaster noted a similar phenomenon when studying wear transitions for dry sliding 60-40 brass on tool steel [53].

The only image provided of a worn surface is for a spheroidal graphite (SG) iron tooth, which could correspond to the description of either severe cold scuffing or abrasive wear, see Figure 2-22. The teeth are heavily scalloped above and below the pitch circle with deep grooves in the direction of sliding. It appears that this gear was run against a case-hardened steel gear, and therefore it is possible that it has been worn by two-body abrasion due to the discrepancy in hardness (142Hv vs. 700Hv). However, it was noted that an aluminium bronze gear wore far more rapidly yet maintained a better surface finish and had a comparable hardness (180Hv). It is also noted that whilst the SG Iron gear appears heavily damaged it was one of the best performing uncoated gears and the photograph was taken after significant running. Loss-of-lubrication tests on gears conducted by Handschuh et al. [54] yielded worn teeth with a similar appearance. See Figure 2-23.

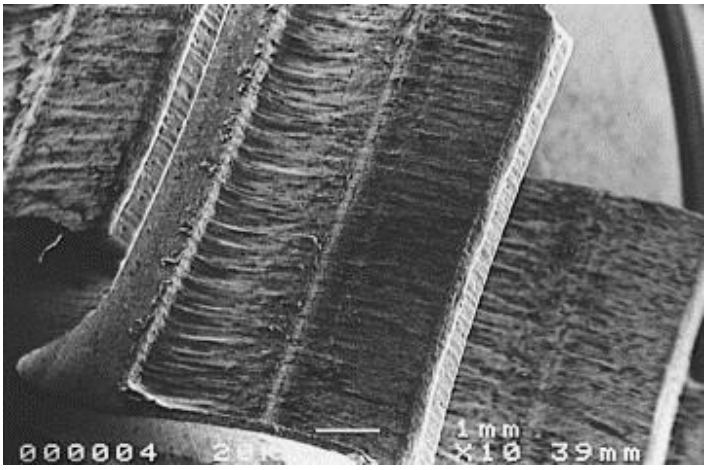

Figure 2-22 Worn Spheroidal graphite Iron Tooth following Dry-Running Operation [51]

Figure 2-23 Failure of a Spur Gear Following Loss-of-Lubrication Testing [54]

Petrik [55] conducted tests on coated and uncoated spur gears with minimum quantity grease lubrication or dry conditions using a modified version of a DIN 51354 test stand. The gears were operated for fixed number of revolutions against gradually increasing loads. Between each load stage the gears were visually inspected for evidence of “seizure” or “galling” of the base material, the presence of which was used as failure criteria. Whilst no detailed analysis of the worn surfaces is presented, the photographs of worn teeth in the paper broadly align with those presented by Walton and Goodwin [51], with a line of lower wear evident at the pitch circle and more heavily worn regions above and below. Heavy score marks are present in worn areas, oriented in the direction of sliding. The exception is the photo for the plasma nitrided, CrN+DLC coated, unlubricated gears, which show small, localised patches of coating damage near the start of active profile (SAP). This appears to be possibly due to delamination, see Figure 2-24, but is not discussed within the text.

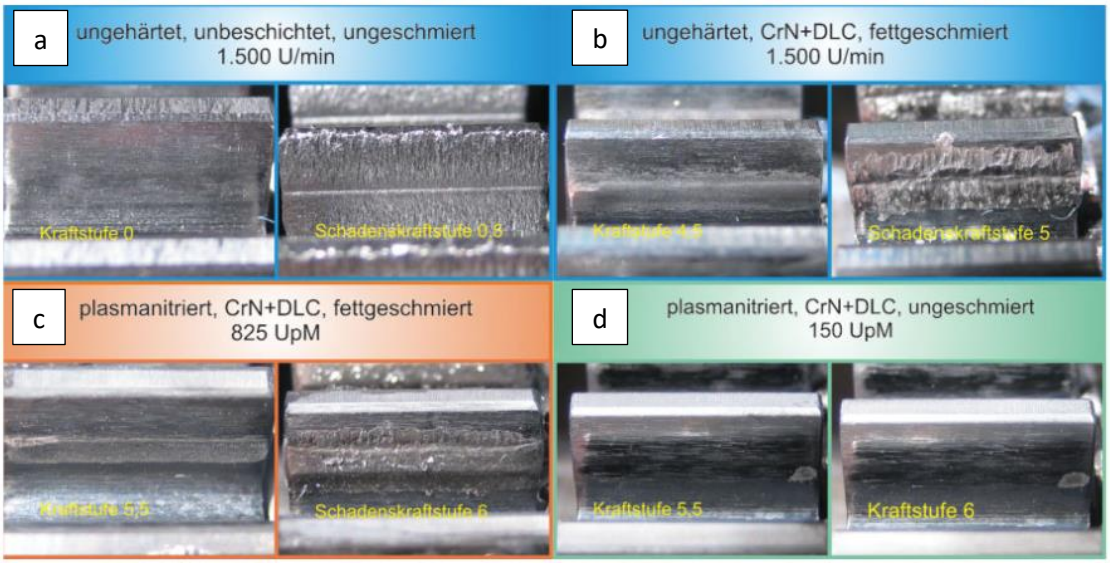

a) unhardened, uncoated, unlubricated, b) unhardened, CrN+DLC coated, greased

c) plasma nitrided, CrN+DLC coated, greased, d) plasma nitrided, CrN+DLC coated, unlubricated

Figure 2-24 Condition of Gear Teeth following Testing with Minimal Quantity Grease or Dry Lubrication [55]

The above evidence would suggest that under dry-running conditions the most likely cause of failure for unlubricated metallic gears is severe adhesive wear. A coating may prevent this severe wear, but only until the substrate is exposed.

None of the descriptions of damage in either study correspond to pitting. Experiments, dating back to those by Way [56] in 1935, show that pitting is only likely to occur when a rolling contact is lubricated. Termed “hydraulic pressure propagation”, the rolling motion causes lubricant to be pumped into surface cracks at high pressure, resulting in crack growth due to the forces acting on the interior of the crack. Without a fluid lubricant present the crack growth rate will be greatly reduced and may simply progress too slowly to present a pitting risk when subject to a high rate of sliding wear.

From considering the above evidence it is concluded that for dry or solid-lubricated gears the primary concern will be the prevention of adhesive wear to the metal surfaces, whether mild or severe (scuffing). However, there is clearly the potential for delamination failure of a lubricating coating to prematurely expose the substrate.

2.2.3 Models of Contact Conditions and Wear of Gear Teeth

This section discusses the analytical methods developed to analyse the contact conditions between spur gear teeth, and those that will prove relevant to the topic of solid lubricated gears. It was shown in the previous section that the most likely failure mode for dry or solid-lubricated gears is adhesive wear. With respect to the standard categories of gear failure this can include both mild wear and scuffing.

Separate analytical approaches have been developed in academia and industry for predicting the behaviour of mild wear and scuffing. Due to the progressive nature of scuffing damage, models focus on preventing its occurrence entirely rather than predicting a component life. As hot scuffing is linked to thermal failure of the oil film and welding of the surfaces, design approaches are most commonly based on limiting the contact temperature to a critical value for a given oil and material combination. In industry an adaption of Blok's equation for flash temperatures in lubricated sliding contacts [58] is used, a notable example being the rating formulae offered by AGMA [59]. These models are of limited use in the study of solid-lubricated gears, being both focussed on the fluid-based lubrication and lacking the life-prediction necessary to determine whether a coating depth is sufficient to endure for the design life of the gear.

Mild wear by comparison has received less attention, it often being considered that if scuffing is avoided then mild wear will result in an acceptable component life. However, several of the models developed to study mild wear attempt to predict the wear depth and distribution on the gear tooth. This is accomplished by assuming a rate of wear in relation to the contact stress and sliding distance in accordance with Archard's law [60].

Although the wear rate for a given pair of surfaces can only be reliably determined by test, this approach could potentially be used as a tool to subsequently predict the performance of a coating across a range of conditions. The subsequent paragraphs will therefore only address those wear models that provide a useful prediction of wear depth in dry or solid lubricated gears.

The contact conditions in terms of stress and sliding velocity are different at each point in the gear action. During gear rotation when a new tooth pair enters mesh the tip of the driven gear ("gear") tooth will initially contact the root of the driver ("pinion") tooth. As the gears continue to rotate the point of contact travels down the gear tooth and up the pinion tooth until the pair leaves mesh. The surface velocity of the point of contact on each tooth is different, resulting in a mixed rolling-sliding motion. Only at the pitch point are the surface velocities equal and pure rolling is present.

Additionally for the majority of gear meshes the contact ratio, the average number of teeth in mesh, is between 1 and 2. Consequently the tooth loads at the start and end of the line of action are carried by two tooth pairs, whilst close to the pitch point it is carried by a single tooth pair.

The fundamental model for understanding the variation in meshing conditions and their impact on surface failure is the equivalent rolling/sliding cylinders model. This treats the contact between the gear teeth as a pair of loaded cylindrical rollers of constantly changing radius and surface velocity. See Figure 2-25. Andersson [61] provided a series of formulae to determine the equivalent radii of curvature and velocities of the tooth surfaces during the mesh cycle in relation to the position of the contact on the line of action. The width of the contact and average contact stress can then be found from the tooth loads according to Hertzian theory. From the contact width and surface velocities for the equivalent rollers, a sliding distance can be calculated according to the principle of single point observation [62]. The wear to each tooth surface for each point on the line of action for a single mesh cycle can then be found according to Archard's Law.

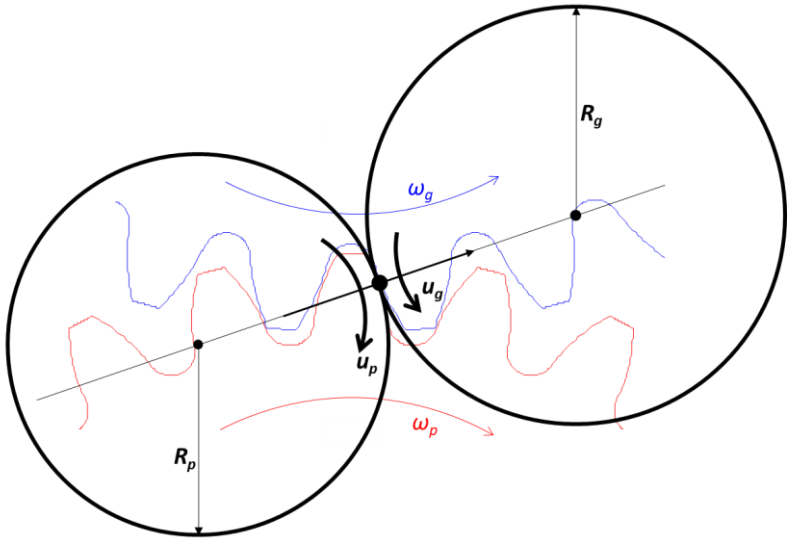

Figure 2-25 Contact between Spur Gears Modelled as Equivalent Rolling/Sliding Rollers per [61]

The equivalent-roller method applies several simplifications to the contact problem:

- The assumption of cylindrical geometry. The radius of curvature will in fact vary slightly across the contact width due to the involute curve of the surfaces.
- The use of a constant, average contact pressure as a point on the tooth surface travels through the contact. Actual pressure distribution will vary across the contact width.
- The assumption of fixed starting conditions for load sharing between pairs of teeth. As a gear pair wears during operation, the tooth loads are redistributed.

- The assumption of constant loads acting through the line of action. This quasi-static approach does not account for dynamic loads induced by stiffness and inertia effects, which are prominent at higher speeds.

The first detailed academic study in mild gear wear is credited to Andersson, who applied the principle of single-point observation to develop a set of equations for determining the effect of involute geometry on sliding distance [63]. This was developed into a wear model in conjunction with Eriksson [64]. In [65] Andersson and Põdra developed a wear model for use in rubbing contacts based on an elastic foundation model. This was then applied to modelling wear in spur gears in his paper with Flodin [61] in order to address the previous simplification that the pressure is constant across the contact zone.

This model also accounted for the change in contact zone geometry and tooth load share due to wear from previous wear cycles. The treatment of the effect of wear on subsequent tooth load share was based on a simplified form of the finite element work on tooth stiffness performed by Wang and Cheng [66]. This treats each tooth pair as a set of springs in series. Each other tooth pair in mesh is then another spring set in parallel with the first. Consequently, tooth wear for a given mesh position reduces the load acting on the tooth pair with the highest wear and increases it for the other pair in mesh. A comparison of the Flodin-Andersson and Andersson-Eriksson methods was provided in [61] and is shown in Figure 2-26.

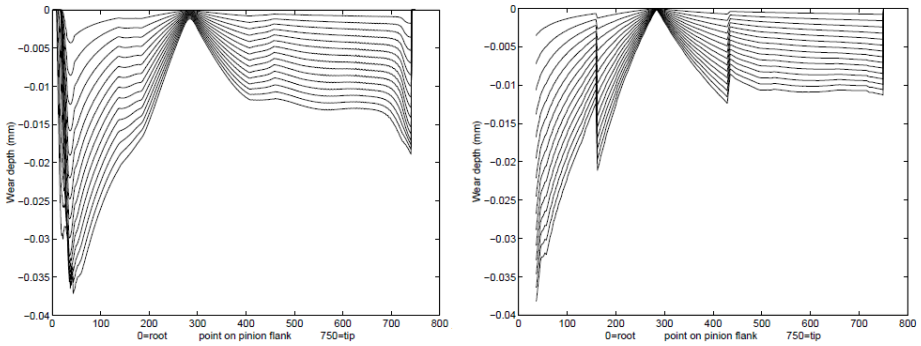

Figure 2-26 Comparison of Flodin-Andersson (left) and Andersson-Eriksson (right) Wear Models for Spur Gears [61]

The aforementioned paper by Wang and Cheng [66] also provides useful solutions for several aspects of gear tooth loading. Andersson and Flodin simplified the tooth stiffness as being constant throughout the meshing action. However, the original model from Wang and Cheng used finite element analysis to produce stiffness values according to the position of contact on the

tooth and the number of teeth on a gear. See Figure 2-27. This stiffness variation was used to calculate the dynamic operating load according to the speed, inertia, and dimensional errors on the gears.

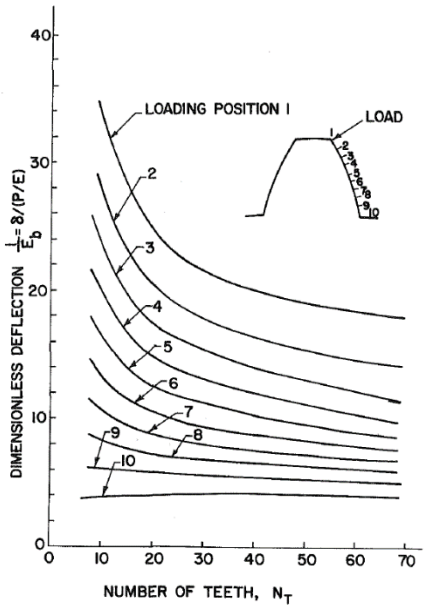

Figure 2-27 Dimensionless Tooth Deflection as a Function of Gear Teeth Number and Loading Position per Wang and Cheng [66]

Separate to works of Andersson et al., in 1993 Wu and Cheng [67] produced a model for calculation of wear in lubricated spur gears operating in the partial EHL regime, based on a rolling-cylinder approach. Not all aspects of the model are applicable to studies of gears operating under dry conditions with solid lubricants. However, they employed Wang and Cheng's approach to tooth stiffness and dynamic loading and provided the comparison between dynamic and static loads shown in Figure 2-28. Wu and Cheng's comparison shows that the dynamic load at a given contact position can differ significantly from the statically determined loads.

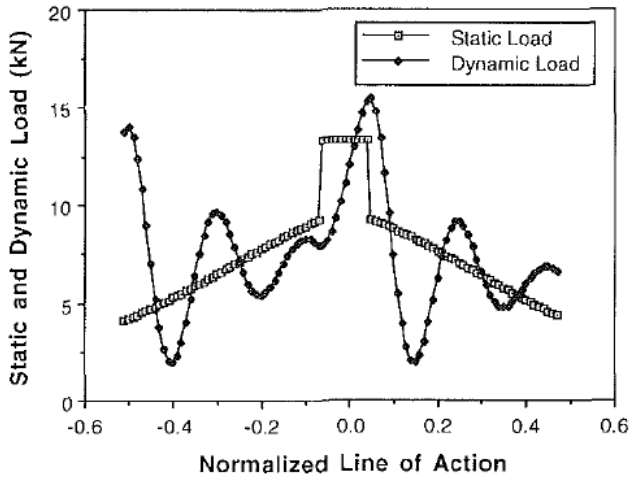

(Example based on 48T pinion, 80T gear, 20° pressure angle, 3.175 module, 1000rpm, and 100kW power)

Figure 2-28 Comparison between Dynamic and Static Load Patterns per Wu and Cheng [67]

Since Andersson's work the most noteworthy efforts to advance the modelling of the contact have emanated from the Gear and Power Transmission Research group at the Ohio State University. Their most recent work with respect to gear wear has been focussed on hypoid gear pairs [68] [69] [70] [71] as these tend to have high sliding velocities that result in sliding wear being a significant concern. However, prior to this the paper produced by Bajpai, Kahraman, and Anderson [72] proposed a fully three-dimensional model for spur and helical gears that used true measurements of tooth geometry including tooth profile modifications and manufacturing errors in the calculation of stresses and sliding distance. The contact pressure distribution was determined using combined surface integral and finite element methods as developed by Vijayakar [72]. Computation of sliding distance was then calculated using single-point observation at each discrete angle of rotation through the contact.

Vitally, this study includes a brief comparison between the results of the simulation and experimental tests, something generally lacking in studies of the modelling of gear wear. Wear coefficients were established from experimental tests on helical gears via Archard's equation and then used to estimate the wear in future cycles. These estimates showed a good correlation between the predicted and actual wear depth, see Figure 2-29. There were some slight discrepancies in the location of maximum wear, but there was broad agreement between the simulation and the experiment, see Figure 2-30.

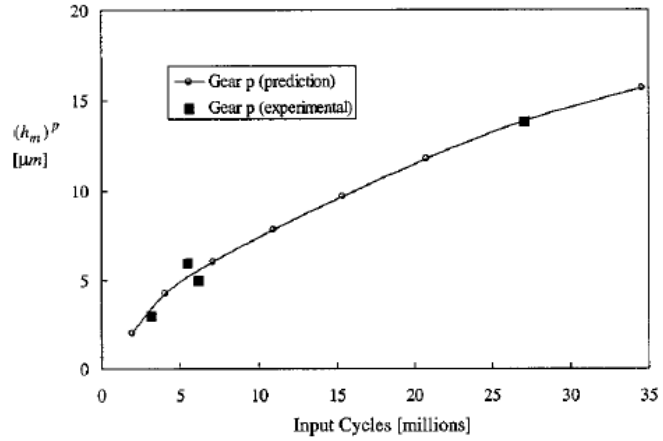

Figure 2-29 Comparison of Actual and Predicted Maximum Pinion Wear using Bajpaj-Kahraman-Andersson Method [72]

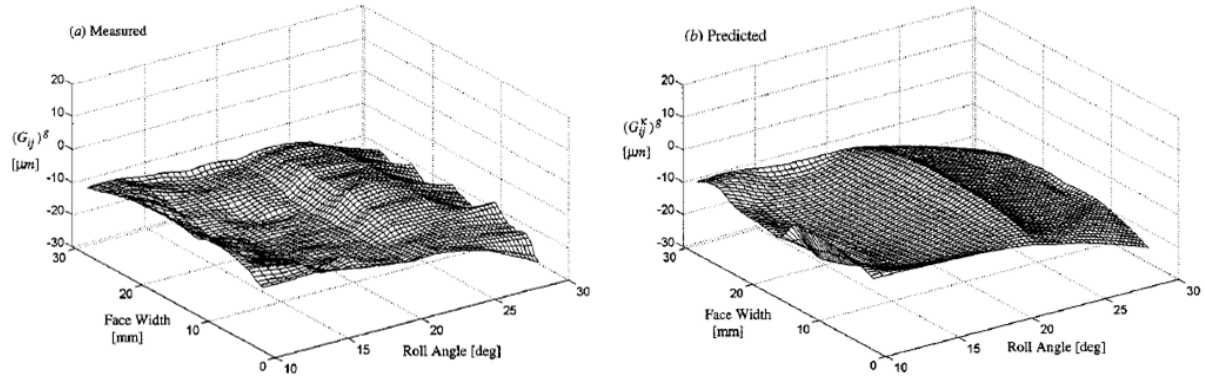

Figure 2-30 Comparison of Actual and Predicted Pinion Wear Distributions using Bajpaj-Kahraman-Andersson Method [72]

2.2.4 Frictional Power Losses from Spur Gears

Load-dependent losses in spur gears stem from friction between the sliding surfaces of the gear teeth. The proportion of sliding and rolling between the surfaces varies across the line of action. The proportion of sliding is at its maximum at the ends of line of action, which corresponds to the SAP and tips of the teeth and is zero at the pitch point. The variation in friction across the line of action depends on many properties such as oil viscosity, temperature, speed, tooth design, and surface finish, but the profile can generally be described as shown in [74]. The coefficient of friction remains relatively consistent over the majority of gear's action, but dips briefly to zero at the pitch circle due to the absence of sliding.

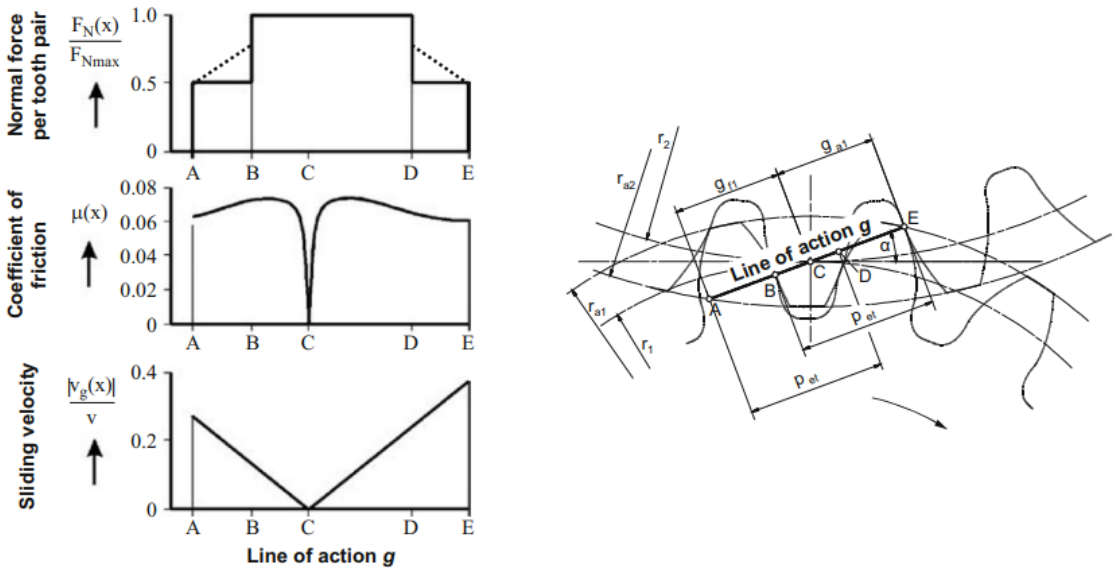

Figure 2-31: Typical Variation in Tooth Load, Coefficient of Friction, and Sliding Velocity on Line of Action [74]

Determining the instantaneous coefficient of friction for different points on the line of action is accomplished by complex simulations requiring the consideration of oil film thickness, temperature, and friction models for mixed and hydrodynamic lubrication regimes. However, a value for the average coefficient over the length of action can be more readily found by studying the power losses. As first proposed by Ohlendorf [75], the frictional power losses between the gear teeth can be found by integrating the product of the normal load, sliding velocity, and coefficient of friction over the length of contact, and dividing by the base pitch.

If the coefficient of friction is assumed to be a constant average value over the length of contact, the load is equally distributed between each tooth pair in contact, and the teeth act rigidly, then the load-dependent power losses from the gear teeth, P_{gl}, can be expressed as:

$$P_{gl} = P_{g\_ip} . \mu_{avg} . H_v \quad (1)$$

Where:

P_{g_ip} = Power at gear input

μ_{avg} = Average coefficient of friction

H_v = Gear loss factor

The gear loss factor H_v is then determined purely from the gear geometry, and various expressions have been provided by different authors [76][77][78].

2.2.5 Techniques for Assessing Wear and Power Loss in Gearboxes

2.2.5.1 Test Rigs

Test rigs utilised in tribological studies of gears and gear lubricants generally fall into two categories: power-absorbing and power-recirculating. Power-absorbing rigs utilise a pair of gears, with one driven by a motor and the other connected to an active or passive torque loading device. This configuration is shown schematically in Figure 2-32.

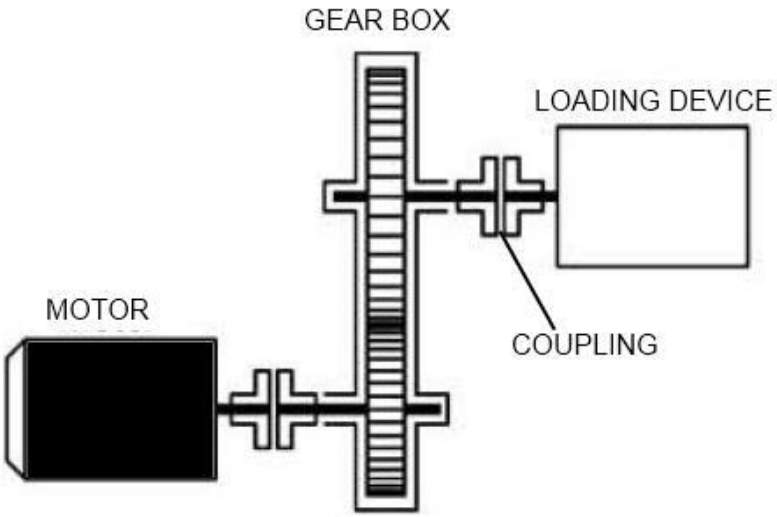

Figure 2-32 Schematic of Power-Absorbing Gear Test Rig [79]

The advantages of this approach are the ability to run variable position-load profiles, low number of parts in relative motion, and the ability to operate closed-loop load control. However relative to other methods this approach also suffers from high cost and complexity as a result of having to provide drive and active control of two powered devices. Figure 2-33 shows a simple power-absorbing gear test rig utilised for studying wear in sintered gears [57].

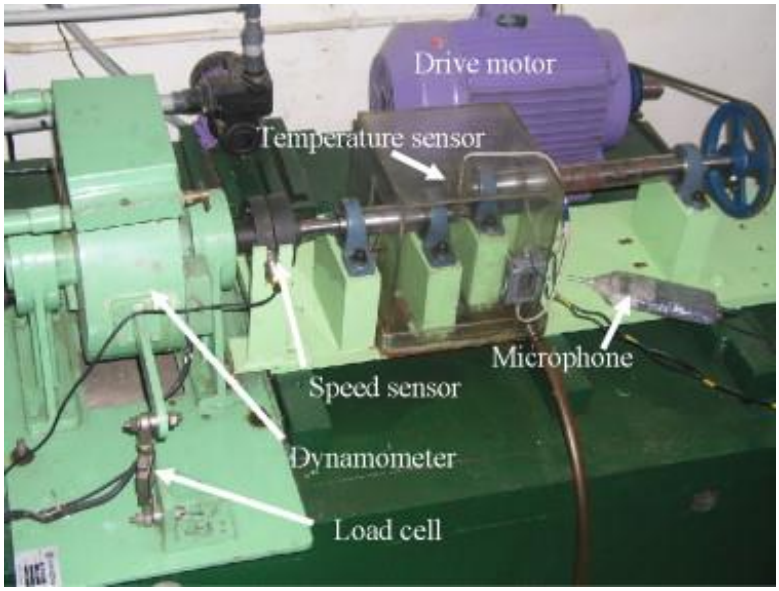

Figure 2-33 Photograph of Power-Absorbing Gear Test Rig for Study of Wear in Sintered Spur Gears [57]

The rig shown in Figure 2-33 utilises an electric drive motor and dynamometer for loading. Whilst AC electric motors are most commonly adopted for input drive the selection of loading devices is more diverse and includes hydraulically controlled disc brakes [80], powder brakes [81], hydraulic pumps loaded by adjustable relief valves [57], electrical generators loaded by rheostats [82] and DC motors [83].

Power recirculating rigs are often referred to as “back-to-back” or “four-square” rigs and function by mounting two gear pairs in line with common shafts connecting their input and outputs. Loading is commonly achieved by trapping a torsion load between the two gearboxes. Consequently, one gearbox operates against an opposing load whilst the other operates with an aiding load. Due to the mechanical recirculation of power the drive motor is only required to supply the losses in the system. This allows a small motor to drive a relatively highly loaded gear pair. One of the two sets of gears is usually operated purely to recirculate power whilst the other forms the test article. The operating principle is shown below in Figure 2-34.

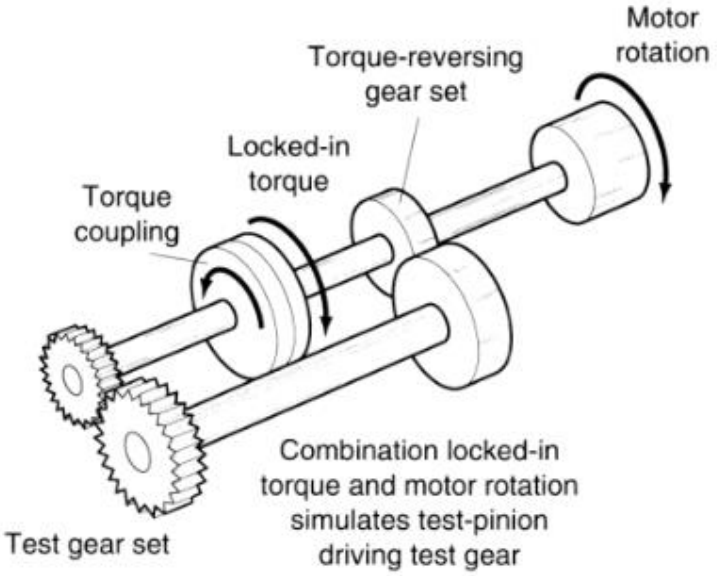

Figure 2-34 Operating Principle of Power-Recirculating Test Rig [84]

At high powers or speeds the tooth accuracy of the reversing gearset can significantly affect the dynamic loads experienced by the test article [84]. Measures are usually taken to minimise this interaction can include incorporating greater tooth face widths and optimising the lubrication regime to prevent wear and ensuring highly accurate reversing gears are used.

A number of different approaches are taken to applying the torque load to a power-recirculating rig. As mentioned previously a common approach is to employ an adjustable coupling and compliant shaft between the two gearboxes. The shaft is displaced as a torsional spring using a detachable load arm and then the coupling is locked to trap the load between the gearboxes. This type of setup has been employed in the testing of gears for scuffing resistance [85] as shown in Figure 2-35, contact fatigue strength [86] [87], efficiency [88], resonant frequency behaviour [89], and wear [90].

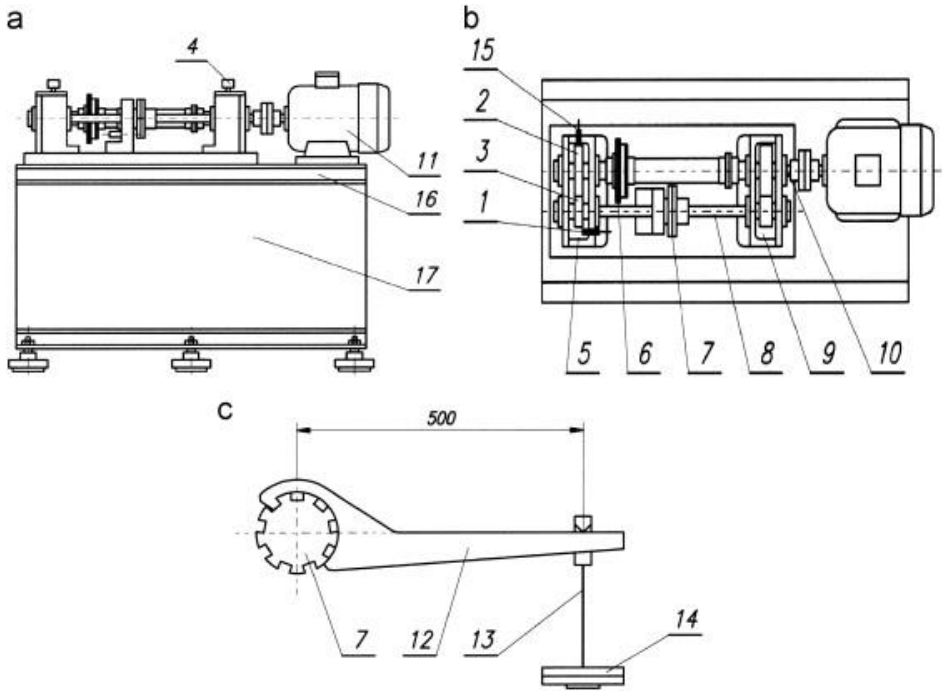

(a)	Front View	5	Test Chamber	12	Loading Lever
(b)	Top View	6	Shaft Angle Indicator	13	Weight Hanger
I	Loading Equipment	7	Load Clutch	14	Weights
1	Thermocouple	8	Front Shaft	15	Heaters
2	Test Wheel	9	Reversing Chamber	16	Frame
3	Test Pinion	10	Drive Clutch	17	Concrete Base
4	Vent	11	Electric Motor		

Figure 2-35 Torsion Bar Power-Recirculating Test Rig for Study of Scuffing Resistance [85]

The primary advantages of recirculating mechanical power are that it allows a high power gear set to be driven by a relatively small motor, and the simplicity of controlling only a single prime mover. However, testing is usually limited to fixed loads, and isolating the power losses of the test and reversing gearboxes is not possible, which impedes the determination of efficiency. In the case of torsion-loaded rigs the load may drift over time due to increases in backlash allowing the shaft to unwind. An alternative approach to loading that mitigates this issue is to mount the test gears in a bearing block as shown in Figure 2-36 and Figure 2-37. The torque load is then applied using weights and a lever arm, which ensures consistent loading. This approach is generally reserved for wear testing, as reported in [91] and [51]. Connections to the test article are made using universal joints to allow for misalignment introduced by movement of the pivot.

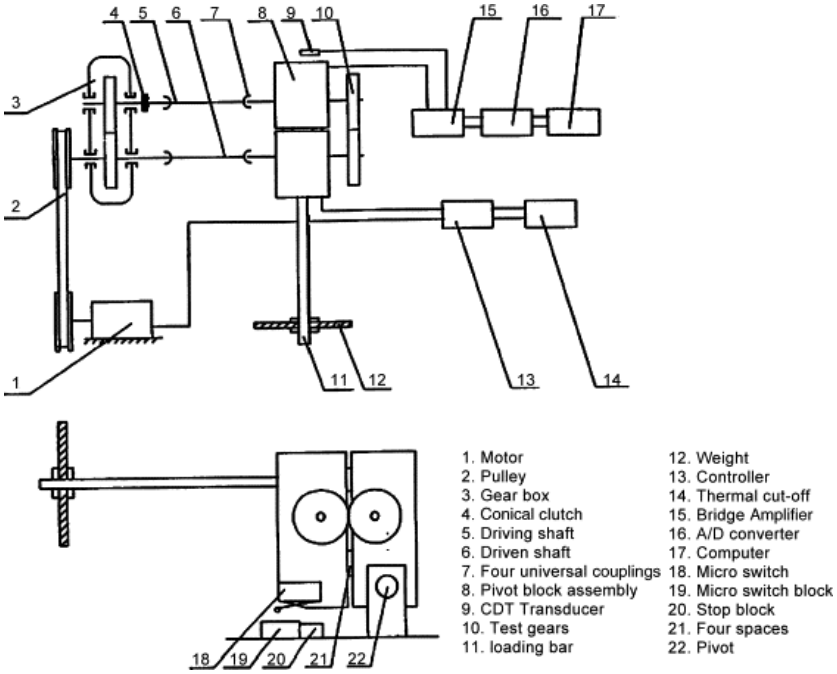

Figure 2-36 Pivot Block Power-Recirculating Gear Test Rig [91]

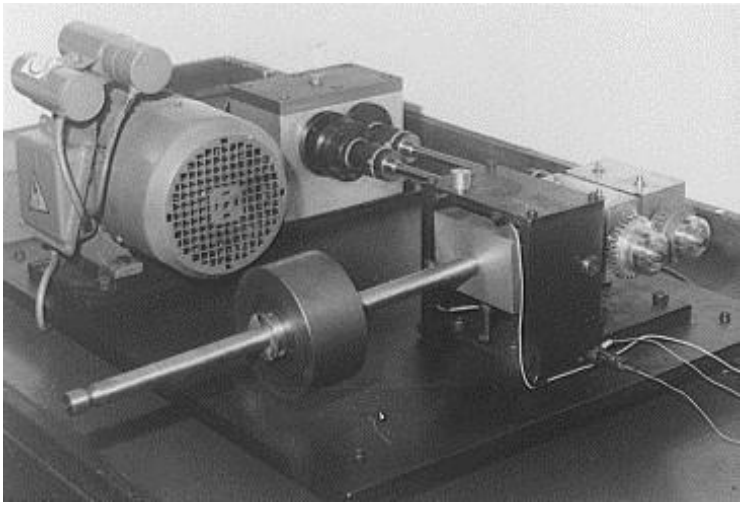

Figure 2-37 Pivot Block Power-Recirculating Gear Test Rig [51]

Another approach to maintain consistent loading is to provide active closed loop control, though this is more difficult to achieve than in power-absorbing rigs. In [96] a rig was developed to apply the load using a helical reversing gear set and a pneumatic actuator as shown in Figure 2-38 . This induces a torque load by applying an axial load to one of the helical reversing gears. In [98] a recirculating rig was used to investigate the effect of lubricant viscosity and additives on wear. Loading was applied by an inline hydraulic vane motor and controlled by regulating the pressure

difference, see Figure 2-39. However, these approaches introduce significant complexity into the design.

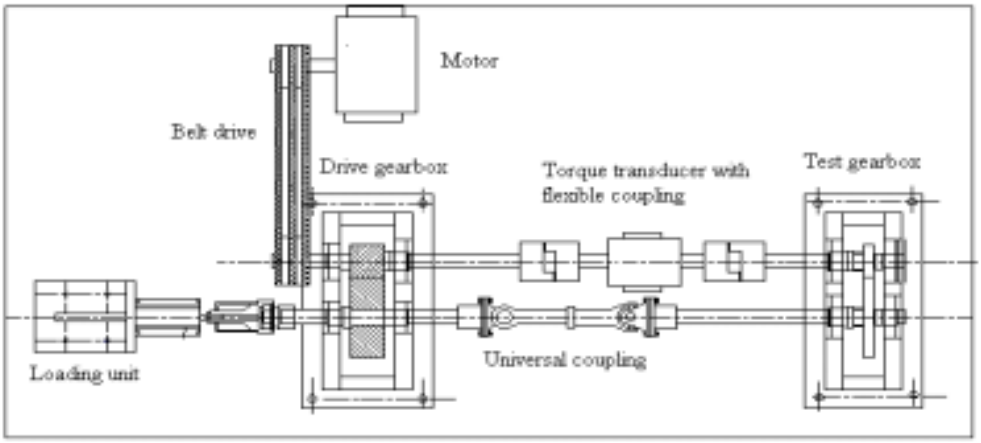

Figure 2-38 Thrust-Loaded Helical Power-Recirculating Gear Test Rig [96]

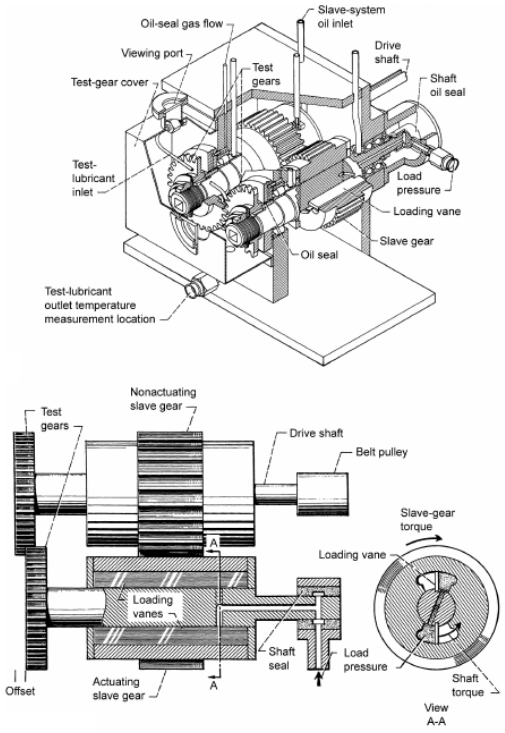

Figure 2-39 Inline Vane Motor Power-Recirculating Gear Test Rig [98]

2.2.5.2 Measurement of Wear Magnitude and Distribution

Studies into wear distribution characteristics of spur gears have employed a variety of measurement techniques. However, few published papers describe the methods used in detail. The specific objective of this study offers several challenges and therefore the measurement technique to be used requires careful thought.

In its simplest form, some studies have utilised pre and post-test weight measurements and material density characteristics to determine the volumetric material loss [51]. However, this method doesn't provide any information on the allocation of wear between individual teeth, or where on the tooth the wear is concentrated.

Other papers make use of profile projectors [57] or shadow graphs [51] to provide two-dimensional profile measurements, with the wear being deduced by comparison of the pre and post-test images. However, this method can only be used for profile measurements. It cannot provide lead measurements and therefore cannot be used to study variations in wear across the lead axis. A similar approach appears to have been taken in [90], where comparisons of overlaid pre and post-test digital photographs were used to quantify the level and distribution of wear. Such methods would be of limited use when testing coatings only a few microns in thickness, and the extent of wear must be monitored to a far higher degree of accuracy.

Other studies have made use of stylus-based measurement systems. The wear testing reported in [99] refers to use of a "stylus profilometer" for wear measurements. [100] describes taking moulds of the gear profiles using aluminium and putty in order to cast a resin replica of the tooth form for subsequent measurement with a stylus instrument. A NASA study into the effects of lubricant viscosity and additives on gear wear [98] provides a comprehensive set of three-dimensional measurements of worn gears, conducted using industrial gear checking CMM equipment. See Figure 2-42.

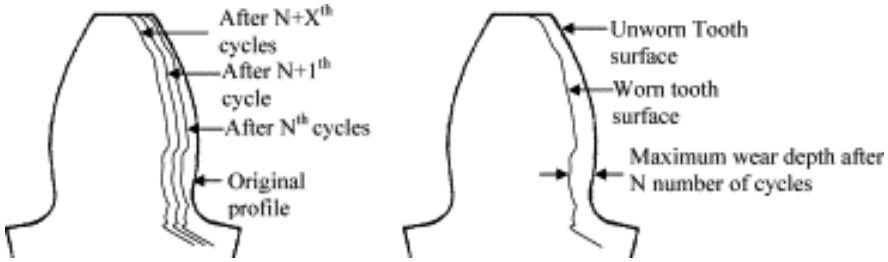

Figure 2-40 Schematic Diagrams of Tooth Wear Depth Produced from Profile Projections [57]

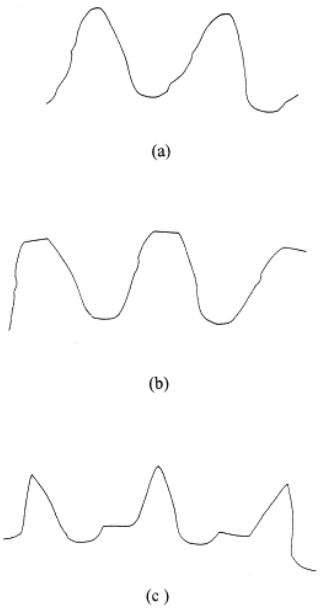

Figure 2-41 Shadow Graph Tooth Wear Profiles [51]

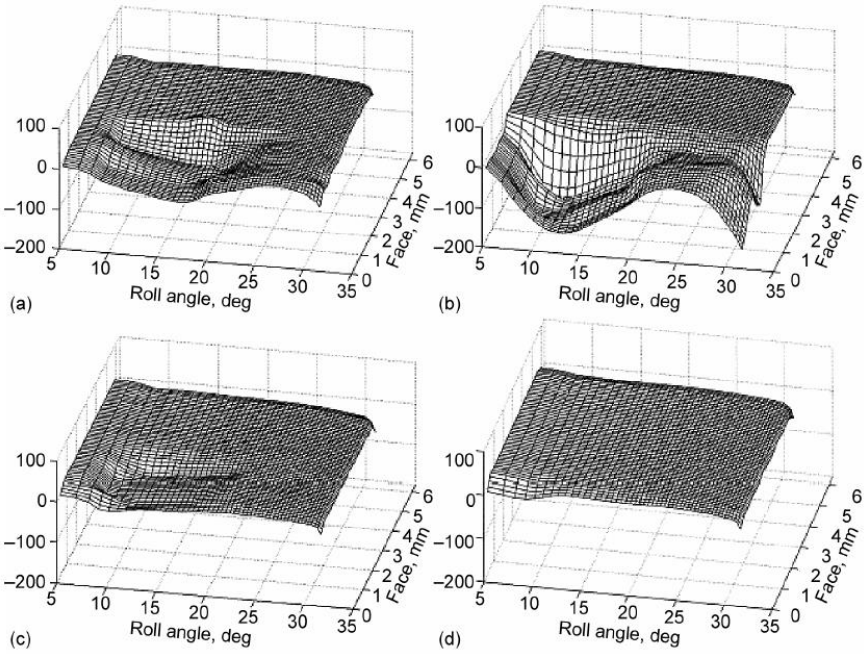

Figure 2-42 3D CMM Inspections of Gear Tooth Wear [98]

2.2.5.3 Standard Test Methods

As shown in sections 2.2.5.1 and 2.2.5.2, a wide array of test rig concepts and measurements techniques have been used in tribological studies on gears, according to the particular demands and objectives of the study. In terms of more standardised approaches, a number of studies utilise a test framework based around the test rig developed by the Technical University of

Munich for assessing the properties of gear oils. Named the FZG test rig ("Forschungsstelle fur Zahnrader und Getriebebau" or "Research centre for gear wheels and transmission construction"), it is based on the principal of mechanical recirculation of power and utilises a trapped torque load as shown previously in Figure 2-34. The test rig design is shown below in Figure 2-43 [92].

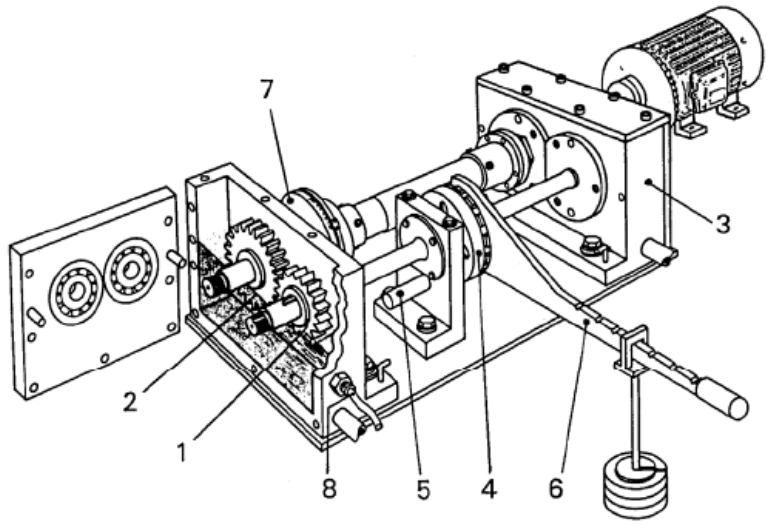

Figure 2-43: FZG Standard Back to Back Test Rig Developed by TU Munich [92]

Tests methods are defined to utilise the FZG rig to determine an oil's influence on scuffing, low speed wear, pitting, and micropitting. Each test procedure mandates the use of gears of fixed design and material and are designed specifically to induce the desired failure mode within the test duration. For each test category multiple variations have been derived, in addition to the standard test, in order to address specific applications.

Scuffing capacity (A/8.3/90 [93]) is assessed by testing gears under continuous operation at a fixed speed through 12 load stages of increasing torque, with the oil temperature set at the start of each stage and then allowed to increase without cooling. Scuffing failure is visually defined as occurring when the summed face width of scuffed areas on all teeth exceeds one pinion tooth face width. Alternatively, the wear rate can be monitored by intermediate weighing of the gears between stages, with the onset of scuffing being detected by a step change in the wear rate

above a pre-set threshold. Oils are then rated according to the highest load stage achieved prior to failure.

Low-speed wear capacity (C/0.05/90:120/12 [94]) is tested by operating the gears at a fixed torque load and low pitch line velocity. This is split between three stages with the oil temperature being increased for the second stage, and the pitch line velocity being increased for the final third stage. Each oil is then assigned one of 5 categories from “low” to “very high” wear rate according to the mass loss of each gear.

Micropitting capacity (FVA 54/I-V [95]), like scuffing, is determined based on testing in stepped load stages of increasing torque. However, the oil temperature is maintained at a constant level, and failure is determined by comparing the mean profile deviations, as measured on industrial stylus-based gear checking equipment, against a threshold. The highest load stage achieved is then reported as the test result. Gears failing in the latter load stages, or completing all stages without failure, are then subjected to a further endurance test at a constant torque load with a higher profile deviation threshold, to provide additional information on the long term performance of the lubricant.

Finally, pitting behaviour (C/9/90 [96]) is studied by tests performed in a single stage at constant torque load and oil temperature. Failure is defined as occurring when more than 4% of the tooth area is pitted or based on profile deviation measurements. The number of tooth cycles to failure is then reported to allow comparison of the pitting capacity of different oil types.

Whilst used throughout industry these test procedures, or modified versions of them, are also commonly used in academic literature in the tribological study of gears, particularly in Europe. However, it can also be seen that in many respects these procedures are unsuitable for a detailed study of dry-running coated gears. Testing in progressive load stages until failure is evident provides little information as to how long a coating may endure under a given set of conditions. The test method does not allow the effects of progressive coating wear and increases in load to be separated. A more suitable approach would be to conduct tests at fixed loads until the coating fails. Furthermore, as the tests are designed for ranking different oil types, they provide little in the way of information that would facilitate an understanding of the causes of failure. Consequently, it is necessary to develop an approach specifically tailored for use on dry coated gears under intermittent operation.

2.2.6 The Tribology of Involute Spur Gears: A Summary

The majority of gears are designed with teeth of involute form in order to transmit conjugate motion. Tooth form is primarily defined by module, pressure angle, and addendum and dedendum proportions. Microscale modifications can be made to basic involute profile in order to improve tooth engagement characteristics at the start and end of their action, and to improve tolerance to misalignment.

Involute gear teeth are conventionally lubricated with oils or greases in order prevent failure of the tooth surface. Due to the counterformal geometry of contacting gear teeth intense shear stresses develop beneath the surface which may lead material loss through macro or micro pitting. Operating at high power levels can lead to break down of the lubricating film and scuffing of the surface, whilst low speed operation inhibits fluid film generation and leads to localised cold welding. Under better lubricating conditions the contacts between larger asperities can lead to milder wear through adhesion or abrasion.

Modelling of tooth wear and the prediction of its magnitude and distribution is limited. More focus has been placed on establishing safe operating conditions to avoid severe wear modes like scuffing. None of the models developed have been done so with the operation of dry or coated gears in mind.

The contact conditions between gear teeth are most easily explained by treating the gear action as a pair of cylinders of constantly changing radius and angular velocity. Hertzian analysis can be used determine the stresses and size of the contact between the loaded teeth, whilst sliding distances can be estimating using single point observation. These two methods can then be combined using Archard's law to predict wear distribution.

Several studies have extended the rolling cylinder model to account for the effects of true involute surfaces, redistribution of tooth loads and dynamic load effects. Since then, more sophisticated models have been developed based on combined surface integral and finite element techniques and allow the use of real measurement data to compute contact stress and sliding distance more accurately. Whilst authors often report unsatisfactory correlations, there is a shortage of models published in conjunction with test data for the purpose of comparison to understand where these deficiencies lie.

Load-dependent losses from spur gears are caused by friction between the sliding tooth surfaces. The instantaneous coefficient of friction at a point of the line of action varies according to the lubricating conditions and the proportion of rolling and sliding between the teeth. Average

coefficients of friction can be more readily determined by test and calculation if the load-dependent losses from the gears can be measured.

Tribological tests of spur gears reported in the literature feature a wide range of different test rig configurations but can initially be separated into power-absorbing and power-recirculating types. Power-recirculating rigs are most common, with loading often applied using a torsion bar. Accurate measurement of wear to the tooth surface is generally accomplished using CMM stylus based equipment. The most common framework of tribological tests for gears are based on the power recirculating FZG rig produced by TU Munich. Standardised test procedures have been developed to rate oils for their capacity to resist scuffing, wear, pitting. and micropitting. However, these procedures are not well suited to the study of dry coated gears.

2.3 Lamellar Solid Lubricant Films

2.3.1 History and Development of Lamellar Solid Lubricants

Solid lubricants perform the same function as their liquid equivalents: they prevent direct contact between metals whilst shearing easily to reduce wear and friction. Lamellar solids form the most widely known and studied category of solid lubricant materials. Their application can be traced back to industrial revolution, where they were used to meet rising demand for the lubrication of slow-moving machinery and rotating axles.

Graphite in particular has been studied since the 1920's as a solid lubricant (e.g. Koethen, 1926 [101]), whilst references to the self-lubricating properties of carbon in technical literature date back to the beginning of the 20th century [102]. Similarly, patents submitted in 1939 mention the use of molybdenite, the naturally occurring form of MoS_2, as a lubricant [103]. Both materials are naturally occurring and could be extracted directly by mining.

Whilst a solid lubricant requires a low shear strength it must also adhere strongly to the substrate. In its oldest form a solid lubricant film would be formed by directly applying the lubricant to a component as a powder using a rubbing motion, a process known as burnishing. For example, Johnston and Moore studied burnished MoS_2 films in 1964 [104] by rubbing a powder-loaded cloth against copper specimens using a reciprocating crank arm.

A later development was to disperse the solid lubricant in an oil or grease, with the subsequent operation of the machinery acting to form a solid film in-situ [105]. Alternatively, the carrying fluid can be a volatile solvent, which is sprayed onto the component and subsequently evaporates to

leave a solid lubricant film behind, or a resinous binder to produce a strong bond to the substrate. However, the modern preference is the application of a thin film using advanced deposition processes to produce coatings of superior uniformity, density, and adhesion [106].

2.3.2 Structural, Mechanical, and Tribological Properties of Lamellar Solids

The low friction and wear rates characteristic of lamellar solid lubricants are a consequence of their layered structure. Within each layer the bonds are covalent, and the atoms are densely packed. The bonds between layers on the other hand are weak van der Waals forces and the layers are spaced further apart. This causes the material to have a high strength in the normal plane yet allows the layers to shear easily from one another and transfer between surfaces. The structure of two such lamellar solids, hexagonal boron nitride (h-BN) and graphite, are shown in Figure 2-44 [107]. Examples of lamellar solids with a self-lubricating capability, per Erdemir [108], include TMDs ("transition metal dichalcogenides", including well-known MoS_2 and WS_2), monochalcogenides, graphite, graphite fluoride, hexagonal boron nitride, and boric acid.

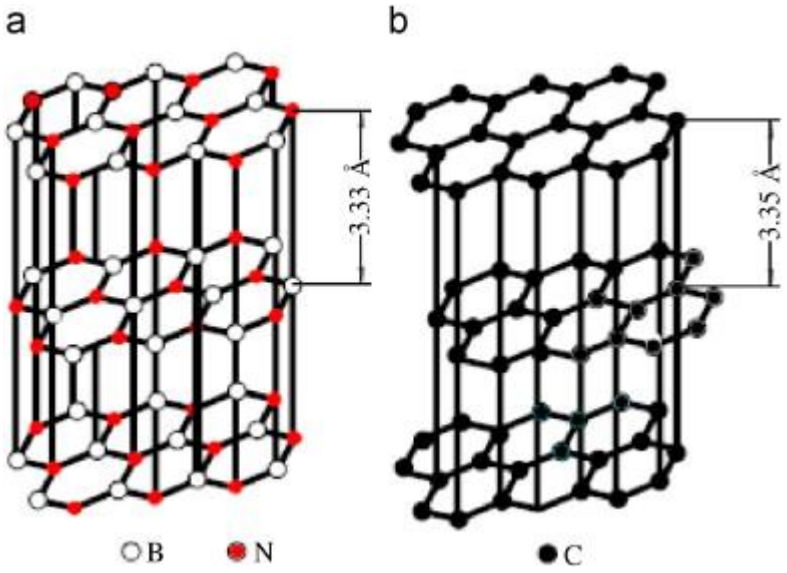

Figure 2-44 Structures of (a) h-BN and (b) Graphite [107]

During sliding the layers can reorient themselves parallel to the direction of sliding [109], even though many deposition techniques result in the basal planes initially being orientated randomly, or even perpendicular to it [110]. Figure 2-45 [111] shows a high-resolution transmission electron microscope (HR-TEM) image of a cross-section through a worn TMD-Carbon alloy coating. Note

how the platelets beneath the surface are oriented randomly, whilst on and just below the surface the platelets have been reoriented parallel to the direction of sliding. Whilst this reorientation is beneficial the depth is limited to the tens of nanometres and the initially disordered or columnar structure exhibited by some deposition techniques is considered to be a significant weakness in the use of the thin TMD films [111].

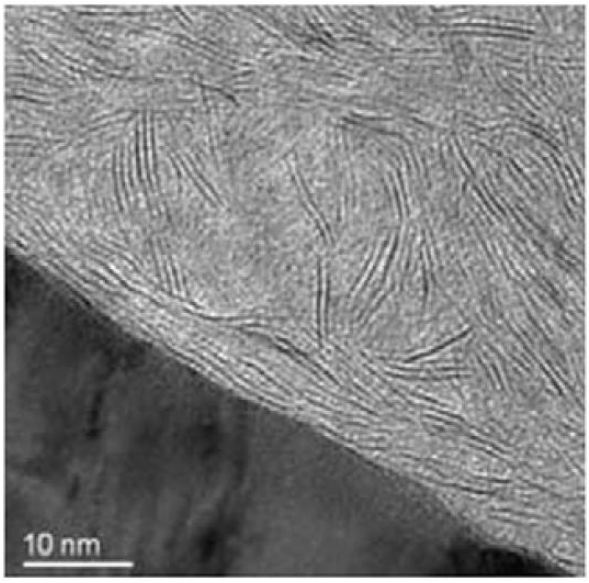

Figure 2-45 HR-TEM Image of Worn TMD-C Coating [111]

A further important aspect of the behaviour of lamellar solid lubricants is their ability to form transfer films on an uncoated counterface during sliding. The friction and wear properties of the sliding interface are predominantly controlled by these transfer films, not the bulk material [112]. Ives and Peterson [113] proposed three mechanisms by which a coating could provide lubrication during sliding against an uncoated counterface:

- Intrafilm flow: the lubricant coating adheres strongly to both substrate and counterface in the contact and flows plastically like a viscous fluid to accommodate sliding.

- Interface slip: the uncoated counterface slides over the lubricant coating without adhering to it.

- Interfilm slip: the lubricant coating adheres to both substrate and counterface and separates into two films which slide over each other at a newly established interface.

These mechanisms are shown schematically in Figure 2-46. Tests have shown that MoS_2 [114] [115], graphite [114] and graphite fluoride [114]-[116] all exhibit intrafilm flow behaviour during sliding and leave transfer films on the uncoated surface. During investigation of WS_2 transfer films Prasad noted that the transfer films were firmly adhered to the steel ball counterfaces [117]. Achieving a good adhesion between the transfer film and the counterface is important to ensure the contact remains lubricated.

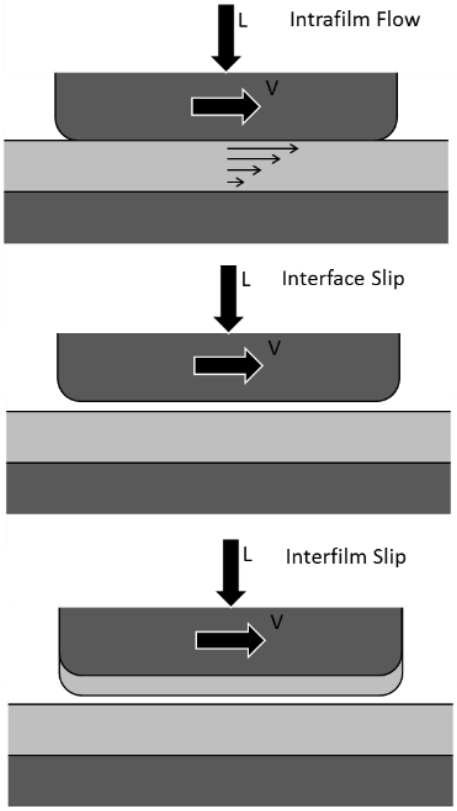

Figure 2-46 Schematic Representation of Solid Lubrication Mechanisms (Adapted from [112])

Whilst lamellar solid lubricants offer coefficients of friction as low as 0.001 [118], dependent on test conditions the range of friction coefficients for a given material can be as much as two orders of magnitude [108]. Firstly, at high pressures thin solid lubricant films do not obey Amonton's 2nd law and instead exhibit decreasing friction coefficients with increasing pressure. Kanakia [119] assembled data on the friction coefficient of MoS_2 in dry sliding from various literature sources and proposed two friction regimes in solid lubrication: a surface (interface) slip regime at low pressures and an intrafilm flow regime at higher pressures.

It was proposed that under light loads the asperities of the film support the load by deforming and that shearing of the junctions produces friction. However, whilst the shear strength of the

contact is determined by the film, the hardness is dominated by the substrate. As the load increases the real contact area increases proportionally and hence the friction coefficient remains constant. Once the load is high enough the apparent and real contact areas become equal and hence the friction coefficient decreases, tending to a constant value. The friction coefficient will not reach zero, as the increase in pressure also produces an increase in the shear strength of the junction [120].

Kanakia modified the equations proposed by Bowden and Tabor [121] to create expressions for each of the two friction regimes:

$$\mu = \frac{S_f}{H_S} + \alpha_L \qquad A_r \propto L \qquad \text{when } P < P^* \qquad (2)$$

$$\mu = \frac{S_f}{P} + \alpha_L \qquad A_r = A_a \qquad \text{when } P > P^* \qquad (3)$$

μ = Coefficient of Friction	P = Contact pressure
S_f = Shear strength of film	P^* = Critical contact pressure
H_s = Hardness of substrate	A_r = Real contact area
α_L = Pressure dependence of shear strength	A_a = Apparent contact area

These equations imply that a film with low shear strength on a harder substrate will act as a solid lubricant. Kanakia's collated data is shown in Figure 2-47. The dashed lines represent equations (2) and (3).

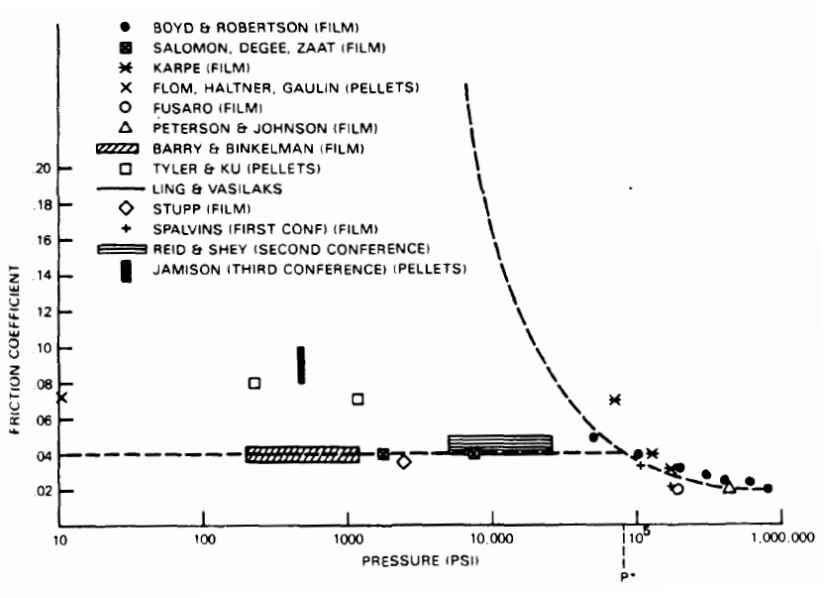

Figure 2-47 MoS_2 Friction Behaviour over a Broad Contact Pressure Range [119]

Lamellar solid lubricants also display changes in friction and wear characteristics according to the environment. In particular TMDs and graphite display opposing sensitivities to humidity. Graphite will not function as a solid lubricant in a vacuum or dry air and relies on adsorbed vapour from the atmosphere to function as one. This issue first rose to prominence during the Second World War, when planes flying at increasingly high altitudes began to suffer from rapid wearing of graphite-metal brushes on electric motors [122], see Figure 2-48.

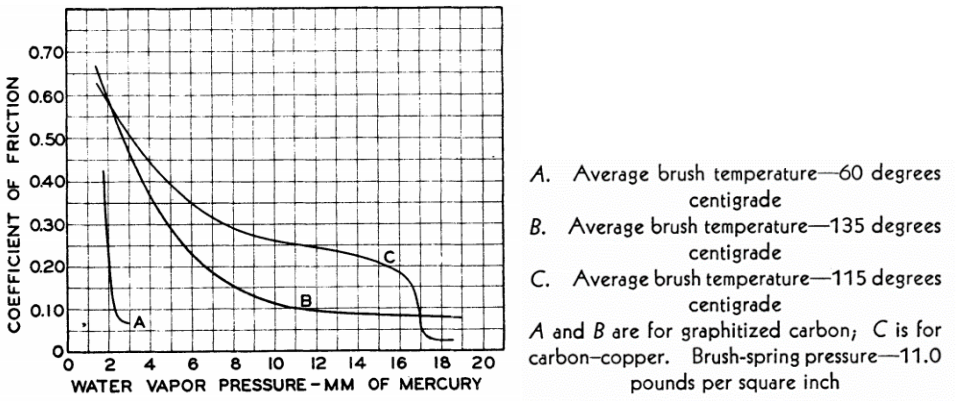

Figure 2-48 Coefficient of Friction vs Water Vapour Pressure for Motor Brushes [122]

Two explanations have been offered for this behaviour. The first, proposed by Rowe [123], suggests that the interlayer bonding between graphite layers is stronger than in other lamellar solids, and that intercalation of vapour molecules weakens these bonds to allow the graphite to act as a lubricant. The second, offered by Deacon and Goodman [124], states that whilst the basal

planes of graphite are relatively inert the edge sites, which may be exposed due to disorder in the structure or damage from wear, are higher in energy and more adhesive due to the presence of dangling carbon bonds. Friction and wear will only remain low when there is water available in atmosphere to neutralise these exposed edge sites. Tests by Yen [125] found no change in the interlayer spacing of graphite in humid or ambient atmospheres, and this would suggest that Deacon's theory is correct.

In a vacuum or inert gas atmosphere the coefficient of friction of graphite is high (0.5-1.0) and the rate of wear is 10^2-10^3 times greater than in air. This wear mode is known as "dusting" due to the very fine wear debris produced [126]. Graphite fluoride (CF_x) does not display the same level of sensitivity to water, maintaining similar levels of friction in dry air or inert gas. Endurance lives in dry conditions are also superior to graphite though greatly reduced compared with moist air [127].

TMD coatings on the other hand exhibit increasing friction and wear when water vapour is present, behaviour first documented by Peterson and Johnson [128]. The disordered and often columnar structure of TMD films leaves them porous and vulnerable to environmental attack by both oxygen and water and exposes the reactive edge sites [111]. The structure of a sputtered WS_2 films is shown as an example in Figure 2-49. In general the behaviour of other TMDs is similar to MoS_2 [110] [126], but molybdenum diselenide has been shown to be less sensitive to water than disulphides [129].

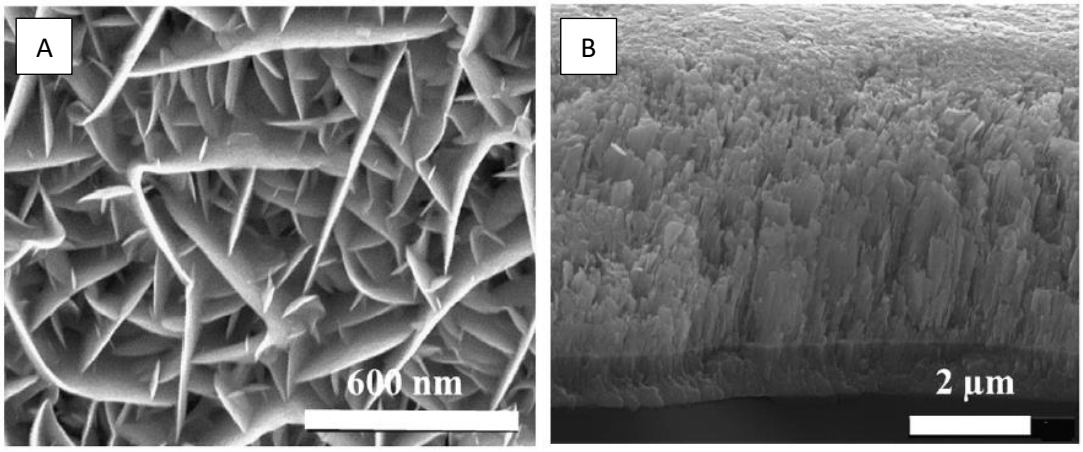

Figure 2-49 SEM Micrographs of Porous (A) and Columnar (B) Structure of Sputtered WS_2 Films [111]

The precise reason for this sensitivity to humidity has been the subject of disagreement. Some hypothesised that this is due to moisture promoting the oxidation of MoS_2 to MoO_3 [130], which then increases the cohesion between particles and inhibits intrafilm flow [104]. Others proposed that bonding between water and chalcogens at edge sites increases the shear strength of the material [131]. Recent studies [132] have shown that at moderate temperatures the latter effect is more dominant. Tests have shown that the change in behaviour can be reversed by alternating the temperature above and below that required for desorption of water. This behaviour would be inconsistent with significant chemical change.

The porous structure of MoS_2 also tends to result in a low density, and consequently it lacks hardness and load bearing capacity. The hardness of a TMD film is typically in the range 0.3 to 2 GPa. It also affects adhesion, and high contact pressures can cause the coating to delaminate [111]. Similarly, graphite is a notoriously soft mineral, with a monolithic hardness of only 0.3GPa [133].

The oxidation of MoS_2 to MoO_3 [130] also limits the temperatures at which it can be used. Other TMDs will similarly oxidise and lose their lubricity, with WS_2 being favoured over MoS_2 for higher temperature applications due to higher temperature of oxidation in air. MoS_2 will begin to oxidise in air at approximately 375°C, whilst the onset of oxidation of in WS_2 occurs between 500°C, see Figure 2-50. The useful temperature range is substantially extended when operating in a vacuum or inert gas [134].

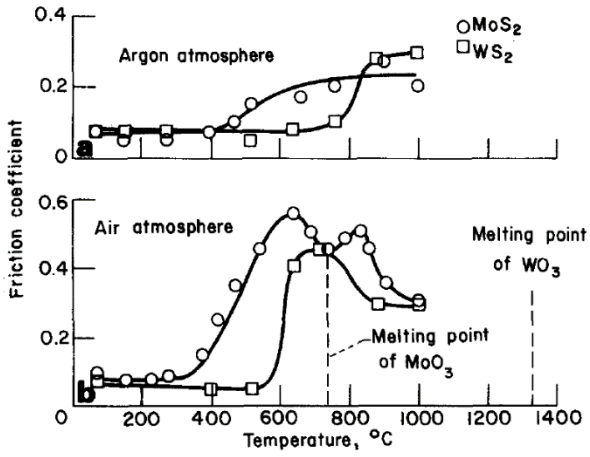

Figure 2-50 Variation of Friction Coefficient with Temperature of MoS_2 and WS_2 in Argon and Air [134]

The oxidation of graphite occurs at approximately 400°C. However, graphite is only effective as a solid lubricant at room temperatures and above 425°C. See Figure 2-51. At intermediate temperatures it is believed that desorption of water occurs, and the graphite loses its lubricity as

a result. When used above its oxidation temperature graphite's lubricity has been attributed to its interaction with the oxides of metal substrate [134]. Of all the lamellar solids the greatest oxidation resistance is shown by HBN, coatings of which have been shown to remain stable at up 1,100°C in oxidizing atmospheres [135].

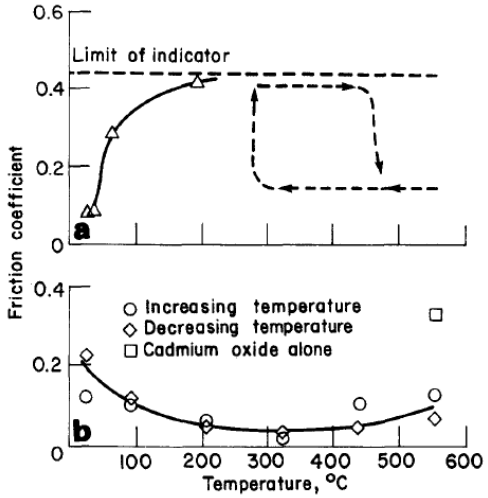

Figure 2-51 Effect of Temperature on Friction Coefficient for (a) Graphite and (b) Cadmium Oxide – Graphite Mixture [134]

2.3.3 Sputtered Lamellar-Solid-Based Thin Films

As discussed in the introduction of this chapter the use of lamellar solids has progressed from simple sprinkling or burnishing of powders through to the use of advanced deposition processes such as physical or chemical vapour deposition (PVD, CVD) and ion beam assisted deposition (IBAD). These modern techniques allow the production of solid lubricant coatings of increasing complexity and can address many of the shortcomings of lamellar solids identified in the previous section. The most prominent coating method is a PVD process known as sputtering.

2.3.3.1 Deposition by Sputtering

Sputtering is conducted in a chamber filled with low pressure inert gas, usually argon. Plasma is generated by applying a high voltage to ionise the gas. In DC sputtering the ions are then accelerated towards a negatively charged target, which is comprised of the material that is to be applied as a coating and placed in the proximity of the specimen. The ion bombardment of the target causes atomic or molecular sized particles to be emitted, which are then deposited on the surface of the specimen [110]. This is shown schematically in Figure 2-52.

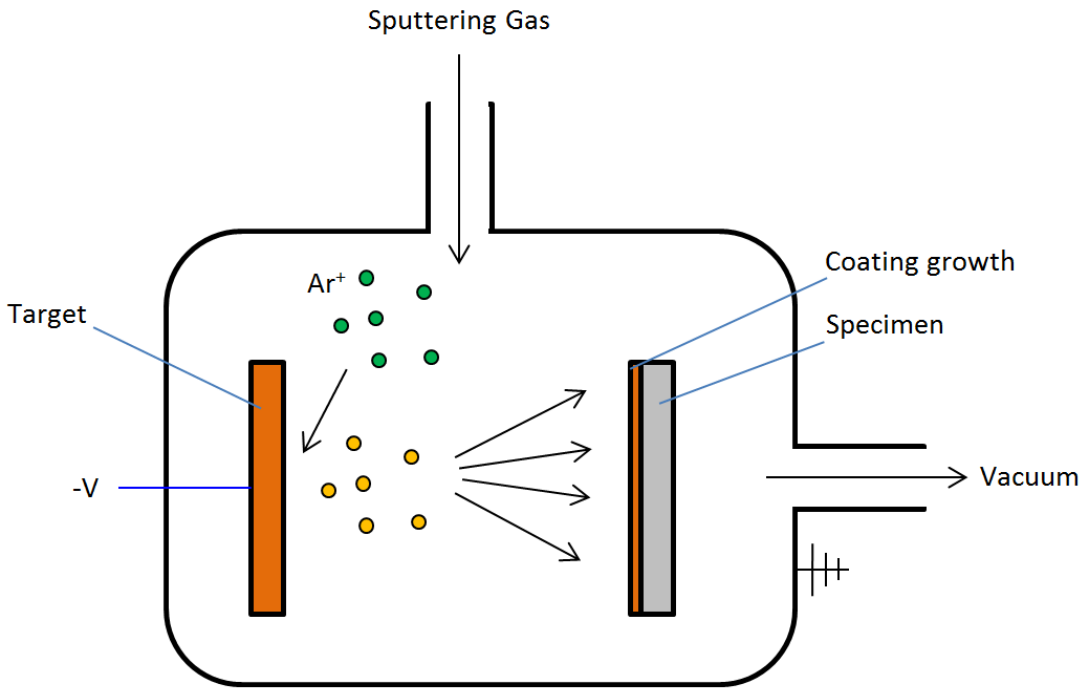

Figure 2-52 DC Sputter Schematic Diagram (Redrawn from [136])

DC sputtering is ineffective when using targets of poor electrical conductivity, as the ions will cause the target to become positively charged which reduces the attraction. This can be overcome using RF sputtering, in which a high frequency alternating voltage is applied to the target. When the target is negatively charged the ions bombard the target and sputtering occurs. When the positive charge is applied electrons from the plasma are attracted and any positive charge on the surface is neutralised [110].

In the 1970s sputtering processes were enhanced by the use of magnetrons [137]. In magnetron sputtering magnetic fields are used to focus the plasma on the target to increase the sputtering rate, and to prevent any electrons emitted by the target from impinging on the specimen, which would result in heating. Consequently, magnetron sputtering is a relatively low temperature coating process and can be used on components where high temperatures might cause tempering and loss of mechanical properties [106].

Magnetron sputtering was further improved by the introduction of unbalanced magnetrons. Rather than entirely constraining the plasma near to the target, in an unbalanced system some of the plasma is allowed to escape and bombard the coating as it grows, resulting in a denser structure. Unbalanced magnetron sputtering is usually conducted with multiple magnetrons in the chamber and the substrate positioned on a rotating holder. By configuring the magnetic poles appropriately, a closed magnetic field can be achieved to ensure a high plasma density around the substrate [137]. An example of an unbalanced closed field sputtering arrangement is shown

schematically in Figure 2-53. Bias voltages may be applied to the substrate in order to intensify or attenuate the bombardment.

Numerous parameters can be adjusted to change the resulting structure of the grown coating. These include [110]:

- Argon pressure
- Sputtering Voltage
- Sputtering Power
- RF Frequency
- RF Power
- Target-Substrate Distance
- Substrate Bias
- Screen Voltage
- Sputter Cleaning Time
- Sputtering Time

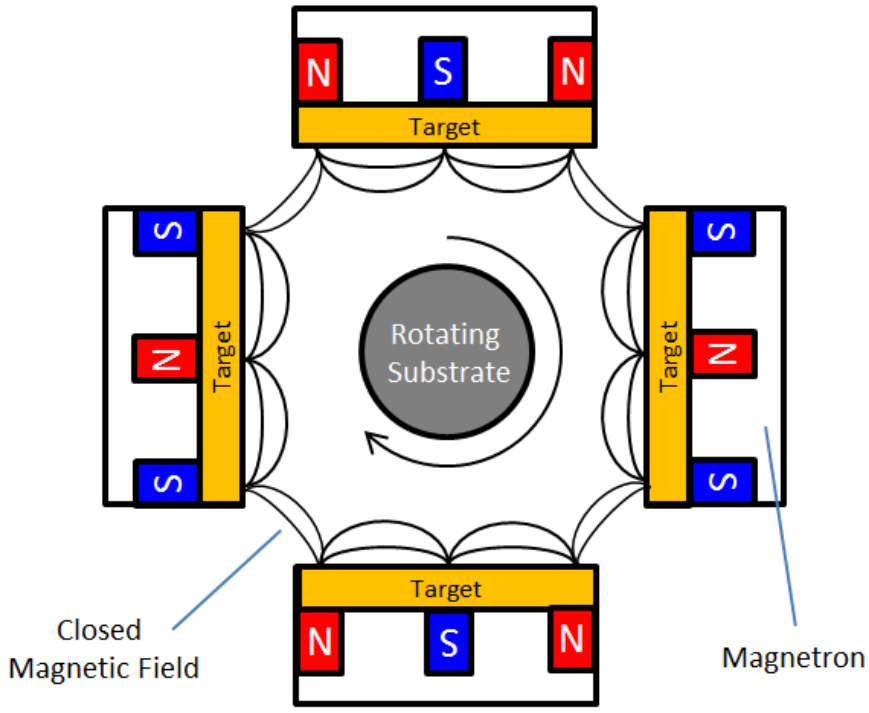

Figure 2-53 Four Target Closed Field Unbalanced Magnetron Sputtering System (Adapted from [138])

2.3.4 Early Improvements to the Properties of Sputtered TMD Films

The early pure MoS_2 coatings, applied using DC sputtering, consisted of a 100nm dense, coherent film followed by a loose powdery film with a columnar structure which could be easily worn away due to fracture at the column bases [138]. They also suffered greatly from the environmental sensitivities previously discussed due to exposure of the high energy edge sites. Other sputtered TMDs such as WS_2 were similarly porous and columnar in structure [139].

RF sputtering techniques were found to produce denser films with a more coherent structure [140]. Further improvements in structure and performance were realised by the lowering of substrate temperature and gas pressure, the application of negative bias voltages to the substrate, the use unbalanced closed magnetic fields, and bipolar pulsed sputtering. Under optimised sputtering conditions coatings can be grown with a greater prevalence of the preferred parallel basal plane orientation, with reduced water sensitivity and improved hardness [141]. Figure 2-54 shows the evolution of the coating morphology with changes in deposition pressure, from "needle-like" columnar structure at high pressure through to flat featureless structure with parallel orientation of the basal planes.

The ability of various thin hard interlayers to improve the adhesion of TMD solids to steel substrates has been studied, including Co, TiC, TiB_2, and BN [142] [143], but typically either Cr or Ti are used [111].

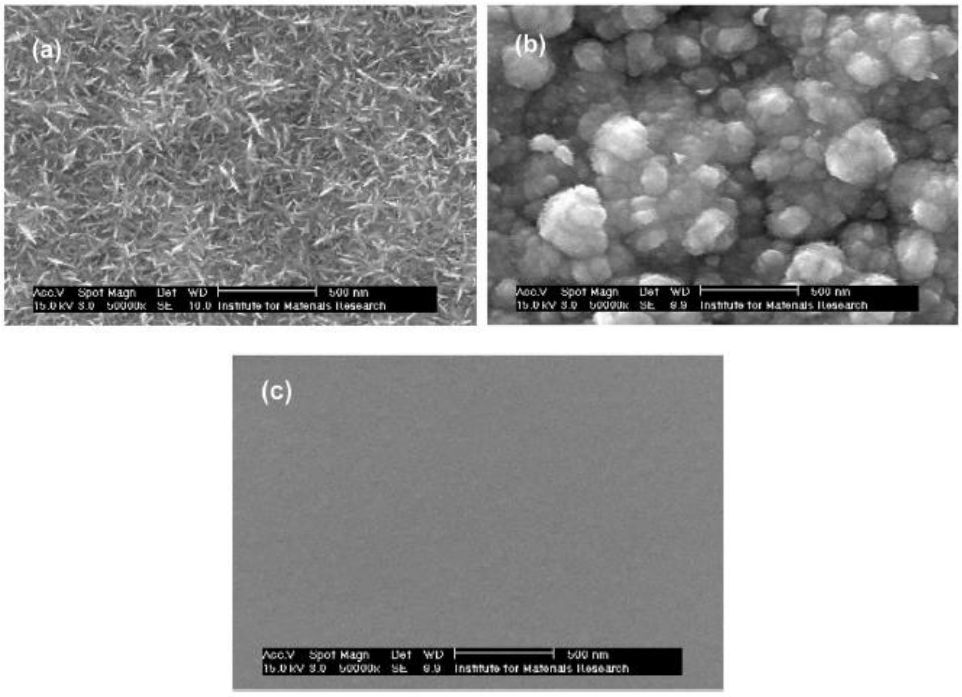

Figure 2-54 Sputtered MoS_2 Morphologies Deposition Pressures of (a) P>1.0Pa, (b) 0.4<P< 1.0Pa, (c) P<0.4Pa [141]

2.3.5 Doping of Sputtered Lamellar Solid Lubricant Films

It is by controlling the structure and composition of the coating at the nanoscale that the performance of lamellar solid lubricants has been most significantly improved. From the mid-1990's onwards a great deal of focus was on the doping of TMD coatings with various metals,

though investigations began in the 1980's [144]. Doping is achieved through co-depositing with multiple sputtering targets of different material compositions. The relative concentrations of each material in the coating can be adjusted through controlling the power to each target. Most prominent amongst doping metals is Ti, which was incorporated into the main body of the coating as an extension of its early use as an adhesion interlayer and as a getter to remove water vapour from the sputtering chamber [138].

Renevier [145] found that co-deposition of Ti with MoS_2 resulted in coatings with improved hardness, adhesion, and wear rate compared to pure MoS_2. Environmental sensitivity was also reduced, with coating performance being maintained in terrestrial air. Low Ti content coatings (5-10%) exhibited the lowest coefficient of friction, whilst increasing the content (10-20%) gave a higher coefficient of friction but lower wear rate. Surprisingly doping in contents of less than 20% resulted in the Ti remaining in solution, despite the use of separate MoS_2 and Ti targets and the anticipation of a superlattice structure. Deposition at greater than 20% Ti resulted in the emergence of the MoS_2/Ti superlattice structure and a loss of tribological properties. Figure 2-55 shows the improvements made to the wear rate performance during the development of MoS_2-Ti ("MoST") coatings.

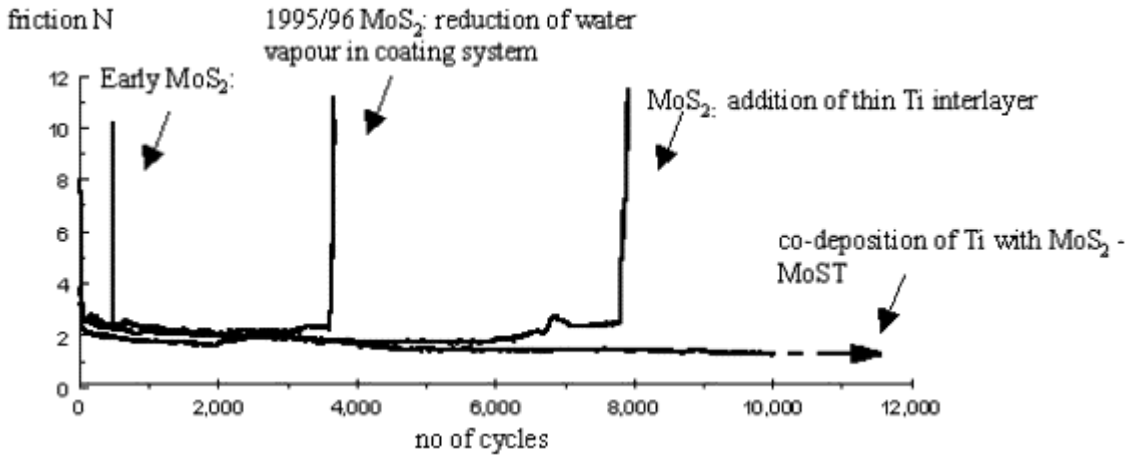

Figure 2-55 Results of 100N reciprocating Wear Tests on Progressive MoS_2 and MoST Coatings [145]

Inspection of sputtered MoS_2-Ti coatings has shown that addition of Ti results in an increase in the density and smoothness, see Figure 2-56. The structure is described as quasi-amorphous, with the Ti appearing to inhibit the formation of crystalline MoS_2. Scharf [139] reported similar improvements in performance and structures when doping WS_2 with Ti.

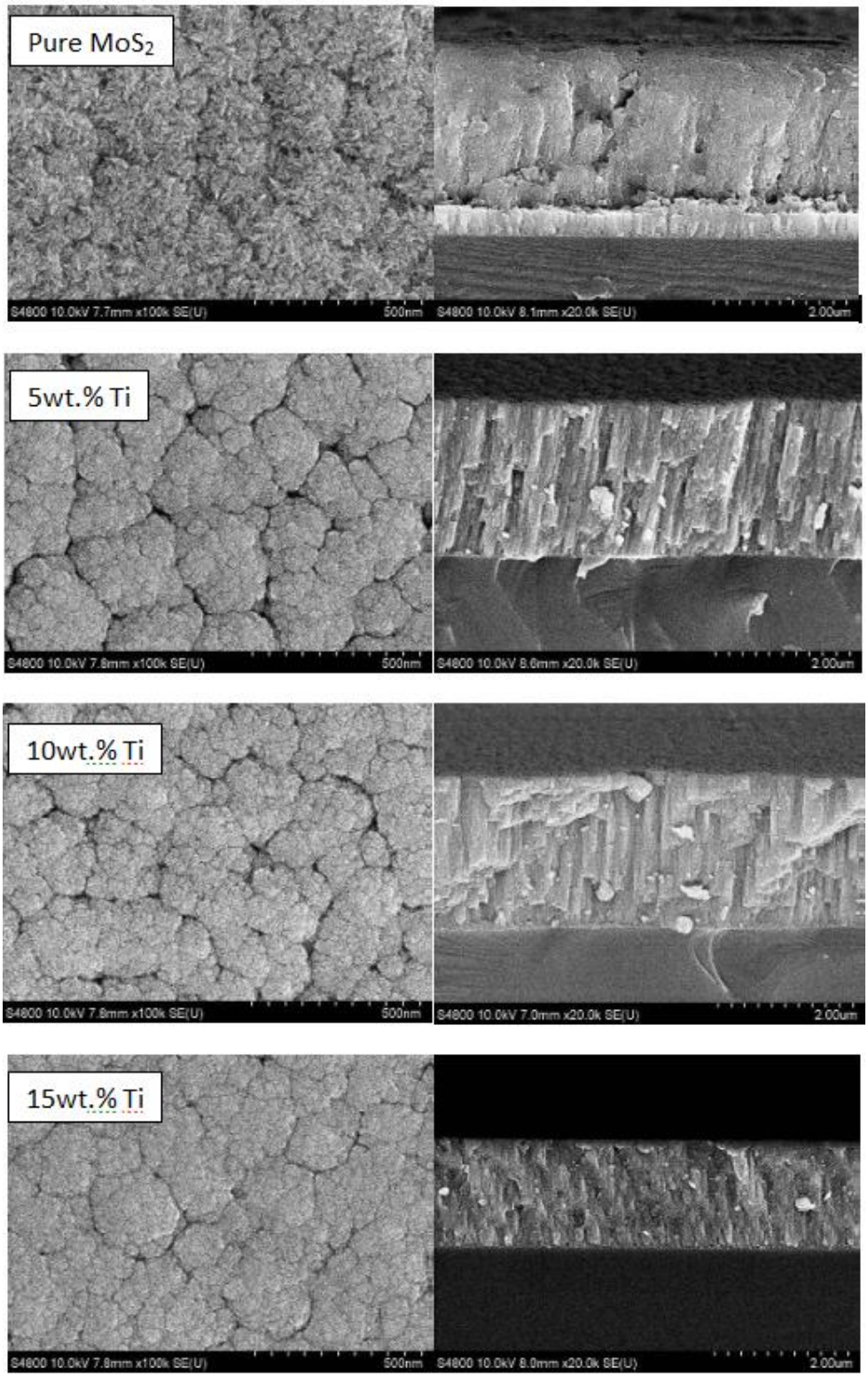

Figure 2-56 Surface and Cross-Section Micrographs of MoS_2-Ti Coatings with Different Ti Content [146]

Another popular adhesive interlayer element, Cr, has been tested in different concentrations [147] [148] and under different sputtering parameters [149]. The initially columnar structure of the MoS_2 becomes increasingly amorphous as the Cr content is increased. Despite producing high

hardness, high concentrations of Cr (25%) produce high friction, wear, and poor adhesion. The optimum concentration of Cr to achieve a compromise between adhesion, friction and wear rate appears to be 5%-10%. Interlayer thickness can also be critical.

Ding [150] conducted direct comparisons of Cr and Ti-doped sputtered MoS_2 coatings in atmospheres of varying humidity. In low doping concentrations both coatings displayed remarkable similarity in tribological properties over the complete range of humidities tested, with low friction and wear rates evident up to 75% RH. In both cases the optimum doping concentration was found to be 10%, with coatings containing more than 20% metal exhibiting the formation of either precipitates or nanoscale multilayers and severe degradation of wear rates.

The variety of dopants that have been studied for sputtered TMD films is very wide. Other metals dopants shown to improve the performance of sputtered TMDs include Al [151], Pb [152] [153], Au [151] [154], Zr [138], Cu [155], Ni [156] [160], Ag [157], and W [138]. Elsewhere none-metallic dopants have been applied such as WSe_2 (another TMD solid lubricant) [147], F [158], TiN [159], and Sb_2O_3 [160]. Direct comparison of the effectiveness of different dopants is difficult due to the wide variety of deposition methods, base TMDs, substrates, doping concentrations, and test conditions. Thus, information on which to base selection of a dopant for a specific application is difficult. A small number of studies have featured a range of dopants tested to identical conditions.

An early study by Zabinski [160] compared the friction and wear characteristics of undoped MoS_2 films and those doped with 11% and 20% Ni, 1.7% Fe, 2.3% Au, and 35% SbO_3. A further 34% Sb_2O_3/Au hybrid doped film was also included. Films were grown using DC sputtering at 20 millitorr (2.7Pa) without substrate cooling, vapour gettering or negative substrate bias and consequently the pure MoS_2 films exhibited the typical highly porous, columnar appearance. No adhesive interlayers were applied. The Fe and 20% Ni doped coatings offered little benefit, the 20% Ni coating in particular being brittle and failing rapidly at high contact stresses. The 11% Ni, Au, Sb_2O_3, and Sb_2O_3/Au all reduced friction and prolonged wear life, with the SbO_3/Au providing the longest wear life and lowest coefficient of friction. All coatings continued to exhibit sensitivity to water in terms of friction and wear life.

Renevier et al. [138] conducted a comparison of MoS_2 films doped with Cr, Zr, W, and Ti through scratch, Rockwell indentation, pin-on-disc, and reciprocating wear tests. Films were grown using unbalanced magnetron sputtering, with Ti used as a vapour getter and interlayer, and a low bias voltage applied to the substrate. The structure of undoped MoS_2 films deposited using this method is described as dense and non-columnar, unlike those shown in Zabinski's study. The doped coatings achieved similar improvements in the properties of the film compared to pure

MoS_2 for each dopant tested. W doping yielded the lowest coefficient of friction under low contact pressures, and Zr doping gave the longest wear life when submerged in water, but the characteristics of the four films were broadly similar.

Simmonds et al. [147] performed a similar range of tests on MoS_2 doped with Au, Ti, Cr, and WSe_2 in various concentrations. Films were grown using RF magnetron sputtering, with Cr applied as an interlayer, at gas pressures of 0.5Pa. The Au and WSe_2 doped coatings were applied with and without Ti gettering for comparison. Ti and Cr produced hard coatings (>8GPa) as expected even in low concentrations whilst those produced by sputtering with Au and WSe_2 were much softer (~4GPa). Despite the low hardness both Au and WSe_2 doped coatings offered significant improvements in wear rate and minor improvements in coefficient of friction over a broad range of concentrations, with the optimised WSe_2 doped coating providing the longest coating life of all samples. The results for these softer coatings suggest surprisingly that a high hardness may not be necessary for good overall tribological properties.

The optimum doping concentration for wear life of the softer Au and WSe_2 doped coatings was slightly lower than that required for minimum friction coefficient but was generally aligned, with a good compromise being found in the region of 15% for Au and 8-11% for WSe_2. The use of gettering did not appear to significantly affect the friction coefficient or wear life of either coating. The harder Ti and Cr doped coatings exhibited a more complex relationship, with low concentrations producing low coefficients of friction and low wear lives, and higher concentrations producing the opposite. Simmonds noted that low Ti content coatings in particular generated significant debris during initial running, which may have resulted in rapid generation of transfer films and consequently low friction.

These findings would appear to contrast with those of Ding [150], who observed a close correlation between optimum concentration for both wear rate and friction for Ti and Cr doped coatings. This may be explained by differences in the coating structure and wear rate definition. Simmonds applied an initial Cr adhesion interlayer, followed by the composite coating. Ding applied Cr or Ti interlayers, but then applied a graded layer prior to the composite layer. Graded layers involve a gradual change in doping concentration. In Ding's case the graded layer was varied from pure Cr or Ti at the interface with the adhesion interlayer, with the MoS_2 content then increased up to the final concentration used in the composite layer.

Both Ding and Simmonds showed that the hardness of the composite increases with increasing Cr/Ti content until approximately 20% concentration. Therefore, a potential explanation is that the use of the graded layer produced a coating of increasing hardness with wear depth. It is possible that during initial sliding the MoS_2 rich layer of Ding's coatings provided the necessary

transfer film to the counterface to give low friction, and then a harder, more wear resistant layer became gradually exposed, reducing the wear rate. However, this cannot be proven from the data contained in the papers. It should also be noted that whilst Ding measured wear in terms of volumetric wear coefficient (mm^3/Nm), whilst Simmonds counted revolutions of the pin-on-disc tribometer until $\mu>0.3$, which makes comparison of the data difficult.

As evident from the preceding paragraphs, even those studies that included multiple dopants only considered a relatively small number. The differences in sputtering techniques, interlayers, concentrations, and test conditions make an assessment of the relative effectiveness of different dopants very difficult.

The precise position of dopants within a sputtered TMD coating has not been proven and may vary between systems. Renevier [140] and later Hui [146] proposed that the most likely role of Ti in Ti-doped MoS_2 was to occupy the space between S planes or form junctions between MoS_2 lattices. This would explain the reduction of sensitivity to water vapour, as the presence of a metal dopant between the planes would prevent ingress of moisture [138].

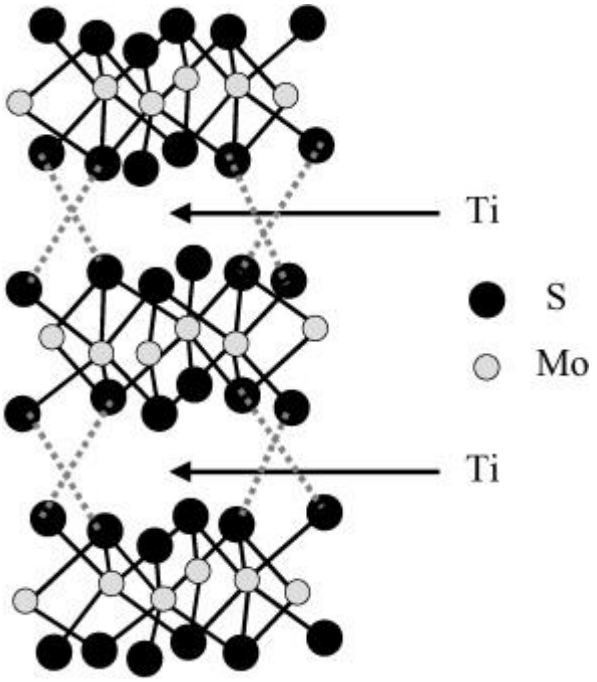

Figure 2-57 The Structure of MoS_2 showing the Probable Positioning of Titanium Atoms in a Doped Coating Structure [140]

It has also been suggested that metal dopants sacrificially protect the MoS_2 from water vapour by being preferentially oxidised [140] [144]. Sb_2O_3 is a common additive in bonded MoS_2 films [110],

with Kinner [161] first producing evidence that sacrificial oxidation to Sb_2O_4 was responsible for the significant improvement in properties. Likewise, Ti is an effective oxygen getter [162] that sees significant use in industrial vacuum processing. The relative success of both dopants in studies has consequently led some to conclude that the dopants fulfil a similar role in sputtered coatings.

However, this theory was strongly disputed by Centers [163], who concluded that the improvements were based on the changes in mechanical properties which allowed parallel basal plane orientation to be more readily achieved. Centers also acknowledged the potential for Sb_2O_3 to act as a both a thermal and oxidation diffusion barrier. Furthermore Scharf [139] noted the absence of TiO_2 in the wear debris of tests on Ti-doped WS_2, also reaching the conclusion that Ti did not act as an oxygen getter. The good performance of films doped with inert metals such as Au also casts doubt on the preferential oxidation hypothesis. Despite the significant use of Ti as a getter during deposition, no significant benefit was observed by Simmonds [147] and hence its significance as a getter even if in this context is cast into some doubt.

However, whilst the structural and chemical role of the dopants is still somewhat uncertain, several common characteristics emerge from the literature:

- Successful dopants increase the density, hardness, and adhesion of coating resulting in greater load capacity and improved wear resistance.

- Doped TMD films are more likely to produce a stable transfer layer, and more readily assume a parallel orientation of the basal planes, which lowers friction.

- Dopants inhibit the formation of crystalline TMD, increasing crystal size or leading to an amorphous structure, and thereby reducing the chance of brittle fracture.

- For most dopant-TMD systems there is a limit of solubility. If the dopant concentration exceeds this limit precipitates or a superlattice structure will emerge resulting in a brittle film with poor characteristics.

2.3.6 Self-Adaptive Sputtered Lamellar Solid Lubricant Films

Self-adaptive coatings, sometimes referred to as “chameleon coatings”, exhibit changes in properties in order to maintain acceptable tribological properties under extreme conditions [106]. With respect to lamellar solids, such coatings are designed to produce more consistent performance in humid air or at oxidising temperatures. The majority of self-adaptive solid

lubricant coatings have been based on co-sputtering with carbon to produce either a nanostructured or superlattice coating containing a matrix or layers of amorphous carbon. As knowledge of the properties of amorphous carbon coatings is required to provide an explanation of their behaviour, these coatings will be discussed in section 2.4.

A small number of other TMD-based self-adaptive coatings have been reported. John [164] studied composite and superlattice coatings of WS_2 and CaF_2 as a potential solid lubricant for both high and room temperature conditions. Composites consisting of 1:1 WS_2 and CaF_2 gave a coefficient of friction of 0.25 at 500°C, which was considered to be very good for the conditions and better than pure WS_2 at these temperatures. However, room temperature performance was poor both before and after heating. The superlattice coatings exhibited acceptable friction characteristics both at room temperature and then at 500°C, but it does not seem that the room temperature performance was checked again after the high temperature test. Analysis of the wear track debris showed that the coating had reacted to form CaO and $CaSO_4$, whilst outside of the wear track the original composition remained. $CaSO_4$ is known to behave as a solid lubricant at high temperatures [165], and hence the high temperature lubricity was explained by this lubricious product.

Several metal oxides have been used in a similar manner in conjunction with TMDs. Walck [166] characterised ZnO-WS_2 using various electron microscopy techniques at increasingly high temperatures. The coatings exhibited an increasing transformation to $ZnWO_4$ at temperatures of greater than 500°C. Tests on similar burnished coatings by Prasad [167], demonstrated that the composite film gave lower coefficients pure of friction than pure WS_2 at room temperature and 300°C. At 500°C the coefficient of friction was initially high but then dropped to 0.22, whilst the pure WS_2 failed quickly. See Figure 2-58. This was considered to be a consequence of $ZnWO_4$ and confirmation of the adaptive behaviour of the coating.

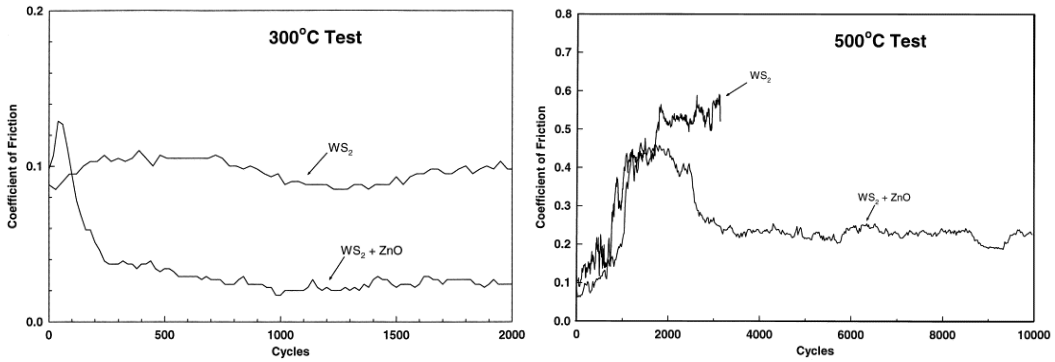

Figure 2-58 Frictional Behaviour of Pure WS_2 and Adaptive ZnO-WS_2 Composite Coatings at 300°C and 500°C [167]

2.3.7 Summary

Lamellar solids such as graphite and MoS_2 are amongst the oldest solid lubricants and lubricate coated surfaces through the low shear strength characteristics and transfer film forming capabilities of their layered structure. However, they exhibit sensitivity to water vapour levels, oxidise at high temperatures and are soft, which limits their load-carrying capability. Sputtering techniques developed during the 1960s offered a new way to deposit TMD lamellar solids as coatings, but these were porous, brittle, poorly oriented and suffered from degraded performance in humid air.

Improvements in sputtering techniques produced coatings of a denser structure, with better crystal orientation and reduced moisture sensitivity, but the most significant development was through the co-deposition of TMDs with metallic or metal-oxide dopants. Doping of sputtered TMDs further increased the density and substrate adhesion of the coatings and produced amorphous structures that allowed good tribological properties to be maintained in humid air. The precise role of dopants in the coating is still the subject of debate, but their concentration must be controlled to achieve the optimum performance and avoid the emergence of precipitants or multi-layered structures that lead to poor durability and high friction.

A new generation of self-adaptive coatings have emerged to provide low friction and wear over a greater range of temperatures and environments. Metal-oxides can react with the TMD under sliding at high temperatures to produce lubricious sulphates, but the most promising coatings have been produced through co-depositing with carbon. These coatings will form part of the discussion in section 2.4.

2.4 Amorphous Carbon Coatings

2.4.1 History and Development of Amorphous Carbon Coatings

The first studies of amorphous carbon films date back to the 1950s. The German physicist Schmellenmeier [168] attempted to produce tungsten carbide films using a glow discharge of hydrocarbon gases onto tungsten-cobalt coated steel. He noted that at low discharge currents a black, hard, amorphous layer formed on the cathode. He later characterised these films using X-ray diffraction and noted that in some cases the coating contained diamond crystallites.

The term “diamond-like carbon” was coined in 1971, when Aisenberg and Chabot [169] generated thin films of carbon using ion beam deposition. The ion generator used graphite electrodes to

ionise argon gas, which resulted in an ion beam of both argon and carbon. This apparatus was used to deposit films onto silicon, glass, and steel, with both crystalline and amorphous phases. The coating was sufficiently hard to scratch glass, electrically conductive, and resistant to hydrofluoric acid.

However, amorphous carbon coatings did not see significant commercial use until the early 1990s, primarily due to the lack of industrialisation of the deposition process, and the persistence of substrate adhesion problems. The incorporation of metal dopants into the coating to improve adhesion and the implementation of large scale magnetron sputtering led to the use of DLC films on machine tools and mechanical components. However, the use of metal dopants resulted in a softening of the film that limited their use in highly loaded engineering applications.

New deposition processes which utilised sputtered adhesive interlayers and Plasma-enhanced chemical vapour deposition (PECVD) for the carbon film itself were developed. These techniques provided reliable adhesion without the use of metal dopants [170]. Amorphous carbon coatings are now used in the optics, biomedical, magnetic media, automotive, and aerospace industries, to provide hard, low friction, wear resistant surfaces.

2.4.2 Structural, Mechanical and Tribological Properties of Amorphous Carbon Films

The properties and classification of amorphous carbon films are based on the hydrogen content and the proportion of sp^2 and sp^3 hybridizations. Sp^3 C will form four bonds, equally spaced 109.5° apart in a tetrahedral configuration. Sp^2 C forms three bonds which are spaced 120° apart in a trigonal planar configuration. Consequently, sp^2 C is graphitic in structure, whilst sp^3 C is diamond-like. The term “DLC” is perhaps somewhat misused, with many so-called DLCs containing minimal sp^3 content. True DLCs contain a significant fraction of C-C sp^3 bonds and its structure can be modelled as a random covalent network of sp^2 and sp^3 bonded C and H [171]. See Figure 2-59 [172].

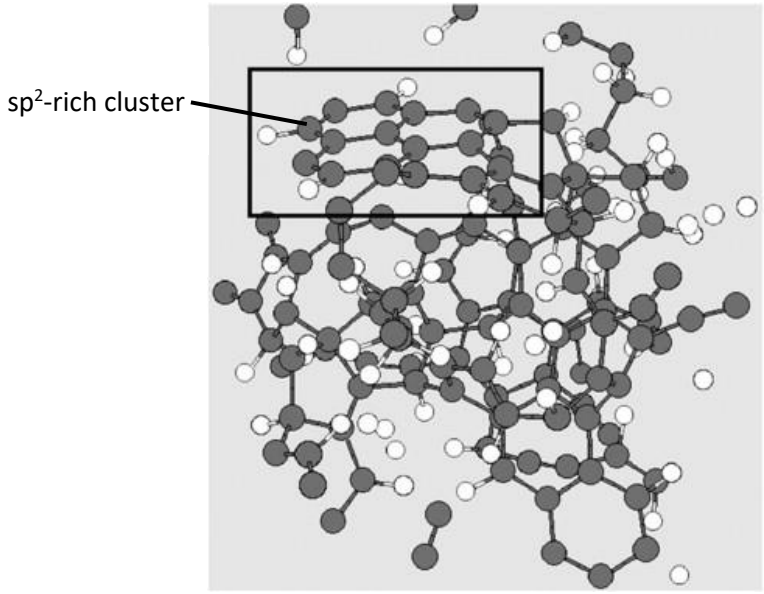

Figure 2-59 Random Covalent Network Model of a-C:H (30% H, 65% sp^2, 20% sp^3) [172]

The relationship of the relative sp^2, sp^3, and H contents to the classification of the film is commonly explained using a ternary diagram, an approach first proposed by Jacob and Moller [173]. Figure 2-60 shows a ternary phase diagram based on data collected by Casiraghi [174].

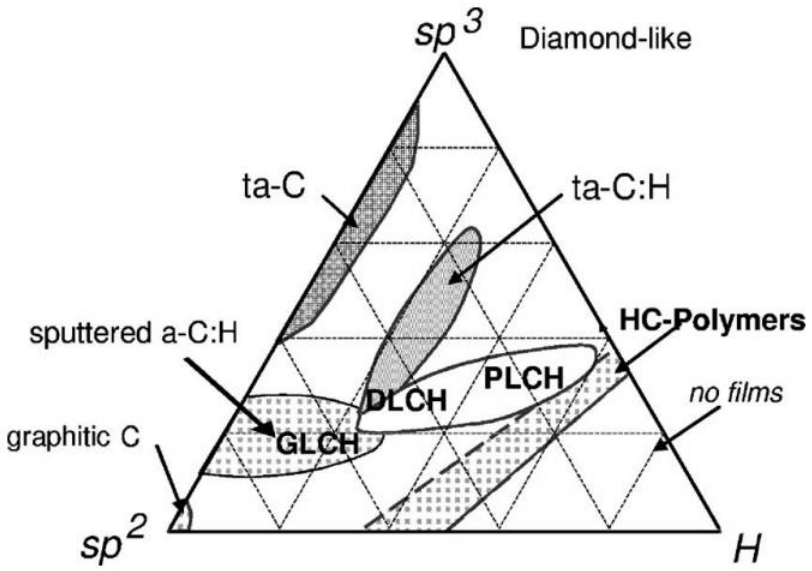

Figure 2-60 Ternary Phase Diagram of Bonding in Amorphous Carbon-Hydrogen Alloys [174]

Casiraghi defined four type of hydrogenated amorphous carbon (a-C:H) based on these relationships:

- Films with high H contents (40-60%). These can contain high quantities (≤70%) of sp^3 bonds, but these are mostly hydrogen terminated. Consequently, the film is soft and lacks density. They are referred to as polymer-like a-C:H (PLCH).

- Films with intermediate H contents (20-40%). Although the overall sp^3 content is lower than PLCH a greater proportion are C-C bonds, which give superior mechanical properties. These are referred to as diamond-like a-C:H (DLCH).

- Films with intermediate H contents but higher proportion (≤70%) of sp^3 bonds. A class of DLCH, they are referred to as hydrogenated tetrahedral amorphous carbon (ta-C:H). They have a higher density and Young's modulus than standard DLCH.

- Films with low H content and a high proportion of sp^2 bonds. These are referred to as graphite-like a-C:H (GLCH).

Further categories amorphous carbon then exists at very low H contents. Those with high sp^3 hybridization levels, potentially up to 95%, are referred to as tetrahedral amorphous carbon (ta-C). Despite the high sp^3 content, without sufficient H to stabilise the covalent network it easily forms graphite under shear stresses induced by sliding [175]. Non-hydrogenated carbon films with minimal sp^3 content are simply referred to as a-C, or graphitic C.

A comparison of the approximate mechanical properties of different amorphous carbon coatings, taken from various sources, was produced in [176], and is shown below in Table 2-3.

Table 2-3 Approximate Categorisation of Amorphous Carbon Coatings and their Mechanical Properties [176]

	sp^3 (%)	Hydrogen (%)	Density (g/cm^3)	Hardness (GPa)	Young's modulus (GPa)
Graphite	0	0	2.267	0.2–2	10
Diamond	100	0	3.515	100	1000
a-C	0–5	< 1%	1.9–2.2	10–20	100–200
a-C:H soft	60	40–60	1.2–1.6	< 10	100–300
a-C:H hard	40	20–40	1.6–2.2	10–20	100–300
ta-C	80–88	0	3.1–3.3	50–80	300–500
ta-C:H	70	30	2.4	50	300

The hardness and inertness of DLC films stem from the strong C-C sp^3 bonds [177]. The proportion of sp^3 content in the film is heavily influenced by the energy of the particles involved in the deposition process. These can be carbon ions (as in ion beam deposition) or bombarding ions from an inert gas (as in unbalanced magnetron sputtering). With increasing particle energy, the film densifies and sp^3 bonds become more prevalent. However, at excessively high energy levels the sp^3 content begins to fall again and desorption of H takes place resulting in graphite-like structures [178].

Lifshitz [179] proposed that this relationship was attributable to subplantation, in which during film growth carbon ions with sufficient energy penetrate the surface of the film and embed themselves beneath it, increasing density and causing the formation of C-C sp^3 bonds. Alternatively, bombardment by inert gas ions causes displacement or "knock-on" of surface carbon into subsurface interstitial sites. Ions without sufficient energy diffuse on the surface and form C-C sp^2 or C(sp^3)-H bonds. Robertson [180] found that maximum sp^3 content in ta-C occurred at ion energies of 100eV and attributed the degradation at higher energy levels to thermal relaxation allowing the subplanted C to diffuse back to the surface. See Figure 2-61 [177]. a-C:H tends to contain less H than the hydrocarbon species used during the deposition process, and this is also dependent on the ion energy. H particles penetrate more deeply into the surface where they form molecules of H_2 which desorb, causing loss of H [181].

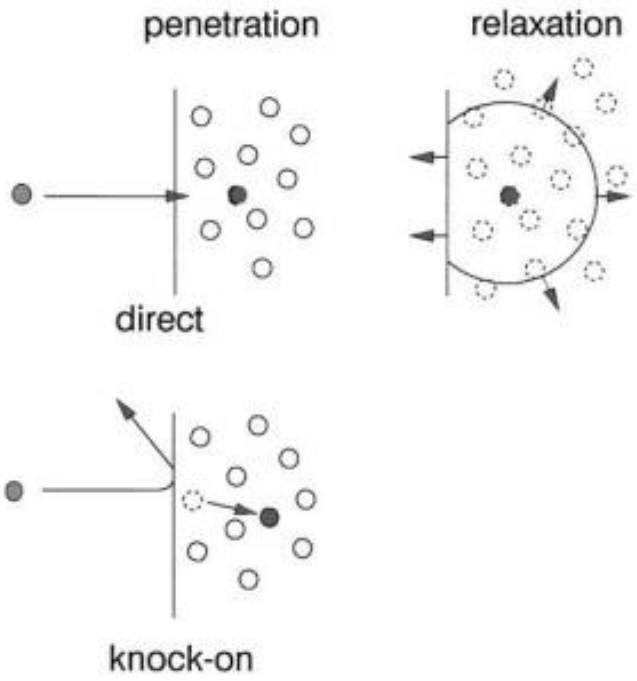

Figure 2-61 Processes of Subplantation in DLC Film Growth: Direct Penetration, "Knock-on" Penetration, and Relaxation [177]

Particle energy also determines the level of intrinsic stress generated during deposition of the coating. Films grown using non-energetic particles (<0.5eV) will develop tensile internal stresses, which is explained using a grain boundary relaxation model. During deposition the film grows from isolated clusters. Attractive forces cause the grain boundaries to deform across gaps between the grains, which is opposed by the constraining effect of adhesion to the substrate. This results in an induced tensile stress [182].

Bombardment by energetic particles during deposition causes a reduction in the volume of intergranular gaps due to subplantation, which prevents tensile stresses from developing. With increasing particle energy, the tensile stress reduces to zero. Further increases in particle energy result in compressive stresses developing due to volumetric distortion [182].

The total internal stress within the coating consists of both the intrinsic stress described above and thermal stresses resulting from difference in the coefficient of thermal expansion between the coating and the substrate. Excessive tensile or compressive stresses can both lead to failure of the film. Tensile stresses may lead to fracture perpendicular to the film, whilst compressive stresses commonly lead to delamination. In both cases the internal stress causes a build-up of stored elastic energy which, when exceeding a critical value, is consumed to cause mechanical failure. As the energy stored per unit area of the film rises with increasing thickness, internal stresses significantly influence the maximum coating thickness that be deposited without failure [183].

In terms of their tribological characteristics carbon films exhibit a wide range of properties. The variety in frictional behaviour in particular could be considered the widest of any group of coatings [175]. When processed correctly they offer a combination of high hardness, low friction, low wear, high elasticity, and good adhesion. Thus, it can be said that they exhibit characteristics that are both ceramic-like and polymer-like [184]. Given that DLC coatings are usually harder than steel, their behaviour seems inconsistent with Bowden and Tabor's [121] equations (see equations (2) and (3)), which suggest that to act as a solid lubricant a thin film should have low shear strength. Most materials capable of acting as a solid lubricant are soft (graphite, TMDs, soft metals etc.).

The lubricating mechanism of carbon coatings is generally one involving the formation of a lubricious tribofilm on both surfaces, followed by sliding of these films over each another [185] i.e., interfilm slip (refer back to Figure 2-46). The tribofilms formed by carbon coatings during sliding are more graphitic in structure [186], and lower in H [187] than the coating itself. Figure 2-62 shows the micro-laser Raman spectra comparison of a coating, wear scar deposit, and transfer film for a ball-on-disc test using a DLCH coating running against an M50 ball in dry

nitrogen. The standard Raman spectrum for graphite is included for comparison. Both the wear scar debris and transfer film exhibit a transformation towards a disordered graphitic structure.

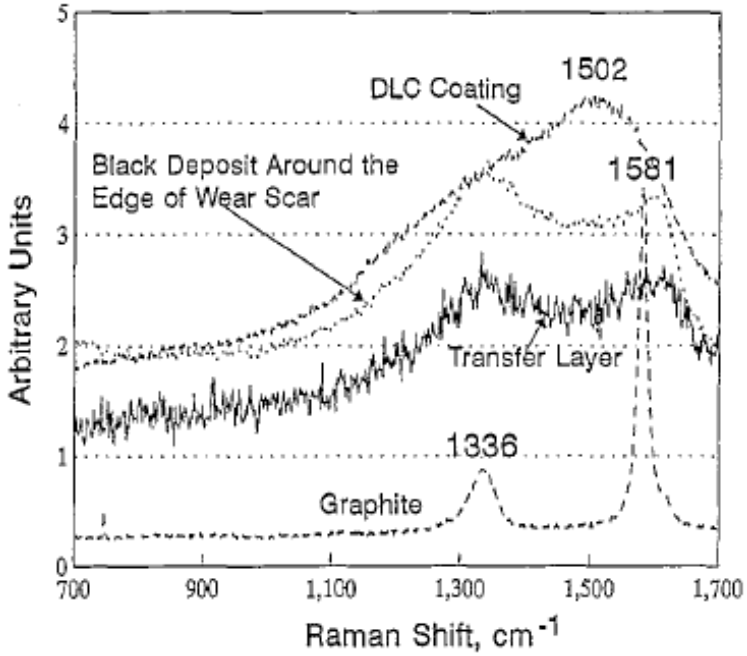

Figure 2-62 Micro-Laser Raman Spectra of Coating, Transfer Layer and Wear Debris from DLHC on Steel Wear Test [186]

As the formation of the lubricious transfer layer is produced by wearing of the film the initial friction between the two surfaces is high. The coefficient of friction reduces as the transfer layer begins to form before reaching a steady state. Sliding between the surfaces induces heat, which could cause the destabilisation of H–C sp^3 bonds in a-C:H, and thus trigger transformation to an sp^2 structure [188]. However, sp^2 enrichment has been observed in contacts unlikely to generate the temperatures required and hence it has been suggested that the sp^2 transformation is stress-induced [189]. In either case higher contact pressure will lead to a more rapid formation of the transfer film and low steady state friction. See Figure 2-63. However, the initial stages of friction reduction are associated more with transfer film formation than graphitization [188]. Consequently, the initial running-in period is crucial to ensure long coating life.

As the transfer layers that give amorphous carbon its tribological characteristics are graphitic it is unsurprising that they also exhibit a dependency on the humidity of atmosphere. However, the relationship appears to be complex and some studies report contradicting relationships. ta-C coatings have been shown by Voevodin [189] to act with increased sensitivity to humidity as the transfer layer forms. Figure 2-64 shows a comparison of the friction-humidity relationship of DLC

sliding against sapphire balls after 10^2 and 10^4 cycles. The divergence of the two lines illustrates how the interface acts increasingly like graphite.

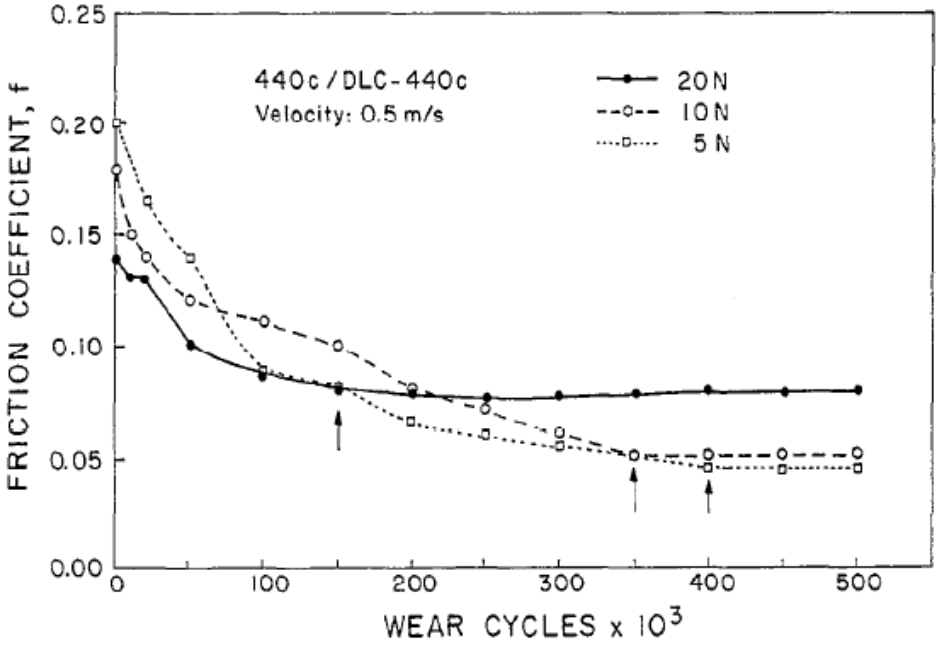

Figure 2-63 Variation of Coefficient of with Sliding Distance for DLC Coating Running against 440C Balls [188]

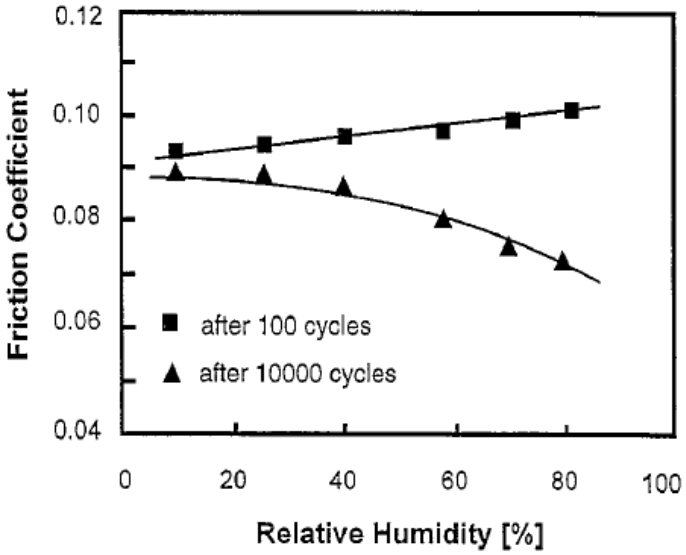

Figure 2-64 Variation of Friction Coefficient for Hydrogen-Free DLC Film Sliding against Sapphire Balls with Increasing Humidity after 10^2 and 10^4 cycles [189]

The results of a study by Enke [190] recorded the lowest friction for a-C:H coatings in very low humidity. It was argued that hydrogenated films are susceptible to tribo-oxidation in the presence of water vapour or oxygen [185]. This was subsequently disputed by Donnet et al. [191] who concluded that oxygen has no effect on frictional behaviour and found no evidence of tribo-oxidation. Under humid conditions thinner transfer films were formed, and Donnet suggested that this was responsible for the increased friction. However subsequent studies such as that by Li et al. [192] have shown that tribochemical reactions, not only oxidation of C but also in the case of steel counterparts reactions between Fe and C, do occur and contribute to high friction and wear in humid conditions.

Elsewhere Voevodin [193] reported a decrease in friction with increasing humidity for both hydrogenated and non-hydrogenated coatings. Another study by Donnet [185] showed that hydrogen content seemed to be an influencing factor, with coatings containing at least 42% H showing much lower friction in a vacuum than coatings with lower H content. The performance in ambient air was very similar for all coatings irrespective of H content, and lower than that in a vacuum for coatings with less than 42% H. These findings agree with those of Grill [194], who showed that loss of H from an a-C:H film resulted in an increase in friction and wear rate. The overall frictional behaviour of amorphous carbon films in different atmospheres may depend on the deposition method, precise sp^3/sp^2 ratio, and their influence on tribofilm formation in addition to hydrogen content.

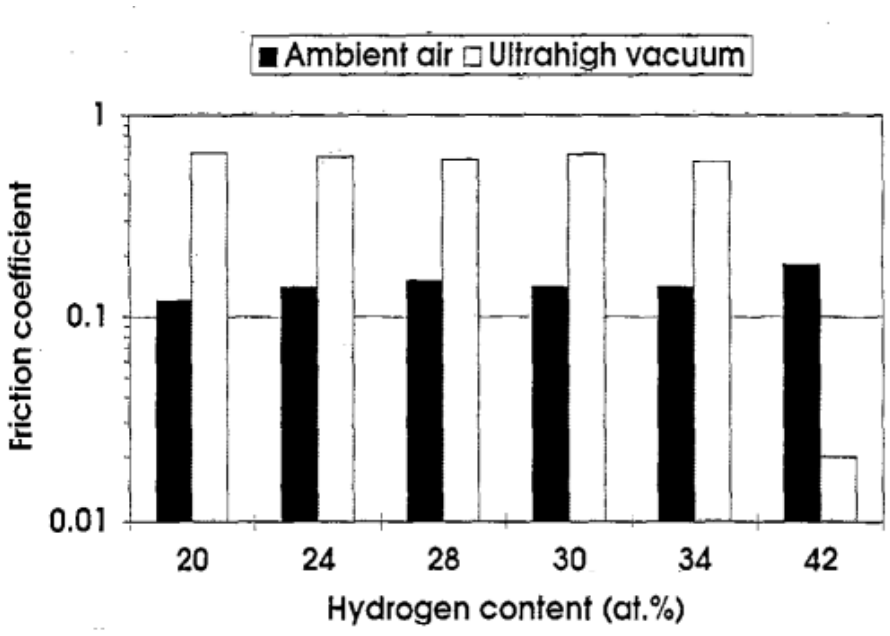

Figure 2-65 Variation in Steady State Friction in Vacuum and Ambient (40-60% RH) for DLC Coatings with Different H Content [185]

2.4.3 The Use of Adhesive Interlayers in Amorphous Carbon Films

High internal stresses and the resulting risk of delamination remained a barrier to the commercial use of DLC coatings for many years and consequently much of the early research examined ways to improve adhesion and reduce stresses through the use of interlayers.

Cr was shown by Chen and Hong [195] to be an effective interlayer material for depositing DLCs onto steel. Cr has high toughness and a coefficient of thermal expansion close to that of Fe, which helps to minimise thermally induced stresses. It is well-known to alloy easily with steel and is able to form carbides. Consequently, Cr interlayers produce diffuse intermixing at both the Fe-Cr and Cr-C junctions when deposited under conditions of high energy bombardment giving good adhesion [196]. Similarly, silicon is an effective adhesive interlayer when depositing DLCs onto silicide-forming metals (E.g., Ti, W, Mo) [197]. The use of Ti as an interlayer has been shown to reduce thermally induced stress on steel substrates [198], and can provide a comparable benefit to Cr [199].

More recently metal-ceramic interlayers have been found to achieve superior adhesion than pure metal [199]. However, the vast majority of studies including these interlayers have been performed on metal doped DLC, or with the inclusion of gradient or superlattice structures, and hence these are discussed in section 2.4.4.

2.4.4 Metal-Containing Amorphous Carbon Films

Much like TMD lubricants, significant improvements have been made to the properties of amorphous carbon films through the use of various dopants. Metal doping of amorphous carbon films was first investigated in the 1980s [200]. In particular carbide-forming metals (Ti, Cr, W) have been of interest, in part for the improvements to adhesion as discussed in 2.4.3. This is usually achieved by sputtering with a metal or metal carbide target using a mixture of Ar and hydrocarbon gas. At low concentrations the metal is able to remain well dispersed and the coating remains amorphous, though some short order clustering of metal atoms may exist [201]. The incorporation of higher metal content results in the formation of larger carbide crystallites, eventually taking on a nanocomposite structure. For example, in Ti-doped sputtered films precipitation of B1 cubic Ti-C will begin between 4% [202] and 8% [201] Ti.

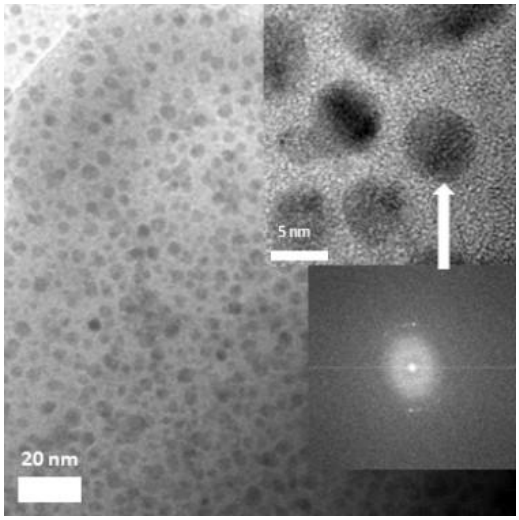

Figure 2-66 TEM Image of DLC Coating with 4.2% Ti with Inset Showing HRTEM Image and Corresponding FFT Pattern of the Film [202]

Ti has been the most commonly studied dopant, probably due to its ability to adhere to a wide range of substrates [203]. Wei [204] observed the reduction of internal stresses of Ti and Cu doped films compared to undoped DLC using Raman spectroscopy. This stress relief was attributed to the greater compliance of transition metals within the random covalent network due to the loose binding of electrons within their outer shell. Wang [198] also noted that the incorporation of Ti also resulted in a lower sp^3 content and suggested that the sp^2 sites may form with their σ plane aligned with the plane of compression, thus resulting in shrinkage and relieving stress.

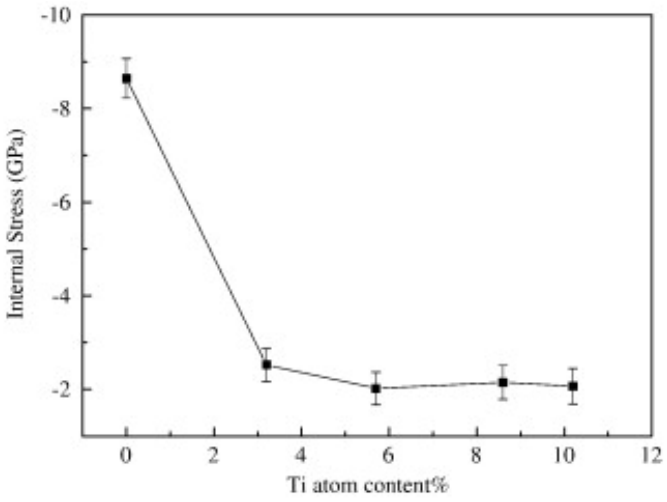

Figure 2-67 Internal Stress of Ti-Doped DLC Film on Steel Substrate as a Function of Ti Content [198]

A loss of sp^3 content will result in the coating becoming increasingly graphite-like and at Ti concentrations below the solubility limit this results in a reduction in hardness. With increasing Ti content, once the solubility limit is exceeded and as carbide precipitates form the hardness begins to rise again [201]. See Figure 2-68. This is accompanied by a smoothing of the surface due to the inhibition of the formation of larger amorphous carbon clusters [205]. See Figure 2-69. If the Ti content is increased sufficiently, it produces a nanocomposite structure with 10-50nm TiC grains separated by a distance of a few nanometres in the amorphous carbon matrix. This produces a significant improvement in coating toughness. See Figure 2-70. Rather than suffering brittle fracture when stressed above the elastic limit as hard coatings are prone to, nanocomposite Me-DLC coatings behave plastically: an example of so-called "load adaptive" behaviour. This has been attributed to grain boundary sliding and nanocrack termination mechanisms [206].

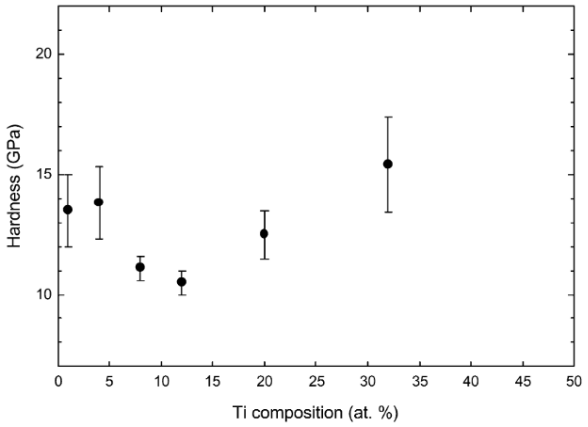

Figure 2-68 Nanoindentation Hardness as a Function of Ti Content for DLC Film [201]

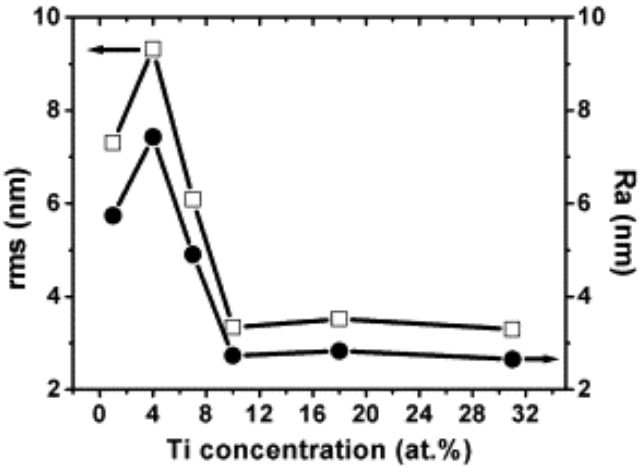

Figure 2-69 Surface Roughness in RMS and Ra as a Function of Ti Content in Ti-Doped DLC [205]

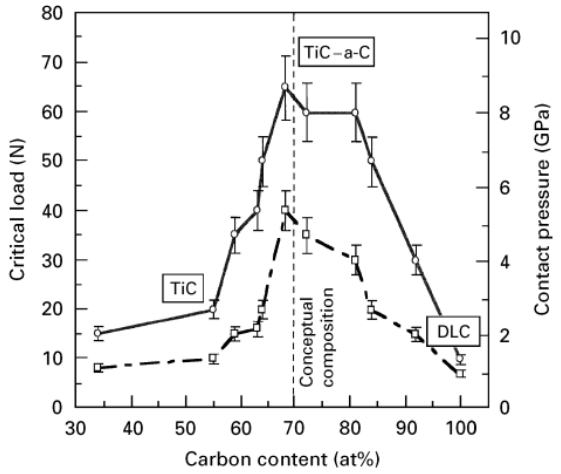

Figure 2-70 Scratch Toughness of Ti-Doped DLC as a Function of C Content (□: Cohesive strength, ○: Adhesive Strength) [206]

Despite the improvements to mechanical properties, high levels of doping cause a degradation of tribological properties. The coefficient of friction and wear rate follows a similar pattern to the film hardness, with initial Ti content causing significant improvements in sliding characteristics, but further increases causing both friction and wear rate to degrade [205]. The initial improvement has been attributed to Ti acting as a catalyst for increasing lubricious sp^2 content, with small carbides possibly being surrounded by a thin layer of graphite-like carbon and embedded in the still amorphous matrix [207]. As the volume fraction of the Ti-C increases the coating acts more like Ti-C, and the friction coefficient becomes closer to that of a ceramic material [205]. Unlike Ti-doped TMDs, Ti-doping of a-C:H appears to have little effect on film performance in high humidity environments and compares unfavourably in this regard with metalloid dopants such as Si [206].

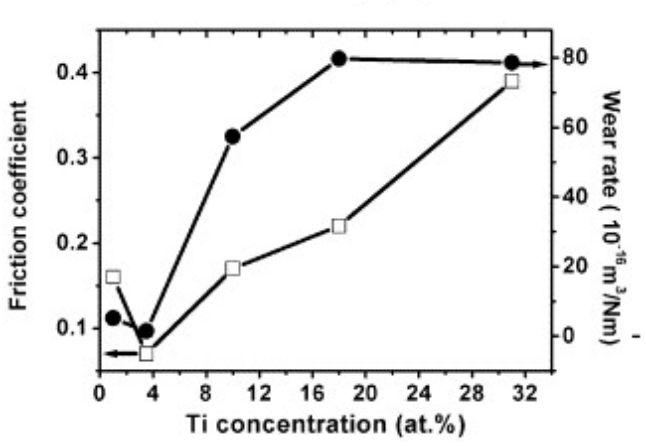

Figure 2-71 Unlubricated Sliding Friction Coefficient and Wear Rate of Ti-DLC Nanocomposite as a Function of Ti Concentration [205]

Ti is one example of a carbide-forming metal that can be used to improve the properties of amorphous carbon films. Another similar dopant is W, which has been of great interest in the automotive industry [208] [209]. Czyżniewski [210] conducted a useful comparative study of the three most common dopants: Ti, W, and Si, which provides an insight as to why W-doping is more suitable in certain applications. Whilst the lowest coefficient of friction and wear rate were found with low concentrations of Ti, the W-doped coating with the tribologically optimum concentration exhibited greater adhesion. Higher hardness and elastic modulus were also possible with W, in part due to a higher limit of solubility. Additionally, WC is known for retaining its hardness at very high temperatures [211].

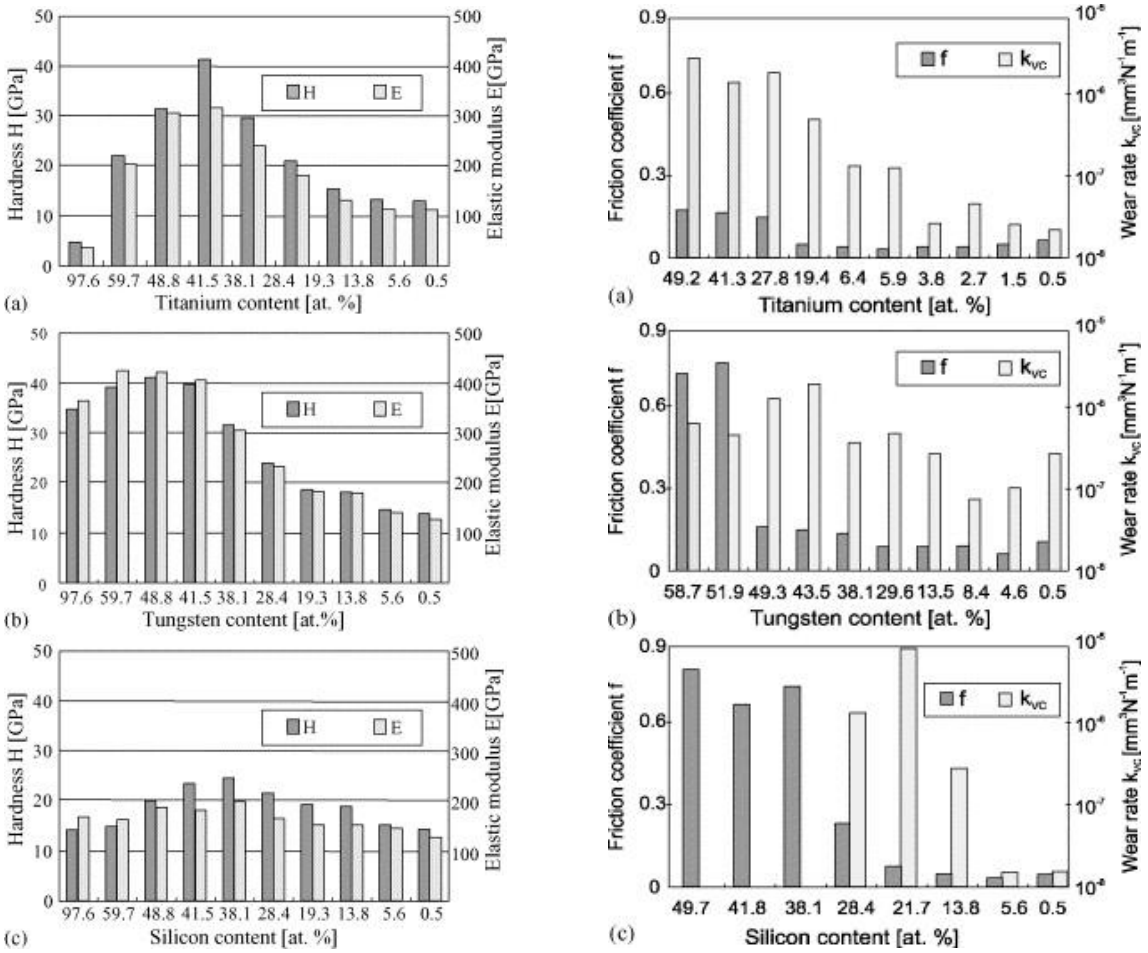

Figure 2-72 Comparison of Hardness, Modulus of Elasticity (Left), Friction Coefficient, and Wear Rate (Right) for (a) Ti, (b) W, (c) Si as a Function of Doping Concentration [210]

2.4.5 Multi-layered and Graded Amorphous Carbon Based Films

Despite the improvements made to the adhesion and internal stresses of amorphous carbon films by the use of adhesive layers and low concentration metal doping, coating failure by brittle fracture may be induced due to deformation of the substrate [212]. This limits the load bearing capability of the coating, particularly in very hard films on softer substrates. See Figure 2-73. As explained the toughness of the film can be improved through higher levels of metal doping but this compromises the tribological properties of the surface.

An alternative approach to improve the load capacity whilst maintaining the sliding properties of the coating is to apply additional pure metallic or ceramic coating layers. A hard ceramic intermediate layer between the adhesion and carbon layers may be used to reduce deformation. Alternating pure metal and carbon layers can be used to provide zones of easy shear, allowing deformation of the harder DLCs without yielding [213]. See Figure 2-74. Layers may also be applied with compositional gradients in order to avoid sharp changes in material properties at the interfaces that may serve as possible locations for crack formation [212]. The application of multilayer and graded composition coating architectures presents a vast array of possibilities. Coating design can be complex, with different layers performing different functions such as adhesion, diffusion blocking, crack braking, stress equalization, and load support in addition to the low friction and wear resistance of the amorphous carbon itself [214].

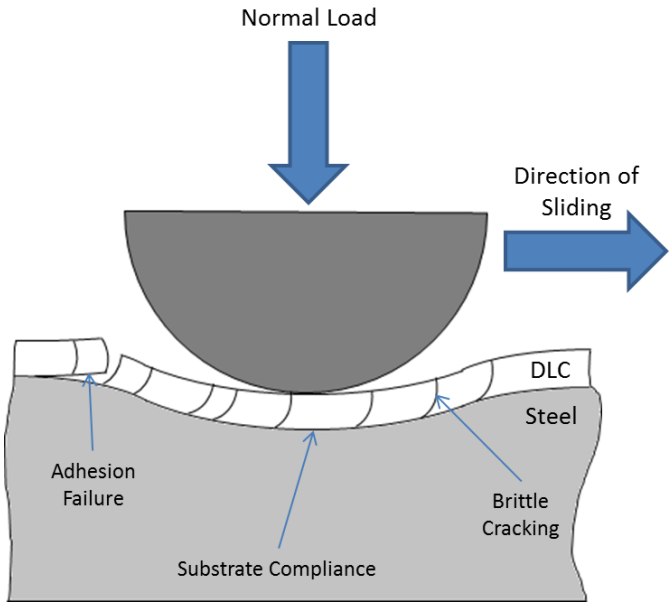

Figure 2-73 Failure of DLC Coatings under High Contact Loads (Adapted from [212])

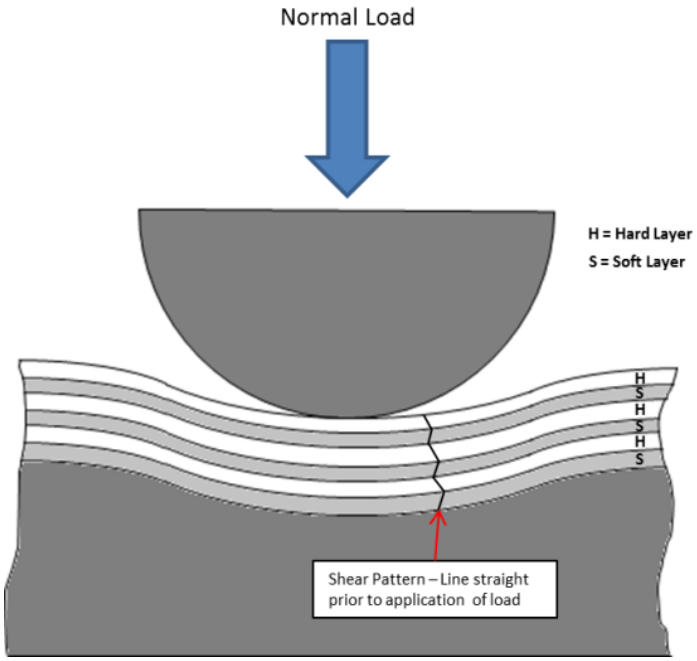

Figure 2-74 Schematic Illustration of Shear Patterns in Multilayer Coatings of Alternating Hard and Soft Layers (Adapted from [213])

Voevodin [212] conducted a thorough comparison of the tribological and mechanical properties of Ti-TiC-DLC coatings of varying architectures. The highest critical loads in scratch tests were obtained using a multi-layered coating consisting of a Ti adhesion layer, an intermediate load supporting TiC layer, a transition layer with a compositional gradient from TiC up to pure C, then 20 alternating layers of Ti and ta-C. At high contact pressure (1.4GPa) its wear life was many orders of magnitude higher than the plain ta-C. However, this coating exhibited a relatively high coefficient of friction and increased wear at low loads compared with a single layer ta-C. A more balanced compromise between friction and durability was achieved using coating consisting of the same structure but omitting the sequence of alternating layers. This coating achieved a single order of magnitude lower wear life at high contact pressure and slightly lower adhesion, but friction comparable to the single layer ta-C.

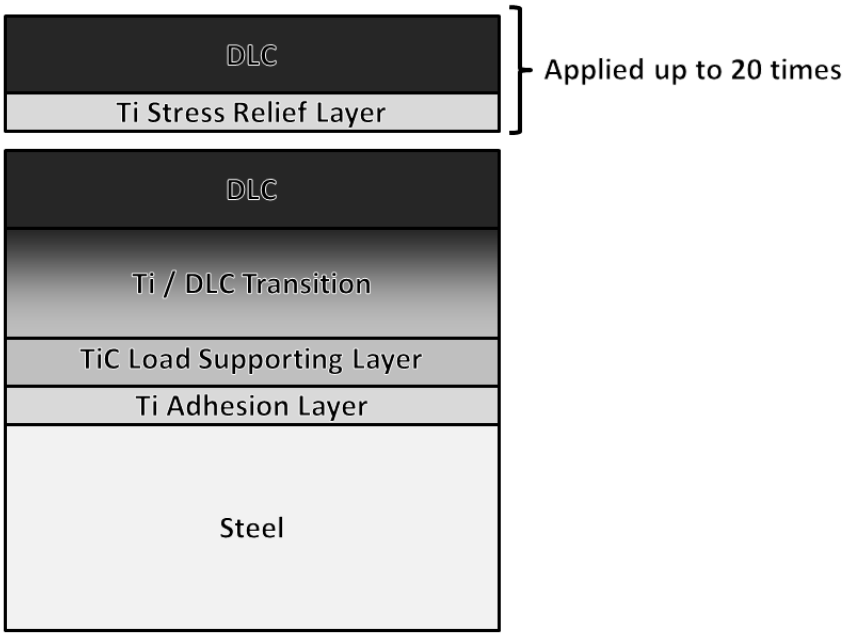

Figure 2-75 Schematic Diagram of Multilayer Ti-TiC-DLC Coating [212]

Voevodin's experiments show how coating architecture can be tailored to produce coatings with specific characteristics for an application. Other multilayering systems include the Ti/TiN/TiNC/DLC coating produced by Choy [215] as a candidate coating for medical applications on stainless steel and Ti-alloy substrates. This system achieved better adhesion and a lower wear rate than Ti/TiC/DLC, particularly on Ti-alloy substrates. This is possibly due to the better matching of thermal expansion characteristics between Ti and TiN than between Ti and TiC. However, the friction was slightly higher. Chen [216] reported on DLC coatings based on a Cr/CrN/CrNC/CrC/WC/W-DLC multilayering system; with the final W-doped DLC layer incorporating a compositional gradient to produce a C-rich surface. A range of surface W contents from 0% to 47.9% were tested, with 17.8% producing the best compromise between friction and wear rate.

Several commercial multilayer amorphous carbon based coatings are available which includes Balinit C by Balzers, based on a structure of Cr interlayer followed by alternating Cr and WC layers and an outer layer of a-C:H doped with 12% W [217]. Teer coatings have produced Graphit-iC, consisting of a Cr interlayer, graded Cr to C transition layer, then 5%-Cr doped graphitic a-C. Dymon-iC, also by Teer, is based on a Cr interlayer, followed by CrC, then DLC [218].

2.4.6 Self-Adaptive Carbon-Based Films

Given the previously described opposing relationship of the friction of TMD and graphitic solid lubricants with humidity, a number of recent coating developments have focussed on incorporating TMDs into carbon based coatings. In humid air such a coating could provide lubrication through the formation of a friction-induced graphite-like tribofilm, whilst in dry air or a vacuum the graphitic surface would be removed as debris, allowing the TMD to provide lubrication in its place.

Voevodin and Zabinski [212] reported on such a coating constructed from WC/DLC/WS_2, the design and functioning principles of which are shown in Figure 2-76. In moist air the coefficient of friction was comparable to that of graphite (0.05-0.15), whilst in dry nitrogen it was equivalent to that of WS_2 (0.01-0.05). See Figure 2-77. This adaptive behaviour was found to be reversible when alternating between the two environments. Raman spectroscopy of the coating in the as-deposited condition and again after sliding in humid air and a vacuum confirmed the formation of the expected transfer films. After sliding in humid air, the worn surface was characteristic of graphitic carbon whilst after sliding in a vacuum the spectra showed peaks corresponding to WS_2 and WO_3.

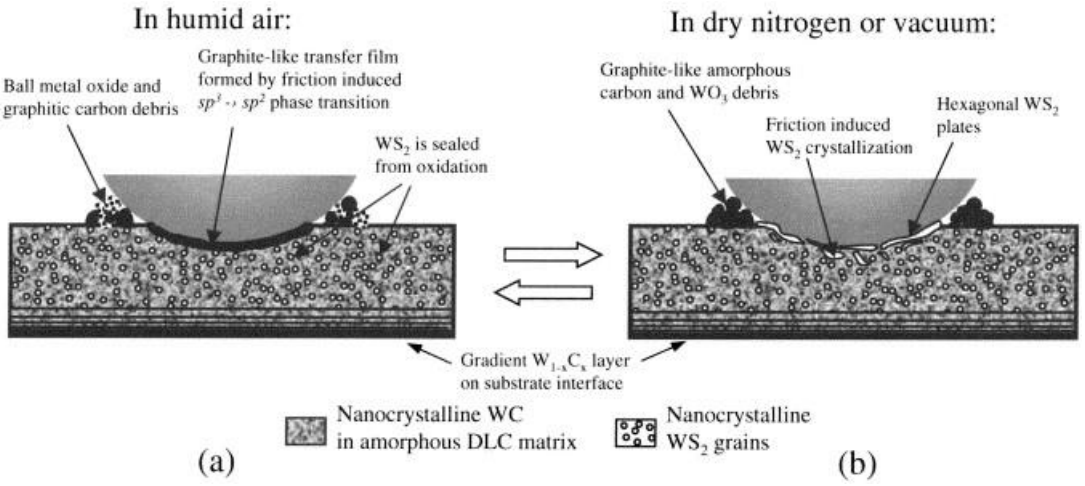

Figure 2-76 Mechanisms of Reversible Self-Adaptation of WC/DLC/WS_2 Coating in (a) Humid Air and (b) Dry Air [212]

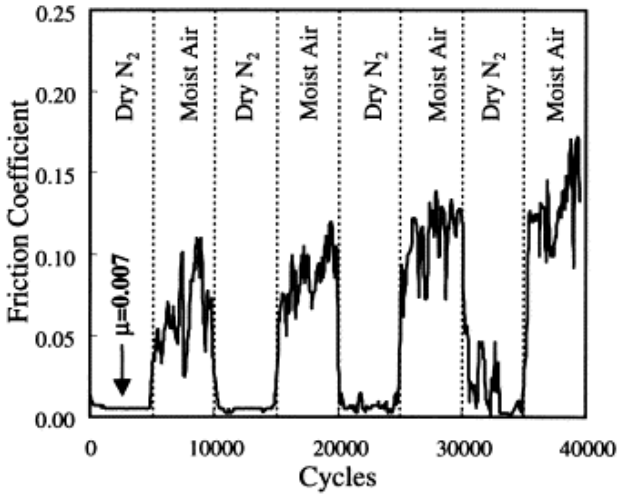

Figure 2-77 Reversible Adaptive Friction Characteristic of WC/DLC/WS_2 During Dry-Humid Environmental Cycling [212]

A further DLC based adaptive coating was developed by Voevodin [219] in an attempt to increase load bearing and high temperature capability. The coating combined YSZ (yttria-stabilised zirconia) nanoparticles for high load wear resistance, MoS_2 for lubrication in dry or vacuum conditions, Au for high temperature lubrication, with DLC to provide graphitic carbon transfer films for lubrication in humid air. Coefficients of friction in dry N_2, humid air, and 500°C air were found to be close to that of MoS_2 (0.03-0.04), partially graphitised DLC (0.1-0.15), and Au (0.25-0.3) respectively. The presence of corresponding transfer films was confirmed by Raman spectroscopy.

Polcar and Cavaleiro [220] conducted a review of W-S-C, Mo-S-C, W-Se-C and Mo-Se-C coatings deposited by magnetron sputtering. All coatings exhibited a reduction in coefficient of friction with increasing load i.e., behaviour in accordance with Kanakia's [119] equation for the intrafilm flow regime (refer back to equation (3) in paragraph 2.3.2). This relationship was more pronounced in humid air, where at high pressures the coefficient of friction was comparable to that in dry air. The carbon matrix had previously been shown to follow Amonton's laws and consequently this is an indication that the TMD phase is more dominant in the lubricating mechanism. TEM images of cross-sectioned worn films and Raman spectroscopy of the wear track indicated that reorientation of the TMD platelets occurs below the surface of film within the carbon matrix. No O was detected in the worn surface, and graphitic C was only found as debris at the sides of the track. Hence it was concluded that the improved performance in humid in air was actually due to the C acting to protect the TMD from oxidation during the reorientation process, not the presence of a graphitic tribolayer.

2.4.7 Summary

Since their accidental discovery in the 1950s, amorphous carbon coatings have been of interest to researchers and industry due to the combination of high hardness, wear resistance and low friction. Amorphous carbon coatings consist of a random covalent network and vary in structure and characteristics based on the proportion of graphite-like sp^2 bonds, diamond-like sp^3 bonds and hydrogen content. The sp^3 bond content is dependent on the energy of the particles used in the deposition process, with high energy particles causing subplantation of carbon atoms beneath the surface, resulting in densification and sp^3 bond formation.

However, this process also causes a build-up of intrinsic stresses, which when combined with thermal stresses from the deposition process leads to problems with poor adhesion to the substrate. Adhesion has been improved by the use of carbide forming metals as diffuse interlayers, which reduce thermally induced stresses. Doping of the carbon film with these same metals reduces intrinsic stresses due to their compliance, but also a reduction in sp^3 content. Metal doping can cause both softening or hardening of the deposited film depending on the concentration used. Hardness can be greatly increased at higher concentration levels at the expense of tribological performance.

Alternative approaches to heavy metal doping have been sought to improve adhesion and load carrying without sacrificing low friction and wear. Multilayering of amorphous carbon films with hard ceramics to provide load support, or with soft metals to reduce shear stresses under deformation have both proved effective. This has led to a new generation of complex multilayer and compositionally graded coatings, several of which are now commercially produced for industrial applications.

More recently researchers have sought to combine amorphous films with TMD solid lubricants in order to take advantage of the opposing sensitivities of graphitic and TMD tribofilms to environmental humidity. These self-adaptive coatings are capable of low friction and wear in a wide variety of environments, though research suggests that the mechanism of low friction in humid air is attributable to the carbon acting to protect the TMD during platelet reorientation rather than the formation of a graphitic lubricant phase.

2.5 The Use of Self-Lubricating Films on Gear Teeth

The majority of studies into the performance of coatings on gears have been conducted with oil lubrication. Under these conditions coatings are often viewed as a way to increase the load carrying capacity of otherwise conventionally lubricated and designed gearboxes against failure by either pitting or scuffing. Coatings are often applied as a remedial measure to counteract a persistent equipment failure mode that emerges in the field [221]. Such an approach is often desirable as it minimises the number of components that require modification.

A further area of interest relates to the interactions between lubricant additives and coatings applied to gears. The majority of conventional lubricant additives have been developed based on their chemical interactions with ferrous surfaces. Therefore, researchers have sought to understand how the effectiveness of the additives is affected by the use of non-ferrous coatings. Alternatively, coatings have been viewed as a potential replacement for oil additives, which are often environmentally toxic, in order facilitate the use of more sustainable biodegradable additive-free oils. The majority of studies in these areas have focussed on coatings that are based on either DLC or TMD lamellar solid lubricants.

Studies into the effectiveness of gears coated with solid lubricants in dry-running conditions are very limited, though there is some interest in aerospace applications, where improved durability in the event of a loss of lubrication event may be required.

2.5.1 Carbon-Coated Gears under Conventional Lubrication

As discussed in the previous chapters, single layer undoped amorphous carbon coatings can suffer from adhesion problems in highly loaded contacts due to internal stresses. The contact between gear teeth is counterformal, which results in intense subsurface shear stresses and elastic deformation of the substrate, both of which are clearly challenging conditions for a coating to tolerate. Consequently, few studies have examined the potential of simpler carbon based films for geared applications. For evidence of their performance, one must look at studies utilising rolling-sliding tribometers as an indication for their performance on gears.

Xiao et al. [222] evaluated the suitability of a-C coatings for geared applications by a four-ball wear scar test, using 52100 steel balls under grease-lubricated conditions. The a-C coated samples exhibited a lower wear rate and greater resistance to seizure than either uncoated or TiN-coated samples. The benefits of the coating became more significant with decreasing lubricant film thickness. It is interesting to note that compared to an a-C:H:W coating the a-C offered a lower

coefficient of friction and near identical wear performance and seizure load despite very high contact stresses (1.5GPa). It appears that the a-C:H:W was applied with a multilayer structure and all coatings were deposited onto a Ti adhesion interlayer.

Amorphous carbon coatings have also been shown to improve resistance to micropitting. Singh et al. [223] conducted tests on soft a-C:H coated rollers undergoing mixed rolling-sliding motion to assess their suitability for use on gears and bearings. Testing was conducted using low viscosity oils to ensure boundary-lubricated conditions and encourage failure by micropitting. The a-C:H coated specimens completed over three times as many cycles as the uncoated samples without any failure. The results also showed that hybrid-mated (i.e., coated roller vs uncoated roller) pairs achieved very similar friction and durability improvements to self-mated pairs. This was particularly true where the roller with the lower sliding distance was the coated component. See Figure 2-78 and Figure 2-79.

The descriptions of the coatings in these two studies are somewhat limited, which makes it difficult to draw detailed conclusions. However, the positive results, particularly compared with more sophisticated coatings, and the lack of studies featuring pure amorphous carbon on gears suggest that simpler coatings may have been somewhat overlooked. It should be noted that even in the previous examples some form of interlayer was applied to the steel substrate prior to the carbon in order to improve adhesion. The majority of studies into carbon-based coatings for gears utilise either Cr or CrN as an initial interlayer.

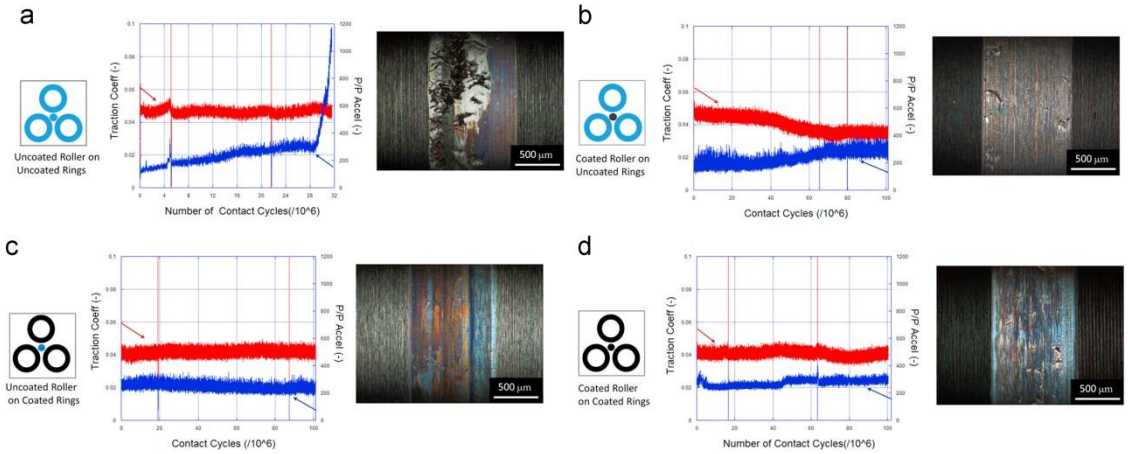

Figure 2-78 Traction Coefficient and Vibration Characteristics of Self-Mated and Hybrid a-C:H Contacts in Mixed Rolling-Sliding Motion [223]

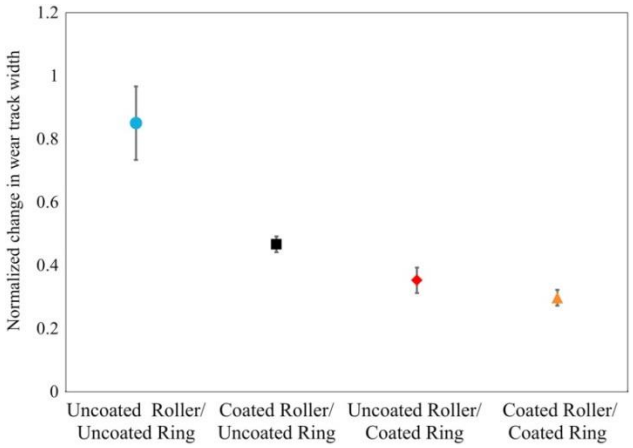

Figure 2-79 Wear Track Width for Self-Mated and Hybrid a-C:H Contacts in Mixed Rolling-Sliding Motion [223]

For studies featuring coatings on gears rather than representative tribometers only a small number have considered single layer metal doped DLC. Fujii et al. [224] showed that a-C:H:W coatings improved the pitting resistance of spur gears, provided that the pitch line contact stress remained less than 1900MPa. At higher contact stresses early adhesion failure of the coating, particularly in the dedendum, led to rapid wear and earlier onset of pitch line pitting. If stresses remain sufficiently low to avoid peeling (~<1700Mpa) the pitting life was significantly improved. The lower the contact stress the greater the benefit of the coating. This study featured gears coated with a-C:H:W both with and without a CrN interlayer. Strangely the coating with the CrN interlayer suffered from earlier delamination failure than the coating with no interlayer, and consequently gave poorer performance than an uncoated gear. The author offered no explanation for this result.

Kržan [225] reported on scuffing tests using a-C:H:W with a Cr adhesive layer on gears lubricated with both mineral and ester oils. In mineral oil the wear rate of the coated gears was significantly lower. In the ester oil formulation, the scuffing capacity and wear rate of the uncoated gears was significantly reduced, whilst that of the a-C:H:W coated gears remained approximately the same. This suggests that the benefits of such coatings are most significant when lubrication is poor and scuffing conditions are prevalent. It was noted that the wear mechanisms of the coated and uncoated samples appeared to be very different. Wear particles from the coated gears were much larger and some showed evidence of an abrasive mechanism.

The majority of studies featuring amorphous carbon coatings on gears have concentrated on those with a multi-layered structure. The coating with the most published research is Balinit C: a commercially available coating from Oerlikon Balzers. It is deposited by magnetron sputtering and consists of an initial Cr interlayer, followed by a transition region of alternating C and WC layers.

The final top layer consists of a-C:H:W [217]. It should be noted that there are discrepancies in the description of Balinit C in different papers. In other studies, the coating description broadly matches that of Balinit C and the coatings were deposited by Balzers, but the coating is not explicitly named.

Jiang et al. [217] applied Balinit C to vapour honed Pyrowear 53 gears and characterised the a-C:H:W layer using scanning and transmission electron microscopy. Their inspections revealed that the outer a-C:H:W layer exhibited a microscale columnar structure with dispersed WC nanocrystals, and nanoscale modulations in W content in alternating planes perpendicular to the direction of column growth. Running the gears in low viscosity oil resulted in an overall smoothening of the surface. Both the adhesion interlayer and transition region were intact, and no coating delamination was observed. Intercolumnar defects present in the upper a-C:H:W layer did not penetrate into the layer below.

Mercer et al. [226] also studied the structure and sequence of material removal in a layered W-DLC coating applied to vapour honed pyrowear 53 gears by Balzers. Mercer observed that during the coating process existing crack-like imperfections in the honed steel surface were uniformly covered by the initial Cr interlayer. As the a-C:H:W was applied a columnar structure was formed, with intercolumnar gaps forming at the site of larger imperfections in the substrate. During operation of the gears the surface asperities were removed, resulting in a smooth surface. This process of asperity removal and polishing was continued as the wear progressed down through the DLC, into the Cr interlayer, and eventually into the steel itself.

Moorthy [227] included Balinit C in contact fatigue tests on coated case-hardened helical gears. The Balinit C coated gears exhibited the lowest visible micropitting of all the coatings studied. Other coatings included Balinit C Star (CrN/a-C:H:W), Nb-S, and two coatings incorporating IFLM (inorganic fullerene-like material) WS_2. The improvement was attributed in part to the wear of the coating in the dedendum of each tooth and subsequent polishing caused by meshing with the still-coated tooth tips of the mating gear. However, the actual tooth deviations produced were small compared with the majority of other coatings tested. A further paper by the same authors [228] confirmed that the development of micropits was linked to the presence of “notch-like micro-valleys” in the as-ground surface of the gear. Polishing these features out or filling them in with a suitable coating led to reduced micropitting.

The Balinit C Star coating included in Moorthy’s study is another commercially produced coating from Oerlikon Balzers, and consists of a CrN adhesive and load supporting layer topped with a-C:H. The performance in terms of average profile deviation was comparable to Balinit C when testing at below 1500MPa contact stress. Testing at higher contact stress resulted in material

removal on the Balinit C Star progressing at a far higher rate than Balinit C. This is likely to be a consequence of the shear stress distribution effect of the alternating Cr and WC layers and demonstrates that a multi-layered coating design is desirable at high contact stresses. Other studies featuring Balinit C Star [229] have noted coating delamination at the wheel root as a dominant failure mode.

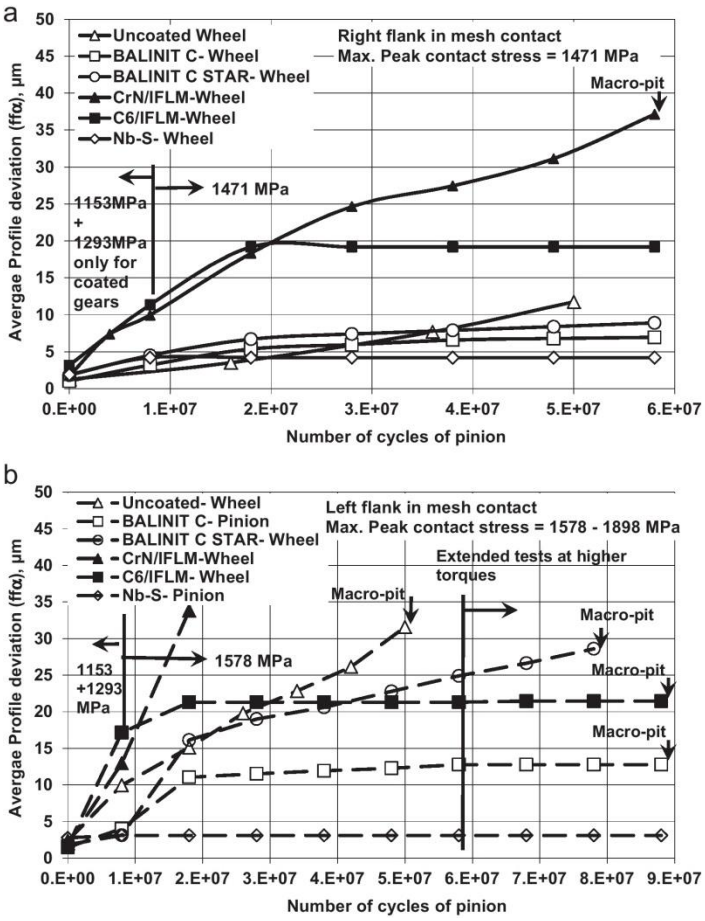

Figure 2-80 Averaged Profile Deviation for Micropitting Tests on Coatings Including Balinit C and Balinit C Star at (a) 1471MPa, (b) 1578MPa [227]

Kalin and Vižintin tested a-C:H:W coatings on spur gears lubricated with biodegradable oils to determine their effect on the lubricant operating temperature [230]. The coatings were applied by Balzers, and the description broadly matches that of Balinit C. Gear scuffing tests to FZG standard A/8.3/90 [93] were conducted, but with a lowered oil preheat temperature (50°C instead of 90°C) in order to more easily differentiate the effect of the coating on lubricant heating. Whilst the wear rate between self-mated a-C:H:W coated gears remained within limits up to contact pressures of 1.4GPa, in fact by far the lowest wear rate was obtained for self-mated uncoated steel gears. Hybrid gear pairs gave higher wear rates overall, with the vast majority of the wear occurring on the uncoated gear.

Kalin's results contrast somewhat with those of Joachim [221], who included a lamellar Balzers a-C:H:W coating, presumably Balinit C, in a series of tests on spur gears. In these experiments the a-C:H:W coated gears achieved a higher scuffing resistance than those obtained for uncoated and superfinished steel gears, over twice the torque capacity, using the same test procedure [93]. The difference would appear to be attributable to changes made to the lubricants used and the operating temperature. Using linear interpolation of the oil temperature-viscosity data and test temperature in Kalin's paper and comparing this with the same data from Joachim's paper shows that the lubricant used in Joachim's test would have been far less viscous at the test start: 8.85cSt compared to 48.33cSt. With all other test conditions the same, this would have produced lower film thicknesses during operation.

None of the samples in Kalin's tests showed any visual evidence of scuffing or adhesion. It is therefore likely that the increased film thickness prevented scuffing during test and that the observed wear was abrasive or simply of a mild type. This implies that under poor lubrication regimes such as in Joachim's test a-C:H:W coatings can increase scuffing capacity and reduce material loss, but under better conditions where film thicknesses are higher and asperity interactions are less frequent the uncoated gears are superior.

Joachim also found that the a-C:H:W outperformed uncoated and superfinished gears in low speed wear testing. In this test the pitch-line velocity of the gears was held to a very low level; 0.03m/s compared to 8.3m/s for the scuffing test. This prevents the formation of a fluid film and ensures boundary-lubricated conditions. The wear rates of both self-mated and hybrid pairs were approximately one quarter of the uncoated samples. Macropitting tests found that the lifetime of the gears was increased by a factor of 2-3, but only in self-mated contacts.

Similarly tests to the FZG standard pitting test method [96] performed by Weck [231] on Balzers a-C:H:W coated gears with a laminate structure in biodegradable synthetic oils showed clear improvement in macropitting performance with self-mated gears. When subjected to standardised scuffing tests [93] the material loss was 2.5 times less than on uncoated gears. On micropitting tests [232] the performance of both coated and uncoated gears were very similar in terms of tooth profile deviations.

Michalczewski et al. [233] included a coating matching the description of Balinit C in a series of tests to investigate the interactions between different lubricants and coatings in rolling and sliding contacts. Cone-ball and four-ball tests were used to assess scuffing and pitting resistance, in addition to scuffing tests on gears. Of the coatings tested only the a-C:H:W demonstrated pitting resistance comparable to uncoated steel, whilst also providing a significant increase in scuffing capacity in plain mineral base oil and those with antiwear or extreme pressure additives.

From the above evidence it can be summarised that Balinit C significantly reduces severe adhesive wear in poorly lubricated gear meshes. Pitting resistance seem more complex, and the results are difficult to interpret due to differences in gear materials, lubricants, and test method. However, all tests have concluded that the pitting resistance is either comparable or superior provided self-mated gear pairs are used.

The effectiveness of chromium as a doping element for amorphous carbon coatings in geared applications was assessed by Amaro [234]. The coating, Graphit-iC is consisted of a Cr interlayer, graded Cr to C transition layer, and 5%-Cr doped a-C. Under standardised scuffing tests [93] the coatings demonstrated a significant improvement in load carrying capacity. As the author noted, the five load-stage improvement over uncoated gears compared favourably with a-C:H:W based coatings subjected to very similar test conditions such as the two load-stage improvement published by both Joachim [221] and Weck [231].

2.5.2 Lamellar Solid Lubricant Coated Gears under Conventional Lubrication

As with amorphous carbon, studies into the behaviour of gears coated with lamellar solid based coatings are dominated by a small number of commercially available films. No studies involving pure sputtered TMD films could be located. It is assumed that their omission is an indication that the load bearing capability and adhesion is insufficient for the high contact pressures that occur between loaded gear teeth. MoST, a titanium-doped MoS_2 coating previously described in 2.3.5, is the only TMD-based coating reported on to a significant depth for geared applications.

Amaro [235] produced the first study into the application of MoST on gears, conducting twin-disc and scuffing tests. The twin disc tests were conducted at several slide-to-roll ratios, whilst controlling lubricant temperature to theoretically ensure constant lubricant film thickness. Despite high contact stresses (1.511GPa) and low film thickness (λ=0.5) no delamination failure or severe wear modes were observed. At lower slide-to-roll ratios the slower cylindrical disc was more severely worn faster spherical disc, whilst at higher ratios this relationship was reversed. Possible explanations given were the better surface finish of the cylindrical disc, or the fact that the faster disc would heat less than the slower one.

Scuffing tests showed a significant increase in the power that could be transmitted by MoST coated gears without surface failure at 3000rpm. At a lower speed (1500rpm) the improvement was more modest. Lowering the gear surface roughness (R_a = 0.4µm vs. 2.4µm) improved the transmittable power at 1500rpm, but not at 3000rpm. The superior performance, particularly at

higher speeds, would indicate lower friction and contact temperature. This would be supported by the results of subsequent tests in which gearbox efficiency was shown to be improved by 0.5%.

Martins [236] expanded on Amaro's work, studying the differences in coefficient of friction, tooth mass loss, and oil temperature rise for coated and uncoated gears. Oil stabilisation temperatures were lower for coated gears, with the temperature difference becoming less significant at higher speeds. This may have been due to increased lubricant film thickness and therefore fewer asperity interactions. Similarly tooth friction was reduced on coated gears, with the difference becoming more significant at higher loads. Whilst higher loads could be tolerated without transitioning to a scuffing regime, Martins found that under non-scuffing conditions MoST-coated gears actually suffered greater wear than uncoated components.

A further paper by Martins [237] provided a comparison between the previous results of gears coated with MoST and the aforementioned Graphit-iC (C/Cr) reported by Amaro [234]. MoST coatings were shown to offer superior scuffing resistance, with no scuffing occurring at any of the tested loads at 1500rpm. At 3000rpm both coatings scuffed at the same load stage. MoST coatings with improved surface roughness gave the best scuffing tolerance at both speeds. Unfortunately, no tests were conducted on Graphit-iC gears with the same surface finish. It is possible that the Graphit-iC coating would have similarly benefitted from reduced roughness. See Figure 2-81.

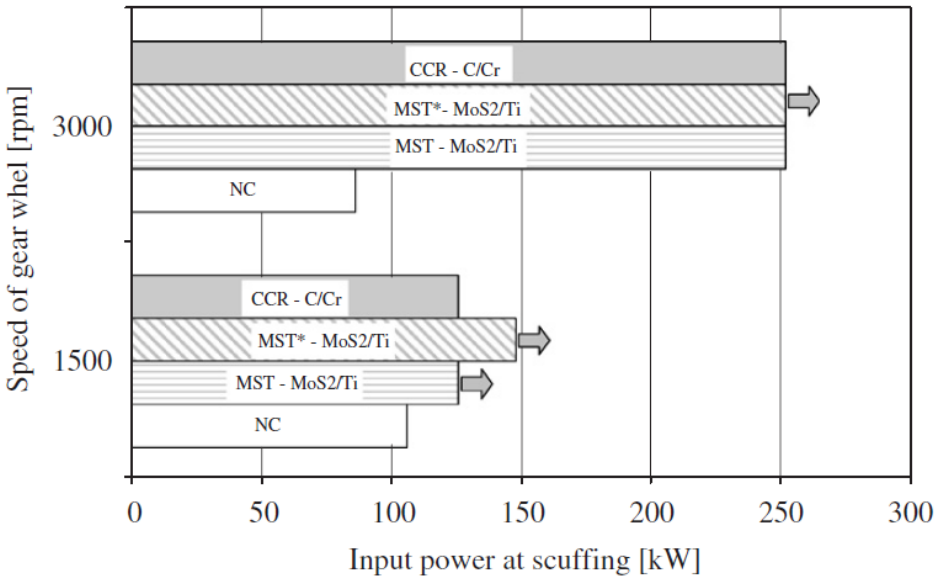

(Denotes Gear with Low Surface Roughness, Arrow Denotes Test Completion without Scuffing)*

Figure 2-81 Comparison of Power Transmitted at Onset of Scuffing for Uncoated and Coated Gears [237]

Friction coefficients for each coating at the point of scuffing were calculated using Höhn's equation [238]. MoST was shown to have a lower coefficient of friction under scuffing conditions than Graphit-iC. Coefficients of friction were lower at higher speeds. See Figure 2-82.

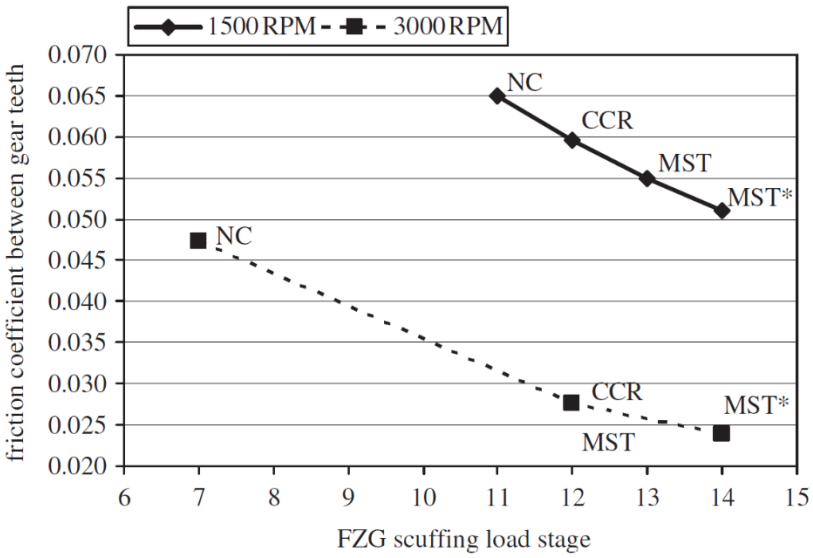

Figure 2-82 Friction Coefficient of Coated and Uncoated Gears under Scuffing Conditions [237]

A further comparison of the performance of MoST and Balinit C is provided by Michalczewski [233]. Scuffing and pitting resistance were determined using ball-and-cone and four-ball test methods respectively. Balinit C was found to have better scuffing and pitting resistance under these conditions, although clearly the test conditions are not completely representative of gear tooth contact.

Beside MoST the only other lamellar solid lubricant coating to be studied on gears is the Nb-S coating included in Moorthy's tests [227] [228]. Unfortunately, there is no description in either paper of the coating composition or structure, other than that a CrN interlayer was used for adhesion. It is stated that the coating was under development and applied by IonBond UK. $NbSe_2$ is a transition metal dichalcogenide, and should therefore have a lamellar structure, but very little information regarding its tribological performance is available. $NbSe_2$ was described by Fleischauer [239] as being a poor solid lubricant in its pure state due to the long-range interactions between Nb atoms in adjacent layers. The coating is included in this section despite the above ambiguities due the excellent performance in Moorthy's work. Referring back to Figure 2-81, this coating produced the lowest profile deviations in micropitting tests of all coatings in the study. Efforts to obtain more details on the coating compositions from the manufacturer were unsuccessful.

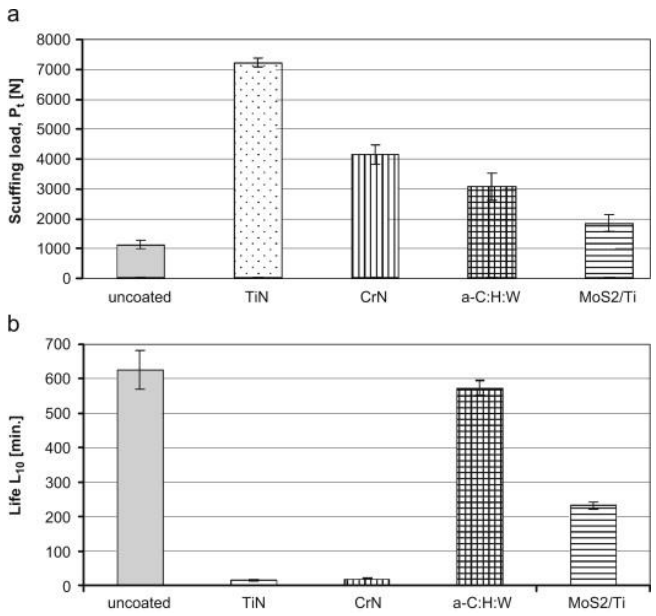

Figure 2-83 Scuffing Loads and Fatigue Lives for Coatings [237]

2.5.3 Performance of Coatings on Dry-Running Gears

Research into the performance of coated gears under dry-running conditions is very limited. The most significant body of work is that conducted by Walton and Goodwin [51]. As mentioned in 2.2.2.4 their work included different uncoated metallic spur gears, but tests were also conducted on a wide range of soft and hard coatings. Tests were conducted using stock spur gears on a power recirculating test rig, with the load applied by mounting the gear pair in a pivoting block with a weighted arm. See Figure 2-37. Wear was indirectly measured by weighing the gears before testing and at intervals. Apart from pauses to take weight measurements the gears were run continuously until the point of failure, which was determined by the observation of ferric oxide debris.

The initial attempts to run self-mated gear pairs resulted in rapid failure and were quickly discontinued. Subsequent tests were conducted using a coated normalised EN8 driven gear, and an uncoated case carburised driver. The coatings, their properties, and durability ranking are shown in Table 2-4. Precise values for test durations to failure are not provided, though it was stated that highest ranking coating, a spray-on heat-treated MoS_2 formulation lasted for 35 hours at a 3Nm torque load and 500rpm. Both of the best performing coatings were commercial spray-on MoS_2-based treatments.

Table 2-4 Properties and Ranking of Coating Durability on Dry-Running Spur Gears [51]

Treatment	Deposition method	Approximate thickness μm	Hardness Hv	Apparent ranking
Molykote MoS_2	Spray (heat treated)	10	Soft	1
Primalife MoS_2	Spray (heat treated)	10	Soft	
Copper	Electrolytic	25–30	Soft	2
Nickel (heat treated)	Electroless	25–30	1000	3
Nitrotec	Chemical gases	25	1000	4
Nickel	Electroless	25–30	500	5
Armoloy	Electrolytic	2–5	1000	6
Ionlube (heat treated)	Electroless	25–30	400	7
Ionlube	Electroless	25–30	300	8
Tufftride	Chemical liquid	10–20	350	9
Lead–tin	Electrolytic	25–30	Soft	10
Parco-lubrite	Chemical liquid	4–8	Soft	11

Further tests were conducted on case carburised pairs, coated with either Balinit C or Tufftride: a salt bath nitrocarburising treatment. At the same 3Nm torque load and 500rpm condition the Balinit C coated pair endured for 200 hours. The Tufftride was not tested at 500rpm, but at 250rpm only lasted for 76 hours compared to 270 hours with Balinit C. Wear rates were calculated by Archard's law, with the sliding distance simply calculated by integrating the sliding velocity with respect to the tooth's time in mesh. At low speeds the wear rate of Balinit C was over an order of magnitude lower than either the Trufftrided or uncoated gears. At 1000rpm the uncoated case carburised gears actually gave lower wear rates. See Figure 2-84.

The authors noted that in part the limited performance of the coatings would be attributable to the loose manufacturing tolerances of the stocks gears relative to the thicknesses of the coatings. The composite error of 0.071μm (assuming the author was referring to total composite error and not tooth-to-tooth composite error) would be equivalent to AGMA quality grade Q8 [240]. Depending on the timing of the gear pairs a total composite error for the mesh could be up to 0.142μm. This is likely to produce significantly elevated stresses, particularly at the start and end of line of action.

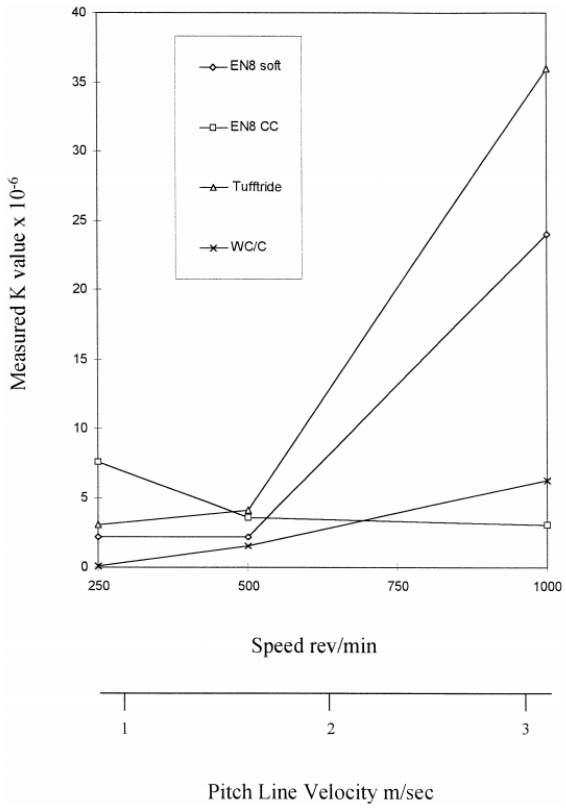

Figure 2-84 Wear Coefficients as a Function of Speed for Coated and Uncoated Dry-Running Gears [51]

A number of other tests on dry-running uncoated gears provided some valuable insights into potential methods to optimise gear designs for dry running. Firstly, tests using the same pitch diameter but a greater number of smaller module teeth (changing from 30x2m teeth to 60x1m teeth) gave greatly reduced wear rates. Tests were also conducted on gears utilising the older 14.5° pressure angle, as opposed the higher 20° that is most commonly used now, and gears utilising a high proportion of recess action (80%). The author referenced literature [241] stating that fully lubricated gears with a high recess action run with lower friction and less noise. Both of these tests actually produced higher wear.

Petrik [55] conducted studied the performance of CrN/DLC coated plasma nitrided gears in dry and minimal grease lubrication conditions, following promising results from tests on rollers. Tests were performed on a modified FZG test stand with the gears being operated against progressively increasing load stages. Visual inspections were conducted between load stages with test failure defined as evidence of seizure or galling of the substrate. The results highlighted the importance of case hardening prior to coating deposition, with plasma nitrided coated gears in dry conditions achieving a higher load stage than unhardened, coated gears with grease lubrication.

Unfortunately, the tests were conducted at significantly different speeds (150rpm vs 1500rpm), which somewhat compromises the direct comparison in performance.

Fujii [242] conducted a series of experiments on self-mated rollers and gears coated with 3µm and 10µm thick DLC coatings, including dry-running tests in vacuum conditions. The coatings consisted of a Ti adhesion layer and two layers of a-C:H:Si: a ramped layer in which Si content was reduced from 20% to 10%, and a top layer containing 2% Si. During rolling-sliding testing the lowest initial friction was obtained using a 10µm thick coating deposited on to a nitrided surface. The lowest wear (as measured by weight loss) was actually recorded for completely untreated rollers. However, this gear exhibited very high friction (µ=0.6-0.9) and the lack of weight loss was attributed to the highly adhesive nature of the wear. All coatings with the exception of the 10µm DLC/nitrided set experienced rapid delamination failure and increase in friction. See Figure 2-85.

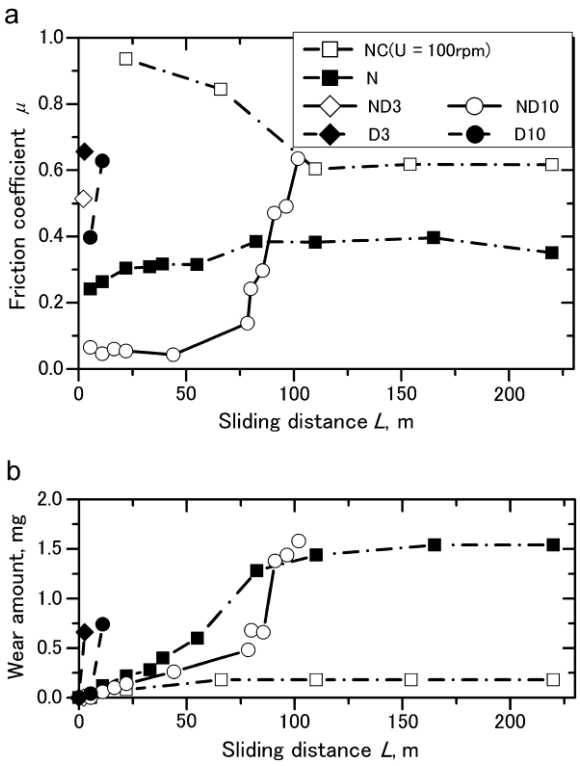

Figure 2-85 Friction and Wear of DLC Coated Rollers in Rolling/Sliding in a Vacuum [242]
(NC: Non-coated, N: Nitrided, D: DLC-Coated, ND: Nitrided and DLC Coated, Number: Thickness)

Tests on spur gears in a vacuum were limited to non-coated gears and the 10µm DLC/nitride treated gears. At maximum contact pressures of 250MPa the gears maintained a steady coefficient of friction (µ=0.1-0.15) and wear rate over the full test duration. At 350MPa the coating exhibited similar characteristics until a sudden change in behaviour at a sliding distance of approximately 75m, when the wear became more progressive. The uncoated gear exhibited

slightly lower wear over the brief duration tested, but friction grew rapidly to μ=0.5 resulting in termination of the test. See Figure 2-86.

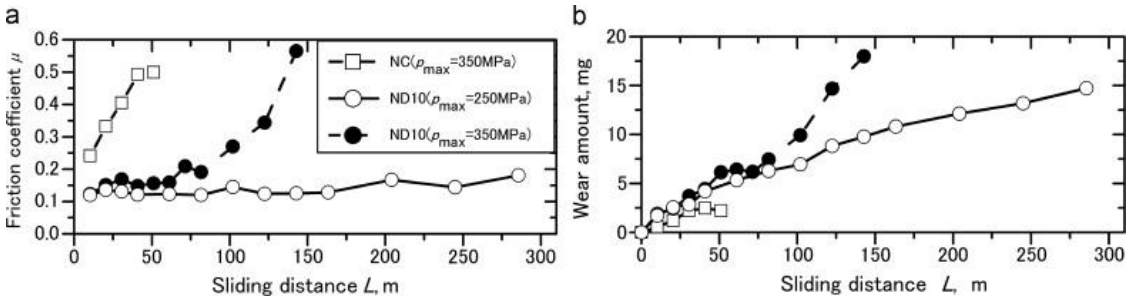

Figure 2-86 Friction and Wear Characteristics of Nitride/DLC Steel Gears in a Vacuum [242]

Farley et al. [243] developed a finite element model of multilayer coatings in dry rolling/sliding and supplemented this with tests on a twin-disc test rig to simulate contact between gear teeth. The model was conducted with 2-dimensional strain elements with each layer of the coating modelled as separate components and "tied" together to prevent slip between layers. The analysis was repeated for uncoated, TiN, Cr/CrN/DLC and Cr/WC-C coated bodies in contact. See Figure 2-87.

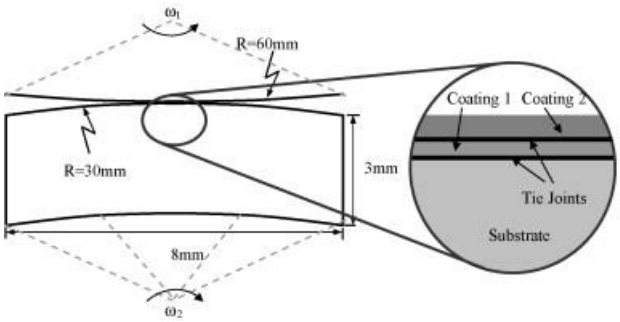

Simulation	Coating layer	Thickness t (μm)	Young's Modulus E (GPa)	Poisson's Ratio	Hardness (HV)	Friction μ
Uncoated (i.e. substrate)	–	–	206	0.29	748	0.7[a]
Coating A	TiN	3.00	480	0.25	2300	0.3[a]
Coating B	DLC CrN Cr	1.88 2.69 0.30	170 210 140	0.20 0.20 0.22	2300 1750 800	0.1[a]
Coating C	WC/C Cr	1.00 0.20	250 140	0.25 0.22	1050 800	0.1[a]

[a] Dry, measured against steel.

Figure 2-87 Summary of Farley's Model for Multi-layered Coatings in Dry Rolling Sliding [243]

Both carbon-based coatings showed significantly lower predicted stresses than the TiN-coated and uncoated discs. The lowest maximum Von Mises stress under load was observed for the

Cr/WC-C coating due to its relative softness and low coefficient of friction. See Figure 2-88. For both Cr/WC-C and Cr/CrN/DLC the peak stresses were predicted to be 30-40µm below the surface, well away from the coatings themselves. In terms of the stresses within the coatings, peak values for the Cr/CrN/DLC occurred at the Cr interlayer with a sharp transition to a lower stress at the substrate. This was due to high hardness of the coating relative to the substrate. For the remaining coatings peak stresses were predicted at the surface. See Figure 2-89.

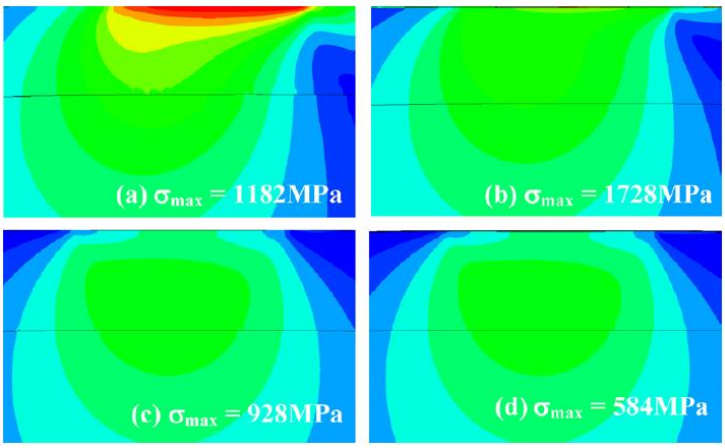

(a: Uncoated, b: TiN, c: Cr/CrN/DLC, d: Cr/WC-C)

Figure 2-88 Von Mises Stress Plots for Simulations of Coated Discs in Dry Rolling-Sliding [243]

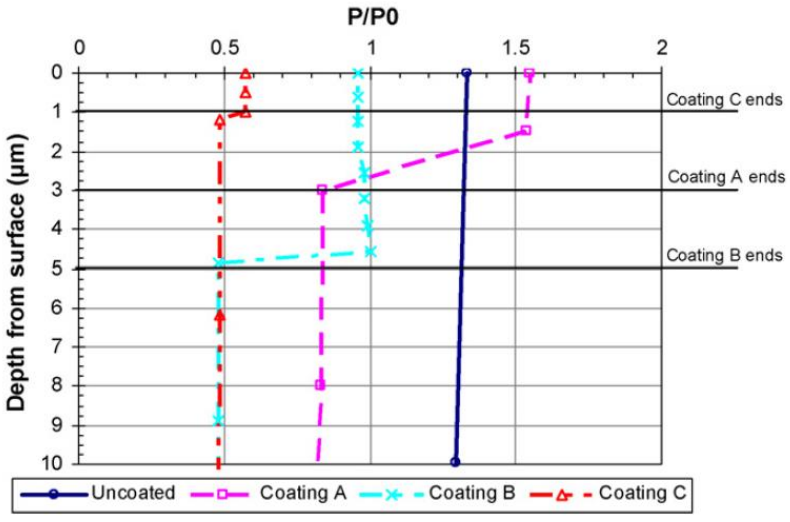

(A: TiN, B: Cr/CrN/DLC, C: Cr/WC-C, P_0: Contact Pressure (1GPa))

Figure 2-89 Stress with Depth for Simulations of Coated Discs in Dry Rolling-Sliding [243]

Subsequent testing of the simulated coatings on a twin disc tribometer with a slide-to-roll ratio of 10% found that both the Cr/WC-C and Cr/CrN/DLC gave significant improvements in wear rate compared with both the uncoated and TiN-coated discs. See Figure 2-90. In both cases delamination of the film played a significant role in the wear process. In the case of Cr/CrN/DLC small pockets formed where the coating was removed entirely. These then coalesced into larger areas of exposed substrate. This demonstrated that the failure of the coating occurred due to delamination from the substrate at the highly stressed Cr interlayer. See Figure 2-91.

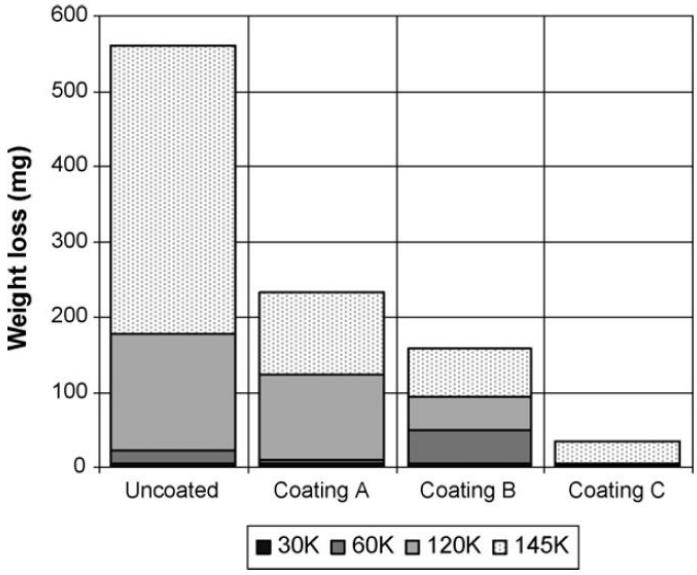

(A: TiN, B: Cr/CrN/DLC, C: Cr/WC-C)

Figure 2-90 Weight Loss of Coated Steel Discs in Dry Mixed Rolling/Sliding at Increasing Numbers of Cycles [243]

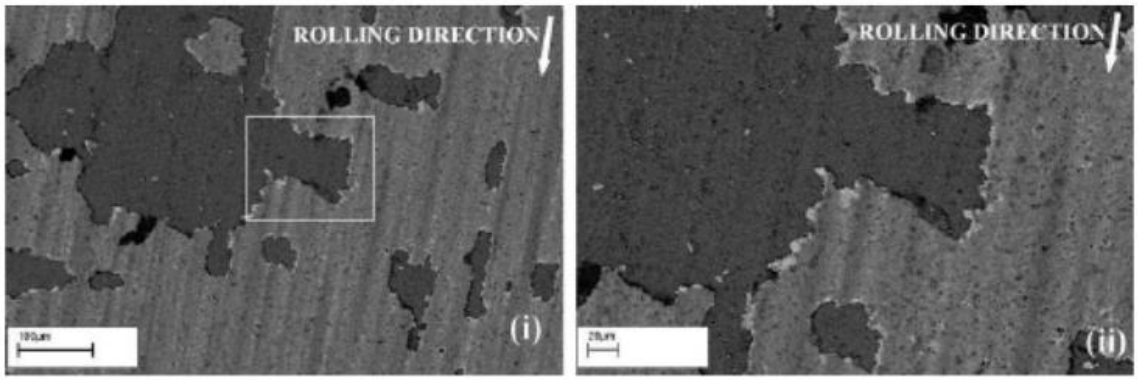

Figure 2-91 Partial Failure of a Cr/CrN/DLC Coating in Dry Mixed Rolling/Sliding [243]

For the Cr/WC-C coating wear bands developed at locations with visible grinding scores, exposing the Cr interlayer but not the substrate. Cracks were formed at the edges of these wear bands suggesting that subsequent removal of the coating around the wear bands in small flakes. See Figure 2-92. Carbon-rich transfer films were found on the counterpart driving disc. The Cr/WC-C gave the lowest rate of material removal by a considerable margin. Farley's results demonstrate that a high coating hardness can actually be counterproductive to preventing wear as it results in elevated stresses that cause delamination and rapid coating failure, even when the coefficient of friction is low.

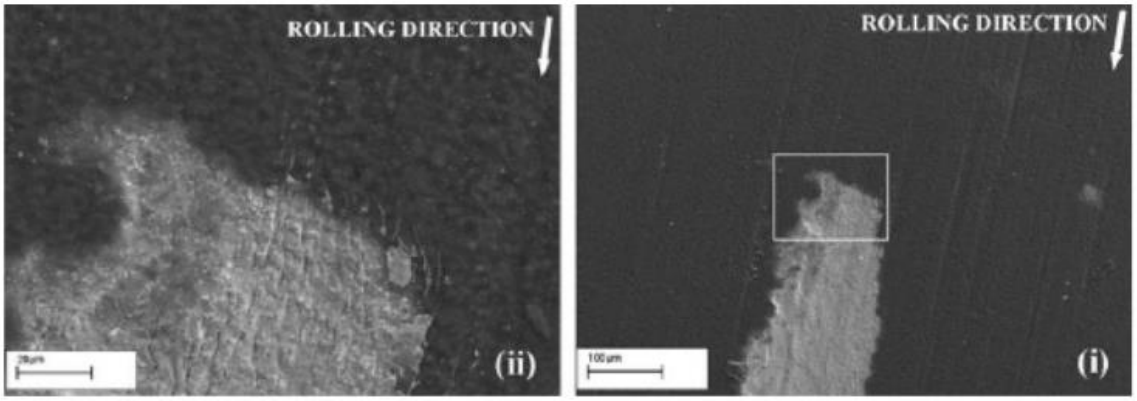

Figure 2-92 Partial Failure of a Cr/WC-C Coating in Dry Mixed Rolling/Sliding [243]

One area of interest in the use of coatings on gears is to increase durability in a loss-of-lubrication scenario. This is particularly of concern in the aerospace industry where equipment may be required to continue safe operation for a time following gross leakage of the lubricating fluid. Whilst the surfaces may not be considered truly "dry" the behaviour of the coating in severely lubrication-starved conditions may still be relevant.

Murakawa et al. [244] investigated the use of multilayer WC/a-C:H:W coatings on gear teeth in loss-of-lubrication scenarios. The coating is believed to Balinit C based on the description given. Failure of the gear pair was deemed to have occurred when gear noise or vibration exceeded a pre-defined threshold, or if scuffing was observed. WC/a-C:H:W coated gears operated for between 2-3 times longer than uncoated gears following draining of the oil from the gearbox. A further 1.3 times improvement was found using gears that had been treated by micro-shot peening prior to coating deposition.

The micro-shot peening process was implemented with the intention of removing grinding traces to prevent delamination. SEM images confirmed that the process was successful in eliminating

the directionality of the surface roughness, which is usually normal to the direction of motion. See Figure 2-93. Failure of the coating was due to delamination in the tooth root, where the proportion of sliding between the surfaces is at its highest.

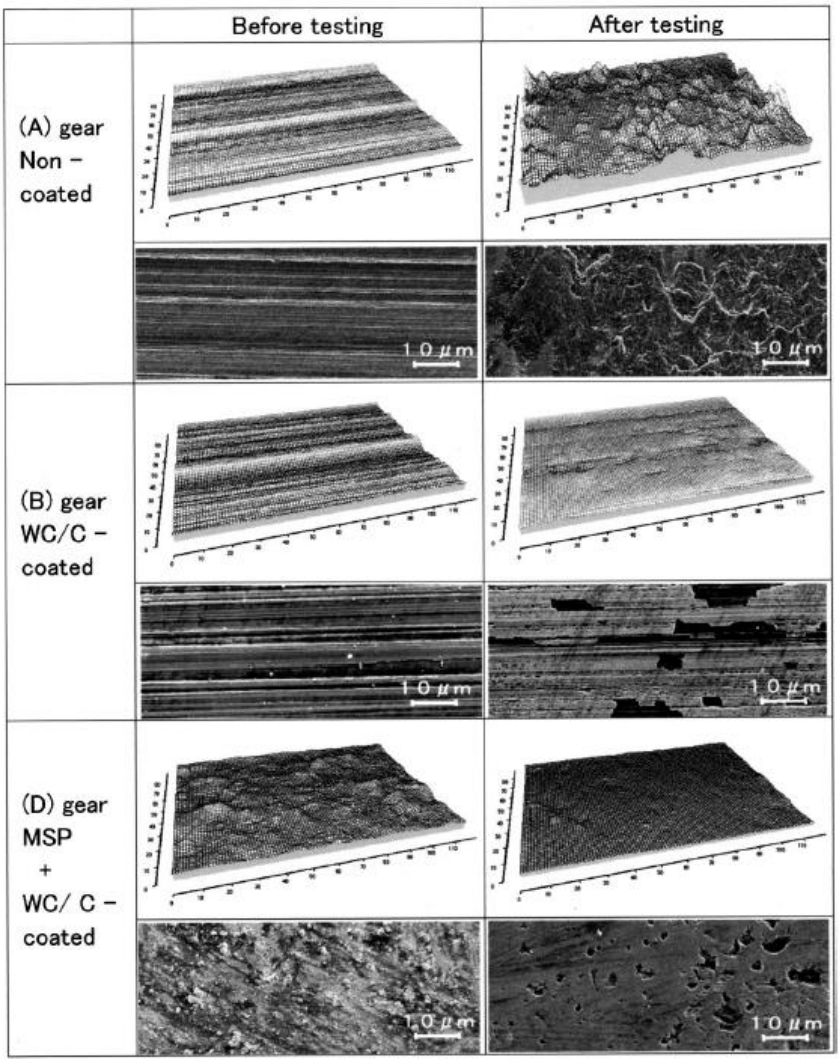

Figure 2-93 Comparison on Pre and Post-Tests Surface Roughness of Gears Subjected to Loss-of-Lubrication Testing [244]

2.5.4 Desirable Characteristics of a Coating for Solid-Lubricated Dry Gears

Holmberg and Matthews [245] provided the following definition of tribological requirements for coated surfaces:

1. The initial coefficient of friction, the steady-state coefficient of friction and the friction instability must not exceed certain design values.

2. The wear of the coated surface and that of the counterface must not exceed certain design values.

3. The lifetime of the system must, with a specified probability, be longer than the required lifetime. The lifetime limit of the system may be defined as occurring when at least one of the earlier requirements is not maintained.

In order to determine the acceptable coefficient friction for a gear coating, the most useful approach would be to select a coating with a dry sliding coefficient of friction equal to or better than the equivalent fluid-lubricated steel mesh. This would ensure that the mesh efficiency is unaffected and would not induce any additional losses that would negate the benefits of eliminating the churning losses caused by the fluid. Rebbechi et al. [246] conducted a series of tests using strain gauges mounted in the fillets of gear teeth to understand the variation in tooth friction with mesh position. They observed that the peak coefficient of friction was generally in accordance with values measured by standard disc tests and varied between 0.04 and 0.06 dependent on the position in the mesh cycle. See Figure 2-94. Similar conclusions were reached by Björling [247]. Fernandes et. al produced an extensive three part study into power losses in gearboxes, including one study [248] focusing exclusively on tooth friction losses. Average coefficients of friction were derived for a range of mineral and synthetic oils, yielding results from 0.02 to 0.06 dependent on speed and lubricant type.

Consequently, it is desirable for a coating for dry running gear applications to offer a steady state dry sliding coefficient of less than 0.06. Separate values for starting and steady state coefficients of friction and friction stability, as suggested by Holmberg and Matthews, are harder to derive but the above figure serves as a useful starting point for identifying potential coatings.

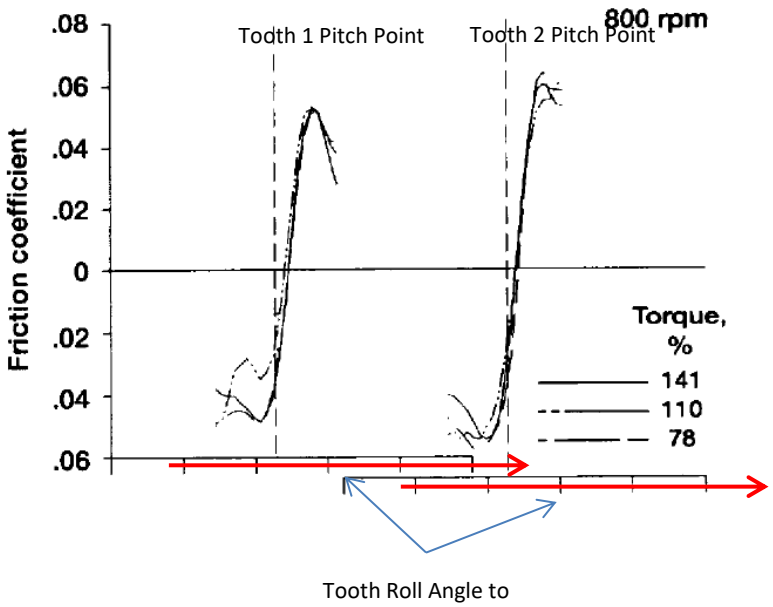

(Example based on 28T pinion and gear, 20° pressure angle, 3.175 module, 800rpm, 100% torque = 71.7Nm, MIL-L-23699B lubrication)

Figure 2-94 Coefficient of Friction vs Mesh Position at Various Torques for Adjacent Teeth [246]

Based on the results of studies such as that by Walton and Goodwin [51], it is clear that in the case of dry running gears the lifetime of the gear mesh will be dominated by the wear resistance of the surfaces. For thin tribological films the life is limited by the low thickness of the coating and therefore a very low specific wear rate is required. When considering sliding wear the required wear rate for a given gear mesh depends on the torque loads applied, the number of tooth engagements incurred in the life of equipment, and the specific design parameters of the teeth. Models such as the rolling cylinders method or dedicated software packages may be used to provide predictions of coating life once the wear rates have been established by test.

However as demonstrated by Farley [243], the removal of the coating in dry rolling/sliding may be caused or exacerbated by delamination effects, either between coating layers or between the coating and substrate. Consequently, whilst gross macropitting is unlikely there may be an effect similar to micropitting that accelerates the sliding wear process due to rolling contact fatigue. Therefore, a balance has to be struck between achieving a high hardness to resist wear, whilst also limiting the coating stresses that stem from applying a hard coating to a soft substrate. Maximising the hardness of the substrate through case hardening, achieving a low substrate surface roughness, achieving good coating adhesion, and minimising coating internal stresses are all important to prolonging coating life.

2.5.4.1 Summary

The application of self-lubricating films to gear teeth has been largely focussed on extending the capability of gears to resist progressive tribological failures modes such as scuffing and pitting under standard oil lubrication, or on replacing the environmentally damaging additives present in many modern oils. Studies have been dominated by a small number of commercially available DLC or TMD-based coatings.

The use of undoped DLC films on gear teeth has not been studied in significant depth, possibly due to their inferior adhesion properties. However, the limited data available suggests that even these simpler films significantly improve the resistance of lubricated steel in rolling-sliding contact to seizure, wear and micropitting. Most commonly W is used as a dopant to improve the tribological properties of the film. Simple single-layer W-doped films have been shown to significantly improve scuffing resistance and pitting resistance of gear pairs when lubricating conditions are poor, provided contact stresses are sufficiently low to avoid delamination.

By far the most studied coating is Balinit C by Balzers: a multilayer coating of Cr, WC, and a-C:H:W. Balinit C has been shown to reduce the wear rate in both high-speed scuffing and low speed wear tests, with the benefits increasing with degrading lubricating conditions. Its performance in gear pitting tests is more questionable, with studies either reporting significant benefits or none at all. Although reported to a much lesser extent, Cr-doped multilayer films such as Graphit-iC by Teer have been reported to increase the scuffing capacity of gears even further than Balinit C. Another coating by Teer, the Ti-doped MoS_2 film MoST, has featured in tests alongside Balinit C and Graphit-iC. The scuffing capacity of MoST coated gears exceeds that of even Graphit-iC at low speeds and can be further improved by depositing onto teeth with a low surface roughness.

The performance of coatings on dry-running gears has not been the subject of many studies. MoS_2 based spray-on formulations offer the best protection amongst softer coatings and are more effective than many harder treatments. Balinit C has featured in limited tests, providing a far greater operating life than nitrocarburising treatments. Si-doped DLC films, when tested on gears or rollers in a vacuum, provided lower friction and wear than uncoated components until failure of the coating, but only when applied as a thicker (10µm) film onto case hardened substrates. Delamination has been shown to play a significant role in the removal of DLC films in dry mixed rolling/sliding. In highly stressed coatings the delamination begins at a microscale before coalescing into macroscale failure at the most highly stressed interface. This failure is most likely to occur at the dedendum or root of the tooth where the highest proportion of sliding occurs. In coatings with lower stresses the delamination occurs at the edges of existing wear bands.

Coating performance can be further improved by depositing onto teeth with a low surface roughness and high machining accuracy. The surface hardness of the uncoated gear teeth should be maximised to reduce coating stresses under contact.

2.6 Summary of Current Gaps in Literature

In general, the topic of dry running gears has received little attention in academic studies. It is likely that the lack of studies reflects the fact that under constant operation there is very little scope for rejection of heat from the tooth surfaces. All of the papers identified in the literature review performed tests using continuous operation of the gears. This is understandable as it reflects the operating conditions for the majority of geared applications, but nevertheless ignores the potential for dry gears in intermittent operation such as those in actuation applications. Consequently, when assessing the use of coated gears for high-lift actuation it would appear vital that intermittent operation should be incorporated into the test regime. This renders many of the more common test approaches unsuitable for direct replication in this study. Therefore, there exists a knowledge gap both in terms of how coatings would perform in such conditions, but also in the correct method to assess this performance.

As coating life will be a function of the coating thickness and the wear rate, defining a method to determine the wear rate would allow life to be estimated across different designs and operating conditions. Simply stating a load stage at which failure occurred, as is common in most FZG-derived tests, provides limited information to inform subsequent design modifications. Whilst Walton and Goodwin's work estimated the wear rate by integration of the sliding velocity over the line of action, this method does not account for increased sliding due to widening of the contact width at elevated loads or the effects of variations in load share, and therefore a more detailed model of the contact is required. Measuring the distribution of wear over the tooth surfaces and comparing this to the predictions from a model should allow for a more accurate derivation of wear rate and provide greater information as to how designs may be improved to extend coating life. Similarly, studies detailing the development of wear models for gear teeth tend to lack test data for comparison. Hence the extent of any inaccuracies in these models are often difficult to quantify or understand. It therefore seems vital to ensure that a study of the wear characteristics of dry coated gears should include both test data, taken under conditions representative of the actual application, and simulation of the wear process by calculation of the contact stress and sliding distances.

Additionally, there seems to be no published data available for the efficiency of dry running gears, with the limited studies available choosing to focus entirely on wear and load-carrying capacity. Power losses on coated gears have only been studied under conventional fluid lubrication. Whilst limited predictions can be made based on the results from standard tribometers, it is currently unknown whether a dry gear with a low friction coating can offer a sufficiently competitive efficiency to justify its use, let alone how the frictional properties may vary under the low temperature environment under which aerospace equipment frequently operates.

Chapter 3 Test, Simulation and Analytical Methods

3.1 Plan of Tests and Simulations

The objectives for the test, simulation and analysis of dry coated gears are repeated below. Standardised methods, or those taken directly from other authors are provided within this chapter. Methods developed specifically to meet these objectives are provided in Chapter 4. For each objective a brief summary of the methods used is provided, along with a reference to the pertinent section that includes the full description.

- Develop test method for determining the wear life of promising coatings when applied to spur gears.
    - A bespoke power-recirculating test rig was developed, as discussed in section 4.1

- Determine the useful life of promising coatings under operating conditions typical of the application.
    - Coatings were selected according to the rationale provided in section 3.2.
    - Candidate coatings were applied to gears, the design and manufacture of which is described in 3.3.
    - Tests were performed on the power-recirculating test rig.
    - Measurements of the tested gears were performed using a CMM gear checker and then processed in accordance with the methods described in section 4.3.

- Calculate the wear rate of the coatings by comparing test measurement data to a model of the loads and sliding conditions on the gear teeth. Utilise the model to evaluate the impact of different design parameters on predicted coating life.

    - Simulation of the contact conditions to determine wear rate were performed on a rolling/sliding cylinder model, the development of which is discussed in section 4.2

- Determine the wear mechanisms involved and identify failure modes.

    - Inspection of the worn tooth surfaces was performed by light microscope, periodically during testing and on completion. Post-test inspection was performed by scanning electron microscope (SEM) imaging, energy dispersive x-ray spectroscopy (EDS), and Raman spectroscopy. The methods and equipment used are defined in section 3.4.

- Develop test method for determining the efficiency of promising coatings when applied to spur gears.

    - A power-absorbing test rig was constructed based on the adaptation of a generic modelling table, the development of which is discussed in section 4.6.

- Compare the efficiency of the coated gears to those operating under conventional fluid lubricants with typical aerospace lubricants.

    - Tests were performed using dry-running and fluid lubricated gears on the power-absorbing test rig.

- Identify the magnitude of load-dependent and zero-load losses in a typical high-lift gearbox under dry and fluid lubrication.

    - The test data from efficiency testing was analysed according to Hohn and SKF, as described in section 3.5.

- Calculate the coefficient friction of the coatings during the mesh cycle.

    - The load-dependent losses calculated from the efficiency data were used to determine the coefficient of friction between the gear teeth in using the formulae of Ohlendorf and Buckingham, as shown in section 3.6

3.2 Selection of Candidate Coatings

Due to the lengthy process of performing wear testing, it was determined that an initial assessment of the wear performance of three candidate coatings would be made at a moderate torque load. Of these three coatings, the coating with the longest wear life would then be used to perform additional wear tests across a range of torque loads. Efficiency testing would also be performed on the selected coating to understand the extent of the benefit exhibited in comparison to a fluid-lubricated gearbox, and to derive a coefficient of friction between the coated gear teeth.

As identified in 2.3, PVD self-lubricating coatings can largely be divided into those based on amorphous carbon in its various forms, and those based on lamellar solids from the TMD family. These coatings display opposing behaviour in terms of sensitivity to environmental humidity, a consideration that has resulted in the development of self-adaptive coatings that incorporate nanocrystalline TMDs embedded with an a-C matrix. The following three candidate coatings were selected to represent one from each of these categories.

The first candidate coating is Graphit-iC: a sputtered coating based on sp^2-rich a-C and Cr. It consists of a 0.8µm Cr interlayer, then a Cr/a-C gradient layer followed by a-C doped with Cr at 5 at.%, with a combined thickness of 2.8µm. The deposition was performed by Teer coatings using closed field unbalanced magnetron sputtering (CFUBMS). The coating deposition process and properties have been previously reported in [249] and [250]. It's use on conventionally lubricated gears has been studied in [234] and [237].

The second candidate coating, MoST, was also deposited by Teer using CFUBMS. The coating is based on Ti-doped MoS_2, and consists of a 0.07µm Ti interlayer, 0.2µm of layered MoS_2/Ti, then 0.9µm of Ti-doped MoS_2 (5-15 at.%). A top layer of 0.05 µm is added for coloration. The coating deposition process and properties have been previously reported in [145]. Martins et al. included MoST into their series of studies on the use of low friction coatings on gears in [235]-[237].

The final coating, WSC, is a novel self-adaptive coating utilising W, S and C, and was deposited by CFUBMS at the Laboratory of Wear, Testing and Materials at Instituto Pedro Nunez. The coating consists of a 0.3µm Cr interlayer, 0.1µm Cr/W-S-C gradient layer, then 1.8µm of W, C and S. The final layer has a C content of ~40 at.%, a W/S ratio of ~1.5, and has a nanocomposite structure consisting of a C-rich amorphous layer with embedded WC and WS_2 nanograins. Initial studies of this coating system were performed using laboratory-scale RF sputtering in [251]-[253]. It has been more recently adapted to CFUBMS as documented in [254]-[255]. There are no previous studies into its performance when applied to gears.

3.3 Preparation of Samples

Test samples were prepared by deposition of the candidate coatings onto gears, the design of which was based on a typical high-lift system spur gearbox. The gearbox was selected based on its adaptability to wear testing in a power-recirculating test rig, the development of which is discussed in section 4.1.

The gearbox consisted of three spur gears: two identical 24-tooth input/output gears, and a central 33-tooth idler gear. The test gears were ground from solid in BS S82: a 4% Ni-Cr-Mo case hardening steel. The gears were then gas carburised to provide a hardened surface for coating, and then cooled in still air. A refine-harden process consisting of heating to 825°C and quenching in oil was applied before a low-temperature stabilisation for two hours at -70°C. The gears were then tempered at 190°C and air cooled. The achieved case layer had a minimum surface hardness of $650Hv_{2.5}$ and a case depth of 0.5mm to $510Hv_{2.5}$.

After heat treatment the gears were finish ground and then wet superfinished in a disc finishing machine to achieve a surface roughness of <0.1µm Ra. The superfinishing is not a standard practice for gears of this type and application, where an as-hobbed finish is usually satisfactory. This was performed to maximise adhesion and minimise localised contact stresses. The finished, coated gears dimensionally conformed to AGMA accuracy grade 12.

For actuation systems, where bending fatigue resistance is prioritised, standard design practice would mandate the application of a full root fillet. Due to the measurement method employed, as described in section 4.3, the fillet size was reduced to provide a region of involute tooth form below the SAP. This acted as a stable datum of unworn profile for comparing pre-test and profile measurements.

Table 3-1 Gear Design Parameters for Test Samples

Parameter	Value		Units
Module	2.25		mm
Pressure Angle	20		°
Numbers of Teeth	24	33	-
Modification Coefficient	0		-
Face Width	6.5		mm
Tooth Surface Finish	< 0.1 Ra		µm
Material	BS S82		
Surface Hardness	> 650		$Hv_{2.5}$
Case Depth	0.5		mm to $510Hv_{2.5}$
Finished Tolerances	AGMA 2000-A88 Grade 12		-

All gears were manufactured as a single batch. Initially each coating was applied to one complete gearset. Additional gears were retained to allow for further coated samples to be prepared, based on the results of initial wear testing at moderate loads. Once coated, the side lands of three equally spaced teeth on each gear were marked with identifying numbers to allow the same teeth to be remeasured and inspected during testing.

3.4 SEM, EDS, and Raman equipment specifications

On completion of the final set of measurements, the three monitored teeth were sectioned from each gear. After a final visual examination, the teeth were inspected using a Tescan Vega 3 scanning electron microscope (SEM), using both secondary and backscatter electron detectors. Material analysis was performed on areas of interest using an Oxford Instruments INCA energy dispersive x-ray spectroscopy (EDS) system. Further analysis of the worn and as-deposited coating was performed using a Horiba XploRA Raman spectrometer with laser excitation at 532nm. The Raman spectroscopy was performed by Tomas Vitu of Czech Technical University in Prague.

3.5 Identification of Sources of Power Loss

As stated in section 2.1.5, the power losses in a gearbox can be attributed to load-dependent and zero-load contributions of the gears, bearings, and seals [14].

$$P_{gbx} = P_{gl} + P_{g0} + P_{bl} + P_{b0} + P_s \quad (4)$$

Where:

P_{gbx} = gearbox power losses

P_{gl} = load-dependent power losses from gears

P_{g0} = zero-load power losses from gears

P_{bl} = load-dependent power losses from bearings

P_{b0} = zero-load power losses from bearings

P_s = zero-load power losses from seals

These individual loss contributions can be isolated and determined through test or calculation, leaving only P_{gl} by elimination. The average tooth coefficient of friction can then be calculated from magnitude of these isolated power losses and knowledge of the tooth geometries.

Initially the combined no load losses of the gears, bearings and seals can be measured simply by running the gearbox with the output unloaded. The losses are then simply determined from the input torque required to maintain the desired speed.

$$P_{gbx0} = P_{g0} + P_{b0} + P_s \quad (5)$$

Where:

P_{gbx0} = gearbox zero-load power losses

The combined load dependent losses of the gears and bearings at a given torque load can then be measured by operating the gearbox against various torque loads, recording the overall power loss, and deducting the zero-load losses.

$$P_{gbx} - P_{gbx0} = P_{gl} + P_{bl} \quad (6)$$

The gear and bearing losses must be isolated by calculation. For this study the model developed by SKF [256] is used to calculate the load dependent losses of the bearings. This model attributes the friction torques in a bearing to four sources:

$$M_t = M'_{rr} + M_{sl} + M_{drag} + M_{seal} \quad (7)$$

Where:

M_t = bearing friction torque (N.mm)

M'_{rr} = rolling friction moment (N.mm)

M_{sl} = sliding friction moment (N.mm)

M_{drag} = drag losses (N.mm)

M_{seal} = seal losses (N.mm)

Both M_{drag} and M_{seal} are independent of the applied load. Therefore, the associated power losses are quantified through the measurements for P_{gbx0} and can be omitted. The rolling friction moment M'_{rr} is found according to:

$$M'_{rr} = \phi_{ish}\phi_{rs}(G_{rr}(n.v)^{0.6}) \quad (8)$$

Where:

ϕ_{ish} = inlet shear heating factor

ϕ_{rs} = kinematic starvation factor

G_{rr} = rolling frictional load/geometry variable

n = rotational speed (rpm)

v = operating viscosity of oil or grease base oil (mm^2/s)

The inlet shear heating factor is applied due to effects of lubricant being expelled from the contact area. This generates heat due to shearing, which reduces the lubricant viscosity and the rolling friction. It is estimated from:

$$\phi_{ish} = \frac{1}{1 + 1.84 \times 10^{-9}(n.d_m)^{1.28}v^{0.64}} \quad (9)$$

Where:

d_m = mean bearing diameter (mm)

During operation of the bearing at high speeds or with very viscous lubricants the displaced lubricant may be unable to replenish the contact zone. This reduces rolling friction, which is reflected by the kinematic starvation factor ϕ_{rs}, which is estimated according to:

$$\phi_{rs} = \frac{1}{e^{\left(K_{rs}\upsilon n(d+D)\sqrt{\frac{K_Z}{2(D-d)}}\right)}} \quad (10)$$

Where:

K_{rs} = starvation constant (6 x 10^{-8} for grease lubrication)

K_z = bearing type related geometric constant (obtained from SKF tables)

d = inside diameter (mm)

D = outside diameter (mm)

The rolling frictional load/geometry variable for a deep groove bearing with no applied axial load is found by the formula:

$$G_{rr} = R_1 . d_m^{1.96} . F_r^{0.54} \quad (11)$$

Where:

R_1 = geometry constant (obtained from SKF tables)

F_r = radial force (N)

The sliding frictional moment is calculated according to the following equation:

$$M_{sl} = G_{sl} + \mu_{sl} \quad (12)$$

Where:

G_{sl} = sliding frictional load/geometry variable

μ_{sl} = sliding friction coefficient

The sliding frictional load/geometry variable for a deep groove bearing with no applied axial load is found by the formula:

$$G_{sl} = S_1 . d_m^{-0.26} . F_r^{5/3} \quad (13)$$

Where:

S_1 = geometry constant (obtained from SKF tables)

The sliding coefficient of friction is estimated from the sliding coefficient of friction under EHL (Elastohydrodynamic Lubrication) and then attenuated according to the operating conditions:

$$\mu_{sl} = \phi_{bl}.\mu_{bl} + (1 - \phi_{bl})\mu_{EHL} \quad (14)$$

Where:

ϕ_{bl} = weighting factor

μ_{bl} = constant depending on movement (0.12 for $n \neq 0$)

μ_{EHL} = sliding friction coefficient in EHL conditions

The weighting factor is calculated from:

$$\phi_{bl} = \frac{1}{e^{(2.6\times10^{-8}(nv)^{1.4}d_m)}} \quad (15)$$

The value of or P_{bl} for a given gear mesh is then found by multiplying the calculated friction torque value for each bearing by its operating speed to obtain the lost power, and then summing the losses together.

With the load-dependent bearing losses determined, the magnitude of the load-dependent losses from the gear teeth can then be found.

$$P_{gl} = P_{gbx} - P_{gbx0} - P_{bl} \quad (16)$$

3.6 Determination of Tooth Friction Coefficient

The average coefficient of friction between the gear teeth can be determined from the magnitude of the losses calculated in section 3.5. The power losses due to friction between the gear teeth at an instantaneous point in the mesh cycle are the product of the normal force between the teeth, the sliding velocity, and the coefficient of friction. During the mesh cycle all three of these

parameters will vary, in addition to the number of teeth in contact. Hence the product of the normal load, sliding velocity, and coefficient of friction must be integrated over the length of contact, and divided by the divided by the base pitch [257].

$$P_{gl} = \frac{1}{P_b} \int_{\xi_r}^{\xi_a} F v \mu\,(x)\, dx \tag{17}$$

Where:

P_b = Base pitch

F = Force

V = sliding velocity

μ = coefficient of friction

Ohlendorf [75] proposed that if the coefficient of friction is assumed to be a constant average value over the length of contact, the load is equally distributed between each tooth pair in contact, and the teeth act rigidly, then this equation becomes:

$$P_{gl} = P_{g\_ip} . \mu_{avg} . H_v \tag{18}$$

Where:

P_{g_ip} = Power at gear input

μ_{avg} = Average coefficient of friction

H_v = Gear loss factor

Multiple authors have proposed their own methods for calculation of the gear loss factor. The most common formulae are those stemming from Ohlendorf's original work, and those proposed by Buckingham, and Niemann and Winter. These do not account for profile shifted gears but are valid for the gears analysed in this study, which are not modified. In this study, the formula proposed by Buckingham [76] is used:

$$H_V = (1+u)\frac{\pi}{z_1}.\frac{1}{\cos\beta_b}\varepsilon_\alpha(2k_0^2 - 2k_0 + 1) \quad (19)$$

$$k_0 = \frac{z_1}{2\pi\varepsilon_\alpha u}\left(\left(\left(\frac{r_{a2}}{r_{p2}}\right)^2.\frac{1}{\cos\alpha_t^2} - 1\right)^{0.5} - \tan\alpha_t\right) \quad (20)$$

Where:

u = Gear ratio

z = Number of teeth

β_b = Base helix angle

ε_α = Transverse pressure angle

k_0 = Geometry factor

r_a = outside (tip) radius

r_p = pitch radius

α_t = Transverse pressure angle

Chapter 4 Wear and Efficiency Testing of Coated Gears

4.1 Development of Wear Test Rig

4.1.1 Selection of Test Rig Concept and Test Article

As discussed in the literature review, the contact conditions between gear teeth vary constantly during the mesh cycle in terms of contact pressure, surface velocity, sliding distance, and the proportion of rolling and sliding. Whilst standardised tribometers may provide indications of promising coatings, they are not suitably representative of the tooth-to-tooth contacts to provide a useful measurement of their performance on actual gears.

The most common method of testing spur gears for the assessment of wear is in a power recirculating configuration. Whilst the actual operating cycles of a high lift gearbox involve significant variations in torque load, to understand the effects of load and determine a wear rate, it is initially more useful to test individual samples against constant torque loads. The effect of load variation can then be understood through separate tests on new samples at different constant torques. When testing at constant loads, a power recirculating test rig eliminates the need for a separate load motor under closed loop control, resulting in an efficient, compact, and reliable design.

The most common power recirculating gear test rig is the FZG test rig described in 2.2.5.3. Whilst the standard FZG test procedures are not appropriate for determining the wear life of coated gears, it is possible that the procedures could be modified. However, the FZG rig is designed for operating with gears with 91.5mm centre distance. This results in test gears that are significantly larger than typical gears in high-lift systems. When assessing the suitability of coated gears for a high-lift system, it is desirable to minimise deviations from typical design parameters in the test setup, and if possible, to directly replicate the parameters from a proven high-lift gearbox. Additionally, being largely designed for the rating of lubricating oils the FZG rig also contains a large number of components and sensors that would be largely redundant for the testing of dry coated gears. Consequently, the approach taken was to directly adapt a high-lift gearbox to a power recirculating configuration in a bespoke test rig.

A small number of high-lift gearbox designs are suitable for testing in a power recirculating arrangement. Small spur gearboxes are sometimes utilised to translate the axis of the transmission line, to route the torque shafts around the aircraft structure. See Figure 4-1, which shows a schematic diagram of a large civil flap and slat system. A similar spur gearbox was

selected to serve as the test article for this study and is shown in Figure 4-2. It consists of three steel spur gears supported on deep groove ball bearings. The bearings are set into machined bores within a pair of cast aluminium alloy housings, which are located with hollow dowels for accuracy. The input and output gears are broached with through-splines for connecting to the transmission shafts in the system, which allows the same gearbox to be utilised on either wing. The adjacent bearings are protected by metal sealing rings, with ground shims used to control the axial float within the assembly. The gearbox is sealed by a silicon gasket between the housings and by PTFE lip seals riding on the protruding diameters of the input/output gears. Detailed definitions of the gear design parameters, materials and treatments are provided in section 3.3.

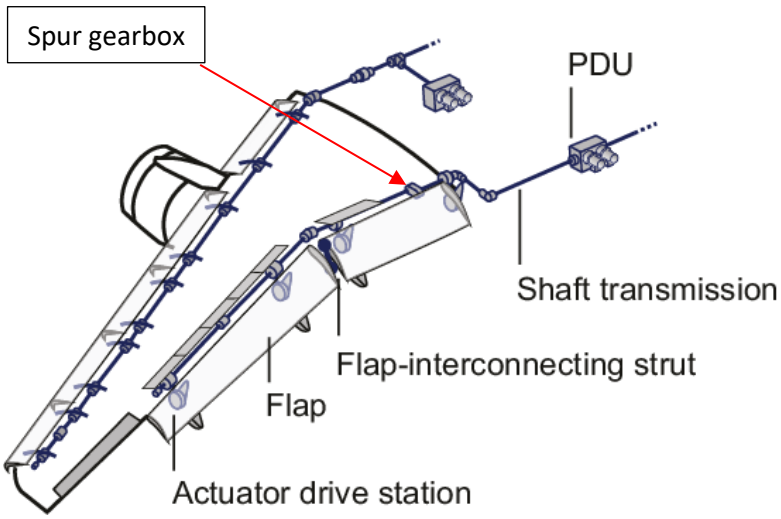

Figure 4-1 Typical Location of Spur Transmission Gearbox in a Flap System (Modified from [258])

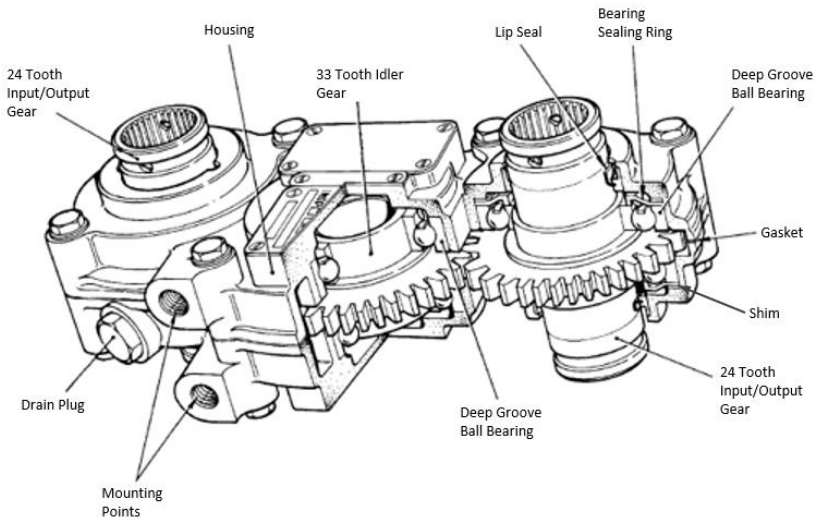

Figure 4-2 Section View of High-Lift Transmission Spur Gearbox

4.1.2 Test Rig Requirements

Based on the real-world application of the test gearbox, the following test requirements were established for wear testing of the coated gears.

Table 4-1 Wear Testing Requirements

Parameter	Test Cycle Requirement
Torque load (Nm)	10 – 40 Nm
Speed	400rpm
Revolutions per Test Cycle	100
Rest Time between Cycles	165 seconds
Input Direction of Rotation	Clockwise

The rest time between cycles is far lower than that experienced in the real-world application, where individual operations of the system may be separated by anywhere between the tens of minutes to several hours. In the interest of compressing test duration, the adopted dwell time was derived to achieve an order of magnitude difference between the test cycle operating time of 15 seconds, and the time at rest. This value was rounded to slightly to give a total time per cycle (inclusive of operating and rest times) of three minutes. Test cycling was limited to a single direction of rotation only, as the central idler gear teeth mesh with the input and output gears on each side. Testing in both directions would hinder the ability to observe any differences in wear performance when the idler gear is acting as the driving or driven gear.

An existing test stand was identified to be adapted to provide drive and control of two test gearboxes in a power recirculating configuration. The test stand had previously been used for performing unloaded cycling of ballscrew actuators, and consisted of a guarded and interlocked enclosure, within which a three-phase squirrel cage induction motor was mounted. A t-gearbox split the drive from the motor between the inputs of two ballscrew actuators. Control was provided by a programmable logic controller (PLC) with the motor speed feedback provided by a photoelectric sensor and a reflective strip on the motor output. The PLC, drive electronics and control panel were housed in an external electronic enclosure. The original test stand is shown in Figure 4-3.

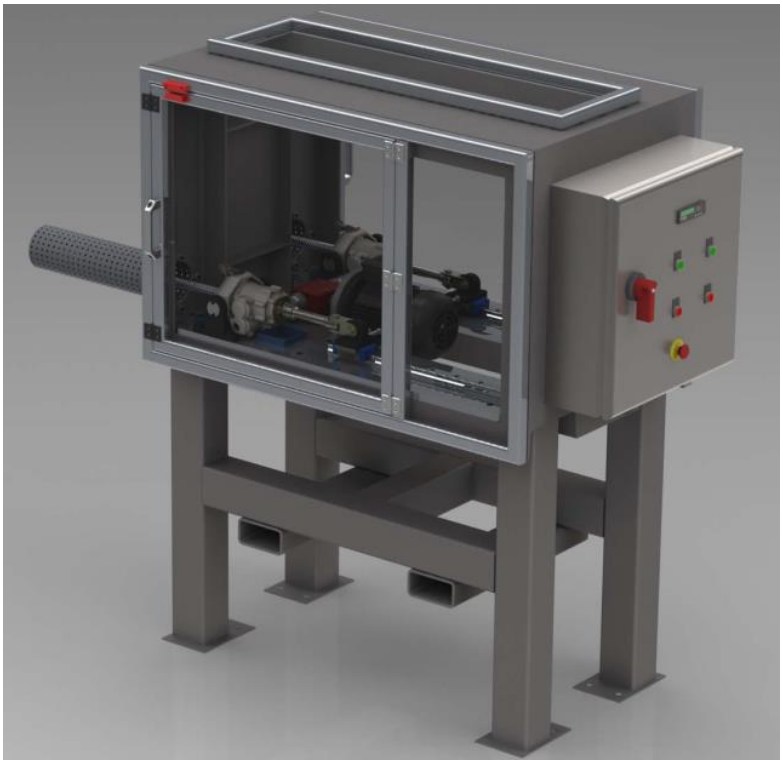

Figure 4-3 Ballscrew Test Stand Prior to Conversion

4.1.3 Torsion Bar Sizing

The first task undertaken was to determine whether the enclosure offered sufficient space to accommodate a correctly sized torsion bar.

A correctly designed torsion bar must offer sufficient compliance to ensure that the required torque load can be consistently applied, and to minimise load relaxation due to any wear or minor slip of components in the system. It must offer sufficient strength to react the required load and avoid fatigue failure. This must be achieved through correct selection of materials and component dimensions.

The torsional stiffness of a circular cross section shaft is given by:

$$k = \frac{G\,J}{L} \tag{21}$$

Where:

k = Stiffness (N.m/rad)

G = Material Shear Modulus (Pa)

J = Torsional Constant (m^4)

L = Length (m)

The torsional constant is given by:

$$J = \frac{\pi\,r^4}{2} \tag{22}$$

Where:

r = Radius (m)

The maximum shear stress at the outer diameter of the shaft is given by:

$$\tau = \frac{T\,r}{J} \tag{23}$$

Where:

τ = Shear Stress (Pa)

T = Torque (Nm)

Therefore, in order to maximise compliance (i.e., minimise stiffness) whilst minimising stress the best solution is to maximise the length of the shaft. Meanwhile the torsion bar diameter should

be minimised but maintained sufficiently large to provide an adequate margin of safety to the torsional proof stress of the material.

BS S162 maraging steel was selected as the material for the torsion bar due to high strength, low distortion during heat treatment and resistance to crack propagation. The pertinent material properties are listed in Table 4-2.

Table 4-2 BS S162 Material Properties [259]

Property	Symbol	Value
0.1% Torsional Proof Stress (B-Basis)	Q_1	1085 MPa
Shear Modulus	G	70 GPa

An initial examination of the internal dimensions of the test rig enclosure showed that the maximum achievable length for the torsion bar was 620mm. To maintain a margin of safety of 0.5 against the proof torsional stress the minimum diameter of the torsion bar was calculated by:

Maximum allowable stress:

$$\tau = \frac{1085}{1.5} = 723\ MPa \tag{24}$$

Minimum Diameter:

$$r = \sqrt[3]{\frac{2T}{\pi\tau}} \tag{25}$$

$$r = \sqrt[3]{\frac{2 \times 50}{\pi\ \times 723\ \times 10^6}} = 0.00353\ m \tag{26}$$

$$D = 7.06\ mm \tag{27}$$

(Rounded to 7mm)

For a 7mm shaft the stiffness is calculated as:

$$k = \frac{G\,\pi\,r^4}{2\,L} \tag{28}$$

$$k = \frac{70\,\times\,10^9\,\times\,\pi\,\times 0.0035^4}{2\,\times\,0.62} = 26.6\,N.m/rad \tag{29}$$

This stiffness results in an angular deflection range of 21.5° (0.376 rad) to 107° (1.50 rad) at the minimum and maximum test loads respectively. The potential angular relaxation of the torsion bar during testing can be calculated by treating the wear as an increase in backlash. The normal backlash of a gear pair can be converted to a tangential distance by:

$$w_t = \frac{w_n}{\cos\alpha} \tag{30}$$

Where:

w_t = tangential backlash

w_n = normal backlash

This can then be converted to an angular displacement in radians by:

$$w_\theta = \frac{2\omega_t}{d_p} \tag{31}$$

Where:

w_Θ = angular backlash

The test gearbox has two gear meshes. If the output is earthed the total accumulated backlash at the input is given by equation (32).

$$w_{T\theta} = w_{\theta 1} + \frac{n_2}{n_1} w_{\theta 2} \quad (32)$$

Where:

w_{Tt} = total angular backlash at the gearbox input

$w_{\vartheta 1}$ = angular backlash at the first gear mesh

$w_{\vartheta 2}$ = angular backlash at the second gear mesh

n_1 = number of teeth on input/output gear

n_2 = number of teeth on idler gear

Assume that each tooth in the gearbox suffers 10µm of wear normal to the surface, sufficient to exhaust most PVD solid lubricant coatings, giving a total increase in normal backlash for each mesh of 20µm. The total resultant angular backlash at the input is:

$$w_{T\theta} = \frac{2 \times (0.020/\cos 20)}{54} + \left(\frac{33}{24} \times \frac{2 \times (0.020/\cos 20)}{74.25}\right) = 0.00158\, rad \quad (33)$$

From the stiffness calculated in equation (29) this would cause a torque load relaxation of 0.042Nm, At the minimum test load of 10Nm torque load this would be 0.42% of the test setting, which is sufficiently small to have negligible effect. These calculations confirmed that the enclosure offered sufficient space to accommodate the desired test setup.

4.1.4 Transducer Selection and Monitoring

To ensure that the applied test conditions were maintained during testing it was necessary to incorporate torque and speed transducers within the load loop of the test stand. An IML TLDM-50/5-A1-V2-S-K combined torque cell and encoder was selected for this purpose, due to suitable torque range (0-50Nm) and standard keyed fittings to ease connection of the transducer to the remaining drive components.

A bench-mounted display unit was procured to provide quick visual indication of torque and speed values, and conversion of the sensor outputs to standard 10V BNC outputs for connection

to a data logger. The BNC outputs were recorded at a PC based data logger at a frequency of 125Hz. Regular calibration checks of both the torque and speed outputs were conducted to confirm accuracy of the readings and continued sensor health.

4.1.5 Test Rig Design

The design concept developed for the rig was to mount a new base plate within the existing frame, whilst spacing the gearboxes as far apart as possible to maximise torsion bar length. The drive line components were designed to clamp to a common keyway running on the baseplate along the axis of the electric motor to aid with maintaining relative alignments.

The first common axis incorporated the splined shaft from the motor to the reversing gearbox, torque cell and encoder, shaft for application of the load torque, and splined shafts for connecting to input and output gears of the test and reversing gearboxes. Flexible bellows couplings were used to make connections between the above components whilst accommodating any minor misalignments. All but one clamp on the couplings were standard keyed connections to prevent any slippage during operation. The remaining plain clamp was unkeyed and placed immediately downstream of the torque application shaft to allow angular displacement whilst applying load though the torsion bar. The torque application shaft was simply supported on bearings mounted in two brackets that both featured grooves for aligning on the baseplate keyway. The torque cell and encoder were mounted on a bracket that was also keyed to the base plate, in order match the shaft height of the mounted gearboxes.

The second common axis consisted of the torsion bar and earthing bracket. The earthing bracket was designed to avoid reducing the potential torsion bar length and consisted of a splined shaft welded to a rectangular block to form a gag. When earthing the gearbox to apply the torque load, the gag that was bolted into a slot on an overhanging bracket. The bracket can be left in place whilst the splined gag is removed to reduce disturbance to the test setup.

Due to the slenderness of the torsion bar the decision was taken to include a bearing support midway along the length of the bar to avoid issues with shaft whirling. To fit the bearing over the splined ends of the torsion bar a mounting boss for the bearing inner diameter was added. The bearing brackets on both axes consisted of simple flat plates with two bolts passing through mounting feet at the base. The bearings were restrained axially within their bores by an internal shoulder on one side and a circlip located in a groove on the other.

The test gearboxes have four threaded holes each in their bases for mounting with bolts. In order to easily mount the gearboxes to the baseplate, two mounting blocks were designed with recesses for the heads of the bolts on the underside and grooves for the main keyway. Each

gearbox was bolted to the mounting block from underneath, and then the mounted blocks bolted down the baseplate by a further four bolts. The test rig components are labelled in Figure 4-4. A photograph of the test stand is shown in Figure 4-5.

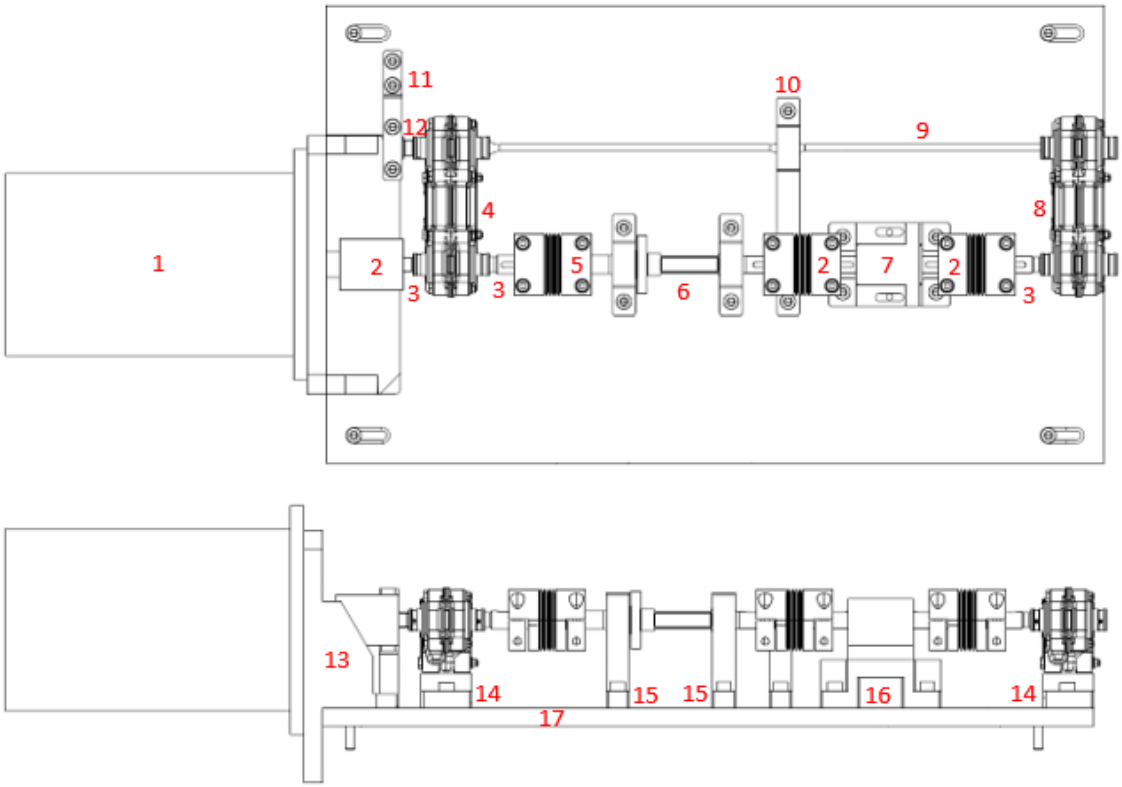

1)	Electric Motor	10)	Torsion Bar Bearing Bracket
2)	Coupling (Key to Key)	11)	Earthing Bracket
3)	Shaft (Key to Spline)	12)	Splined Gag
4)	Slave Gearbox	13)	Motor Bracket
5)	Coupling (Key to Plain)	14)	Gearbox Mounting Block
6)	Shaft (Torque Application)	15)	Bearing Bracket
7)	Torque Cell & Encoder	16)	Torque Cell Mounting Block
8)	Test Gearbox	17)	Base Plate
9)	Torsion Bar		

Figure 4-4- Test Rig Diagram

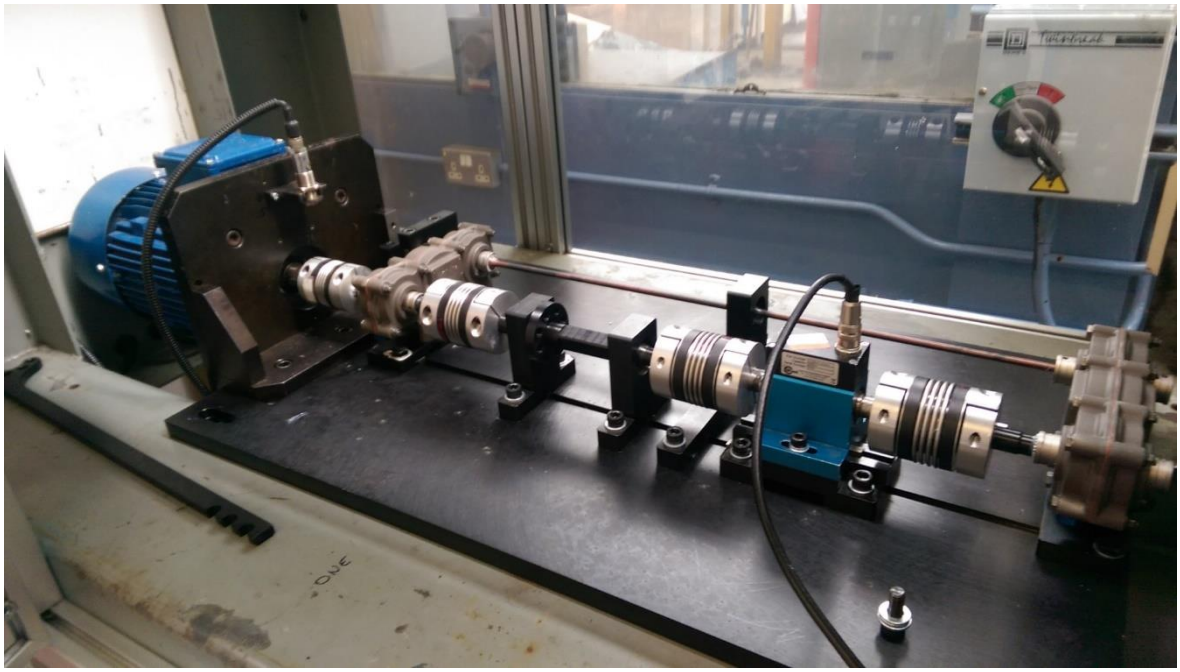

Figure 4-5 Test Rig Photograph

4.1.6 Application of Test Load

The method of load application was designed to allow safe, repeatable setting of the test load by a single operator. When applying the torque, initially the torsion bar was earthed by inserting the splined gag into the through shaft of the reversing gearbox and then locking it in place with the earthing bracket. The plain clamp on the coupling between the reversing gearbox and torque application shaft was then loosened.

The torque was applied to the shaft using a lever arm and hanging masses. This approach was chosen instead of using a torque wrench to allow the load to be held steady when retightening the plain clamp, without the assistance of a second operator. The torque application shaft included a hub with 8 holes equally spaced on the circumference of a reference circle. The lever arm attached to the shaft hub with bolts and an arc of 5 corresponding holes. Although only two bolts were required for attaching the lever arm the inclusion of multiple holes allowed the operator some flexibility to position the lever arm perpendicular to the baseplate regardless of the precise angle at which the shaft had been locked.

The masses were suspended from the lever arm using a hooked carrier. The hook sits in one of three recesses at the end of the lever arm. Three such notches were included to allow the perpendicular distance to be adjusted as a further option for fine tuning of the torque loads. The nominal perpendicular distance from the shaft axis to the centre position on the arm was 50cm. Therefore, hanging masses were selected and purchased to allow a maximum of 100N to be applied, in addition to ensuring that mass could be added in increments to achieve intermediate

loads. Flats were included on the outer diameter of the shaft to allow manual adjustments to be made with a wrench if necessary.

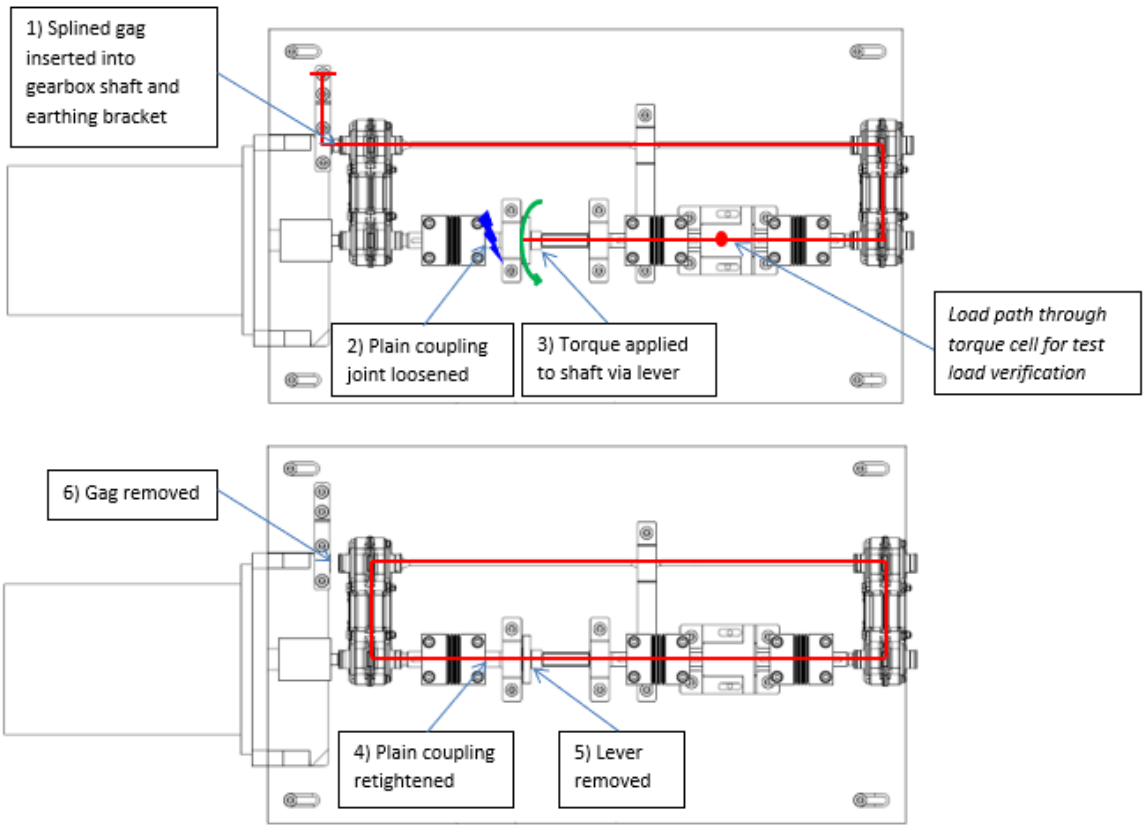

Figure 4-6 Application of Torque Load

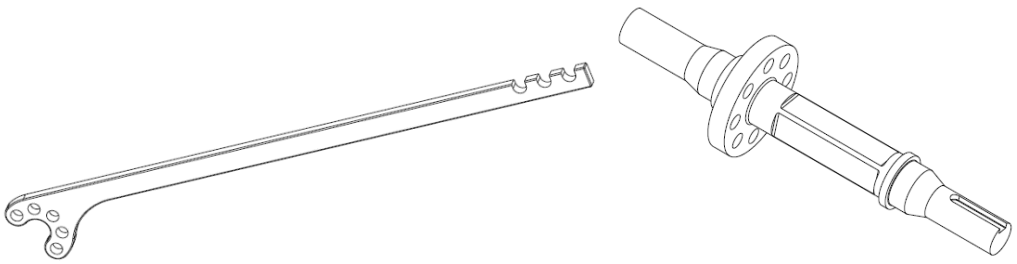

Figure 4-7 Isometric views of Lever and Torque Application Shaft

4.1.7 Test Rig Control Logic

To apply the desired test cycles the existing PLC on the test rig required reprogramming. The PLC is a Siemens LOGO! 12/24RC model with two expansion modules, providing a total of 20 inputs, 4 relay outputs, and 12 transistor outputs. The PLC program for the running of test cycles is shown in Figure 4-8.

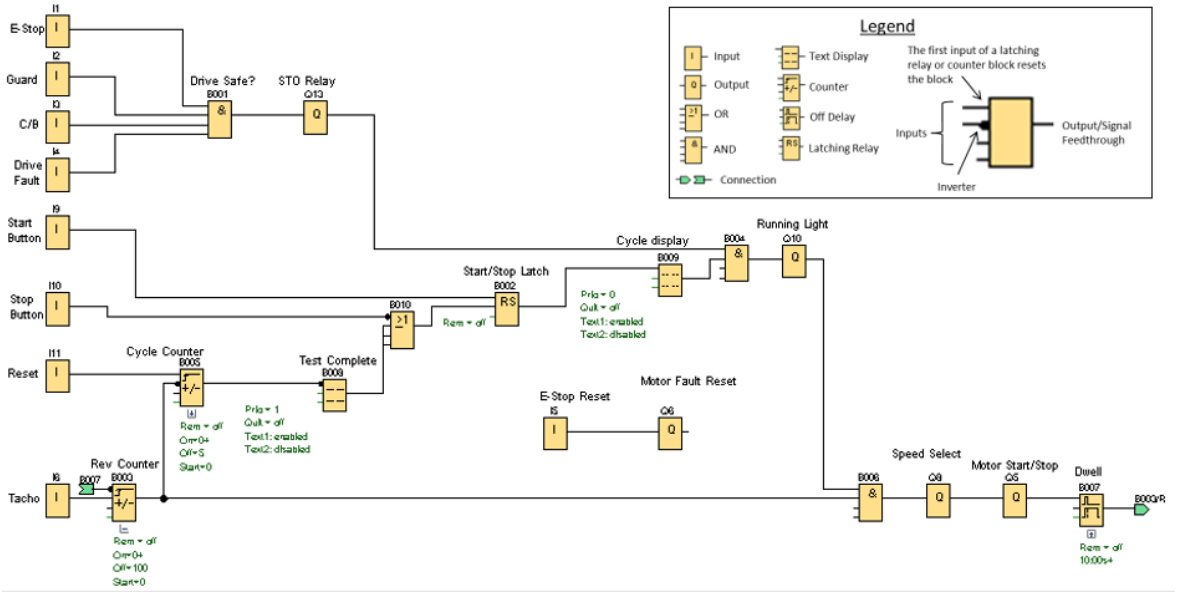

Figure 4-8 Test Rig Control Logic

Five inputs for the E-Stop relay, guard relay, circuit breaker and drive fault statuses are connected to an AND block (B001) which when true powers the relay that connects the STO ("safe torque-on") pins of the motor drive. This in turn is connected to a further AND block (B004), the other input of which is connected to a latching relay that is set to true when Start button is pushed. Once true, this connects power to the "Test Running" light on the control panel and a further AND block (B006). AND blocks B004 and B006 are kept separate to ensure that the "Test Running" light remains lit during dwell periods.

For AND block B006 to be true the revolution counter block (B003) must also be true. When this is the case, block B006 powers the speed select and motor start pins of the motor drive in order to commence motor rotation at the pre-set speed value. When the motor is rotated the optical tachometer receives one reflected pulse from the target strip on the motor output shaft for each revolution. Once the revolution counter reaches 100 the output becomes false and causes the motor speed select and motor start outputs to be switched off. When this occurs a delay, equal to

the desired dwell time between test cycles, expires before setting the reset input of the counter block to true. This resets the counter back to zero and causes the motor to resume rotation.

The number of changes of state of counter block B003 are monitored by a further counter (B005). This counter is programmed with the desired number of test cycles that to be completed. When the required number of test cycles are completed, or the Stop button is pushed, an OR block sends a signal to the reset input of the latching relay. This sets the signal to AND block B004 to false which halts the test.

Two text display blocks provide indications on the front panel display module of the number of revolutions competed in the current cycle, the number of cycles completed, and a “test complete” message when the required number of cycles are completed. The value of the test cycle counter is reset by pushing the reset button on the front panel. A small secondary circuit connects the E-stop reset button on the front panel to the fault reset pin of the motor drive. No other software connections to the E-stop reset are required as the other necessary connections are hardwired.

4.1.8 Modifications and Configuration of Test Gearboxes

A small number of modifications were made to the two gearboxes from their standard configurations to enable their use for wear testing. One was lubricated with a partial fill of ISO VG 150 hypoid EP gear oil to prevent wear and acted as the reversing gearbox. The bearing sealing rings were omitted from the reversing gearbox to allow flow of oil through the bearings, with the adjacent shims ground oversize to maintain the same overall axial float. The second gearbox was used to house the coated test gears. The standard gearbox bearings were replaced with sealed equivalents to ensure no egress of grease that might contaminate the tooth contacts.

Modifications to the detailed design of the gear teeth are addressed in section 3.3

4.2 Development of Rolling Cylinder Gear Wear Model

Quantification and prediction of the wear suffered by sliding components is often based on Archard’s Law [60], which states that the volume of material worn from rubbing surfaces is proportional to the applied normal force and the sliding distance. When considering a coating, where the useful life is dependent on the thickness, this can be rearranged to consider the wear depth instead of volume.

$$h = k\sigma s \tag{34}$$

Where:

h = Wear depth (mm)

k = Wear coefficient (mm^3/N.mm)

σ = Contact pressure (MPa)

s = Sliding distance (mm)

During the meshing action between gear teeth the radius of curvature, loads, and sliding velocities of the contacting gear teeth vary during the mesh cycle. Therefore, the sliding distance and contact pressure must be calculated for each position on the tooth surfaces. The following method simplifies the contact between the gear teeth to a pair of loaded cylindrical rollers of constantly changing radius and angular velocity and is based on the work of Flodin and Andersson [14].

When calculating contact geometry, velocities, and loads, it is useful to define the points of contact with regards to their position on the line of action.

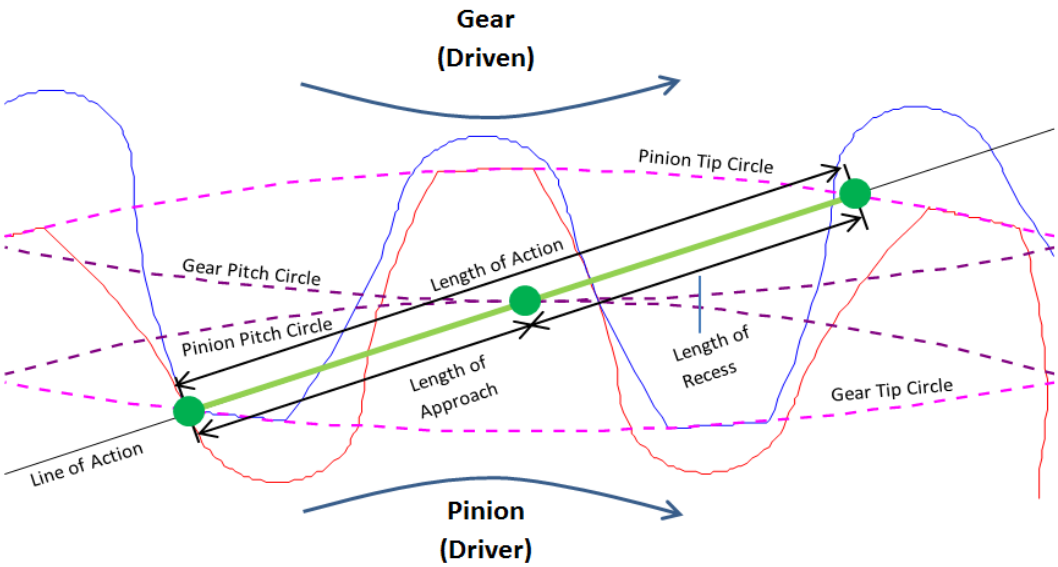

Figure 4-9 Line of Action between Meshing Gears (Redrawn from [19])

Initially the pitch and outside (tip) radii must be found for the driving (1) and driven (2) gears:

$$r_{p1} = \frac{mz_1}{2} \tag{35}$$

$$r_{p2} = \frac{mz_2}{2} \tag{36}$$

$$r_{o1} = r_{p1} + (1 + M)m \tag{37}$$

$$r_{o2} = r_{p2} + (1 - M)m \tag{38}$$

Where:

r_p = pitch radius (mm)

r_o = outside radius (mm)

z = number of teeth

m = module (mm)

M = modification coefficient

The lengths of approach and recess can then be found according to:

$$L_a = \sqrt{r_{o2}^2 - \left(r_{p2}.\cos\alpha\right)^2} - r_{p2}.\sin\alpha \tag{39}$$

$$L_r = \sqrt{r_{o1}^2 - \left(r_{p1}.\cos\alpha\right)^2} - r_{p1}.\sin\alpha \tag{40}$$

Where:

L_a = Length of approach (mm)

L_r = Length of recess (mm)

α = Pressure angle (°)

The total length of the line of action is found from the sum of the lengths of approach and recess:

$$L = L_a + L_r \tag{41}$$

Where:

L = Length of action (mm)

The position of contact on the line of action is designated as ξ, where the value at pitch circle is zero and the extremities are $-L_a$ and L_r. At each point of contact the radius of curvature for each of the teeth is:

$$R_1 = \frac{d_{p1}}{2}\sin\alpha + \xi \tag{42}$$

$$R_2 = \frac{d_{p2}}{2}\sin\alpha - \xi \tag{43}$$

Where:

R = Radius of curvature (mm)

d_p = Pitch diameter (mm)

ξ = Position of contact on the line of action (mm)

This in then converted to an equivalent radius of curvature for later assessment of the hertzian contact stresses and deformation.

$$R^* = (R_1^{-1} + R_2^{-1})^{-1} \tag{44}$$

Where:

*R** = Equivalent radius of curvature (mm)

The angular velocity for the gear and radius of curvature can then be used to find the peripheral speed of the roller surfaces:

$$\omega_1 = \frac{2\pi n}{60} \tag{45}$$

$$\omega_2 = \omega_1 . \left(\frac{z_1}{z_2}\right) \tag{46}$$

$$u_1 = \omega_1 R_1 \tag{47}$$

$$u_2 = \omega_2 R_2 \tag{48}$$

Where:

ω = Angular velocity (rad/s)

n = Input speed (rpm)

u = Peripheral speed (mm/s)

With the geometry and velocities of the surfaces defined for each point of contact, the loads acting on the teeth must be found. For the majority of gear meshes the contact ratio is between 1 and 2. Consequently the mesh loads at the start and end of the line of action are carried by two tooth pairs, whilst close to the pitch point it is carried by a single tooth pair. By tracing the point of contact as it travels through the line of action, the regions of single and double tooth pair engagement can be determined.

When two pairs of teeth are in mesh, the points of contact are separated by a distance equivalent to the base pitch of the gear. The base pitch of both gears is found according to:

$$p_b = \pi m . \cos \alpha \tag{49}$$

Hence the limits of single tooth contact can be found according to:

$$\xi_{lpstc} = L_r - p_b \tag{50}$$

$$\xi_{hpstc} = p_b - L_a \tag{51}$$

Where:

ξ_{lpstc} = position on line of action corresponding to lowest point of single tooth contact (mm)

ξ_{hpstc} = position on line of action corresponding to highest point of single tooth contact (mm)

For values of ξ between ξ_{lpstc} and ξ_{hpstc} a single tooth pair carries the force transmitted through the line of action. The force per unit of face width is then simply:

$$F = \frac{2T}{bd_b} \tag{52}$$

Where:

F = Force per unit face width (N/mm)

b = Face width (mm)

T = Torque (N.mm)

d_b = Base diameter (mm)

When two tooth pairs are in mesh, the load is shared between them according to the stiffness of the teeth and the sum of the deviations to the tooth surfaces from the perfect involute. The deviations may be present due to manufacturing inaccuracies, or due to wear from previous tooth engagements. As the points of contact are separated by a distance equivalent to the base pitch:

$$F = F_{\xi} + F_{\xi+p_b} \tag{53}$$

$$F_{\xi} = \frac{F}{2} - \frac{C_{\Sigma T}}{2}\left[\left(h_{1,\xi} + h_{2,\xi}\right) - \left(h_{1,\xi+p_b} + h_{2,\xi+p_b}\right)\right] \tag{54}$$

$$F_{\xi+p_b} = \frac{F}{2} - \frac{C_{\Sigma T}}{2}\left[\left(h_{1,\xi+p_b} + h_{2,\xi+p_b}\right) - \left(h_{1,\xi} + h_{2,\xi}\right)\right] \tag{55}$$

Where:

F = Force per unit face width (N/mm)

$C_{\Sigma T}$ = Tooth deflection constant (N/mm^2)

h = Normal deviations to tooth profile (mm)

The tooth deflection constant is related to the modulus of elasticity of the material and is the combined stiffness of each tooth in bending. Treating a tooth pair as two springs in series:

$$\frac{1}{C_{\Sigma T}} = \frac{1}{C_{T1}} + \frac{1}{C_{T2}} \tag{56}$$

Where:

C_{T1} = Tooth deflection constant for pinion (N/mm^2)

C_{T2} = Tooth deflection constant for gear (N/mm^2)

The stiffness of each tooth in bending varies according to the position of the contact, decreasing from root to tip. Flodin stated that during the meshing action the root of one tooth will contact the tip of the other and vice versa, hence the stiffness variations tend to cancel each other out, and $C_{\Sigma T}$ can be considered constant. Flodin selected tooth deflection constants from the finite element work of Wang and Cheng [66], utilising a single constant value for all positions in mesh based on the calculated stiffness for each tooth when loaded at the pitch circle. The same approach is followed in this study, yielding:

$$C_{T1} = \frac{E}{8} \tag{57}$$

$$C_{T2} = \frac{E}{9} \tag{58}$$

Where:

E = Young's Modulus (MPa)

Having determined the radius of curvature and normal forces at each point, the contact conditions may now be calculated by treating the teeth as parallel cylinders in contact using Hertz's formulae. Under load the two cylinders will deform to form a rectangular contact area of half-width *a:*

$$a = \sqrt{\frac{4FR^*}{\pi E^*}} \tag{59}$$

Where:

a = Contact half-width (mm)

*E** = Equivalent modulus of elasticity (MPa)

The equivalent modulus of elasticity is given by:

$$E^* = \left(\frac{1-\nu_1^2}{E_1} + \frac{1-\nu_2^2}{E_2}\right)^{-1} \tag{60}$$

Where:

v = Poisson's Ratio

The mean contact stress of a point on the tooth surface as it passes through the contact area:

$$\sigma_m = \frac{F}{2a} \tag{61}$$

Where:

σ_m = Mean contact pressure

With the width of the contact established, the peripheral speeds of the rollers can be used to calculate the sliding distance using the method of single point observation, as proposed by Andersson [62].

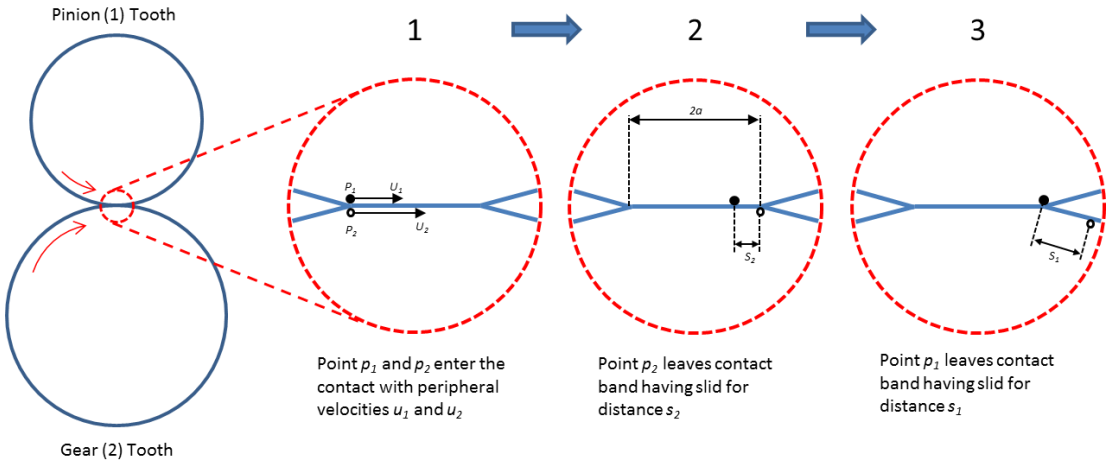

Figure 4-10 Sliding Distances in Rolling-Sliding Contact between Cylinders (Adapted from [62])

$$s_1 = \frac{|u_1 - u_2|}{u_1} . 2a \tag{62}$$

$$s_2 = \frac{|u_1 - u_2|}{u_2} . 2a \tag{63}$$

Where:

s = sliding distance

With the sliding distance and contact stress established, this yields the following expression for the normal wear to a point *p* on the tooth surface after a single mesh cycle:

$$h_{p1} = k\sigma_m 2a \frac{|u_1 - u_2|}{u_1} \tag{64}$$

$$h_{p2} = k\sigma_m 2a \frac{|u_1 - u_2|}{u_2} \tag{65}$$

This can be extended to calculate the cumulative wear over many cycles by breaking up the total duty into discrete periods and integrating equations (64) and (65). This gives the following expression for the wear at a point *p* after *n* cycles:

$$h_{p,n} = h_{p,n-1} + ek\sigma_{p,n}s_{p,n} \tag{66}$$

Where:

e = number of tooth engagements per step

If the total duty for the gear pair is divided into N steps, the number of engagements per tooth for the pinion (1) and wheel (2) per step is:

$$e_1 = \frac{R}{N} \tag{67}$$

$$e_2 = \frac{z_1}{z_2} \cdot \frac{R}{N} \tag{68}$$

Where:

e = Pinion tooth engagements per step

R = Total revolutions at pinion

N = Number of steps

z = Number of teeth

After each step the distribution of loads between the tooth pairs at each position was recalculated to understand the redistributive effects of the tooth wear. The model is shown schematically in Figure 4-11. The input parameters are defined in Table 4-3.

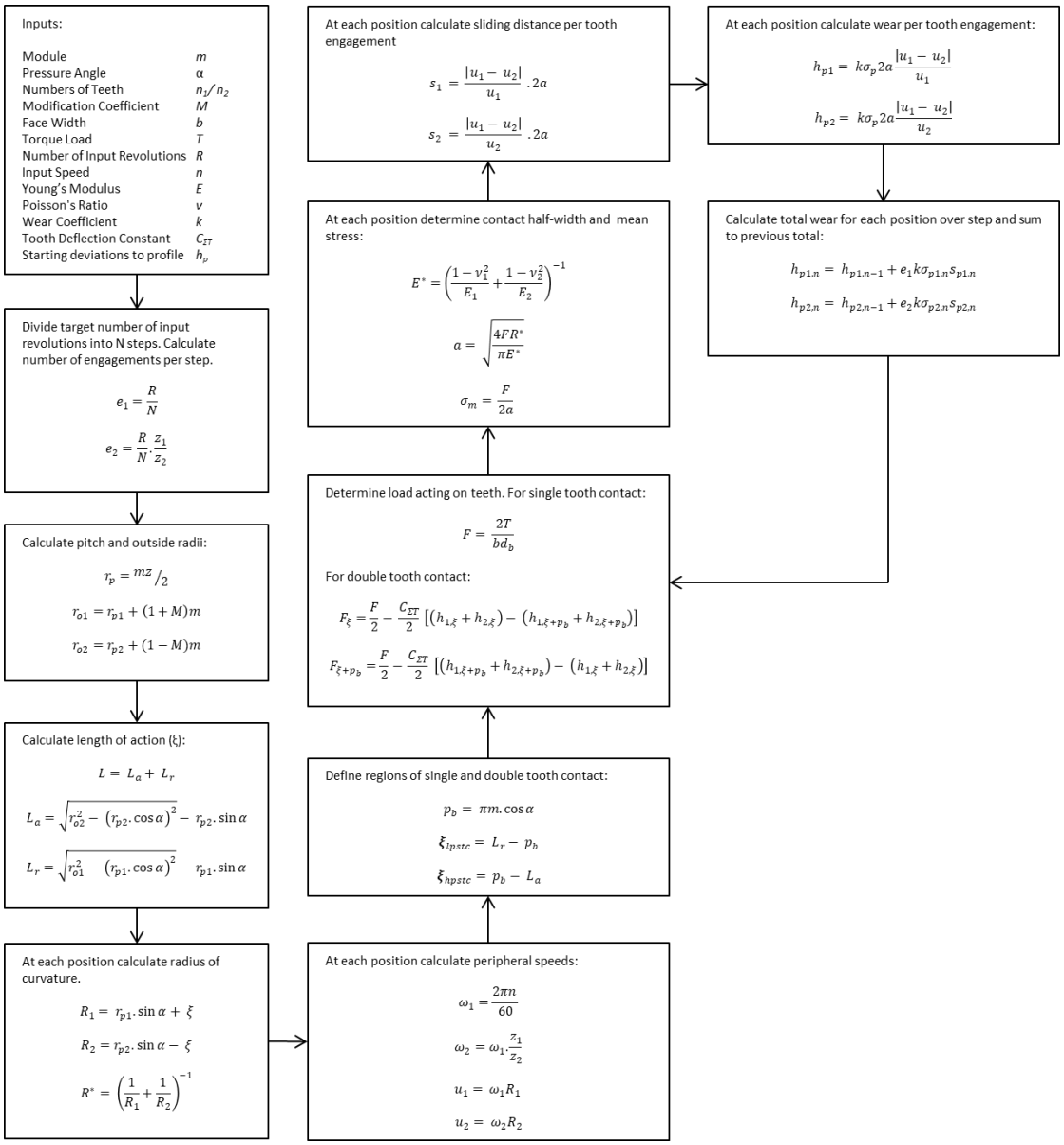

Figure 4-11 Rolling Cylinder Model Schematic

Table 4-3 Input Parameters to Rolling Cylinder Model

Parameter		Value		Units
Module	m	2.25		mm
Pressure Angle	α	20		°
Numbers of Teeth	n_1/n_2	24	33	
Modification Coefficient	M	0		
Face Width	b	6.5		mm
Torque	T	According to test conditions		Nm
Number of Input Revolutions	R	According to test conditions		revs
Input Speed	n	400		rpm
Young's Modulus	E	176		GPa
Poisson's Ratio	v	0.3		
Wear Coefficient	k	Derived from fitment to measurements		$mm^3/N.mm$
Tooth Deflection Constant	$C_{\Sigma T}$	$1.04x10^4$		N/mm^2
Starting deviations to profile	h_p	According to measured profiles		mm

4.3 Measurement of Magnitude and Distribution of Wear

Prior to commencing testing on each set of test samples, three equally spaced teeth on each gear were marked from 1 to 3 using a vibro-peen tool on the non-working side lands to aid identification. During initial assembly and subsequent reassemblies of the gearbox these marks were used to ensure the original timing of the tooth engagement was maintained. As the number of teeth on the pinion (24) and gear (33) share a common denominator of 3, the gear pair does not have a hunting tooth ratio. Figure 4-12 shows the tooth engagement cycle for the test gearbox. Note that a marked tooth on the pinion only engages with one marked tooth on the mating gear during the full mesh cycle. The teeth engaged by each marked tooth also do not engage with any of the teeth engaged by the other marked teeth.

	Gear Teeth																														
	1	2	3	4	5	6	7	8	9	10	11	12	13	14	15	16	17	18	19	20	21	22	23	24	25	26	27	28	29	30	31	32	33

Gear Revs	Pinion Teeth																														
1	1	2	3	4	5	6	7	8	9	10	11	12	13	14	15	16	17	18	19	20	21	22	23	24	1	2	3	4	5	6	7	8	9
2	10	11	12	13	14	15	16	17	18	19	20	21	22	23	24	1	2	3	4	5	6	7	8	9	10	11	12	13	14	15	16	17	18
3	19	20	21	22	23	24	1	2	3	4	5	6	7	8	9	10	11	12	13	14	15	16	17	18	19	20	21	22	23	24	1	2	3
4	4	5	6	7	8	9	10	11	12	13	14	15	16	17	18	19	20	21	22	23	24	1	2	3	4	5	6	7	8	9	10	11	12
5	13	14	15	16	17	18	19	20	21	22	23	24	1	2	3	4	5	6	7	8	9	10	11	12	13	14	15	16	17	18	19	20	21
6	22	23	24	1	2	3	4	5	6	7	8	9	10	11	12	13	14	15	16	17	18	19	20	21	22	23	24	1	2	3	4	5	6
7	7	8	9	10	11	12	13	14	15	16	17	18	19	20	21	22	23	24	1	2	3	4	5	6	7	8	9	10	11	12	13	14	15
8	16	17	18	19	20	21	22	23	24	1	2	3	4	5	6	7	8	9	10	11	12	13	14	15	16	17	18	19	20	21	22	23	24

Figure 4-12 Tooth Engagement Cycle for Test Gearbox

During each wear test, cycling was paused at set intervals and the gearbox was disassembled to allow inspection and measurement of the marked teeth. The first two inspections were conducted at 100 and 500 test cycles to provide early information on the running in process. Subsequent inspections were performed at intervals of 1000 cycles.

At each interval, following disassembly, the gear teeth were blasted with filtered air to remove any loose debris without disturbing the formation of any transfer films. Visual inspections were conducted on a light stereomicroscope. Dimensional inspections were performed using a Klinglenberg P26 CNC-controlled gear measuring centre. Measurements consisted of 7 profile traces taken at equal spacing over the face width of the teeth. A single lead trace was used to form a datum and connect the profile traces. The lead measurement was taken below the SAP on the tooth to avoid worn areas of the tooth and ensure stability.

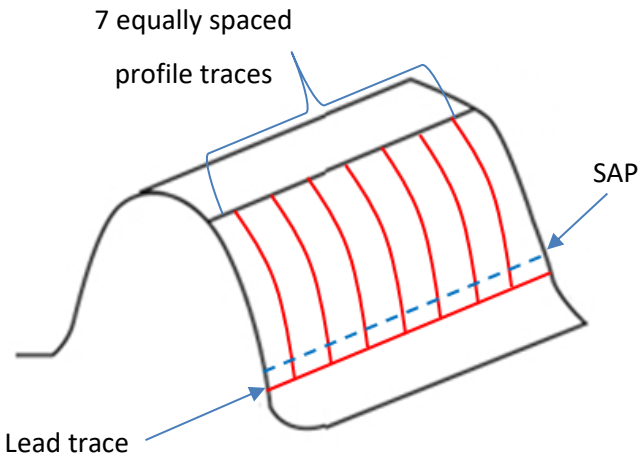

Figure 4-13 Measurements of Gear Teeth

For each set of measurements to a gear the P26 produced an ASCII file containing the measurement data. Each trace consists of 480 data points distributed evenly over the tooth surface from root to tip. The reported value is the normal deviation of the tooth surface from the perfect involute. The ASCII data was imported into a spreadsheet, where comparisons of the pre-test and worn profiles were used to generate wear maps of the teeth at each inspection interval. The maximum wear depth from each tooth was recorded at each inspection.

To integrate the measurements into the rolling cylinder model, a profile of each gear tooth was created using the average of the 7 profiles. The pre-test average profile was used to define starting conditions for h and the contact between each tooth and its corresponding tooth on the mating gear was simulated. The predicted tooth wear profile was compared to the average profile of the worn teeth at the end of testing. The average wear rate k was derived by adjusting its value

to achieve the combined least squares fit between the predicted and measured profiles. The process of determining maximum wear depth and the wear rate is shown schematically, along with example plots of each stage, in Figure 4-14.

To monitor the repeatability of the measurements during testing, one gear of each type was retained as a reference article. Prior to commencing each set of measurements of the test gears, the reference gears were also remeasured. These results were then compared to the pre-test measurements to understand the repeatability. Figure 4-15 shows the distribution of errors for all measurements of the reference gears taken during the test program, and the predicted normal distribution of errors based on mean and standard deviation. 95% of all data points were within 0.27µm of the pre-test values.

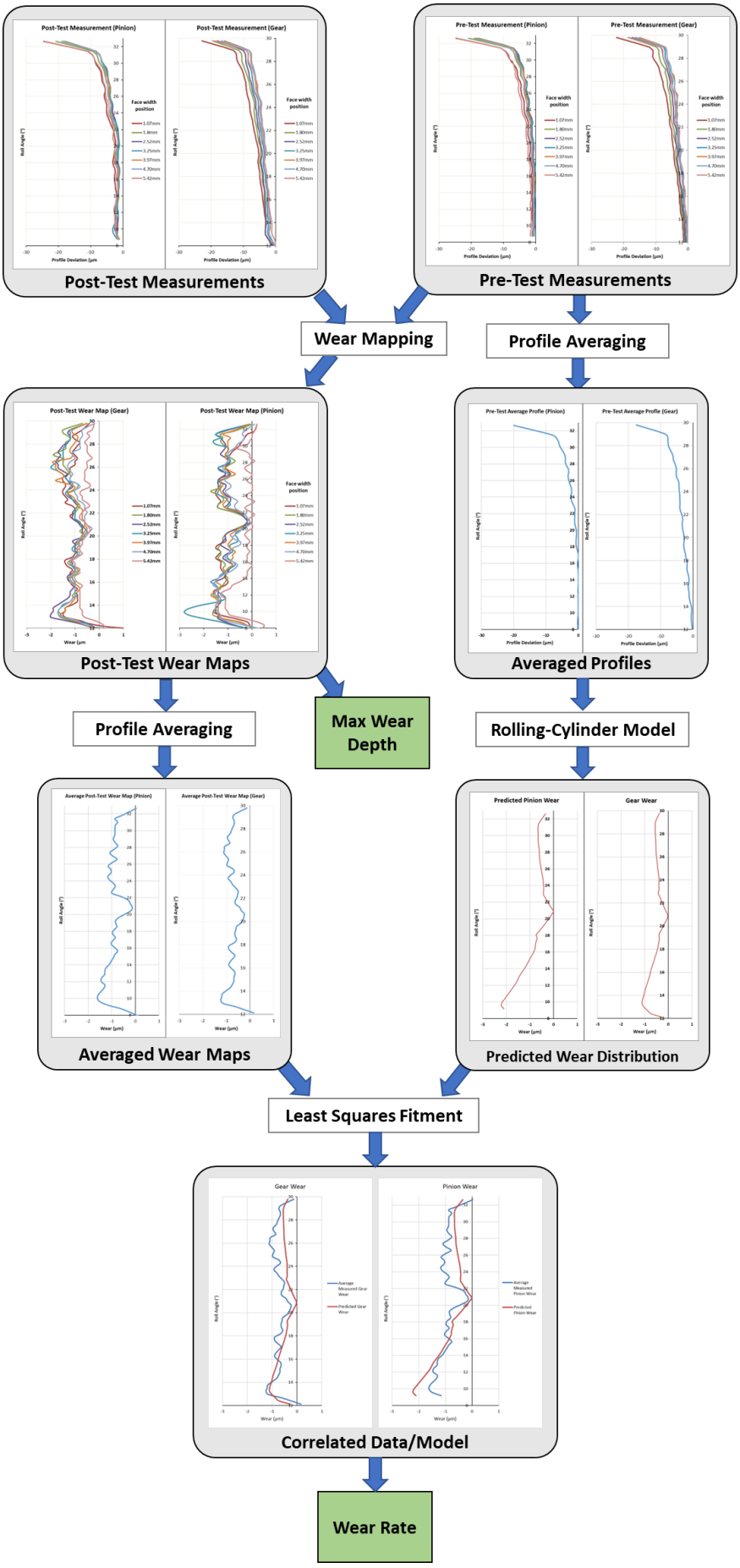

Figure 4-14 Process of Determining Maximum Wear Depth and Wear Rate

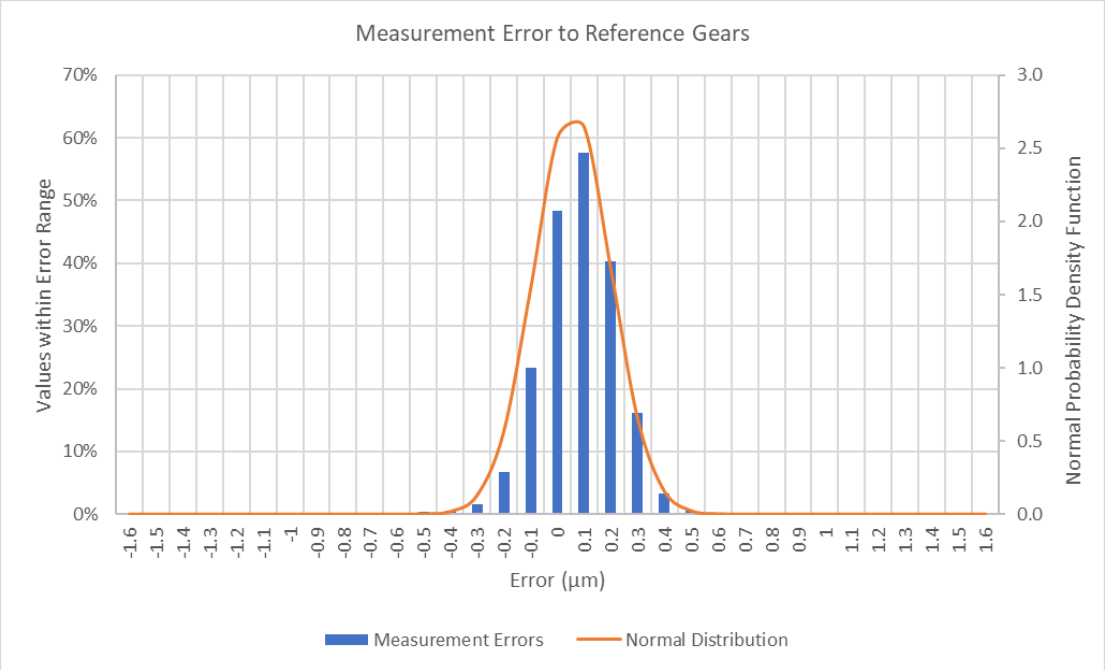

Figure 4-15 Measurement Error to Reference Gears

4.4 Results of Wear Testing

4.4.1 Tests at 20Nm Torque Load

4.4.1.1 MoST

During the first 100 cycles the wear was negligible across the whole active tooth surface, although contact was visibly evident across the majority of the face width. The region at the pitch circle showed no change in appearance from the as-deposited coating, whilst other areas in contact were darkened and more polished. Measurements indicated slight growth of the surface in some areas on the addendum and tips of the driving gears, and significant growth of the surface in the roots of the driven gears. Both observations correlated to the visual observation of the formation of black deposits in these areas. See Figure 4-16 and Figure 4-17.

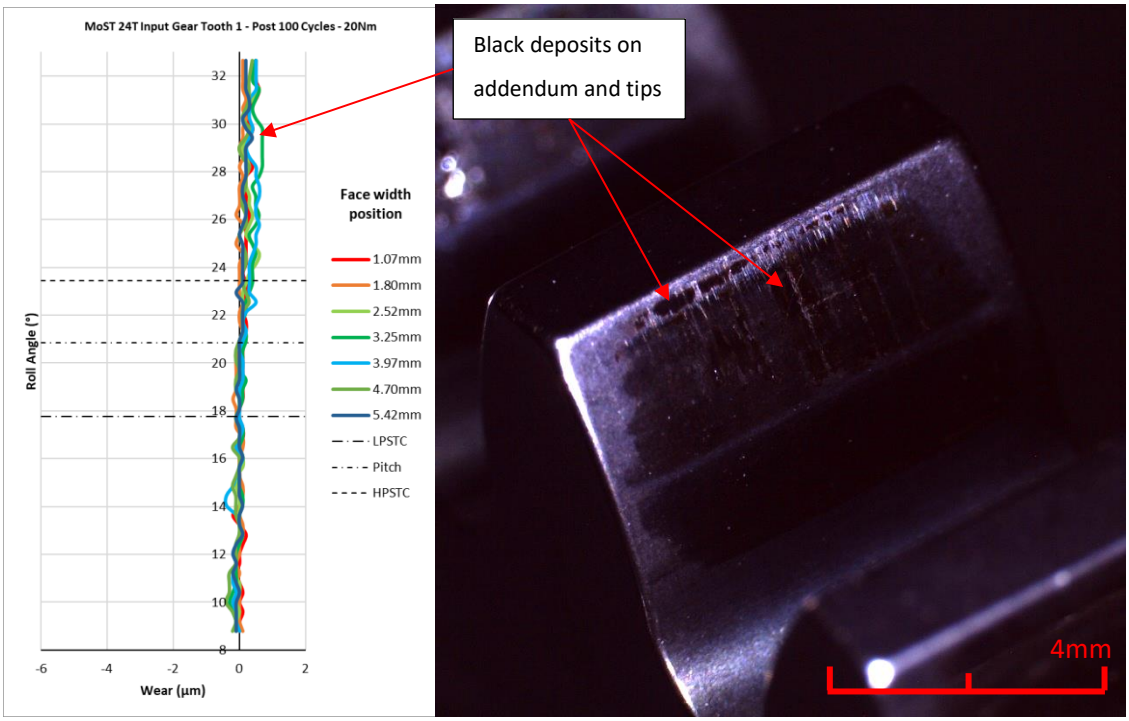

Figure 4-16 – Wear Map and Image of MoST-Coated 24T Input Gear Tooth (Driving Gear) after 100 Cycles at 20Nm

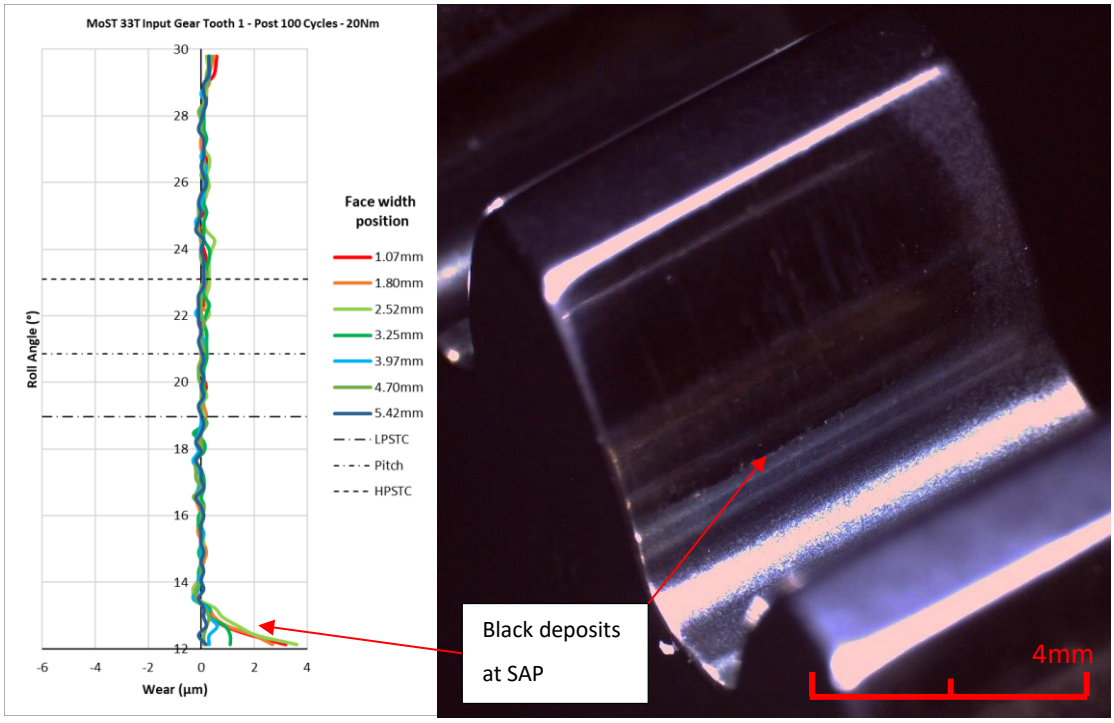

Figure 4-17 – Wear Map and Image of MoST-Coated 33T Input Gear Tooth (Driven Gear) after 100 Cycles at 20Nm

However, during the following 400 cycles the coating failed suddenly across a large section of the faces of the teeth. The failed areas took the form of a stripe, extending from root to tip and occupying up to half of the tooth width. Wear depths of up to 6µm were recorded, with maximum depths being found midway between the SAP and the LPSTC. The surfaces were stained an orange-brown colour, with some areas covered in black deposits.

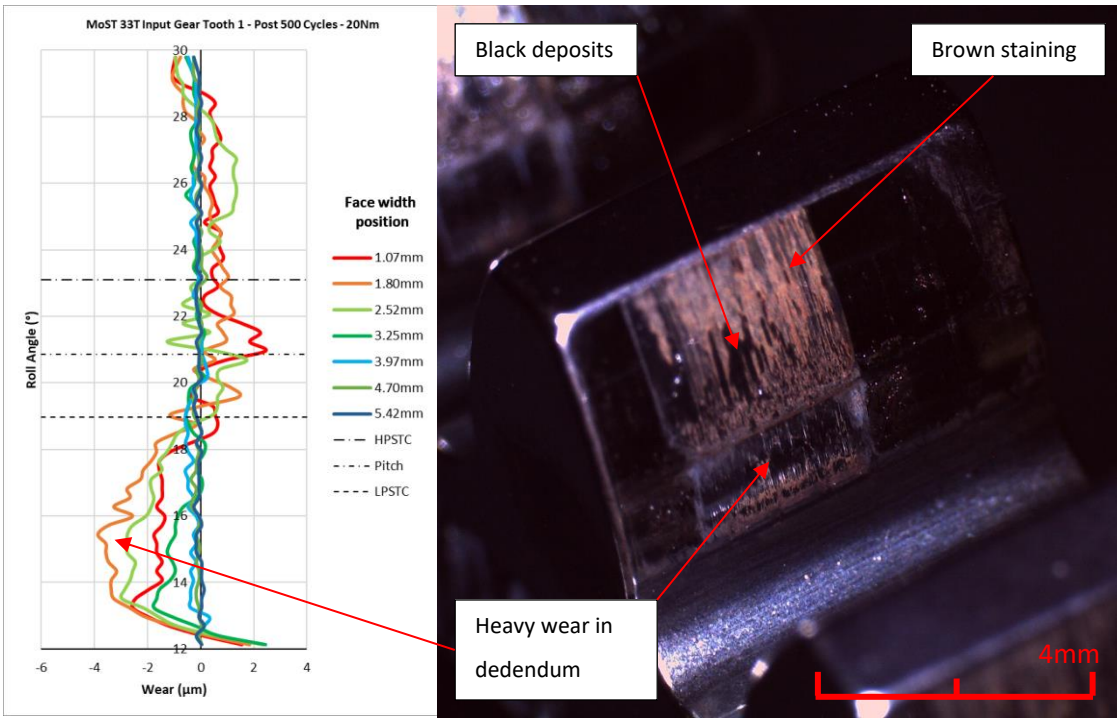

Figure 4-18 Wear Map and Image of MoST-Coated 24T Output Gear Tooth (Driven Gear) after 500 Cycles at 20Nm

On some teeth measurements indicated growth of the surface within the failed band, in a region stretching from the LPSTC up to the mid addendum, possibly due to an accumulation of debris or surface oxidation. Black deposits were still visually evident in some areas. Testing was halted as it was clear that the remaining coating would not survive further cycling.

Figure 4-19 provides an example of the wear prediction of the rolling/sliding cylinder model to the measurement data, in this instance for the 24-tooth pinion and 33-tooth gear of the input mesh. The point of minimum wear correctly predicted at the pitch circle, and the maximum wear being located slightly above the SAP. This was, however, compromised by the aforementioned growth of the surface on the addendum and close to the SAP of some teeth. Wear rates to achieve the best fit between the model outputs and measurements were in the range 5.73E-10 to 2.57E-10mm^3/N.mm.

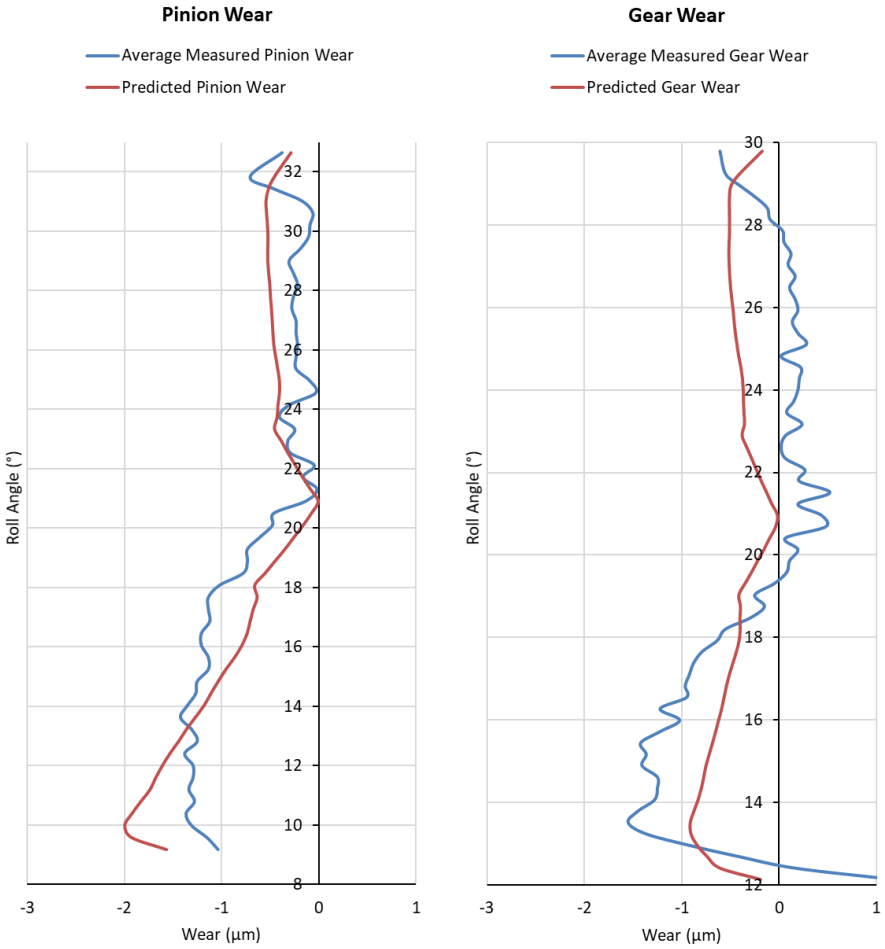

Figure 4-19: Comparison of Predicted and Measured Wear for MoST Coated Teeth (Wear Rate = 4.10E-10 $mm^3/N.mm$)

Figure 4-20 provides images of a typical whole tooth on completion of testing, under light microscope and SEM using both secondary and backscatter electron detectors. When using the backscatter detector relatively little contrast was obtained between the substrate and coating. However significant contrast was observed between the coating and substrate against the oxide layers that had formed on the surface, which appear darker in shade.

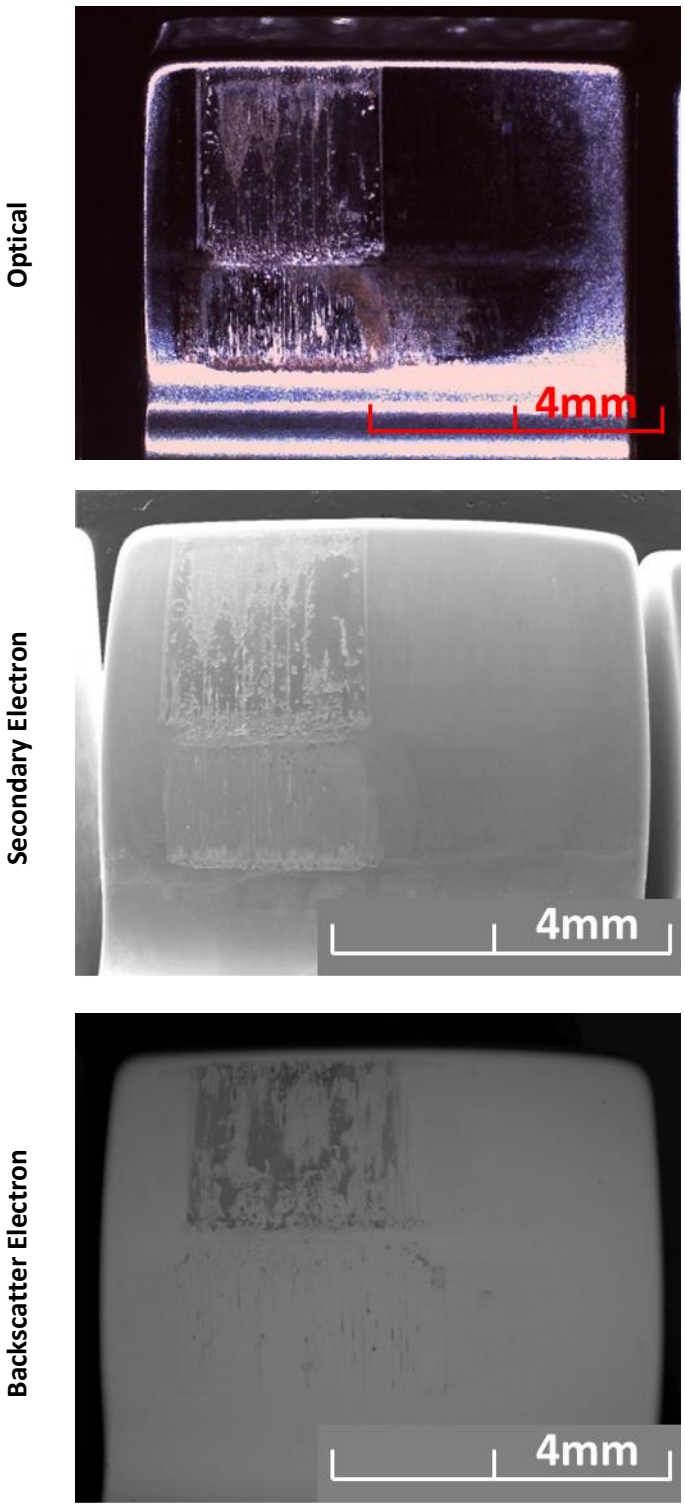

Figure 4-20 Optical, Secondary, and Backscatter Electron SEM Images of MoST-Coated Tooth after 500 Cycles at 20Nm

Figure 4-21 provides detailed views of the heavily worn areas. The results of the EDS spectra for these two regions are shown in Figure 4-22 and Figure 4-23.

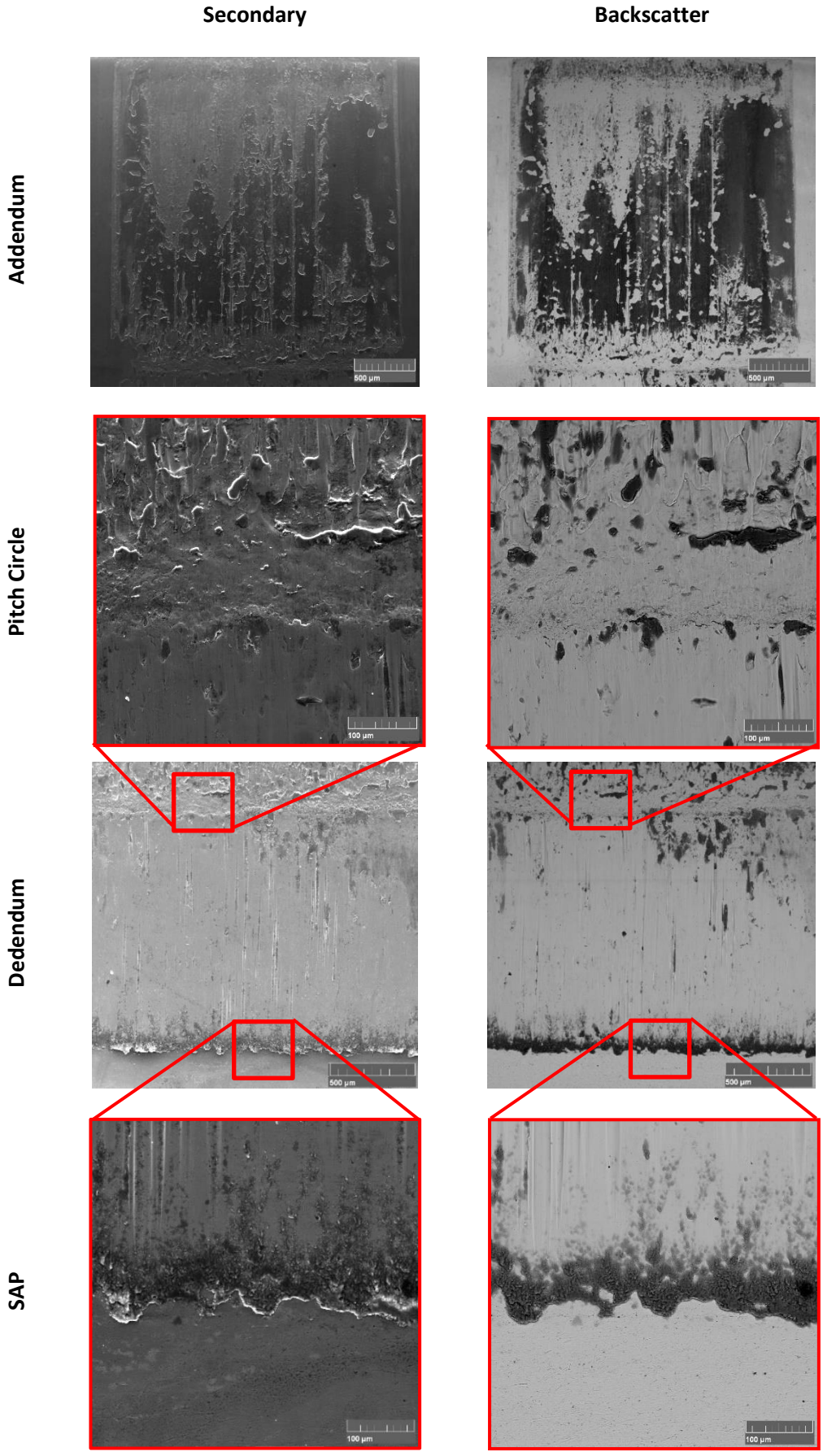

Figure 4-21: Backscatter and Secondary Electron SEM Images of Wear on MoST-Coated Tooth after 500 Cycles at 20Nm

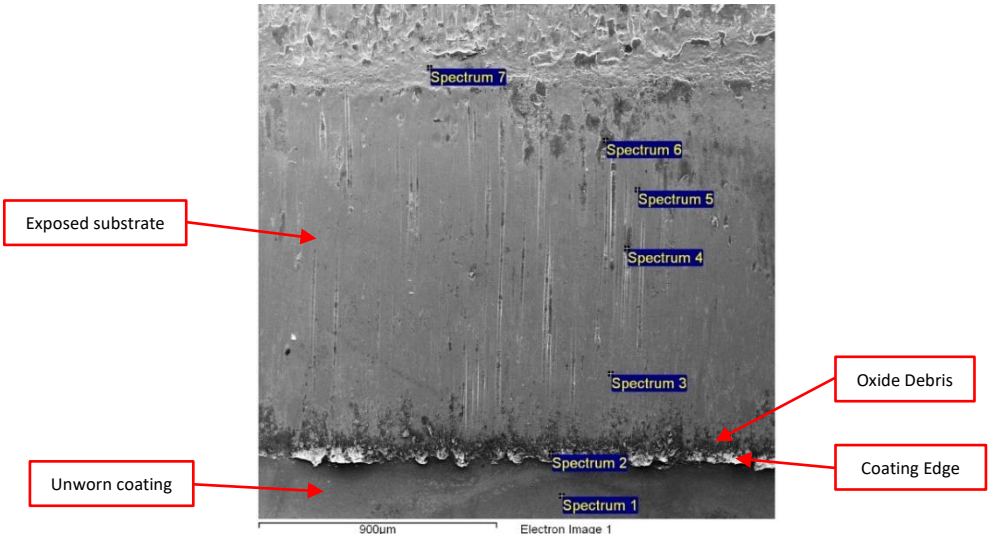

Spectrum	C	O	S	Ti	Cr	Fe	Ni	Mo
Spectrum 1			11.7	5.1	1.1	66.3	2.7	13.2
Spectrum 2	8.5	32.2	0.7	0.3	0.8	55.4	2.2	
Spectrum 3	4.6				1.3	90.3	3.8	
Spectrum 4	6.1	38.0	0.7	0.4	0.7	52.0	2.1	
Spectrum 5	4.5				1.3	90.5	3.8	
Spectrum 6	5.5	31.0	1.8	1.2	0.8	57.2	2.4	
Spectrum 7	4.4				1.2	90.7	3.7	

Figure 4-22 EDS Results by % Weight for Areas of Interest on Tooth Deddendum of Worn MoST Coated Tooth

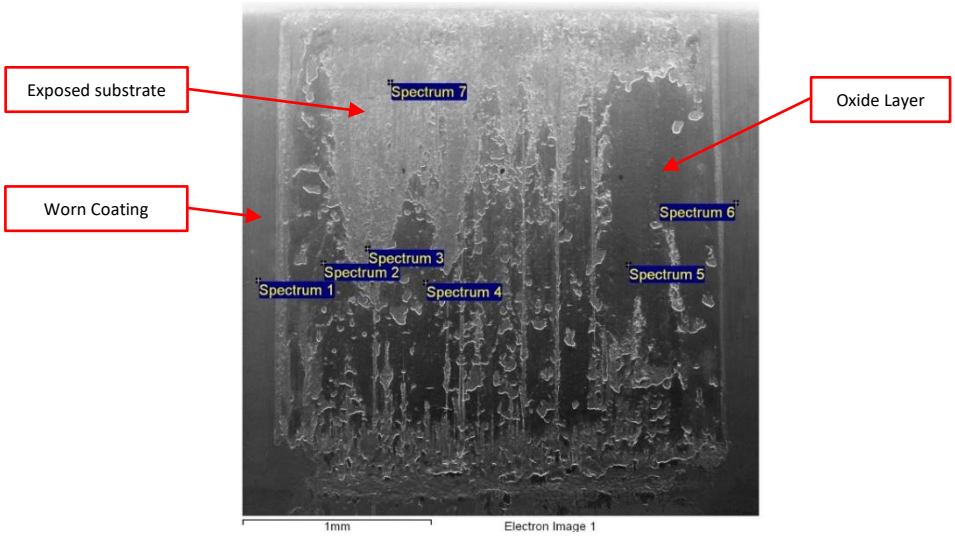

Spectrum	C	O	Si	S	Ti	Cr	Fe	Ni	Mo
Spectrum 1		5.1		16.2	8.9	0.9	46.9	1.9	20.2
Spectrum 2	4.9	28.1		0.8	0.5	0.9	62.5	2.3	
Spectrum 3	4.6		0.4			1.2	90.2	3.6	
Spectrum 4	3.7	30.6		0.3		0.9	62.2	2.4	
Spectrum 5		31.5		2.7	3.4	0.8	55.8	2.0	3.9
Spectrum 6				5.2	4.8	1.2	77.9	3.5	7.4
Spectrum 7	4.3					1.2	90.8	3.7	

Figure 4-23 EDS Results by % Weight for Areas of Interest on Tooth Adendum of Worn MoST Coated Tooth

The EDS results of the unworn coating and underlying substrate can be found in spectrum 1 of Figure 4-22, and consist of 11.7% S, 13.18% Mo, 5.05% Ti, 66.27% Fe, and trace amounts of Ni and Cr. In the heavily worn dedendum of the tooth the coating had been completely removed. The exposed substrate was smooth but occasionally scored in the direction of sliding. No S, Mo, or Ti was detected (see spectra 3 and 5 of Figure 4-22). The edge of the coating at the SAP appeared to be peeling from the surface, and an accumulation of fine oxide debris was present (see spectrum 2). Further up the tooth towards the pitch circle, larger oxide particles were embedded in the surface (see spectrum 6). The EDS spectra for both types of oxide debris showed minimal presence of S or Ti (<2%) and no Mo was present, hence it is concluded that both are iron oxides. The visual appearance of the two types of oxide debris differed. The fine debris in the root and around the contact edges had the typical red/brown colouration of Fe_2O_3, whilst the larger embedded particles appeared black and more typical of harder [260] Fe_3O_4.

The damaged area on addendum, the measurements of which had indicated growth, was coated in patches by a smooth oxide layer that appeared to be well adhered to the surface. O content was 28%-32% with little or no (<4%) Mo, S, or Ti (see spectra 2,4, and 5 of Figure 4-23). Whilst the oxide did not exhibit any evidence of cracking or spalling, it was penetrated by scratches in the direction of sliding and pits, which were ~100µm in size. Areas within the damaged region that were not coated with oxide were found to be bare, unoxidized substrate with >90% Fe.

The Raman spectra for the as deposited and partially worn MoST coating are shown in Figure 4-24 and Figure 4-25. The as-deposited coating exhibited only two significant peaks at 375cm^{-1} and 402cm^{-1}, corresponding to E^1_{2g} (in-plane vibration of the Mo and S atoms) and A^1_g (out-of-plane vibration of S atoms) modes respectively [261], and consistent with other studies of sputtered MoS_2 films [262].

The spectra for partially worn coating showed only a single smaller, broader peak close to 400cm^{-1}, and were instead dominated by a strong peak at 670cm^{-1}, with a minority of samples also showing an additional peak at 1320cm^{-1}. The strong peak at 670cm^{-1} is characteristic of Fe_3O_4, whilst the peak at 1320cm^{-1} is observed in Raman spectra for α-Fe_2O_3. Whilst γ-Fe_2O_3 can display bands in the both regions, a further strong peak at ~720cm^{-1} forms a doublet with the peak at ~670cm^{-1}, which was not present on any sample. Most worn samples also only displayed the peak at 670cm^{-1}, with no peak in the 1320cm^{-1} region. Consequently, the most likely explanation is that the oxides formed are primarily Fe_3O_4, with a smaller quantity of α-Fe_2O_3 [263]. None of the characteristic wavenumbers of MO_3 (820cm^{-1}) [264], or rutile (445cm^{-1}, 610cm^{-1}) or anatase (380cm^{-1}, 500cm^{-1}, 620cm^{-1}) TiO_2 [265] were observed.

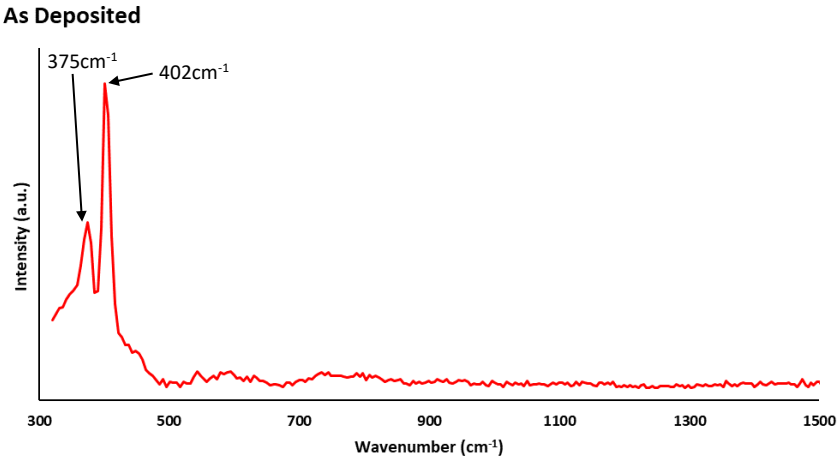

Figure 4-24: Raman Spectrum for As-Deposited MoST (532nm excitation)

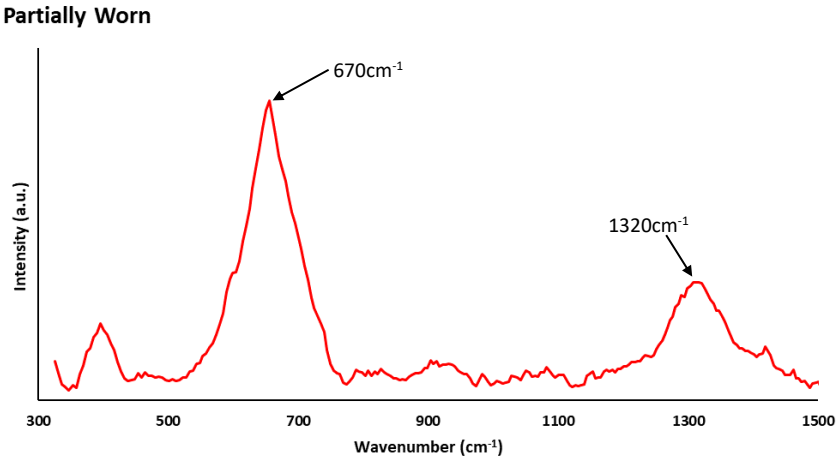

Figure 4-25 Raman Spectrum for Partially Worn MoST (532nm excitation)

4.4.1.2 WSC

During the initial 100 test cycles of the WSC-coated gears, most teeth developed a broad region of wear up to 1.75µm in depth, stretching from the SAP to the mid-dedendum. A number of teeth also suffered from irregular damage around the edges of the teeth, which appeared to be due to delamination, producing a speckled appearance. However, the wear to the other areas of the teeth was minimal. The contact area was darker in colour than unworn regions of the teeth, with the exception of the region around the pitch circle, which was lighter and less reflective.

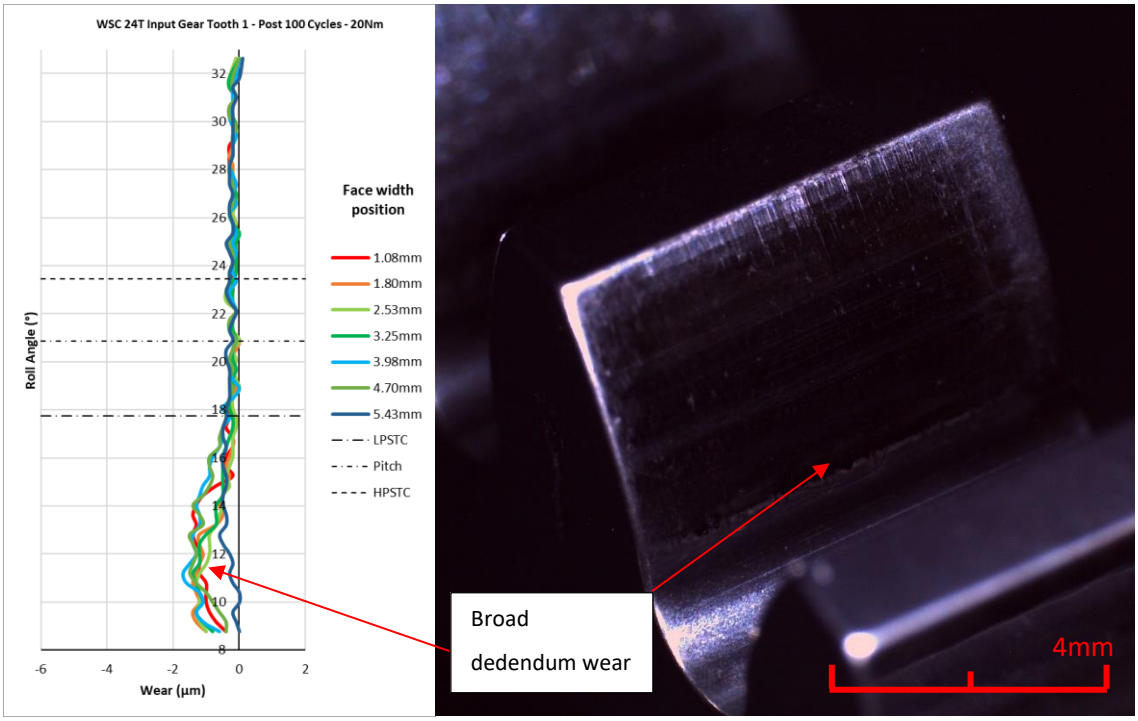

Figure 4-26: Wear Map and Image of WSC-Coated 24T Input Gear Tooth (Driving Gear) after 100 Cycles at 20Nm

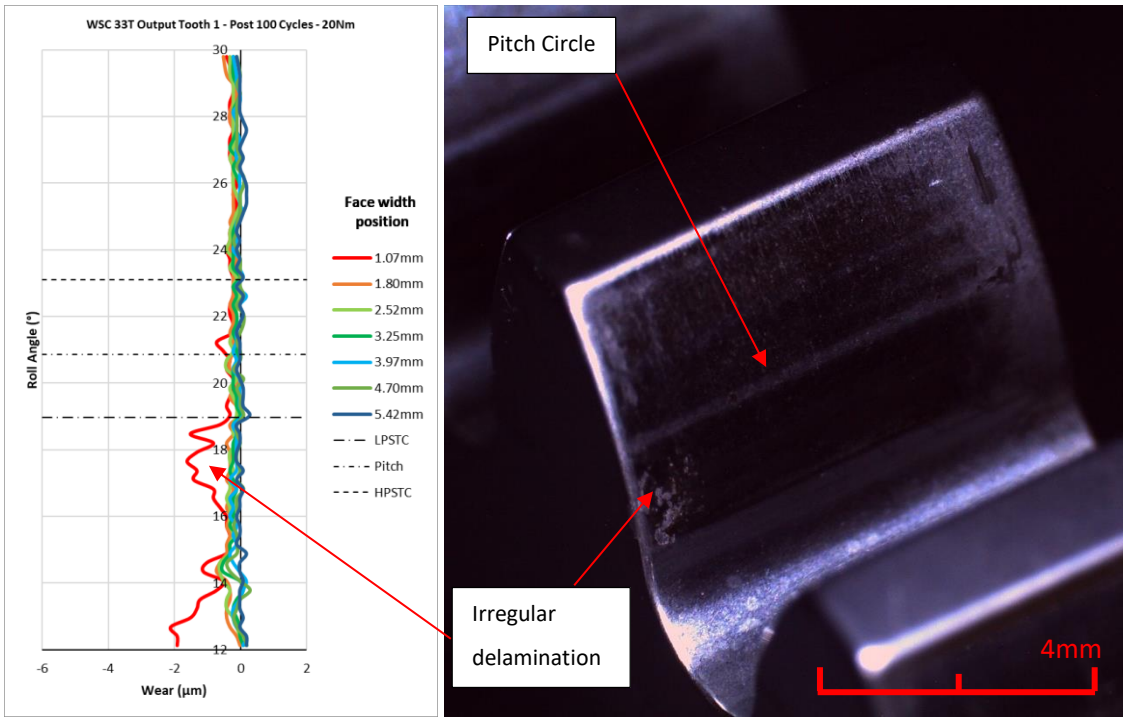

Figure 4-27: Wear Map and Image of WSC-Coated 33T Input Gear Tooth (Driving Gear) after 100 Cycles at 20Nm

With further cycling the condition of the input and output meshes of the gearbox began to diverge. Both sets of teeth for the output mesh experienced a broadening of initial wear to the dedendum with little increase in depth, which rarely exceeded 2µm. Wear to the addendum was very limited (<1µm), with the depth increasing towards the tips.

In comparison, the 33-tooth gear of the input mesh suffered from rapid wearing of the addendum (see Figure 4-28), with one tooth exhibiting signs of substrate oxidation and coating breakthrough after only 500 cycles. The 24-tooth gear, which acts as the driver, subsequently developed heavy wear (4µm) in the dedendum corresponding to the same position in mesh cycle (see Figure 4-29), whilst wear on the addendum remained minimal. After 1500 cycles all monitored teeth in the input mesh showed evidence of coating breakthrough and the test was terminated.

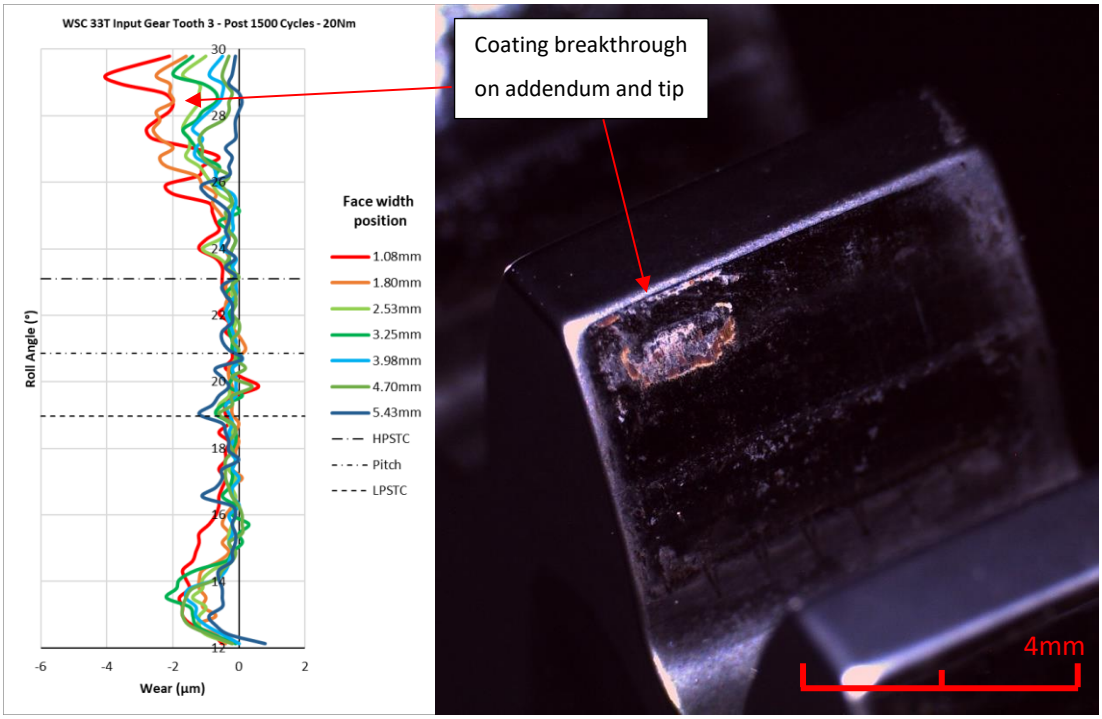

Figure 4-28: Wear Map and Image of WSC-Coated 33T Input Gear Tooth (Driven Gear) after 1500 Cycles at 20Nm

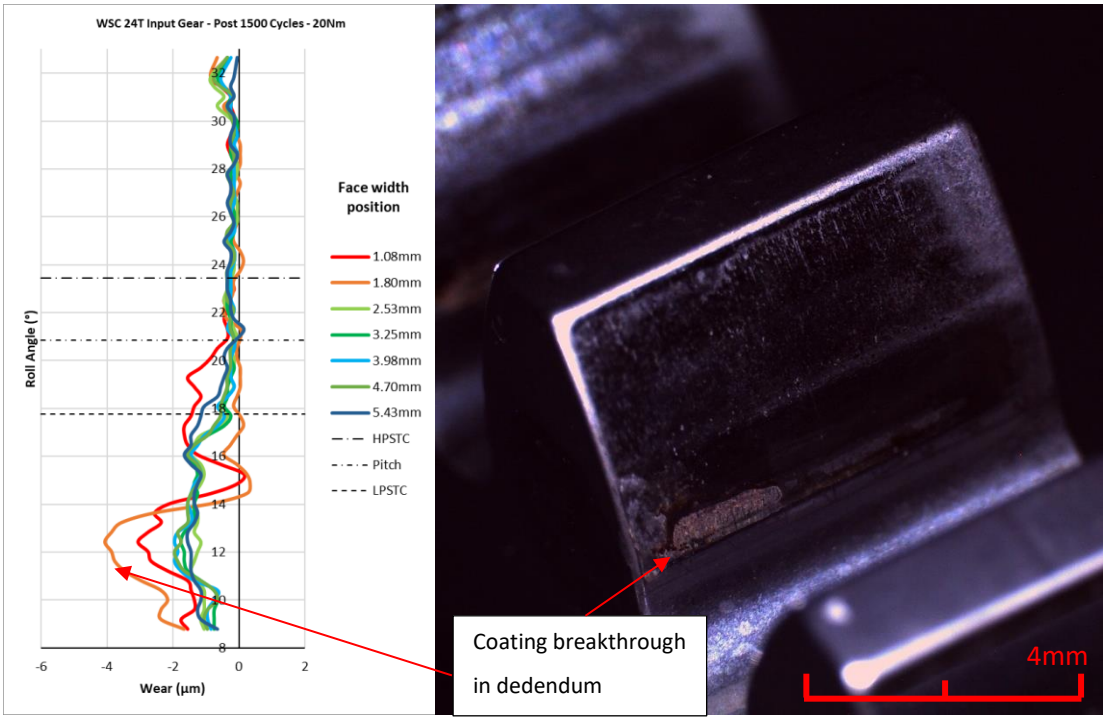

Figure 4-29: Wear Map and Image of WSC-Coated 24T Input Gear Tooth (Driving Gear) after 1500 Cycles at 20Nm

Figure 4-30 displays an example of the correlation between the model output and measurement data for a tooth pair in the input mesh. The measured wear exceeds the prediction in the region of failure on the addendum and tips on the 33-tooth gear, and the corresponding point on the dedendum of the 24-tooth driver. By comparison the wear to the addendum of the driver is negligible. This indicates a locally higher wear rate at the point of tooth engagement of the mesh cycle, which may be a consequence of the loss of lubricity following the initial breakthrough of the coating on the gear addendum. Wear rates to achieve best fit between the measurements and model ranged from 9.04E-11 to 1.30E-10mm^3/N.mm.

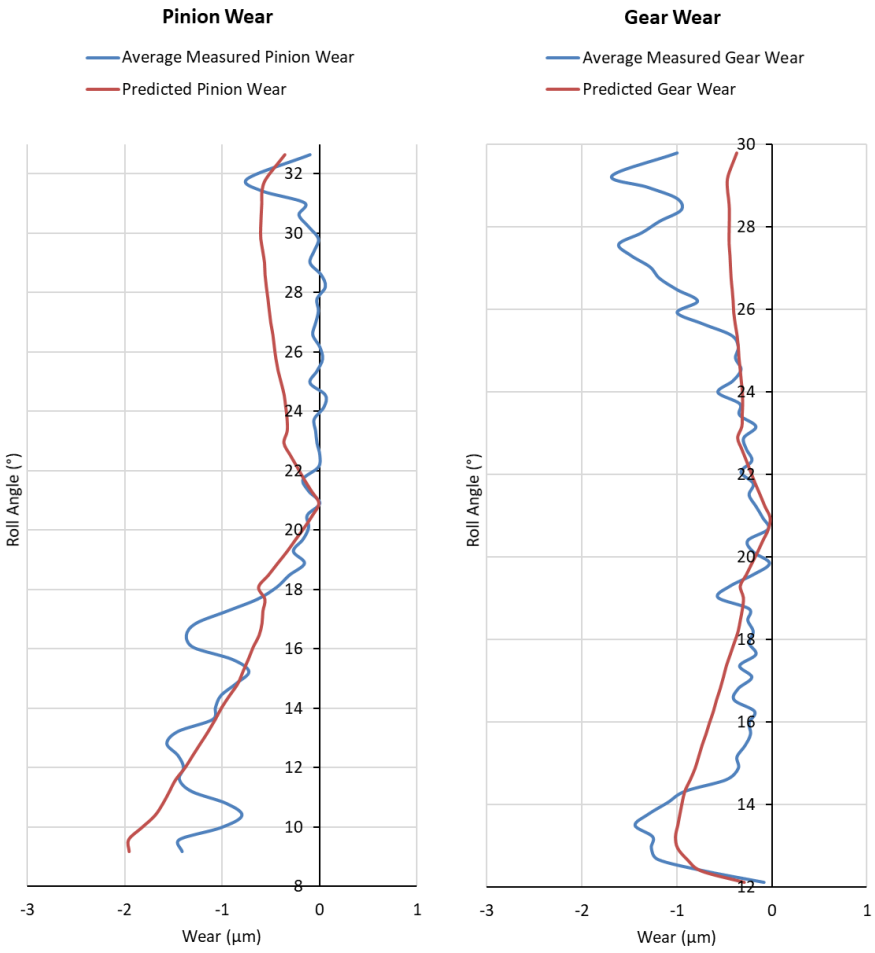

Figure 4-30: Comparison of Predicted and Measured Wear for WSC Coated Teeth (Wear Rate = 1.10E-10 $mm^3/N.mm$)

Figure 4-31 shows comparative images of one of the failed teeth from the input mesh using an optical microscope, and SEM using secondary and backscatter electron detectors. When using the backscatter detector, a significant contrast was obtained between the coating and exposed substrate due to the difference in atomic number. Due to the subsurface emission of backscattered electrons, the images display more heavily worn areas of the tooth with a darker shade. Figure 4-32 shows secondary and backscatter electron images of the worn regions on the addendum and dedendum, in addition to a delaminated region from the side of the tooth face. Figure 4-33 and Figure 4-34 show the EDS results in % weight.

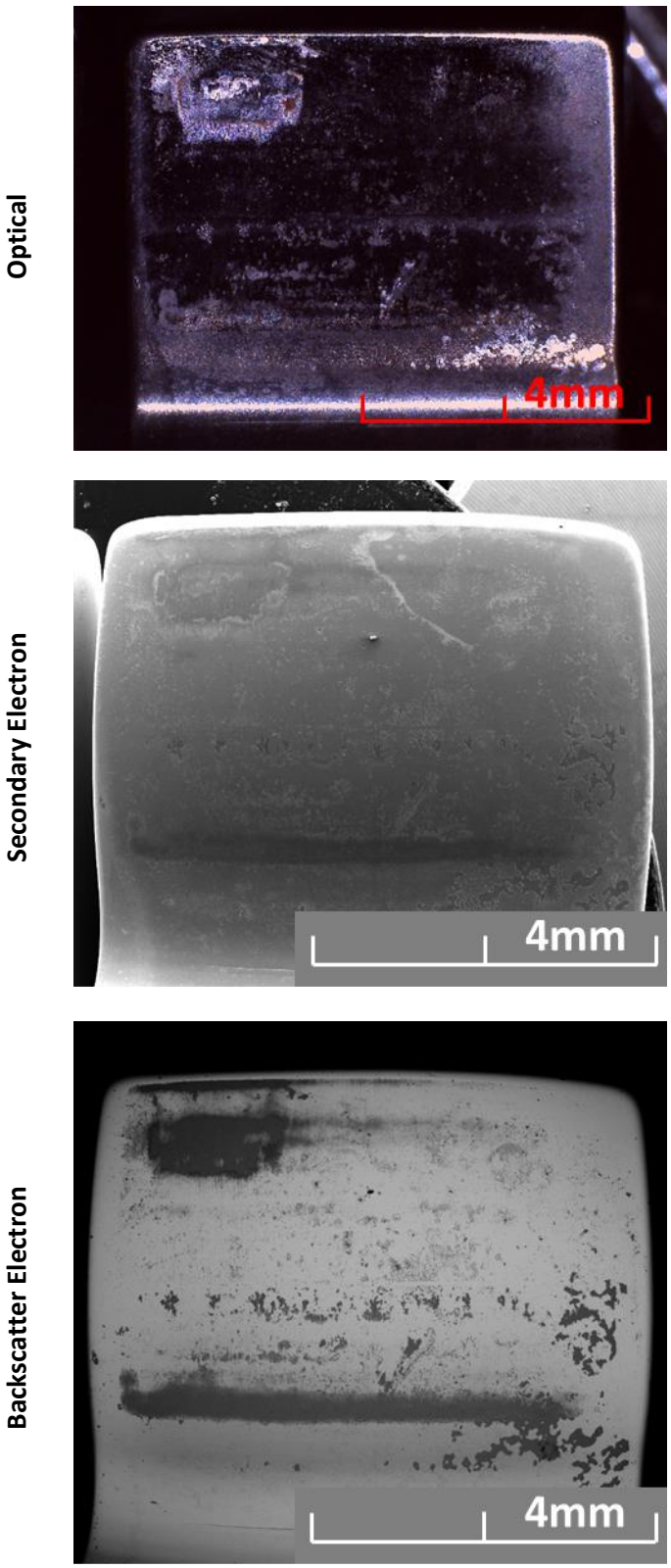

Figure 4-31 Optical, Secondary, and Backscatter Electron SEM Images of WSC-Coated Tooth after 1500 Cycles at 20Nm

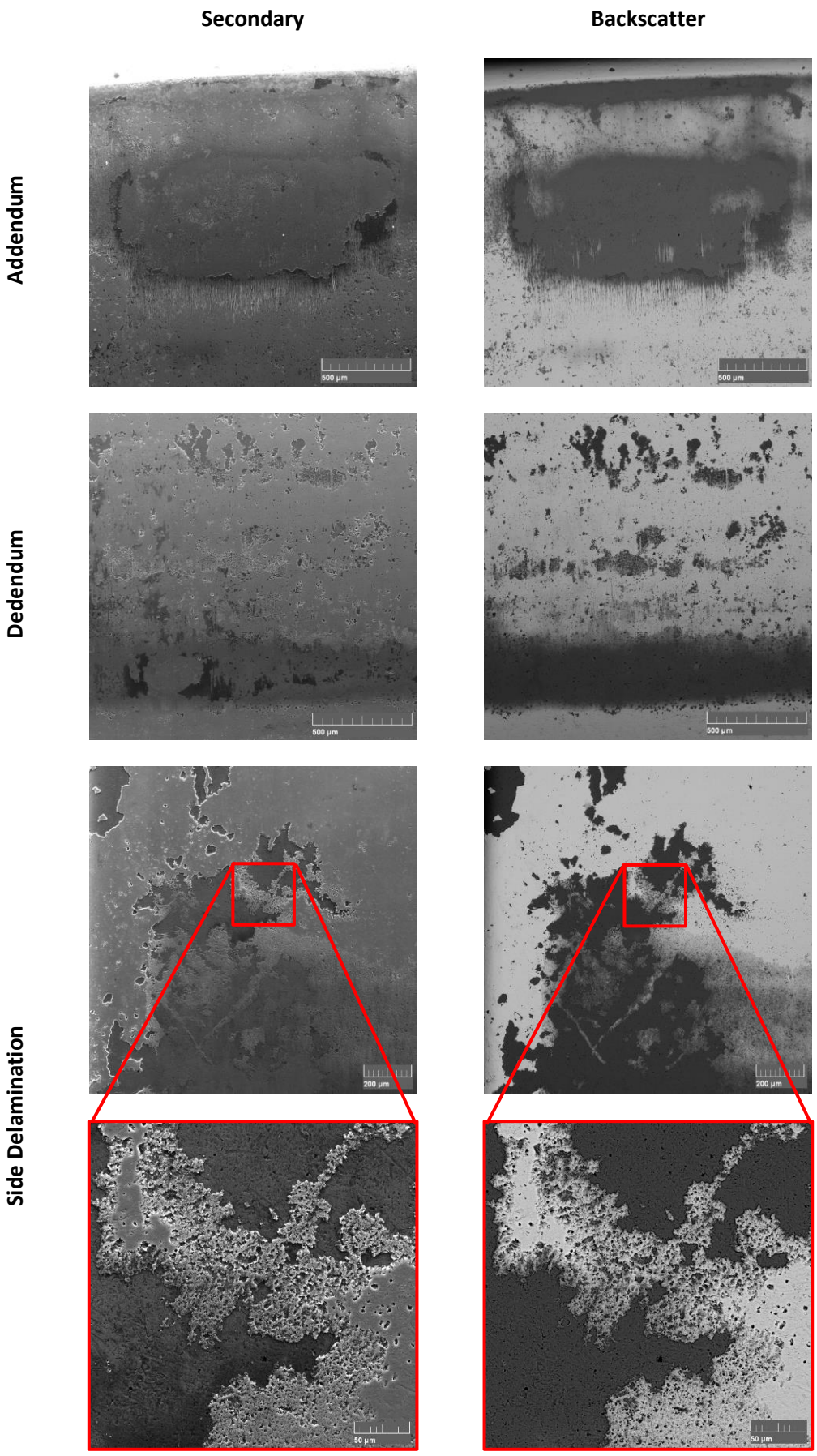

Figure 4-32 Backscatter and Secondary Electron SEM Images of Wear on WSC-Coated Tooth after 1500 Cycles at 20Nm

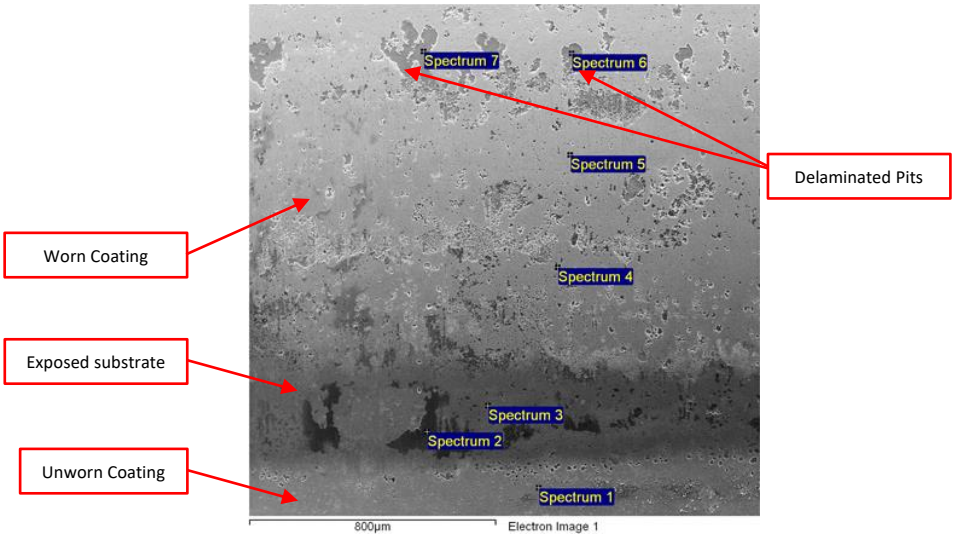

Spectrum	C	O	S	Cr	Fe	Ni	W
Spectrum 1	14.6	1.4	15.3	6.2	31.8	1.3	29.5
Spectrum 2	12.3	9.4	0.7	4.7	66.5	3.0	3.5
Spectrum 3	6.8	3.0	0.8	7.7	77.4	3.4	0.9
Spectrum 4	19.0		16.7	6.5	24.9	1.0	31.9
Spectrum 5	18.6		18.3	6.2	19.4	0.8	36.8
Spectrum 6	9.6	4.2	0.9	7.9	72.9	3.2	1.3
Spectrum 7	8.4	3.1	0.9	10.4	73.1	3.0	1.1

Figure 4-33 EDS Results by % Weight for Areas of Interest on Tooth Dedendum of Worn WSC Coated Tooth

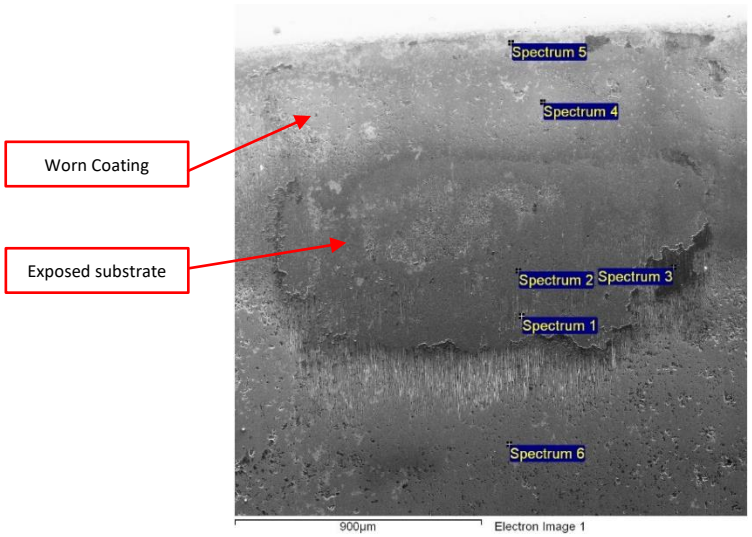

Spectrum	C	O	S	Cr	Fe	Ni	W
Spectrum 1	16.0		8.9	14.6	41.5	1.6	17.4
Spectrum 2	6.5	3.1		6.8	80.3	3.4	
Spectrum 3	8.7	19.5	0.7	9.8	55.5	2.2	3.8
Spectrum 4	18.6	2.1	13.6	11.8	23.6	0.9	29.5
Spectrum 5	6.8		2.6	1.4	85.0	4.3	
Spectrum 6	21.0	7.0	16.6	6.6	13.9	0.7	34.4

Figure 4-34 EDS Results by % Weight for Areas of Interest on Tooth Addendum of Worn WSC Coated Tooth

When inspected optically, the active regions of the teeth were found to have an inconsistent appearance with mottled, frosted patches and streaks of varying size scattered over the surface. These were often particularly concentrated in a line stretching over the region of high contact stress, just below the pitch circle at the lowest point of single tooth contact (LPSTC). Backscatter electron imagery showed that these regions consisted of either large numbers of very small voids of varying density, or large singular delaminated pits. In both cases the coating had been removed, exposing the substrate. In areas where small voids were concentrated this gave the surface a porous appearance. Many larger delaminated regions were found below the SAP, completely outside of the contact zone.

The large areas of heavy wear on the addendum also appeared to have resulted in complete exposure of the substrate, though some small patches of intact coating were found with the boundaries of the failure. The extremities of these areas were smoothly blended into the surrounding coating, with the edges of the coating not being clearly visible. A thick red-brown oxide layer was found to have formed close to the fringes but was absent from the centre. The very low W content in the oxide layers (see spectrum 3, Figure 4-34) and the red-brown colouration indicate the formation of Fe_2O_3. The boundary of the failed region corresponding to the contact exit was often visibly abraded, possibly due to coating debris being dragged through by the sliding action of the teeth.

Regions of high wear in the dedendum were similarly blended into the surrounding coating, with the coating edges not being visible. Whilst this area did exhibit a red-brown hue, no large oxide patches were initially observed with the optical microscope. However, the secondary electron images and EDS did reveal some oxidised regions (see spectrum 2, Figure 4-33). The O content of these layers were much lower than the layers on the addendum: 9% compared to 19%. This may indicate that the oxide layers in the dedendum were thinner.

When assessing the EDS results, it was noted that outside of the regions of heavy wear there was no significant difference in composition relative to the unworn coating. Spectrum 1 of Figure 4-33 was taken below the SAP and can be used as a reference. This indicated 15% C, 15% S, and 30% W, with the substrate contributing 32% Fe, 6% Cr, and 1-2% Ni. Regions of partially worn coating only differed significantly in the amount of C content, which was typically 4-6% higher at the expense of Fe. Due to the limited penetration depth of the electron beam, wearing of the coating would be expected to result in an increase in the detection of Fe and alloying elements in the substrate. The fact that the detected C content increased, with the Fe content decreasing, may indicate the formation of a C-rich transfer film on the surface. Moreover, the general lack of

change in the EDS spectra between regions of intact but active coating and the as-deposited coating agrees with the dimensional measurements: the coating either experienced minimal wear or complete failure. However, only at the very centre of the failed regions on the addendum (spectrum 2, Figure 4-34) was there no detectable W or S. Even in the bottom of the pits left by delamination some traces of the coating were detected.

The Raman spectra for the as deposited and partially worn coating are shown in Figure 4-37 and Figure 4-38. The as deposited coating spectrum exhibits a sharp shouldered peak at 426cm^{-1}, and a broad response over the range 1000cm^{-1} to 1700 cm^{-1}. Much like MoS_2, the Raman spectra for WS_2 largely consist of peaks corresponding to E^1_{2g} and A^1_g and are typically found at ~355cm^{-1} and ~420cm^{-1} respectively. Splitting of the A^1_g peak to form an A^*_g shoulder can occur depending on the extent of the stacking of WS_2 layers and the excitation wavelength. The A^1_g peak and associated A^*_g shoulder are clearly present in the spectrum of the deposited coating as a result of the WS_2 content. However, there was no response corresponding to the E^1_{2g} in any of the samples.

Raman spectra of disordered C are dominated by two bands [267]. The E_{2g} or "G" (graphite) band is attributed to in-plane stretching of pairs of C atoms and can be found between 1500cm^{-1} to 1600cm^{-1}. The A_{1g} or "D" (disorder) band is found around 1335 cm^{-1} and is caused by breathing of sp^2 rings. In disordered C these peaks can be very broad and deconvolution of the spectrum into multiple gaussian peaks is used to determine the relative intensities and positions. Due to additional minor modulations a four or five curve fit is usually required to achieve satisfactory fitment. Figure 4-37 shows the deconvolution of the as deposited coating over the 1000cm^{-1} to 1700 cm^{-1} range. The G band was located at 1558cm^{-1}, with the D band being found at 1331cm^{-1}. However, the extent of the additional modulations in this case made precise determination of the D band position and intensity difficult.

For the partially worn coating, the peak corresponding to the A^1_g mode of the WS_2 was greatly diminished and was no longer visible on a number of samples. Unlike the partially worn MoST there was no evidence of any surface oxides.

When using Raman spectroscopy to determine structural changes in C coatings a number of techniques are used. Ferrari [267] proposed a three-stage model, in which structure of C films can understood by considering the G band position and the ratio of the D and G band intensities (I_D/I_G ratio). Whilst the uncertainty regarding the precise position and intensity of the D prevented the use of I_D/I_G ratio, the G band position for the samples of partially worn coating was found to have increased to 1577cm^{-1}. As the sp^2 content in a-C increases the size of sp^2 clusters also increases. The longer chains result in higher vibrational frequencies. The worn coating's increase in G peak

wavenumber therefore indicates that the wear process has caused a conversion of sp^3 bonding to sp^2, and a transition towards a nanocrystalline graphite structure. Furthermore, the observed separation of the G and D band into more distinct peaks is consistent with the observations of Erdemir [186], who noted similar characteristics in the Raman spectra of DLC transfer films in his experiments, refer back to Figure 2-62.

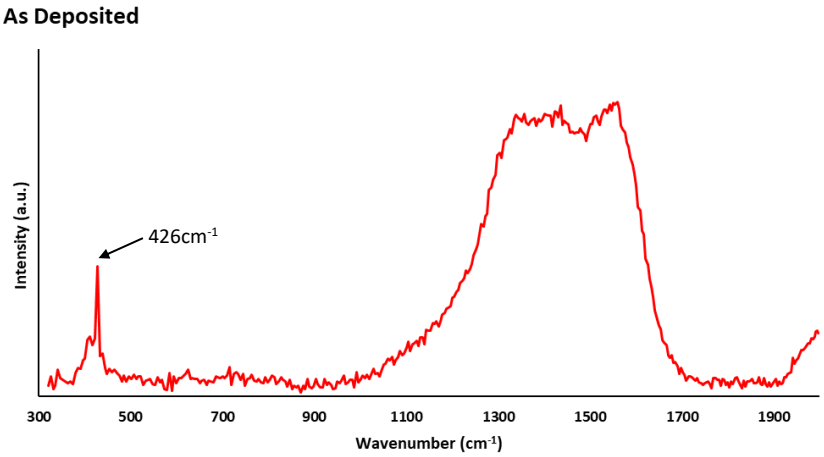

Figure 4-35: Raman Spectrum for As-Deposited WSC (532nm excitation)

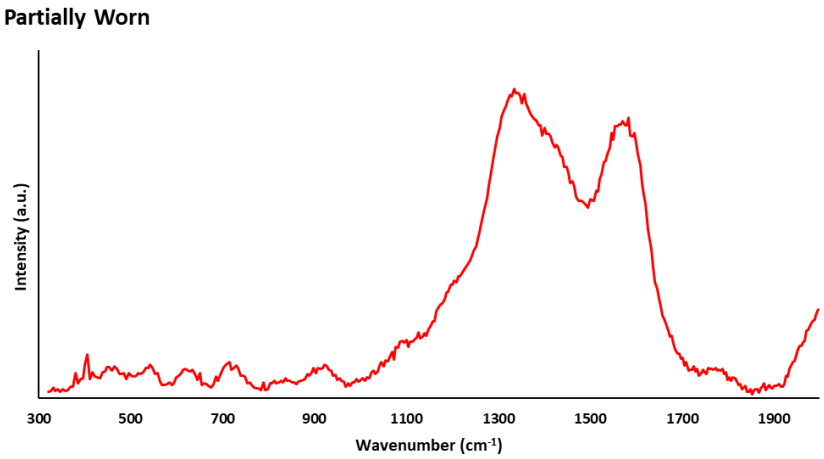

Figure 4-36: Raman Spectrum for Partially Worn WSC (532nm excitation)

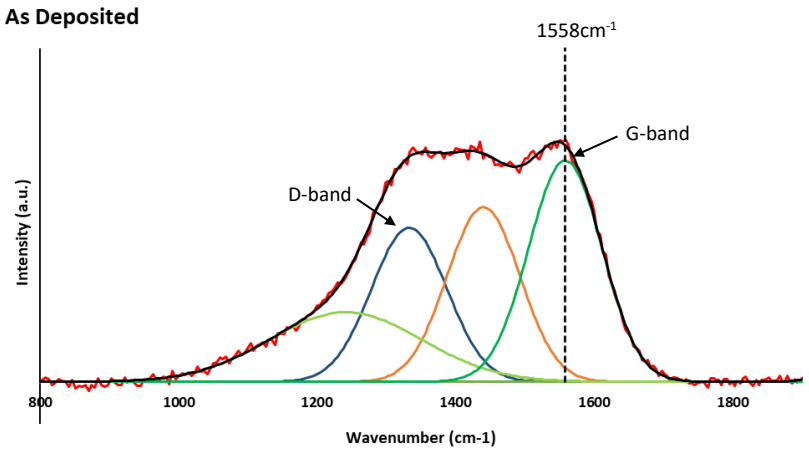

Figure 4-37 Deconvoluted Raman Spectrum for As-Deposited WSC (532nm excitation)

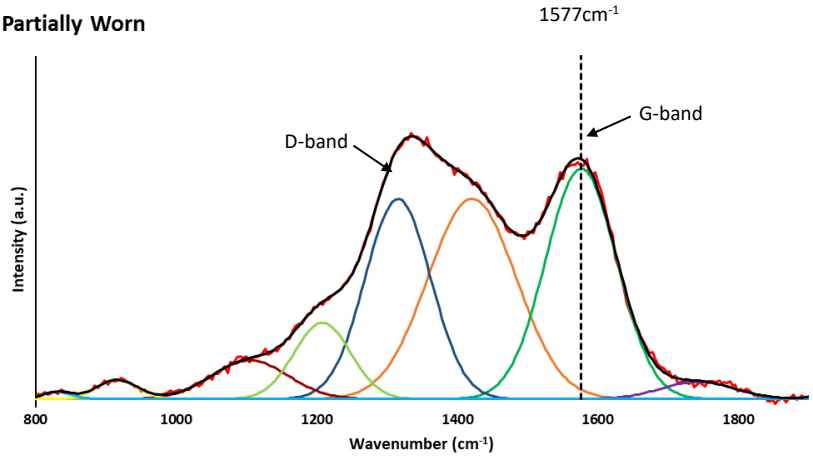

Figure 4-38 Deconvoluted Raman Spectrum for Partially Worn WSC (532nm excitation)

4.4.1.3 Graphit-iC

During wear testing the first 100 to 500 test cycles resulted in localised wear ~1.5µm in depth around the SAP. However, during subsequent cycling this localised wear deepened very slowly and remained bright and reflective. The overall contact area was clearly visible as a darker and more reflective region when compared with the as-deposited coating. A line of unworn, unreflective coating was visible at the pitch circle.

With further operation most samples began to display the wear pattern predicted by the model. Wear at the pitch circle was negligible, whilst in the dedendum the wear was deeper with increasing distance from the pitch circle, eventually blending with the band of initial wear at the

SAP, which had broadened both across the face width and up the profile. On the addendum the wear tended to be highest approximately midway between pitch circle and the tips.

The wear rate of the Graphit-iC coated gears was significantly lower than the previously tested coatings. Cycling continued with no further evidence of coating failure until 5,500 cycles, when bright reflective lines, oriented across the face of the tooth, were observed on the mid-addendum. With further cycling these regions increased in size and developed a brown colouration, indicating complete removal of the coating and oxidation of the underlying substrate. Testing was terminated at 8,500 cycles, when substrate oxidation was evident on the majority of teeth.

Due to the far longer period of cycling when compared to the results for MoST and WSC, more inspections were performed, and it is possible to examine the evolution of the wear distribution during the test. See Figure 4-39.

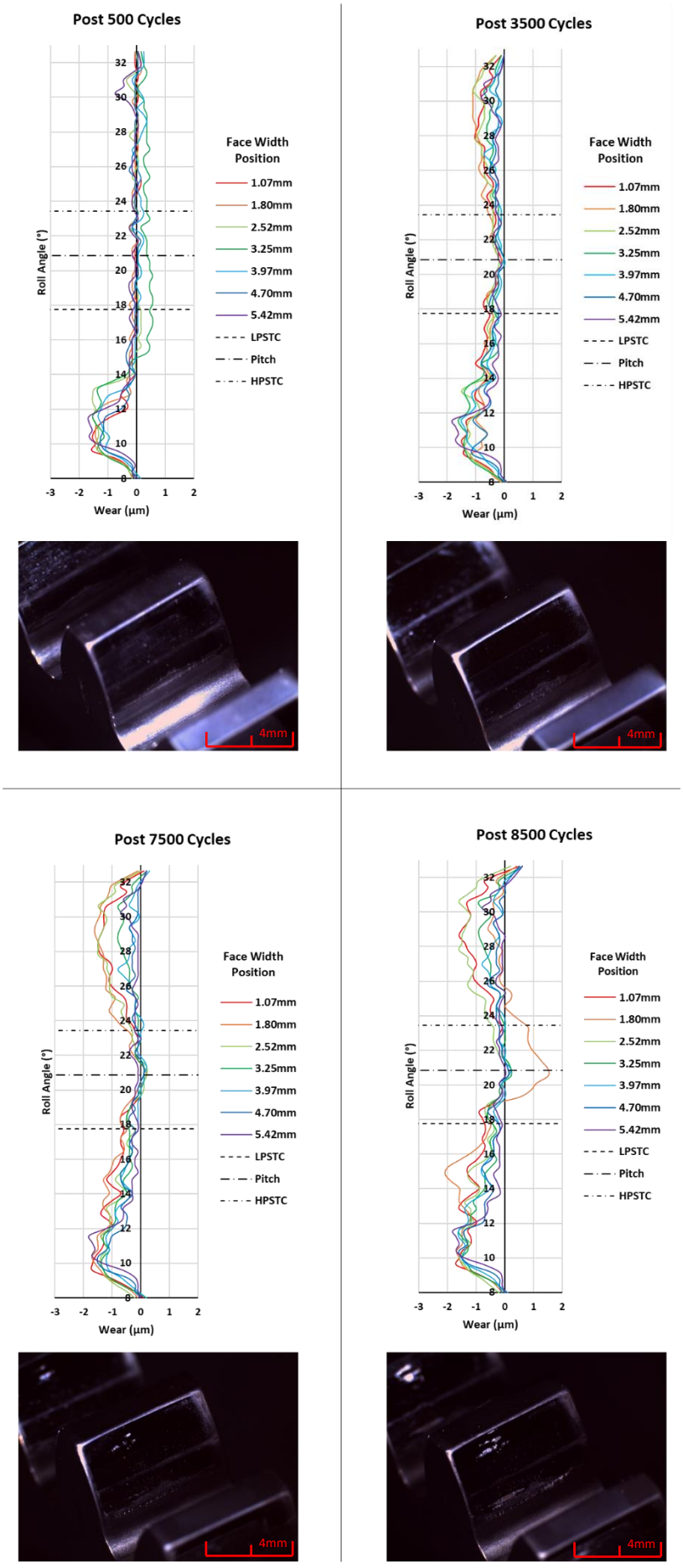

Figure 4-39: Evolution of Wear to Graphit-iC Coated Gear Tooth during Cycling at 20Nm

Figure 4-40 provides a comparison between predicted and measured wear for a typical tooth pair. The model correctly predicts the region of minimal wear at the pitch circle, with the wear depth increasing with distance towards the SAP. However, the model consistently underestimated the extent of wear to mid-addendum, where the failure of the coating was observed on the majority of teeth.

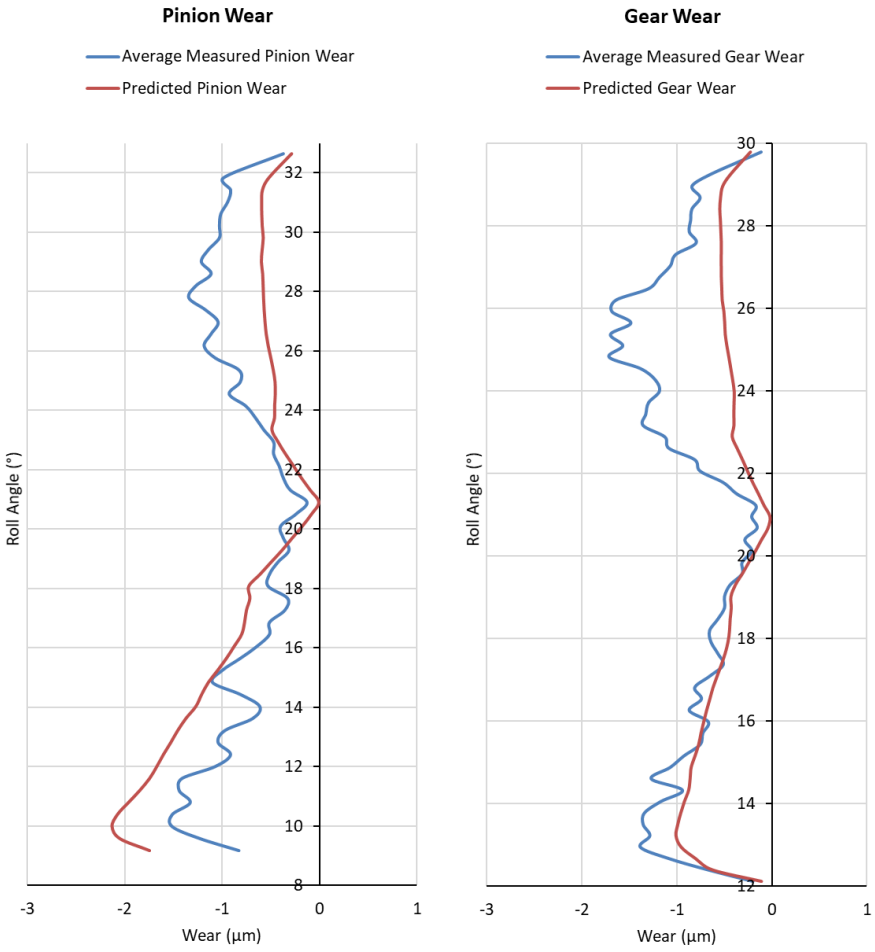

Figure 4-40: Comparison of Predicted and Measured Wear for Graphit-iC Coated Teeth (Wear Rate = 2.66E-11 $mm^3/N.mm$)

Whole tooth images from the post-test SEM and optical inspection are shown in Figure 4-41. Backscattered electron images provided sharp contrast between the coating and substrate, with the substrate being shaded brighter due to the higher atomic number. These images proved very valuable due to the change in shade generated by the reduced coating thickness of more heavily worn regions. Delaminated regions were clearly identifiable by the sharp contrast between the edges of the exposed substrate and the remaining coating, whilst regions of coating failure due to

sliding wear were marked by a far more diffuse boundary. Areas of interest from the worn regions are shown in more detail in Figure 4-42. EDS data for the damaged regions at the SAP and mid-addendum are shown in Figure 4-43 and Figure 4-44 respectively.

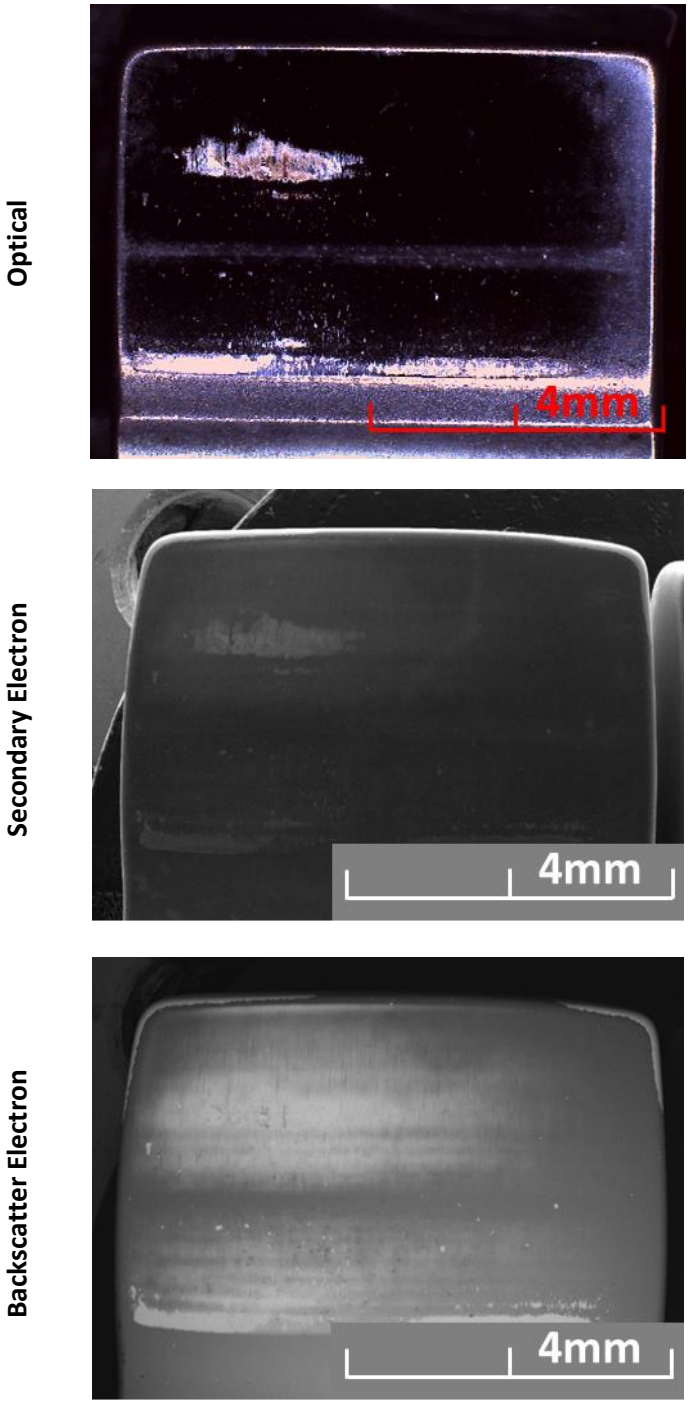

Figure 4-41: Optical, Secondary, and Backscatter Electron SEM Images of Graphit-iC Coated Tooth after 8500 Cycles at 20Nm

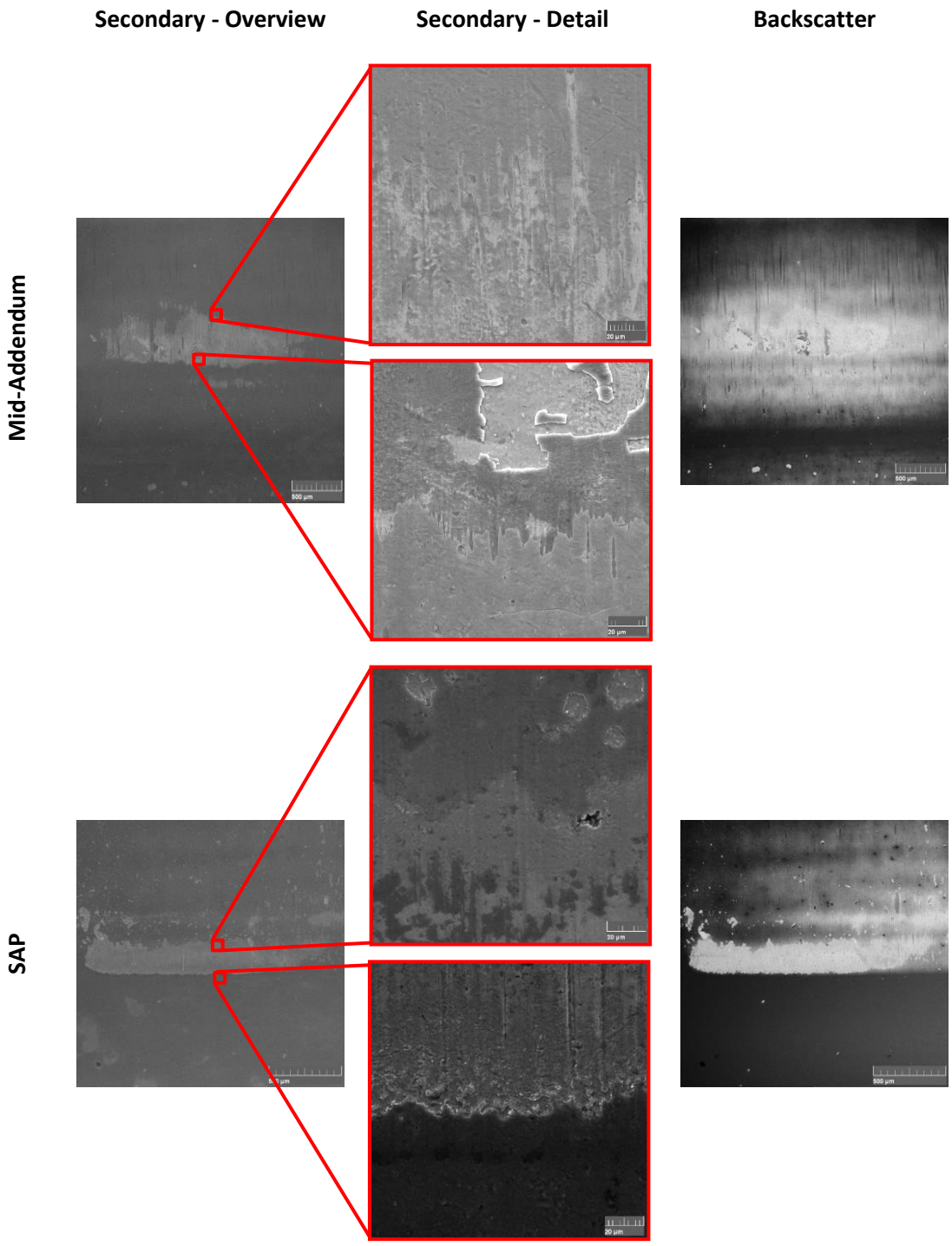

Figure 4-42: Backscatter and Secondary Electron SEM Images of Wear on Graphit-iC Coated Tooth after 8500 Cycles at 20Nm

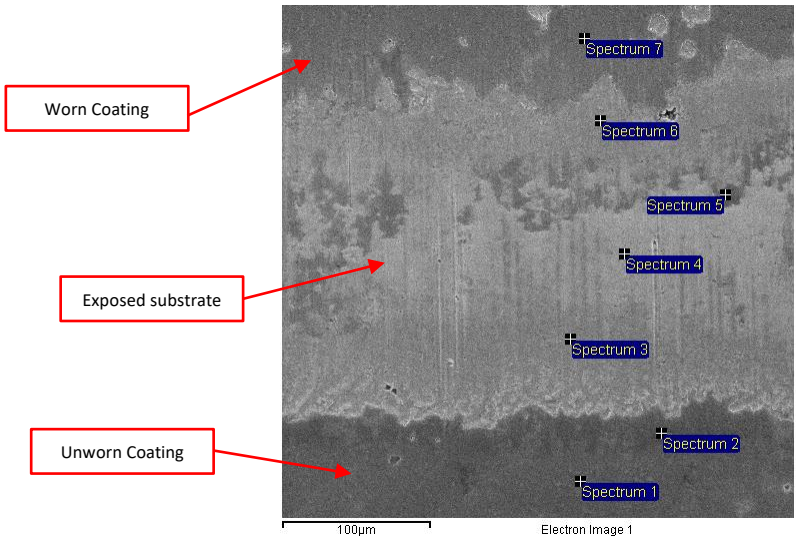

Spectrum	C	O	Ar	Cr	Fe	Ni
Spectrum 1	53.9	1.5	1.5	22.2	20.1	0.9
Spectrum 2	55.4	2.3	1.4	21.5	18.8	0.7
Spectrum 3	28.7			27.8	41.9	1.6
Spectrum 4	9.9	3.8		19.3	64.5	2.5
Spectrum 5	11.0	20.6		17.8	49.0	1.7
Spectrum 6	25.4	3.1		28.4	41.6	1.5
Spectrum 7	52.3		0.7	22.4	23.5	1.1

Figure 4-43: EDS Results by % Weight for Areas of Interest on SAP of Worn Graphit-iC Coated Tooth

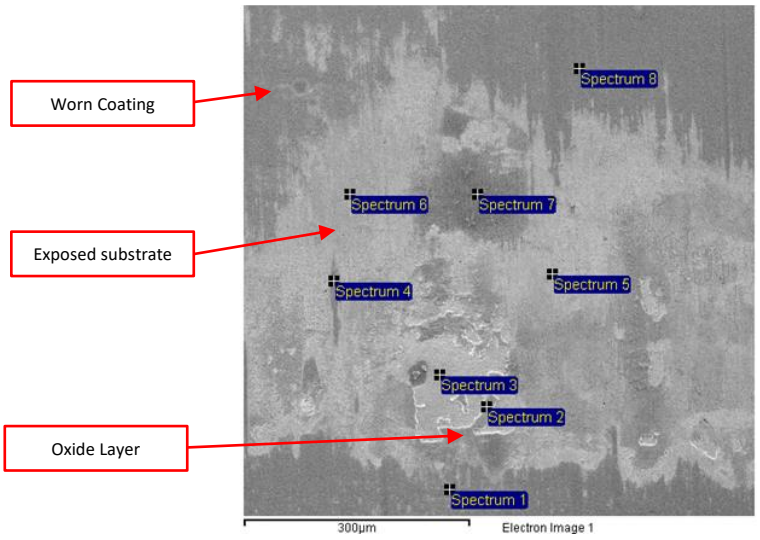

Spectrum	C	O	Ar	Cr	Fe	Ni
Spectrum 1	44.9		0.4	28.1	25.5	1.1
Spectrum 2	8.7	32.3		5.9	51.3	1.9
Spectrum 3	6.4	2.3		3.9	84.0	3.3
Spectrum 4	42.3		0.5	28.9	27.2	1.1
Spectrum 5	8.1	3.4		1.5	83.7	3.3
Spectrum 6	10.1	10.4		22.8	54.8	1.9
Spectrum 7	20.7	12.7		18.4	46.5	1.7
Spectrum 8	36.6		0.2	33.3	28.9	1.1

Figure 4-44: EDS Results by % Weight for Areas of Interest on Addendum of Worn Graphit-iC Coated Tooth

Two main regions of coating failure were generally evident: one close to the SAP, extending across the face width, and a more localised region on the mid-addendum. The coating also appeared to have delaminated in some regions around the top and side lands of the teeth, but the boundaries of these areas terminated on the tip and side radii and did not appear to encroach on the active portion of the tooth surface.

The boundaries of the region of coating damage in the SAP were mostly sharp and clearly contrasted with the intact coating further up the tooth. In places the top boundary was more irregular and diffuse and appeared to have been blended out by subsequent sliding wear, but along the entire bottom boundary the edge of the coating was clearly visible. This indicates that the initial high wear to the SAP is caused by delamination. The tooth surface just above this region was pockmarked in places with small round delaminated pits 10-20µm in diameter.

The EDS results from just below the SAP (see spectrum 1, Figure 4-43) can be used as a baseline for the as-deposited coating, and indicate 54% by weight C, 22% Cr, 20% Fe, with 1-2% O, Ar, and Ni. The presence of Ar is due to its use as a sputtering gas during deposition of the coating. Partially worn areas of the tooth showed a reduction in the detected C content, and a corresponding increase in the detected Cr and Fe due to the wear of the coating bringing more of the Cr interlayer and steel substrate within the penetration depth of the electron beam. In the failed delaminated region at the SAP the C content was greatly reduced to as little as 10%, the remaining C potentially being due to continued transfer film formation from meshing with coated regions with the mating tooth. However little change was observed in the Cr content, with all spectra indicating at least 17% Cr. This may provide an explanation for the absence of brown staining in these regions: sufficient Cr was present to protect the surface from gross oxidation. Minimal O was detected with the exception of some small patches of accumulated debris (see spectrum 7, Figure 4-43). The continued presence of significant Cr may also indicate that the apparent delamination had not occurred between the interlayer and substrate, but between the interlayer and transition layer instead.

On the region of mid-addendum coating failure both the upper and lower edges were jagged and irregular in appearance, with the peaks and troughs oriented in the direction of sliding and the edge of the coating not being visible. The brown-stained areas of the exposed substrate were covered in a thick oxide layer, which was cracked and spalling away in places. Some small patches of intact coating remained within the zone of failure and were also oriented in the direction of sliding. When using the backscatter detector there was little contrast between the edges of the exposed substrate and the intact coating, indicating a process of gradual material removal by sliding wear.

In this area the EDS continued to detect 6-11% C in all spectra. The presence of O varied significantly between 32% in regions with thick oxide layers, to as little as 2% in others. In and around the heavily oxidised regions very little C or Cr content was present: 6-9% and 1-6% respectively.

The results of Raman spectroscopy on the as-deposited and partially worn coating are shown in Figure 4-45 and Figure 4-46 respectively. The spectrum for the as-deposited coating is dominated by a broad response over the range 900cm^{-1} to 1700cm^{-1}, similar to that seen in WSC analysis and typical of a-C. In the spectrum for partially worn coating a strong shouldered peak was developed at 715cm^{-1}

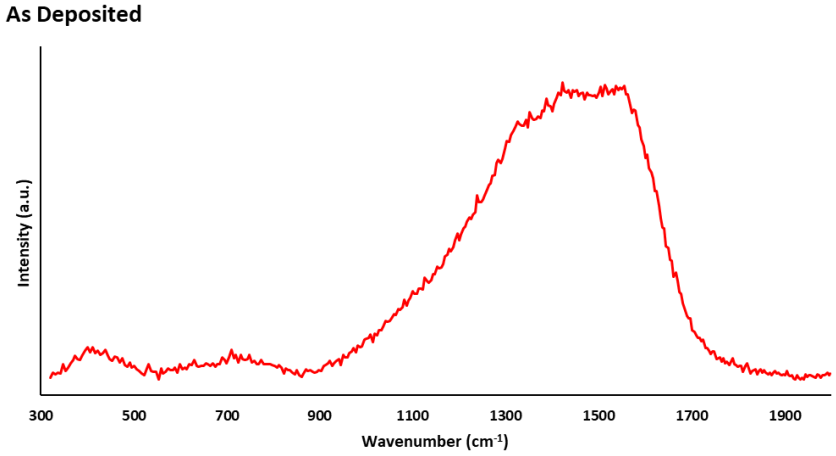

Figure 4-45: Raman Spectrum for As-Deposited Graphit-iC (532nm excitation)

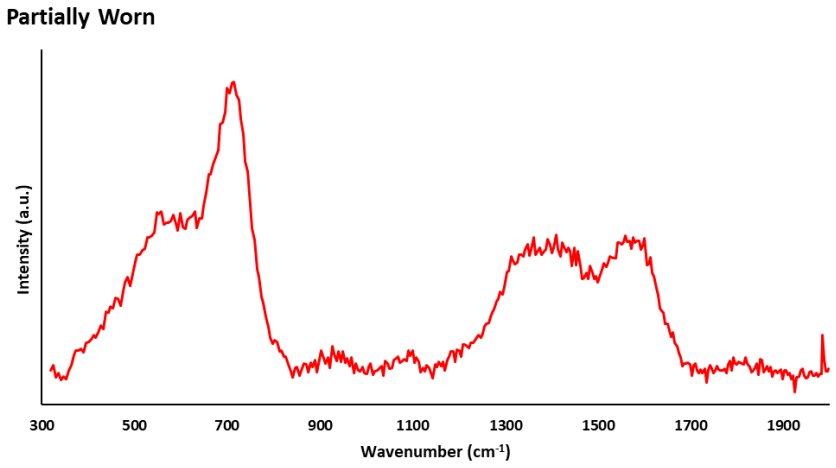

Figure 4-46: Raman Spectrum for Partially Worn Graphit-iC (532nm excitation)

The differences in the broad responses at 900cm^{-1} to 1700cm^{-1} can be further analysed through deconvolution, the results of which are shown in Figure 4-49 and Figure 4-50. Similar to the post-test spectrum for the WSC-coated teeth, the precise position and intensity of the D peak was difficult to determine accurately due the magnitude of other peaks in this region, and I_D/I_G ratio could not be calculated. However, there was a clear shift in the position of the G band from 1556cm^{-1} to 1583cm^{-1}, indicating a transition towards a more graphitic structure.

The shouldered peak at 715cm^{-1} indicates the presence of γ-Fe_2O_3 [263]. It should be noted that broad peaks around 1320cm^{-1} to 1560cm^{-1} have also been reported for γ-Fe_2O_3 in some studies [263][268]. Hence the difficulty in precisely identifying the D band (nominally found at ~1335cm^{-1}) may be due to interference from the surface oxides.

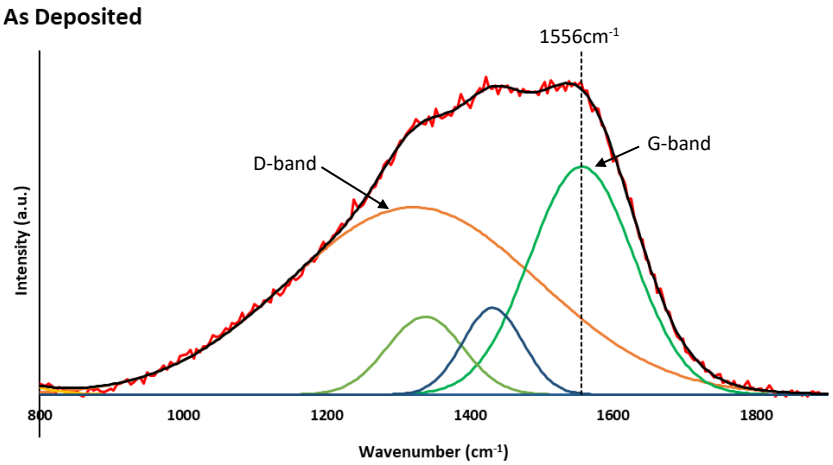

Figure 4-47 Deconvoluted Raman Spectrum for As-Deposited Graphit-iC (532nm excitation)

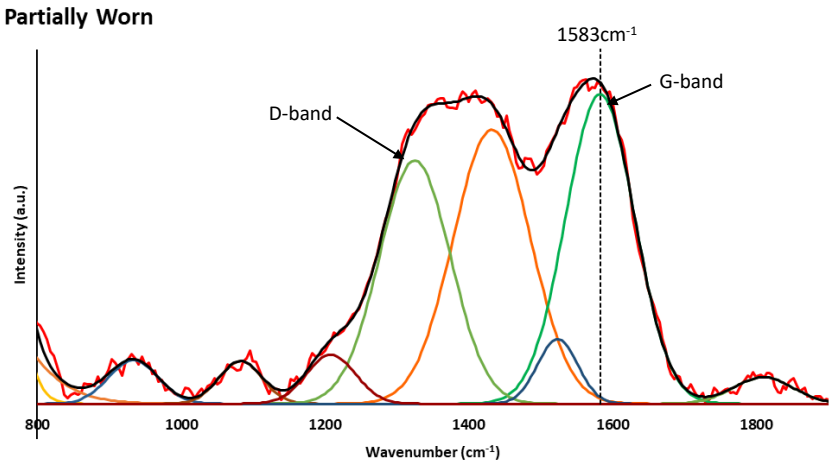

Figure 4-48 Deconvoluted Raman Spectrum for Partially Worn Graphit-iC (532nm excitation)

4.4.1.4 Comparison of Coating Performance at 20Nm

Figure 4-49 provides a comparison of the range of calculated wear rates by coating and mesh position. The trend in maximum wear depth with respect to test cycles is shown in Figure 4-50. This is calculated as the average of the maximum wear depth on each of the 12 monitored tooth surfaces in the test gearbox.

The superior performance of the Graphit-iC coating when compared to MoST or WSC is clearly evident. Following the initial heavy wear to the region around the SAP, the Graphit-iC coating then entered a long period of steady wear until the termination of the test. The initial cycling of the MoST coated gears yielded minimal wear. Whilst the initial performance was promising, the subsequent cycling resulted in very rapid wear and coating failure. The initial performance of the WSC coating was in many ways similar to that of Graphit-iC, with the initial cycling resulting in wear around the SAP, which then seemed to be beginning to stabilise, albeit more slowly. However, due to the inconsistency in performance some teeth suffered from destructive wear, resulting in test termination.

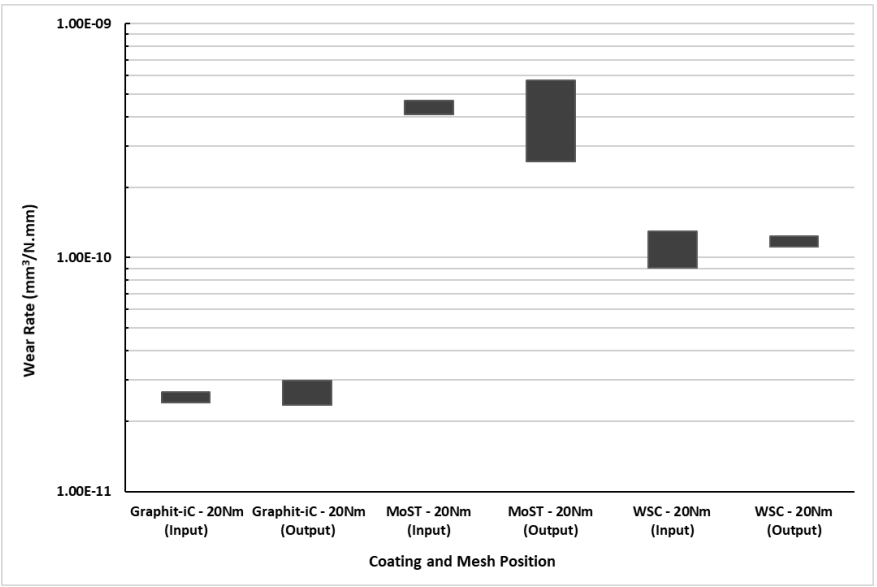

Figure 4-49: Comparison of Calculated Wear Rate Ranges by Coating and Mesh Position

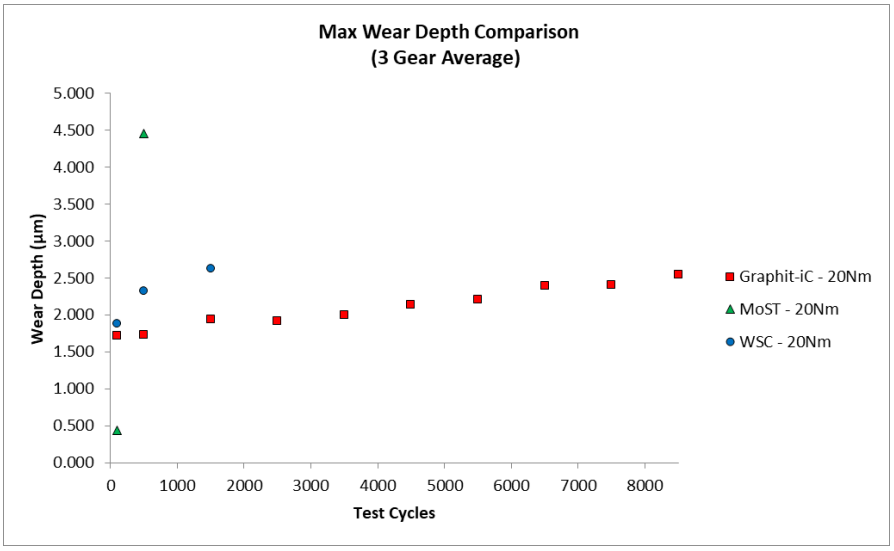

Figure 4-50: Comparison of Maximum Wear Depth (3 gear average) vs. Test Cycles

4.4.2 Additional Graphit-iC Tests

As the performance of Graphit-iC was clearly superior to that of both MoST and WSC, a further set of samples were coated to study the effects of variation in the applied torque load. Tests were performed at torque loads of 10Nm and 30Nm. One set of samples was set aside for use in the efficiency tests reported in section 4.7. To check for consistency between the two batches, the layer thicknesses, hardness, and friction coefficients for the two batches were checked and compared.

The comparative tests were performed on 30mm M42 coupons loaded into the chamber during deposition of the coating onto the gears. Friction measurements were taken using a TCL Pin-on-Disc test machine using a 5mm diameter WC/6 wt % Co ball, loaded to 40N with a linear rubbing speed of 200mm/s. Hardness was measured using Fischerscope HM2000 microhardness tester in accordance with DIN EN ISO 14577-1,2,3, with a maximum test load of 50mN. The layer thicknesses were measured following ASTM E1182-93. A 30mm ball was rotated against the sample using a diamond paste. The resulting section through the coating was inspected optically to determine the layer thicknesses.

The results are reported in Table 4-4. The layer thicknesses were very consistent, but there were some slight differences in the measured friction coefficient and hardness, owing to the different erosion state of the sputtering targets.

Table 4-4: Comparison of Coating Properties between Graphit-iC Coated Sample Batches

Tests	Cr Interlayer thickness (µm)	Cr/Carbon layer thickness (µm)	Total thickness (µm)	Friction coefficient	Hardness, (kg/mm^2)
20Nm	0.8µm	2.8µm	3.6µm	0.09	1643
10Nm, 20Nm, Efficiency	0.8µm	2.9µm	3.7µm	0.06	1348

4.4.2.1 Wear Test of Graphit-iC at 10Nm

During the tests at the reduced torque load of 10Nm the first 100-500 cycles resulted in localised wear at the SAP, similar to the tests at 20Nm. However, the depth and width of the worn area was reduced, with the maximum depth being 1.5µm and some teeth showing virtually no wear at all. With further cycling there was little change in the wear at the SAP, and the wear at the pitch circle remained negligible. The wear began to develop above and below the pitch circle, with the highest wear depths being found on the mid-addendum, and either at the SAP or just below the LPSTC dependent on the magnitude of the initial SAP wear.

The first signs of coating breakthrough were observed on the mid-addenda of the teeth of the 33-tooth output gears after 6500 cycles. Again, this was evident as bright reflective lines oriented across the face. However, the gears continued to cycle without any evidence of brown staining until 12500 cycles, at which point the test was terminated. Figure 4-51 shows the evolution of wear to one of the failed teeth from the output side of the 33-tooth idler gear.

Figure 4-52 shows a comparison between the measurement data and fitted curve from the rolling/sliding cylinder model. The most significant deviations between the model and data are found in highly worn region on the mid-addendum of the 24 tooth output gear, in which the test produced significantly more wear, and at the SAP, where the wear was actually lower than anticipated.

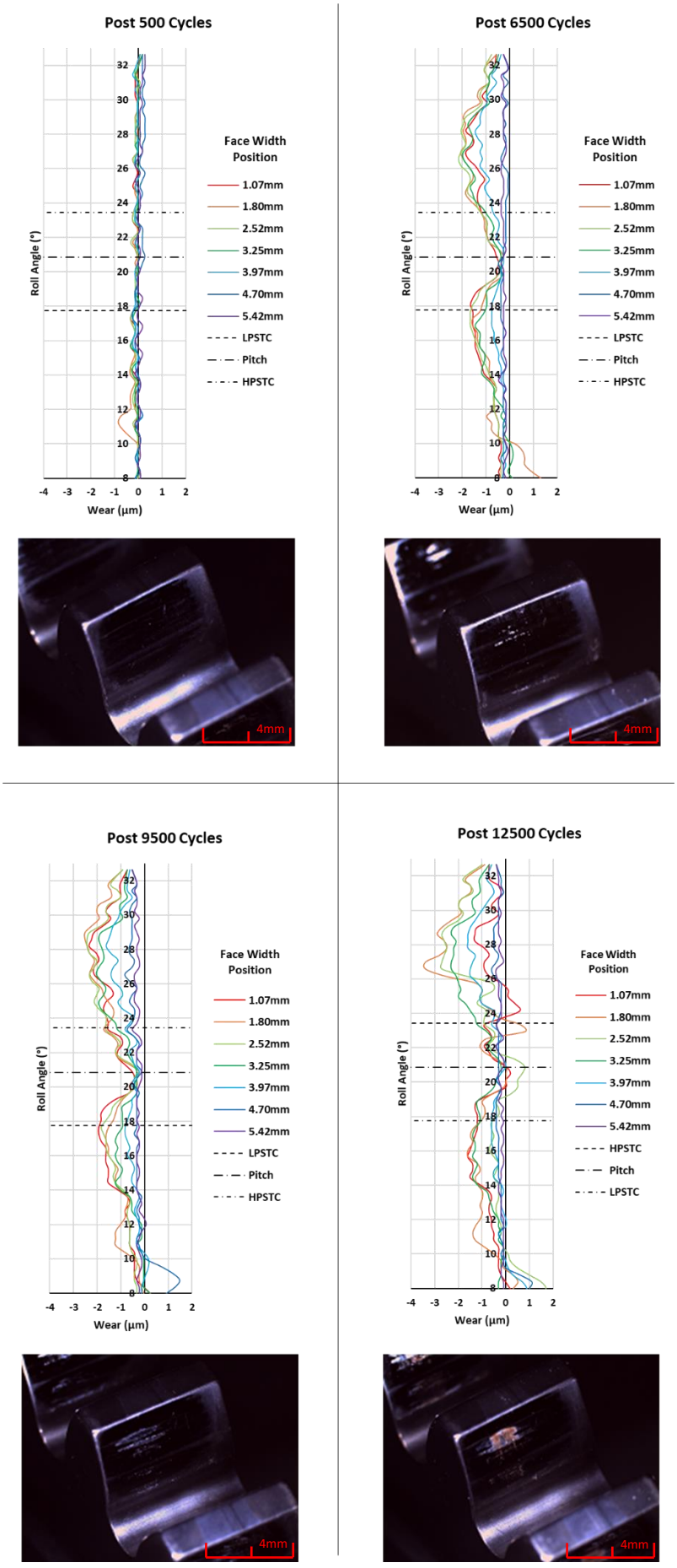

Figure 4-51: Evolution of Wear to Graphit-iC Coated Gear Tooth during Cycling at 10Nm

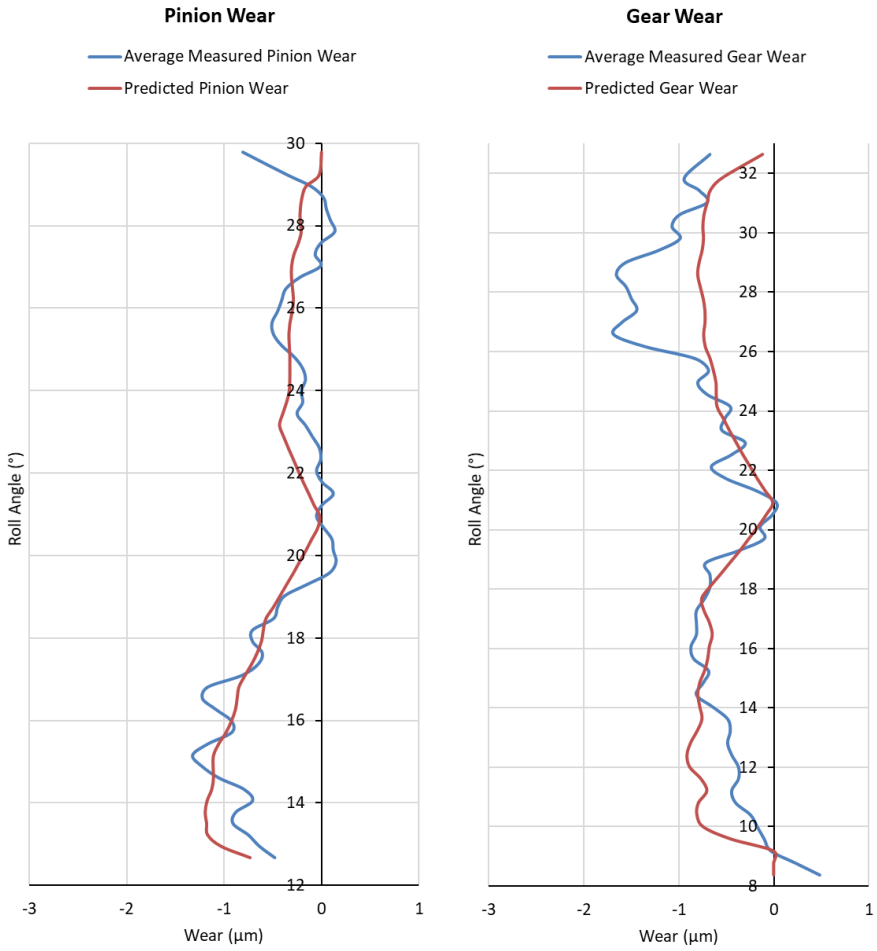

Figure 4-52: Comparison of Predicted and Measured Wear for Graphit-iC Coated Teeth after Testing at 10Nm

(Wear Rate = 2.86E-11 mm^3/N.mm)

4.4.2.2 Wear Test of Graphit-iC at 30Nm

When tested at an elevated torque load of 30Nm, the Graphit-iC coated gears exhibited the same initial damage to the SAP of the teeth. This initial wear was both deeper (up to 2µm) compared to the test at 20Nm, and also occupied more of the profile. With further cycling the typical wear profile was established, with minimal wear evident at the pitch circle and the wear depth increasing closer to the SAP and tips. Gradually this wear blended with the initial damage to the SAP, which exhibited a slow increase in depth.

The first evidence of coating failure on the addendum was observed on the teeth of the 24 tooth output gear after 4500 cycles, with several faint pale lines appearing at the mid-addendum and tips, oriented across the face width. However, unlike on previous tests on Graphit-iC the wear in this region of the line of action subsequently accelerated significantly, and within a further 1000

cycles both the addendum and tip of the idler teeth and the corresponding meshing point on dedendum of the 33 tooth idler gear teeth exhibited significant wear and brown staining. The maximum measured wear depths were over 4µm, greatly exceeded the coating thickness and resulting in termination of the test. Figure 4-53 shows the evolution of the wear profile during testing of one of the teeth from the output side of the 33 tooth idler gear.

Figure 4-54 shows a comparison between the predicted and measured wear for a tooth pair in the gearbox output mesh. Unlike in previous tests the wear in the dedendum of the 33 tooth idler gear significantly exceeded the model prediction due to the sudden acceleration of wear over the final 1000 cycles. This relationship was inverted for the 24 tooth output gear, which showed heavier than anticipated wear to the failed regions on the mid-addendum and tips.

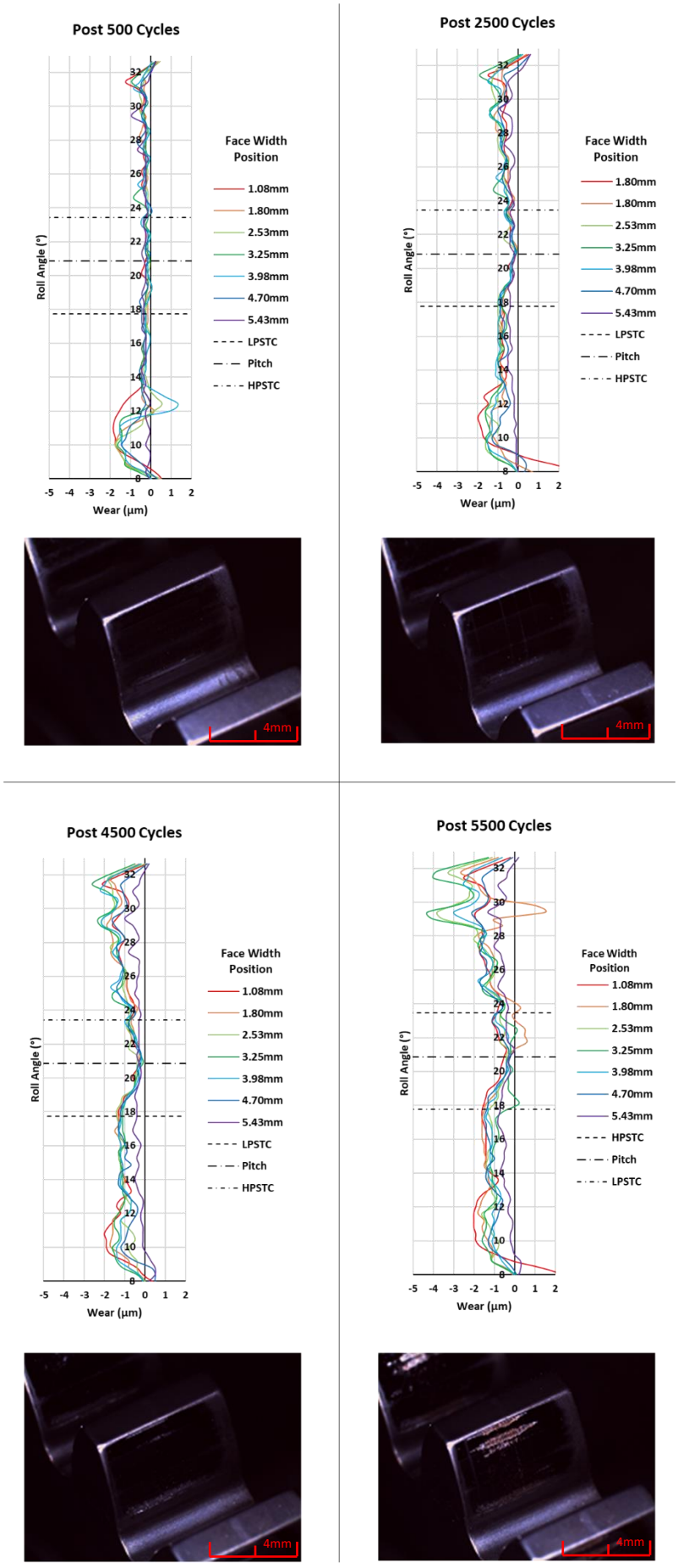

Figure 4-53: Evolution of Wear to Graphit-iC Coated Gear Tooth during Cycling at 30Nm

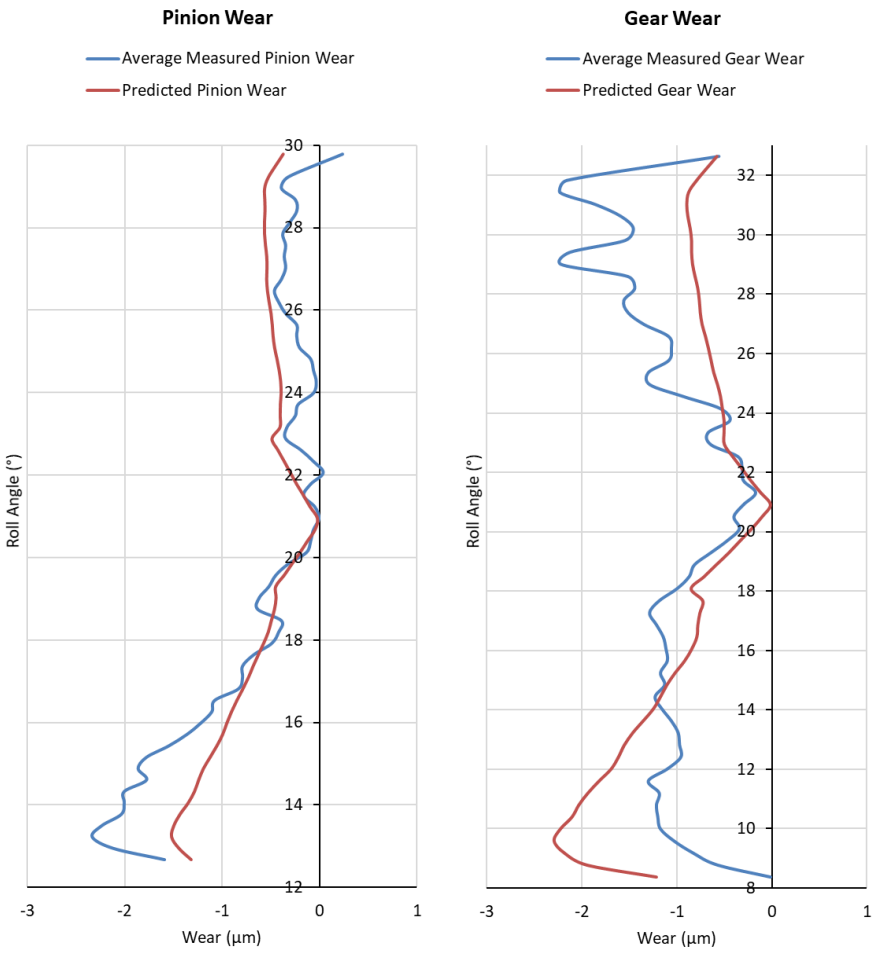

Figure 4-54: Comparison of Predicted and Measured Wear for Graphit-iC Coated Teeth after Testing at 30Nm

(Wear Rate = 3.20E-11 mm^3/N.mm)

4.4.2.3 Comparison of Graphit-iC Coated Gear Wear at Tested Torque Loads

The wear performance of the coating at different torque loads is compared in Figure 4-55 and Figure 4-56. The lowest wear rates ($2.34x10^{-11}$ mm^3/N.mm) were exhibited during testing at 20Nm, with lower torque loads producing a higher wear rate. The highest wear rates ($4.25 x10^{-11}$ mm^3/N.mm) were exhibited during testing at 10Nm. The widest range of wear rates were measured during the test at 30Nm due to the sudden localised acceleration in wear on teeth following coating breakthrough. This is also reflected in the sudden change in maximum wear depth in Figure 4-55 at 6500 cycles. The overall wear rates were higher at 30Nm than at 20Nm, but there is overlap with the ranges of wear rates encountered.

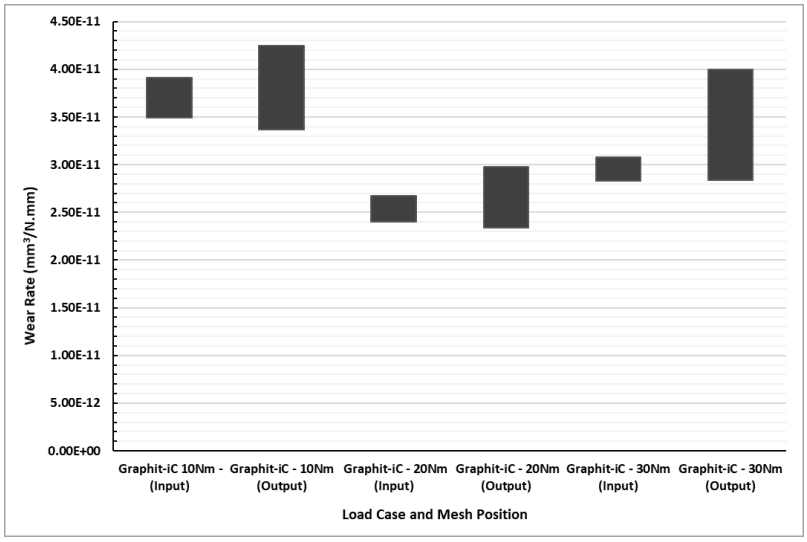

Figure 4-55: Comparison of Calculated Wear Rate Ranges for Graphit-iC by Torque Load and Mesh Position

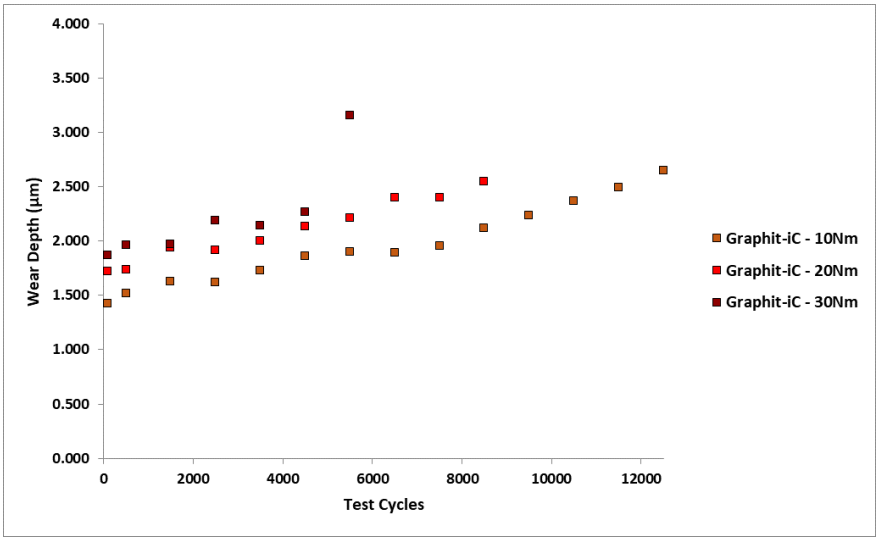

Figure 4-56: Maximum Wear Depth (3 Gear Average) vs. Test Cycle

4.5 Influence of Manufacturing Errors and Design Parameters on Predicted Wear

In addition to comparing the model wear profile outputs to the measured data, it is also useful to examine the intermediate parameters, such as contact stress, and sliding distance, and to study the potential effects of manufacturing errors or design modifications on the predicted wear.

Figure 4-57 shows the model outputs for mean contact stress, sliding distance per mesh, and predicted wear for the input mesh of the test gearbox with nominal geometry i.e., assuming perfect involute tooth form across the entire profile. The torque was set to 20Nm and a wear rate of $2.93E^{-}11mm^3/N.mm$ was applied based on the results of testing on the Graphit-iC coated gears. The number of test cycles was set to 8,500 cycles, as was achieved during wear testing. In order to display the influence of wear on the contact conditions each graph displays separate data for the first and last cycle. The wear predictions display the wear distribution at increments of 10% of the total cycles. Figure 4-58 then displays the same parameters with pre-test measured deviations from one of the tested gears applied.

The plots for contact stress show a significant change in form in the regions of tooth engagement and disengagement, and in the transfer between regions of single and double tooth pair contact, when the real measured geometries are considered. Despite the lack of defined tip relief on the gear design, the majority of samples produced for this study exhibited a negative deviation slope from root to tip i.e., more material has been removed from the tips than at the roots. Whilst remaining within the specified profile tolerance, this produces a mild tip relief effect that eases the load transfer between tooth pairs and lessens the contact stresses at the start and end of the line of action. Furthermore, the ideal involute form does not consider the effect of the tip radius, which again appears to significantly affect the engagement and disengagement characteristics. As the starting deviations in this instance provide a more favourable loading condition, the extent of load redistribution induced by the subsequent wear is lower for the measured gear than for the ideal involute, as can be seen by comparing the magnitude of change in loads and contact stresses between the first and last cycle.

The changes to the contact stress profile subsequently affects the sliding distance due to the change in the contact width. As Hertz's formulae show the contact width, and therefore sliding distance, to be proportional to proportional to $F^{0.5}$, the wear in a rolling/sliding contact is in fact proportional to $F^{1.5}$ according to Archard's Law. The result is a significant reduction in the maximum wear, which is predicted to occur at the SAP of the driving gear. The consideration of measured geometry also eliminates the sharp jagged features at the edges of the region of single tooth pair loading.

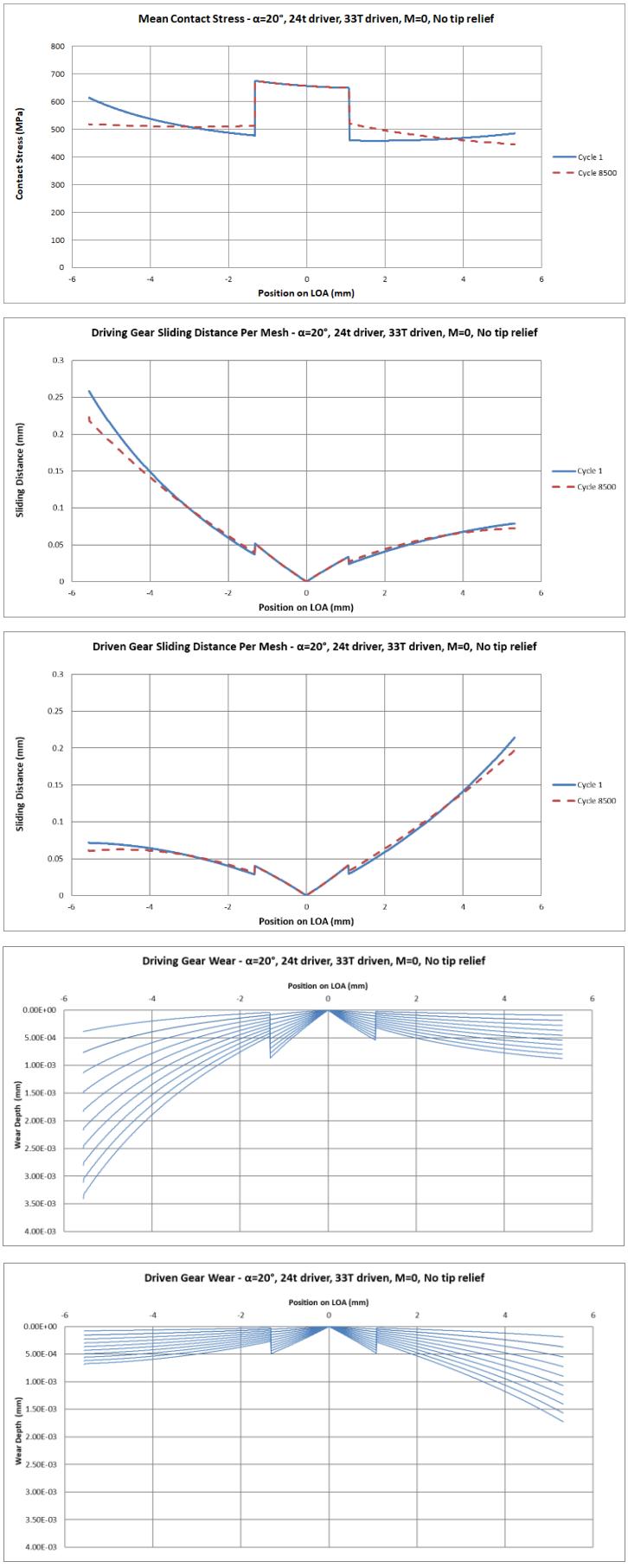

Figure 4-57: Plots of Contact Stress, Sliding Distance and Predicted Wear based on Nominal Involute Geometry and Unmodified Design

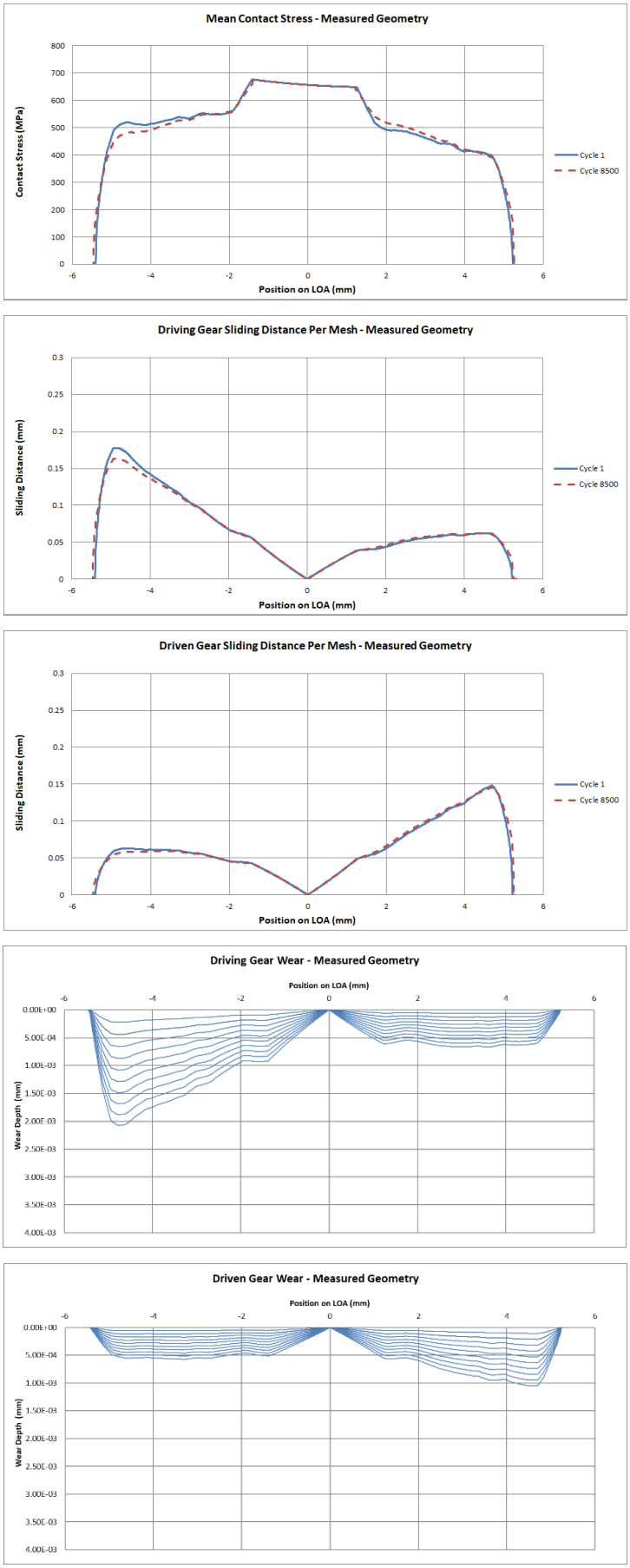

Figure 4-58: Plots of Contact Stress, Sliding Distance and Predicted Wear based on Measured Geometry

The influence of various design parameters was then studied as follows:

- Pressure angle: increasing the pressure angle was found to result in a reduction of predicted wear. The length of action was reduced, which reduced the sliding distances at its extremes. The peak contact stress at the LPSTC was reduced, though the zone of single tooth contact was widened. Figure 4-59 shows the model outputs for the highest standard pressure angle of 25°.

- Number of teeth: the effect of varying the number of teeth on the driving and driven gears was studied whilst maintaining the same overall gear mesh ratio (0.727) and centre distances. Increasing the number of teeth was found to result in a reduction in contact stress, sliding distance, and predicted wear at the ends of the line of action, which was shortened in length. Figure 4-60 shows the model outputs with the tooth counts increased from 24 on the driver and 33 on the driven gear to 32 and 44 respectively. The module was reduced from 2.25 to 1.6875 to maintain the distance between centres.

- Modification: modifying the tooth proportions was found to result in a rebalancing of the sliding and wear distribution between the driving and driven gear. Applying a positive modification to the driving gear and a corresponding negative modification to the driven gear resulted in a reduction in wear to the driving gear and an increase on the driven gear. A modification factor of 0.22 was found to achieve equal maximum wear on both gears. Additionally, the modification shifts the zone of single tooth contact towards the end of the line of action. The model outputs for this case are shown in Figure 4-61.

- Tip relief: tip relief was studied by applying a negative linear slope to involute, starting at the HPSTC on the tooth and increasing to its maximum value at the tip. This had the effect of reducing the predicted wear, contact stress, and sliding distance at the start and end of the line of action and moved the points of maximum wear inwards towards the pitch circle. A maximum benefit was obtained by adjusting the amount of tip relief to provide a smooth transition between the zones of single and double tooth contact, which occurred with 0.012mm of tip relief to both gears. See Figure 4-62.

Finally, all four of above improvements are combined, with the outputs shown in Figure 4-63. Maximum wear depths are tabulated for each design in Table 4-5.

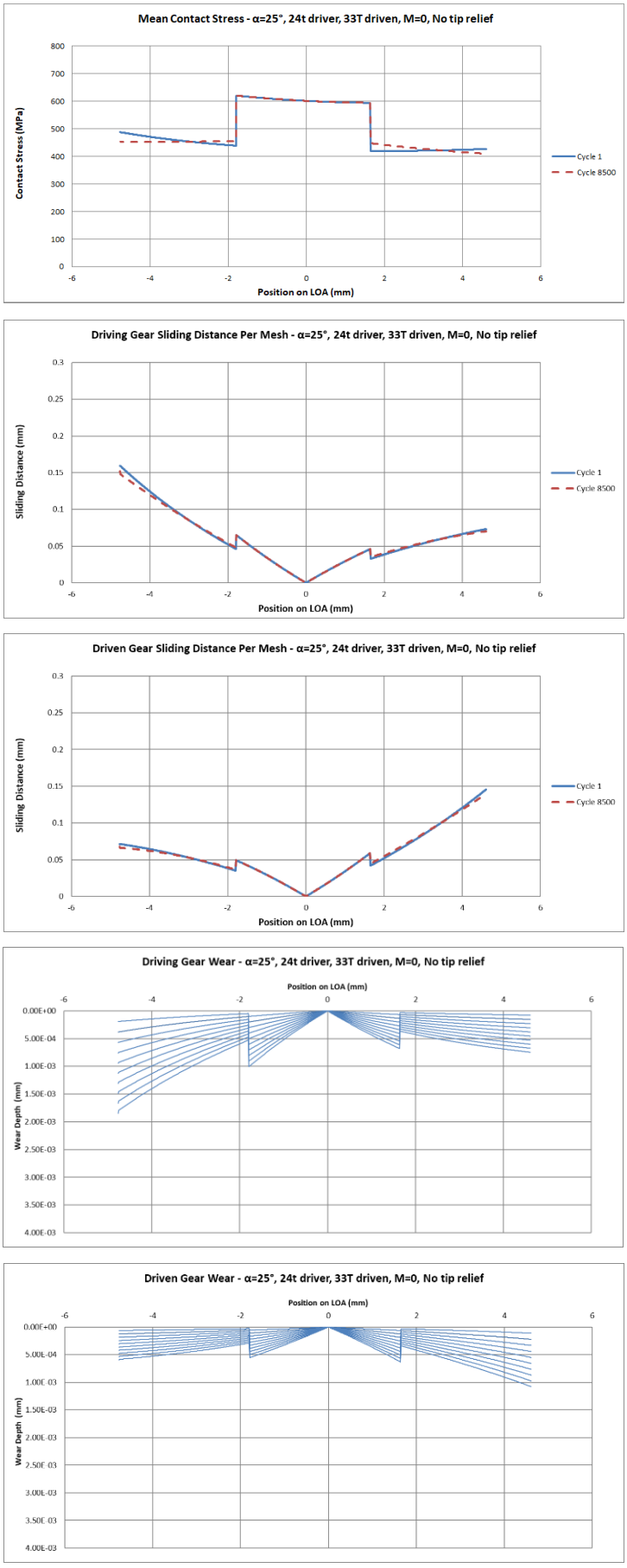

Figure 4-59: Plots of Contact Stress, Sliding Distance and Predicted Wear based on Nominal Involute Geometry and Increased Pressure Angle (α = 25°)

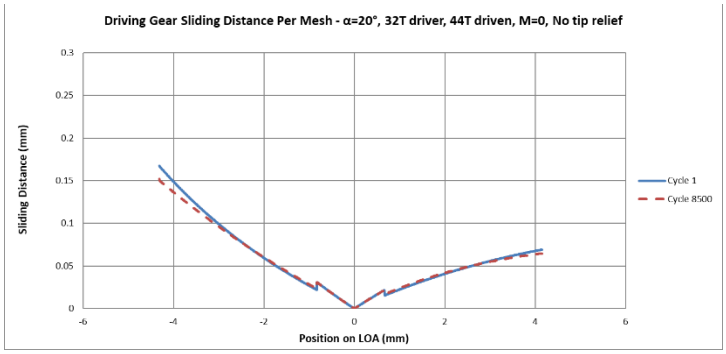

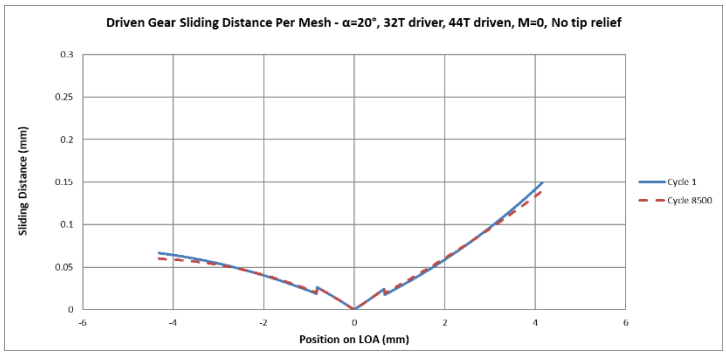

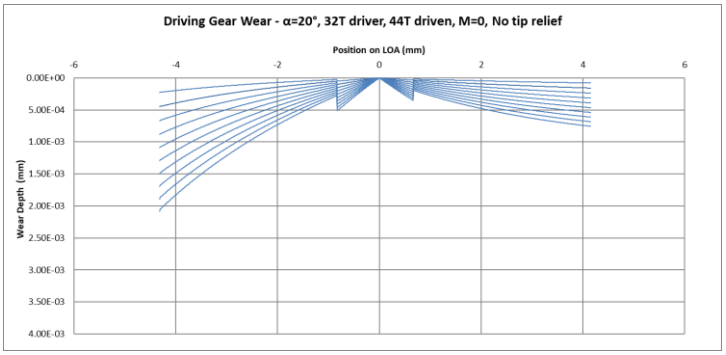

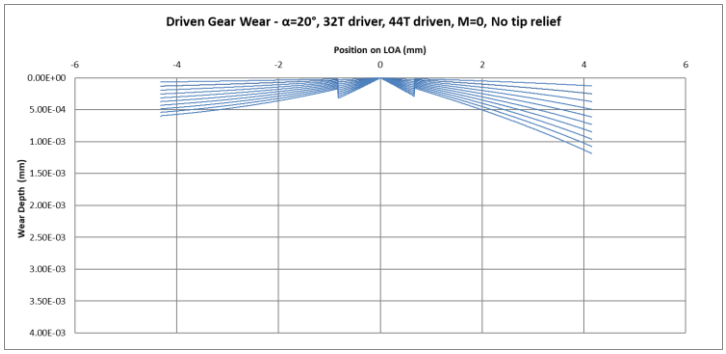

Figure 4-60: Plots of Contact Stress, Sliding Distance and Predicted Wear based on Nominal Involute Geometry and Increased Tooth Count (z_1 = 32, z_2 = 44)

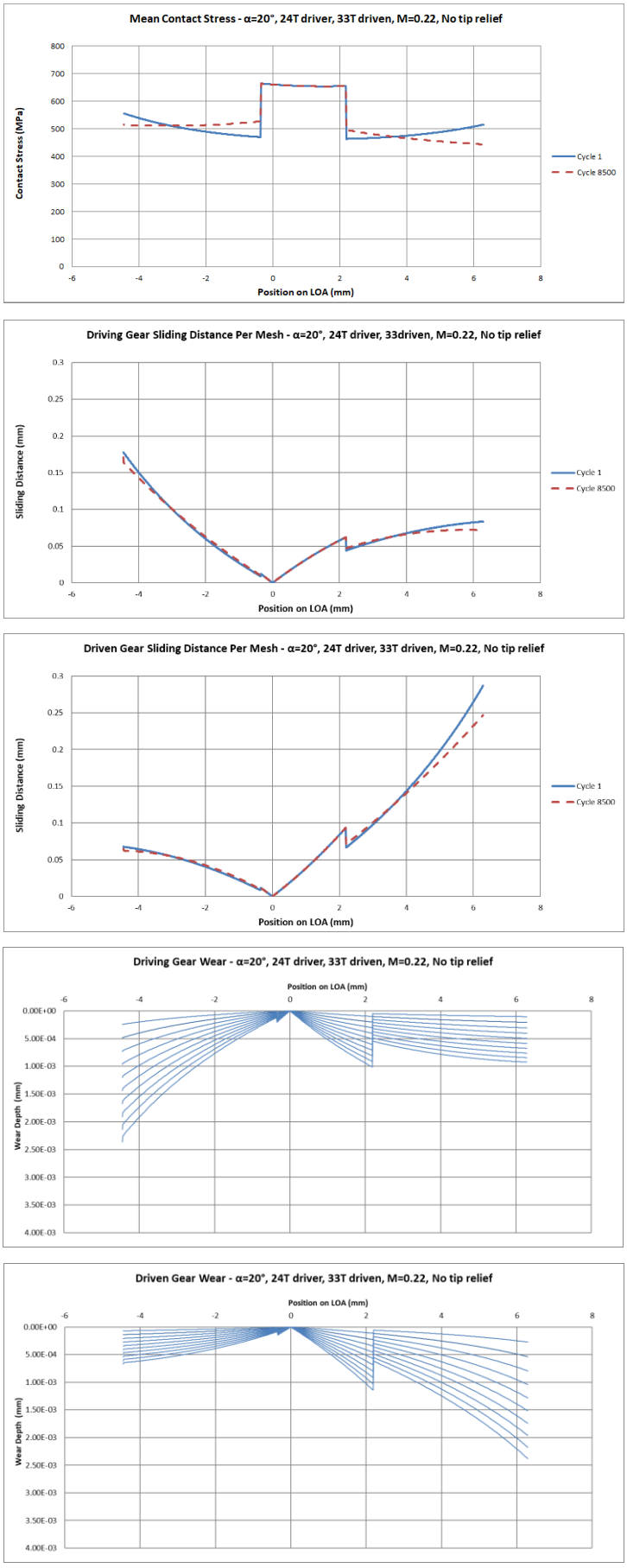

Figure 4-61: Plots of Contact Stress, Sliding Distance and Predicted Wear based on Nominal Involute Geometry and Modified Tooth Proportions (M = 0.22)

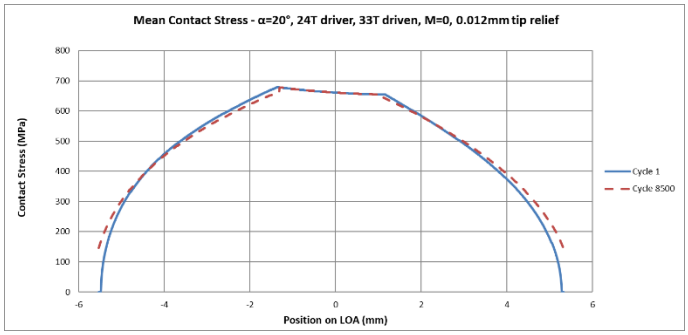

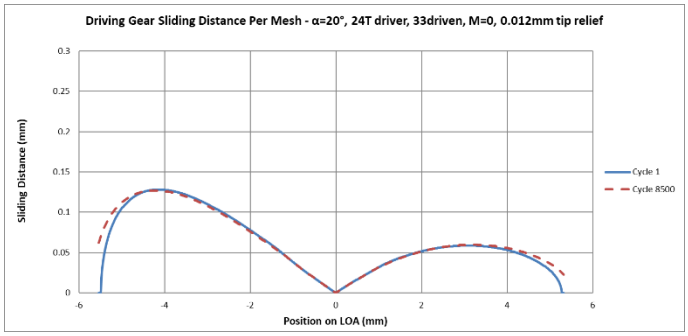

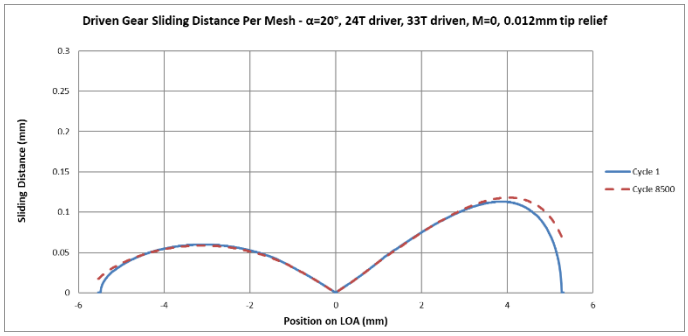

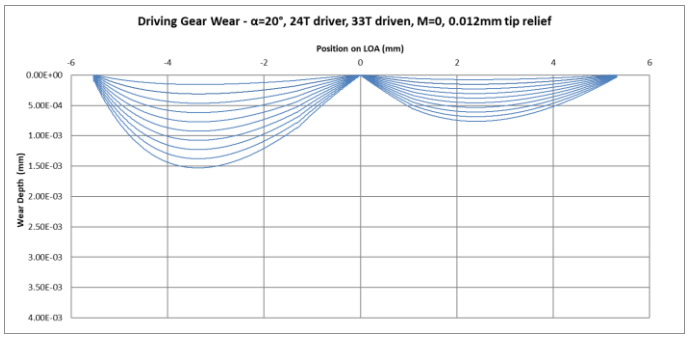

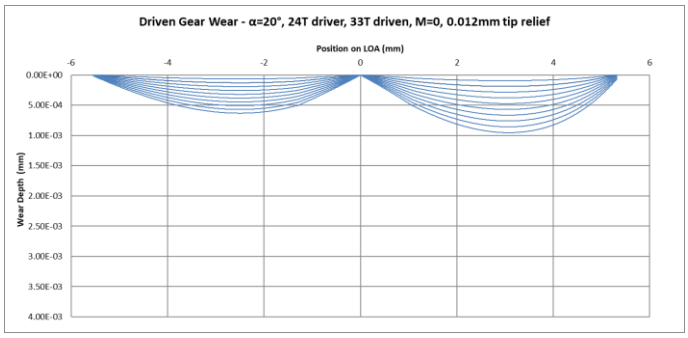

Figure 4-62: Plots of Contact Stress, Sliding Distance and Predicted Wear based on Nominal Involute Geometry with Tip Relief (δ_t = 0.012mm)

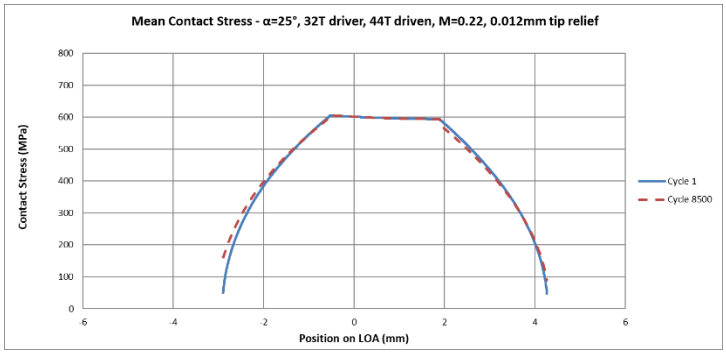

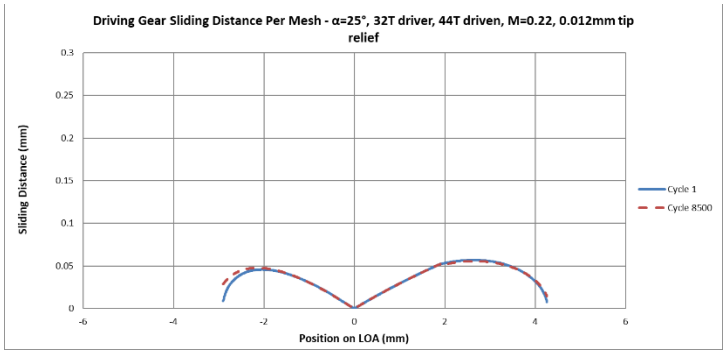

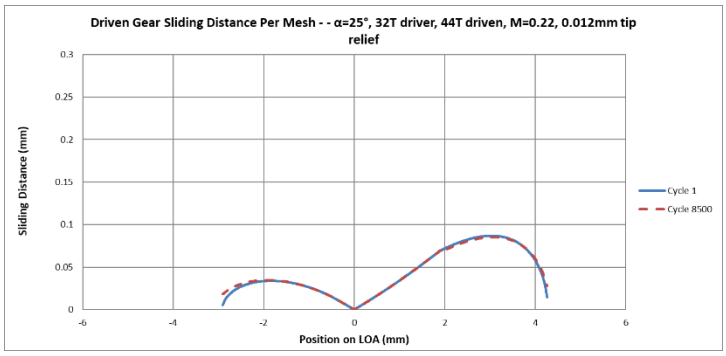

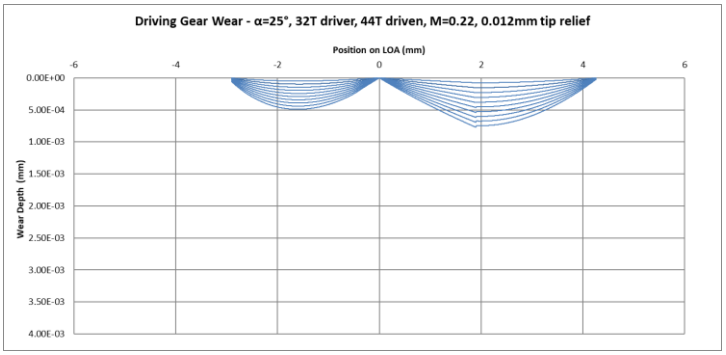

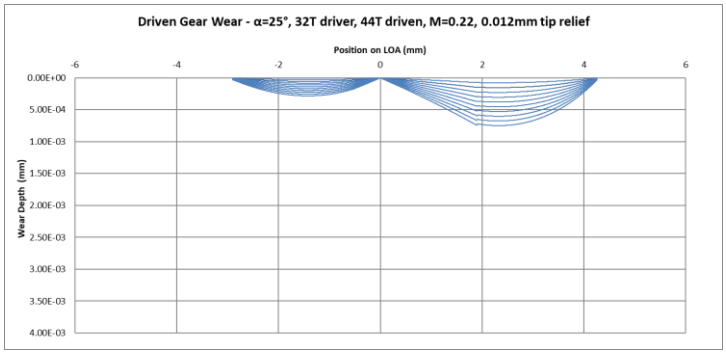

Figure 4-63: Figure 4-64: Plots of Contact Stress, Sliding Distance and Predicted Wear based on Nominal Involute Geometry with all Improvements Embodied

Table 4-5: Wear Predictions for Input Mesh with Improvements from Design Parameters

α (°)	z_1	z_2	M	δ_t (mm)	Wear – Driven (µm)	Wear – Driving (µm)
20	24	33	0	0	3.41	1.73
25	24	33	0	0	1.85	1.08
20	**32**	**44**	0	0	2.08	1.19
20	24	33	**0.22**	0	2.37	2.37
20	24	33	0	**0.012**	1.53	0.95
25	**32**	**44**	**0.22**	**0.012**	0.76	0.76

4.6 Development of Efficiency Test Setup

4.6.1 Selection of Test Rig Concept

Whilst a power recirculating test rig was identified as the most suitable method for wear testing, it was not deemed as suitable for performing efficiency tests. Whilst the total mechanical losses in the test stand could be simply monitored by introducing a torque transducer between the motor and input shaft, it would not be possible to separate the losses of the test and reversing gearboxes. Additionally, when performing efficiency testing it is useful to run the test gearbox against a linearly increasing output load in order to provide a single continuous set of data covering the entire load range.

For the reasons above a power absorbing configuration was selected for performing the efficiency tests. This configuration allows for separate torque transducers to be positioned at the input and output to the gearbox to allow precise measurements of the power losses. By implementing closed loop control of the input motor (based on speed sensor feedback), and output motor (based on torque load feedback) it is possible to vary the applied torque during the test and produce continuous efficiency curves across a range of loads whilst maintaining constant speed.

The test gearbox selected for wear testing was also selected for the efficiency tests in order to utilise the same pool of prepared samples.

4.6.2 Test Rig Requirements

The test rig requirements for efficiency testing remained similar to that use for the wear testing, in order to remain within the typical range of operating conditions for the gearbox. Hence the output torque requirement was to increase from 0Nm to 40Nm over a single, 100 revolution operation. The standard operating speed of 400rpm was maintained.

The most significant difference in the test setup requirements for efficiency testing was the requirement to perform tests at low temperature. The maximum zero-load losses in a high lift system occur during a system deployment in preparation for landing, following a prolonged cold soak at high altitude. The typical lower temperature limit at which performance requirements must be met is -40°C. Lower temperatures, typically -56°C, may be specified but these are regarded as a survival cases. Whilst testing at these temperatures significantly increases the test complexity and monitoring requirements, the potential efficiency benefits of a dry lubricated

gearbox will be maximised under these conditions where fluid viscosity in conventionally lubricated gearboxes are at a maximum.

Table 4-6: Efficiency Test Rig Requirements

Parameter	Test Cycle Requirement
Torque load (Nm)	0 – 40 Nm linearly increasing
Speed	400rpm
Revolutions per Test Cycle	100
Input Direction of Rotation	Clockwise
Temperature	-40°C to 20°C

4.6.3 Test Rig Design

The test rig selected for this purpose was an existing adaptable rig referred to as a “modelling table”. The basic rig consists of a pair of 3 phase AC electric motors, a power and control cabinet, and a T-slotted base plate. The motors and any brackets required to mount the equipment under test can be repositioned as required and then held in place with toggle clamps that engage with the slots in the base plate. Each motor output is fitted with a combined torque and speed sensor.

The built in torque and speed sensors are rated for a torque range of 200Nm, which far exceeded the requirements for the planned tests. In order to ensure satisfactory accuracy of the torque readings when testing at lower torque the test setup was adapted to utilise a pair of the same IML TLDM-50/5-A1-V2-S-K transducers with a 50Nm range that was used during wear testing. Brackets were designed and manufactured to mount the gearbox and torque transducer shafts at the same height as the motor outputs. A pair of adaptor shafts were manufactured to connect the motor outputs to the torque transducers using flexible bellows couplings. The mechanical components of the efficiency test setup are shown in Figure 4-65.

In order to perform testing at low temperature a thermal enclosure was constructed around the test gearbox using polyisocyanurate insulation board. Air inlet and outlet holes were cut in the enclosure and connected to insulated flexible ducting to receive a flow of cooled air. One T-type thermocouple was positioned at inlet to monitor the temperature of air entering the enclosure. Additional thermocouples were bonded to the external surfaces of the gearbox casing in two locations to monitor the gearbox temperature.

A centrifugal blower was used to circulate air through the enclosure and a separate mixing chamber, into which liquid N_2 was vented. Control of N_2 supply was provided by a solenoid valve, the operation was which was commanded by a controller based on the reading of the inlet thermocouple. The torque cells, encoders, and gearbox thermocouple were connected to a data logging system for data collection and condition monitoring. The test setup with the enclosure installed is shown in Figure 4-66. The complete test setup is shown schematically in Figure 4-67.

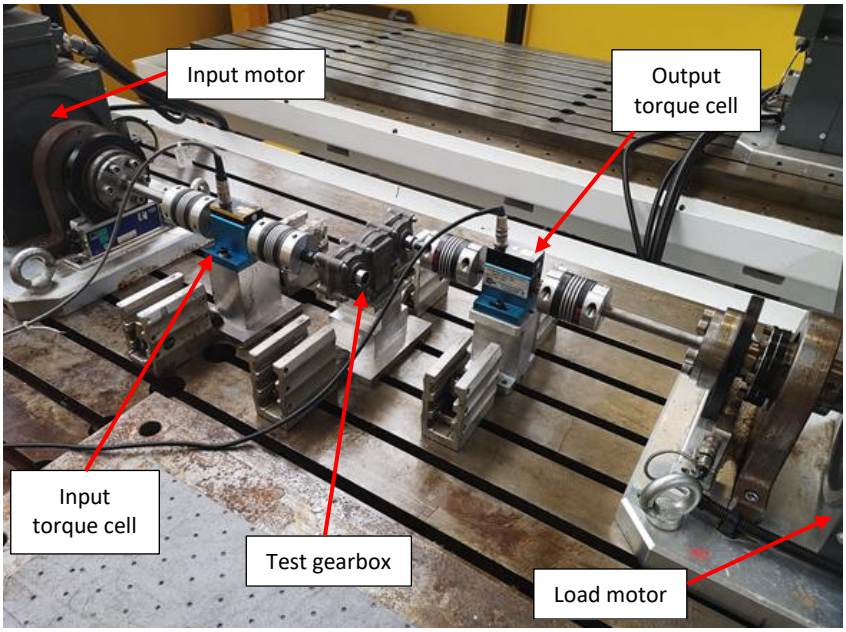

Figure 4-65: Efficiency Testing Setup

Figure 4-66: Efficiency Testing Setup with Thermal Enclosure Installed

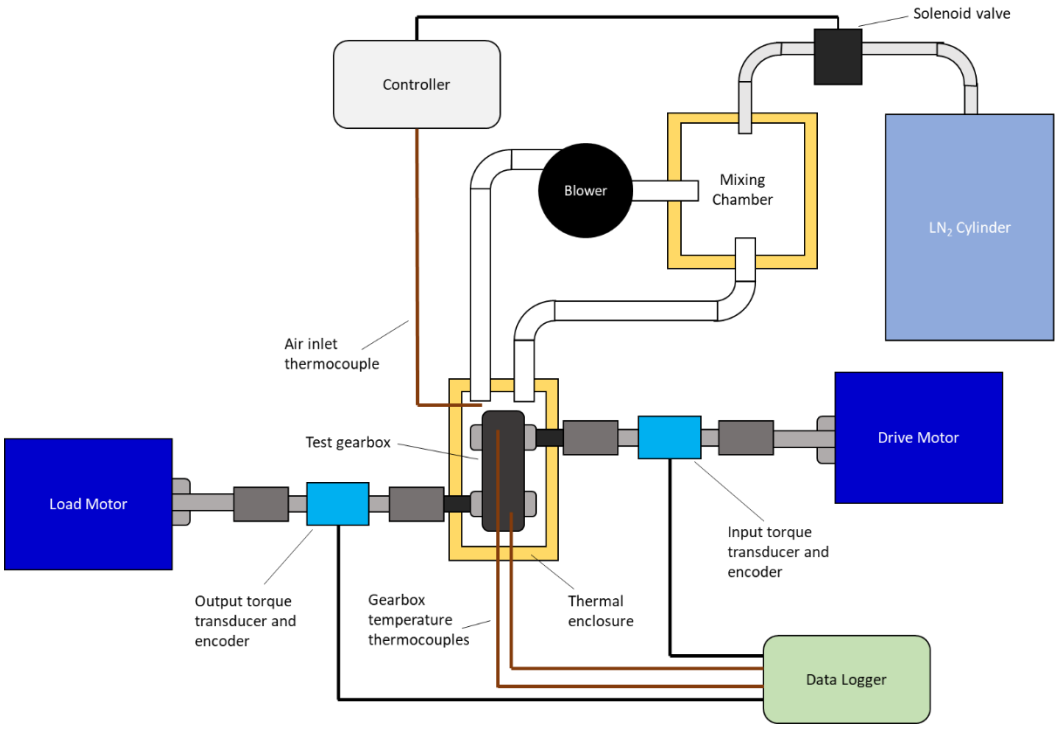

Figure 4-67: Efficiency Test Setup Schematic

4.6.4 Test Gearbox Configuration

In order to assess the relative power losses of the gearbox under dry and fluid lubricated configurations tests were performed with three different lubrication regimes.

- Graphit-iC coated gears with no fluid lubricant
- Uncoated gears with AMS 3057 semi-fluid grease
- Uncoated gears with MIL-PRF-7808 turbine oil

The two fluid lubricants were selected based on their common use in high lift systems. MIL-PRF-7808 is commonly used as a lubricant in higher speed gear stages such as PDU gearboxes, whilst AMS 3057 is the most common lubricant for transmission gearboxes and GRAs. In both cases the gearbox was filled sufficiently to immerse the lower 25% of the shaft seal lips, which is a common design approach to minimise no load losses whilst still ensure lubrication of the seals. In all other respects the gearbox configuration was identical for each test. The uncoated test gears were manufactured to the same specification as the coated gears. Prior to conducting tests on each gear set the gearbox was operated on the wear test rig for 100 test cycles at a low torque of 10Nm to provide some initial running in of the surfaces.

4.6.5 Test Cycle Definition

Prior to each test the controller was set to regulate the temperature of the circulated air to the target temperature. This condition was then maintained until thermocouple readings for the gearbox temperature had stabilised. The air temperature was then adjusted to ensure both gearbox thermocouples reached the target temperature. A two-hour soak period was then implemented to ensure uniform temperature distribution throughout the gearbox internals. During the soak period a +/-2°C tolerance was applied to the gearbox thermocouple readings. On completion of the soak period a single efficiency test cycle was performed. This process was then repeated on completion of each test to re-establish the required conditions.

For each efficiency test the gearbox was initially accelerated to 400rpm over 2 seconds and then operated with no applied output torque until the input torque readings had stabilised. During testing at -40°C the zero-load input torque exhibited a time-dependent decay, hence a stabilisation period (typically ~15 seconds) was required in order to ensure consistency of the zero-load losses throughout the test cycle. Once the input torque reading had stabilised the output torque was then increased linearly over 100 gearbox input revolutions from 0Nm to 40Nm.

However, the higher no load losses immediately following system breakout and acceleration can be a significant design driver for high lift systems due the short duration of the system movements. Therefore, in addition to the tests using the linearly ramped load profile a further set of low temperature tests were performed. In these tests the gearbox was operated against a range of starting torques and the efficiency was analysed immediately once the target speed was reached when the no load losses were at their peak. Whilst this does not produce a continuous set of data for the load range it does provide useful data for the point in the operating cycle where the power losses are at a maximum.

4.7 Efficiency Test Results

During steady state efficiency testing at room temperature, the zero-load losses for both the Graphit-iC coated and fluid-lubricated gearboxes were broadly similar. The no load losses showed no time dependency and the lowest no load losses were actually exhibited when using MIL-PRF-7808 oil. Additionally, the load-dependent losses exhibited by the coated gears were higher than for both fluids. Consequently, the coated gears exhibited a slightly lower net efficiency across the load range than the fluid-lubricated gears.

At -40°C the zero-load losses became far more significant and were the dominant type of power loss. Whilst the load dependent losses of the coated gears were again higher than those of the fluid lubricated gears, due to the lower zero-load losses on the coated gears the net efficiency was higher. The efficiency benefit became smaller with increasing load, and by 40Nm the net efficiencies for all three lubrication regimes were roughly equal. It is notable that the no load losses for the Graphit-iC coated gears still showed a significant increase when testing at -40°C, despite the absence of a fluid. The net efficiencies are plotted against load for each test case in Figure 4-68.

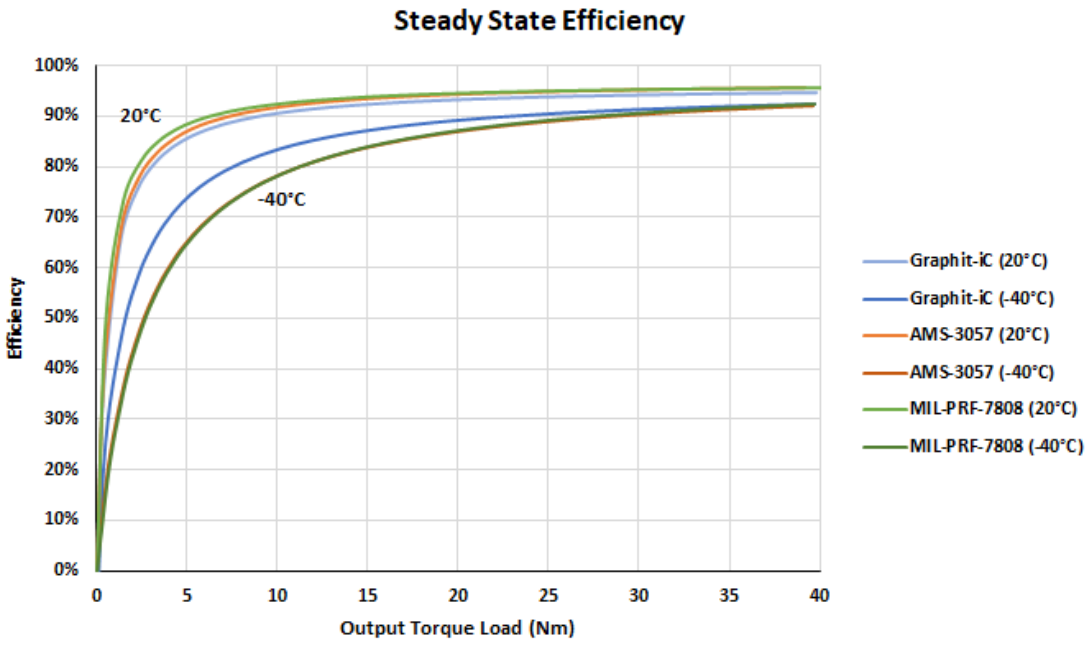

Figure 4-68: Steady State Efficiency for Coated and Fluid Lubricated Gears

In all test cases the load dependent losses remained highly linear over the load range. Figure 4-69 shows a typical plot of output torque against input torque from the efficiency tests. A linear line of best fit has been overlayed to highlight the consistency. The no load losses are visible as a shift in the intercept between the linear slope and the x-axis.

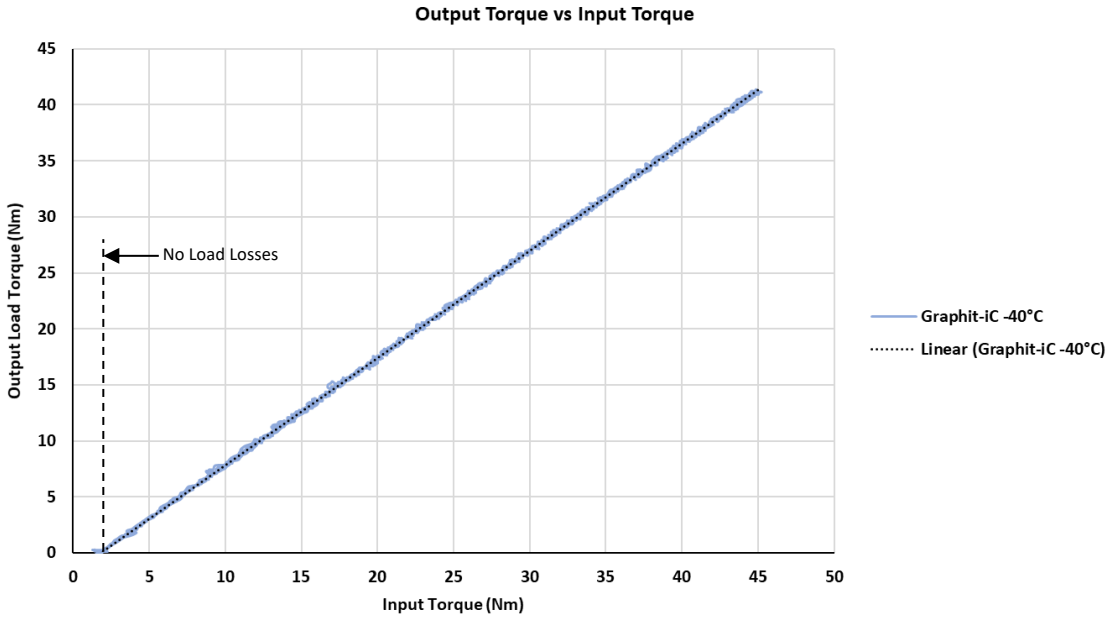

Figure 4-69: Typical Test Plot of Input vs Output Torque

During the initial efficiency tests, the benefit of the Graphit-iC coated gears was even more pronounced. The zero-load losses formed a more significant proportion of the overall losses for the fluid-lubricated gears. Consequently, a net efficiency benefit was maintained over the entire range of output loads tested. The net efficiencies are plotted against output load in Figure 4-70.

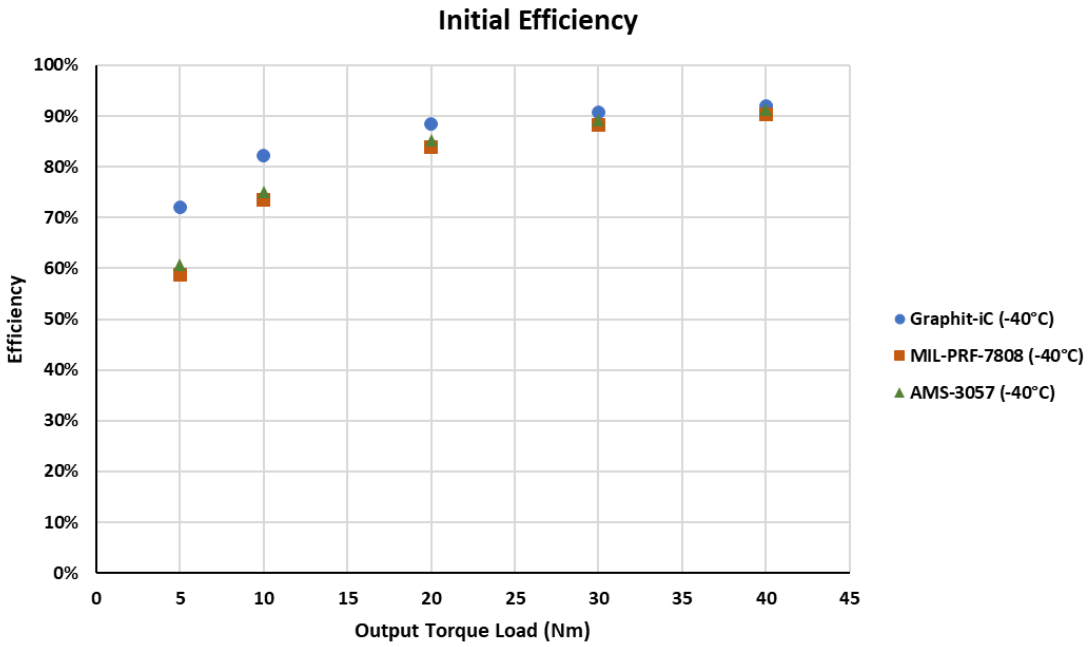

Figure 4-70: Initial Efficiency

Figure 4-71 shows a comparison of the no load input torques against time for each lubricant and test temperature. This illustrates the time dependency of the no load losses of the fluid lubricants at low temperature, compared to the consisten

cy of the Graphit-iC coated gears. The Graphit-iC coated gears, however, exhibited greater noise in the input torque data at low temperature. At 20°C all lubrication regimes showed consistent, low zero load losses.

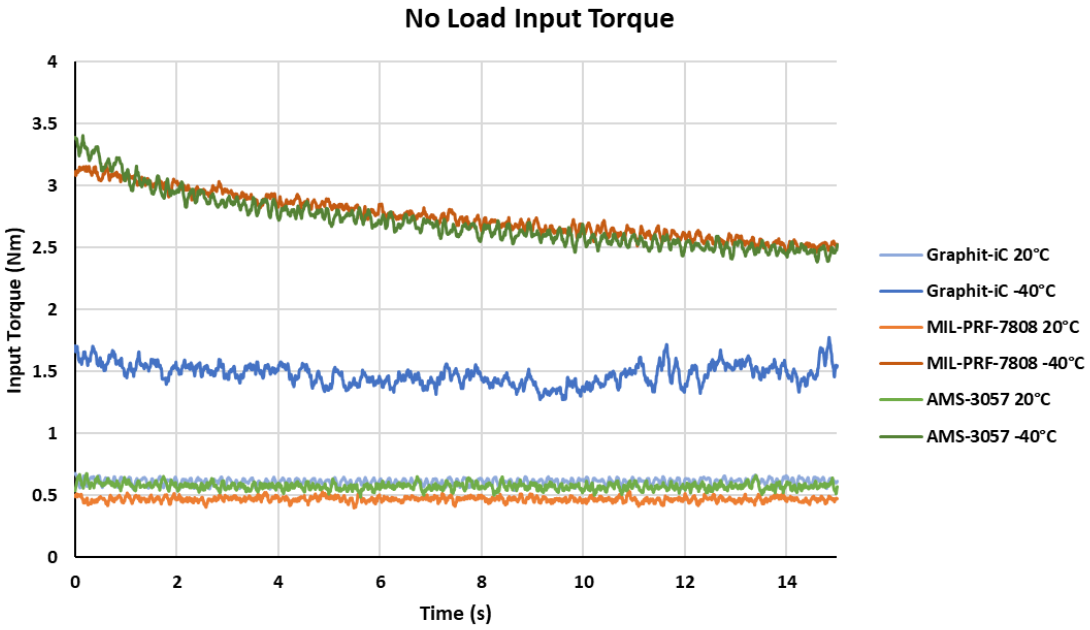

Figure 4-71: No Load Input Torque vs. Time

Figure 4-72 provides a breakdown of the different sources of power loss at discrete torque loads for each lubricant and test case. Note that the predicted load-dependent losses in the bearings were calculated to be negligible during the tests at -40°C. This is due to the effects of kinematic starvation and inlet shear heating, see equations (9) and (15). Hence the increased grease base oil viscosity within the bearings resulted in a reduction of the M'_{rr} and M_{sl} terms.

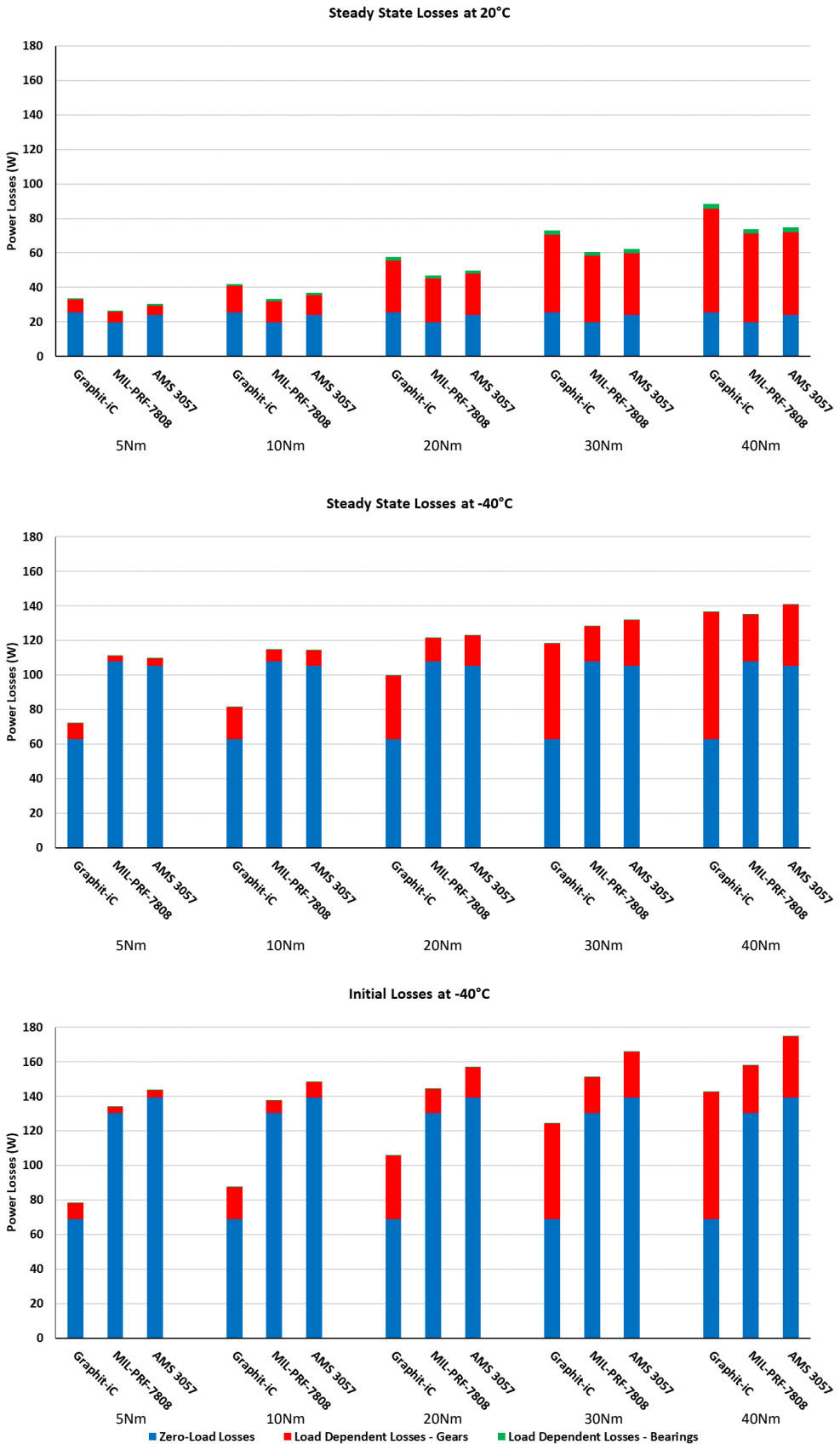

Figure 4-72: Magnitude and Sources of Power Loss for Coated and Fluid Lubricated Gears

The load dependent power losses from the gears were used to calculate average tooth friction coefficients for the gearbox at each of the load increments in Figure 4-72. The calculations were performed as defined in section 3.6. As the gearbox contains two meshes in series the no load losses were considered to be evenly distributed between the two meshes, and the load dependent losses were calculated in series. A single average coefficient of friction was selected for both gear meshes to match the input and output torques from the test data.

The average coefficient of friction is plotted for each load, temperature, and lubricant in Figure 4-73. For both fluid lubricants a lower coefficient of friction was calculated at -40°C. For the Graphit-iC coated gears this relationship was inverted, with the coefficient of friction increasing by up to 16.4%. Despite the high linearity in the load dependent losses (see Figure 4-69), all coefficients of friction exhibited a slight increase with the increasing load. This effect was very small for tests at -40°C, but higher at 20°C and particularly pronounced at lower torque loads.

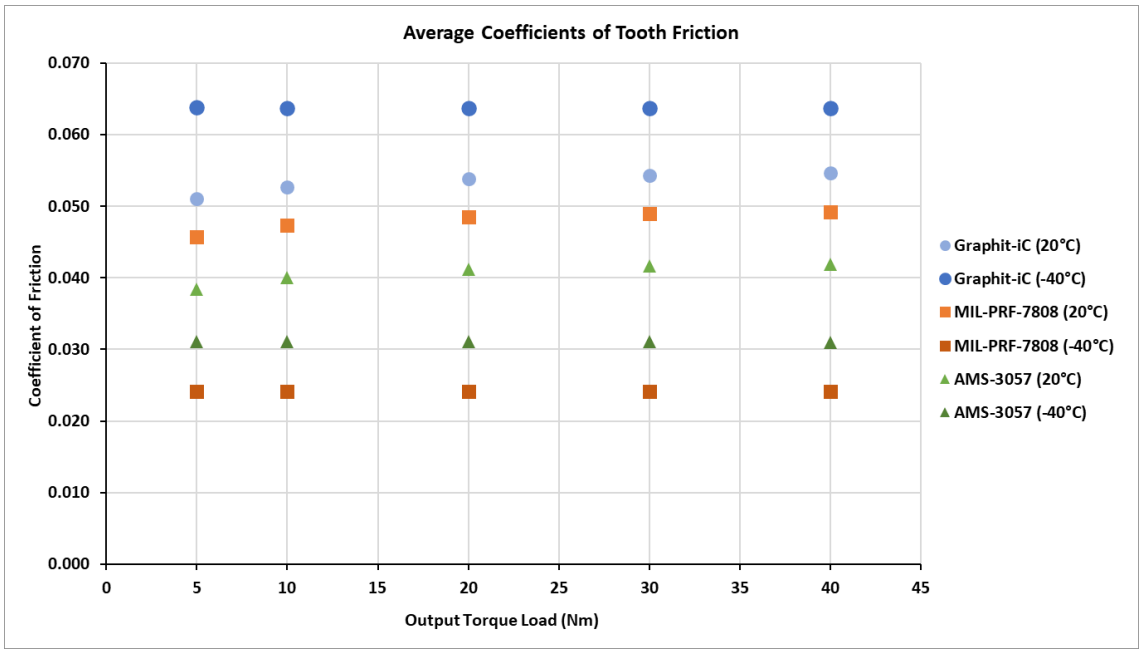

Figure 4-73: Average Coefficients of Tooth Friction

Chapter 5 Discussion

5.1 Wear Performance of Tested Coatings

5.1.1 MoST

MoST exhibited the highest wear rate of all tested coatings and failed rapidly during wear testing. The range of wear rates measured and calculated ($2.57x10^{-10}$ to $5.73x10^{-10}$ $mm^3/N.mm$) significantly overlaps the data obtained in pin-on-disc tests performed by Renevier et. al [138] using coated AISI M42 tool steel discs and uncoated WC-6%C balls ($1.01x10^{-11}$ to $4.21x10^{-10}$ $mm^3/N.mm$). Whilst the substrate and counterface in these experiments differ from the gears tested in this study, the wear rates observed are not surprising. Amaro [236] observed during oil lubricated scuffing and efficiency tests that whilst MoST coated gears had a higher scuffing capacity, reduced coefficient of friction, and lower operating temperature, the actual worn volume was higher than for uncoated gears. Given the high wear rates observed in the wear tests, and the relatively low thickness of the coating (1.22µm nominal, including interlayer) it is clear that the coating lacks the durability for the application.

Due to the rapid nature of the failure, significant coating penetration and substrate wear was incurred prior to test termination. This somewhat impedes the post-test analysis of the worn surfaces. The prevalence of iron oxides detected on the partially worn surface, primarily Fe_3O_4 with occasional α-Fe_2O_3, may simply be as a result of contamination from regions where the substrate had been exposed. However, it is also possible that it plays a direct role in the failure. The observation of black deposits forming on the tooth surfaces during the inspection at 100 cycles would be consistent with the formation of Fe_3O_4 and no evidence of either MoO_3 or TiO_2 was observed in the Raman spectra. If the coating had failed to adequately act as a diffusion barrier, it is possible that some oxidation of the substrate could occur prior to complete removal of the coating, or it may be that the coating was already removed in these regions and the Fe_3O_4 formation and subsequent surface growth acted to mask the failure.

The oxide layers on the addenda of inspected teeth appeared to be relatively stable, with a shiny smooth appearance. These parts of the tooth also generally experienced low wear, despite the rapid failure in the dedendum. The appearance and low wear rate are consistent with the formation of a “glaze” layer, formed of compacted oxide particles and with lower friction and wear rates than the unoxidized substrate [270].

The observation of Fe_3O_4, differs significantly from the worn Graphit-iC coated gears, where iron oxides observed on teeth after testing were found to primarily be γ-Fe_2O_3. Fe_3O_4 tends to form conditions of higher temperatures and lower oxygen potentials [269], which again may indicate a process of oxidation through diffusion through the coating, and significant frictional heating.

The one area where MoST appeared to perform well is the adhesion. MoST was the only tested coating not to suffer any instances of immediate delamination or wear at the SAP. In fact, the results of the first 100 test cycles initially appeared to be very promising, However, based on the results of the subsequent wear cycles and the correlation between the calculated wear rate and examples in literature, the prospect of utilising MoST for dry geared applications appear to be very limited.

5.1.2 WSC

During wear testing WSC exhibited lower wear rates than MoST, but still substantially higher than Graphit-iC. Comparisons can be drawn to the results of pin-on-disc tests conducted by Vuchkov [255] using uncoated 100Cr6 balls against coated AISI M2 steel coupons. The range of wear rates observed during the wear tests on gears ($9.04x10^{-11}$ to $1.30x10^{-10}$ mm^3/N.mm) overlap with the lower threshold of the range reported by Vuchkov (~$1x10^{-10}$ to $7x10^{-10}$ mm^3/N.mm). Whilst the substrate and counterface materials, and test kinematics differ, the wear rates observed appear consistent.

However, the performance of the coating, when both comparing different teeth or even different locations on the same tooth, varied significantly. Some teeth suffered from both minimal wear in some areas and catastrophic wear in others. Intermediate and post-test inspections showed that the coating often delaminated in irregularly shaped patches. Whilst there was concentration of delaminated regions around the pitch circle where the peak contact stresses were encountered, others appeared to be somewhat randomly distributed over the tooth surface, often completely outside zone of contact. In other instances, concentrations of smaller pits were concentrated in “streaks” that were neither oriented in the direction of sliding or across the contact width.

The Raman spectra for the partially worn coating exhibited the anticipated shift in the G peak wavenumber, indicating a more sp^2 rich surface. This, combined with the slight increase in C content on partially worn surface in the EDS spectra, and the overall low wear rates on the majority of the tooth surface, indicates the formation of a lubricating graphitized transfer film. This suggest that where the coating was able to maintain adhesion it actually functioned as intended. It is the inconsistent adhesion that appeared to be the primary cause of failure.

The most likely cause of the adhesion issues, given its inconsistent occurrence, would be inadequate cleaning prior to deposition. No examples of coating delamination have been reported for WSC elsewhere in the literature, and it is unclear why adhesion proved so problematic in this instance. Until this issue can be understood and resolved it is unlikely that this coating could see further use in geared applications.

5.1.3 Graphit-iC

Graphit-iC exhibited by far the lowest wear rate of the three coatings tested. As with MoST and WSC, the calculated values are comparable to those reported in literature for dry sliding in pin-on-disc tests. Yang et. al [250] tested Graphit-iC using coated M42 tool steel discs and WC-6%Co balls and observed that at higher loads the coating exhibited a critical speed, above which the wear rate dramatically increased. This varied according to load, with the lowest threshold of 400mm/s being established for the maximum load. Below the critical speed approximate wear rates of ~$1x10^{-11}$ to $6x10^{-11}$ mm^3/N.mm were reported. The range of wear rates calculated for all tests performed on Graphit-iC coated gears was $2.34x10^{-11}$ to $4.25x10^{-11}$ mm^3/N.mm, which falls comfortably within the range reported in Yang's experiments. The peak sliding velocities of the tested gear pairs are found at the start and end of the line of action, with a maximum value of 401.52mm/s at 400rpm. When the combined effects of the greater coating thickness and lower wear rates are considered, the superior performance of Graphit-iC over MoST and WSC coating is line with expectations.

The majority of gears followed a pattern of initial delamination failure near the SAP, which subsequently stabilised. The wear distribution then broadly followed the distribution predicted by the model. However, this initial delamination is not considered by the model, and therefore the model predictions and measured wear for the initial period of cycling differ greatly. The presence of significant Cr in the delaminated regions indicates that the delamination occurred within the layers of the coating, and not between the Cr adhesion layer and substrate.

Amaro's studies using Graphit-iC coated gears with oil lubrication [234] [237] state no delamination occurred during testing, although delamination was observed during tests on rolling discs. However, studies on other carbon-based coatings applied to gears often mention delamination at the root as a leading cause of failure [229] [244].

There are a number of possible explanations for this behaviour, which largely relate to the magnitude of contact stress, and the sliding conditions. As the SAP and tips of the teeth represent the points of tooth engagement and disengagement, errors in tooth pitch or transmission errors

due to bending can cause the teeth to carry a greater proportion of the load at the start and end of the line of action. In the case of heavily loaded teeth the combined errors may result in interference at the point of tooth engagement. This causes the tip of the driven gear to initially contact the driver above the SAP. The point of contact will briefly slide down the surface of the driver before travelling back towards the tips as normal. Furthermore, the termination of the tooth surface due to the tips limits the width of the contact zone and can result in very high contact stresses. See Figure 5-1 and Figure 5-2. Neither of these effects are considered in the model developed for this study, and therefore the real contact stresses may exceed those predicted.

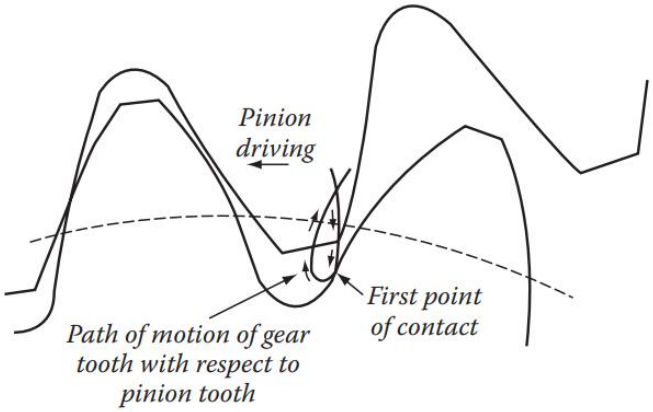

Figure 5-1: Early Engagement of Teeth due to Pitch or Transmission Errors [20]

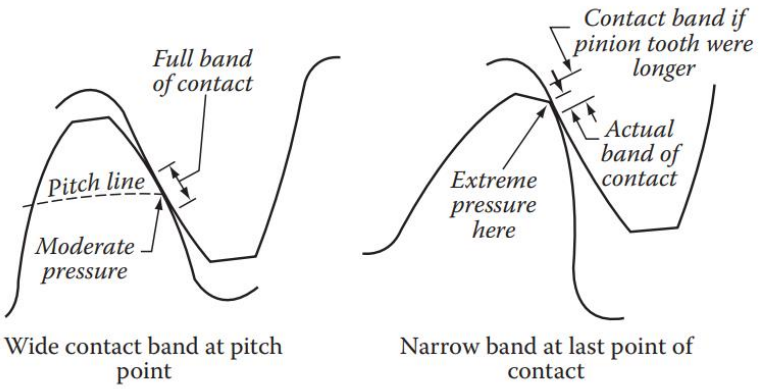

Figure 5-2: Truncation of Contact Width due to Tips [20]

In addition to the potential for high contact stresses, the start and end of the line of action are also where the slide-roll ratio is at its highest. As discussed in section 2.2.2.1 sliding and friction cause the subsurface shear stresses developed in a hertzian contact to increase in magnitude and shift the peak closer to the surface. The shear stresses in a mixed rolling-sliding contact are higher

than for either the pure rolling or sliding cases. Negative sliding conditions, where the rolling and sliding velocities oppose one another, occur in the dedenda for both the driving and driven gear, as shown in Figure 5-3. Figure 5-4 shows the slide-roll ratio for the driving and driven gears used in the wear tests. Negative sliding is understood to be a key factor in the propagation of surface or near-surface cracks that lead to micropitting in conventionally lubricated gears. This has generally been linked to the friction forces, which oppose the contact movement, causing the crack to open and allowing oil to enter, and the subsequent rolling motion causing the crack to propagate due to hydraulic forces [271][272]. However, more recent analyses have shown that in mixed rolling-sliding contacts the asperities of the slower moving surface experience a greater number of micro stress cycles due to the greater sliding distance, which leads to a more rapid initiation of surface or near-surface cracks [273]. This provides a very plausible explanation for the preferential delamination on the dedendum over the addendum.

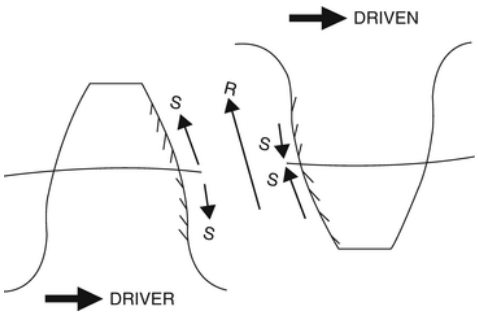

Figure 5-3: Direction of Rolling and Sliding Velocities on Meshing Gear Teeth [274]

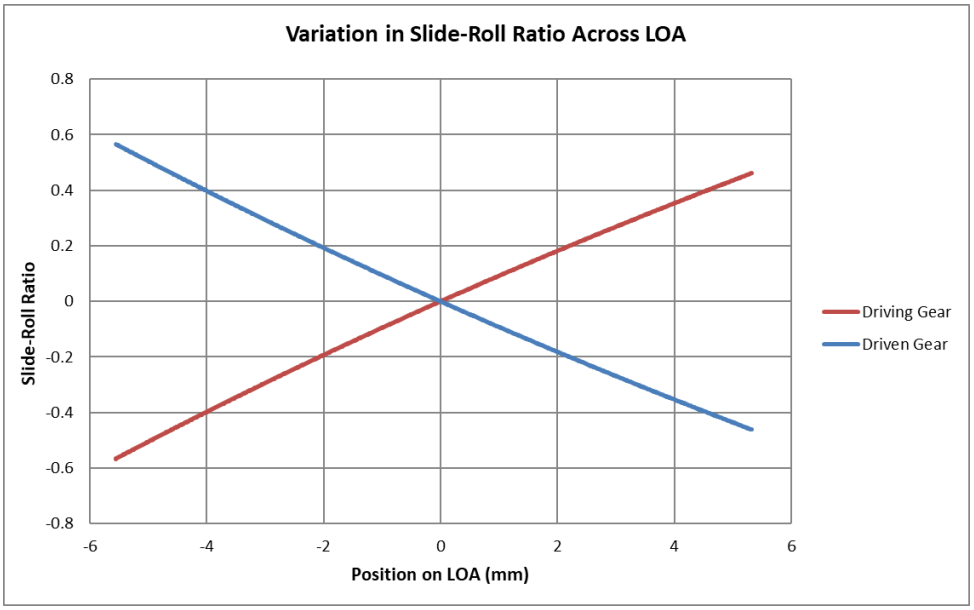

Figure 5-4: Slide-Roll Ratio Variation for Tested Gears

The tendency for coated gears to suffer root delamination can therefore be understood as a consequence of high contact stress and negative sliding conditions. The absence of reports of delamination in other studies using Graphit-iC applied to gears is likely due to the use of oil lubrication, which would lower friction and therefore shear stress. The significant Cr content detected in the EDS spectra for the delaminated regions indicates that the delamination potentially occurred within the coating, rather than at the interface between the Cr interlayer and steel. This aspect of the failure is surprising, given the implementation of the graded Cr/C transition layer to provide a smooth transition of mechanical properties between the Cr and Cr-doped a-C layers.

The extent of wear to the mid-addendum of most gears is harder to explain. It might be expected that the coating failure close to the SAP would result in an increase in the wear to the corresponding point on the addendum of the mating gear, and that the points of maximum wear for the two gears should be closely located on the line of action. In fact, this was only seen in the tests at 30Nm. Figure 5-5 shows the wear distribution for a tooth pair from the tests at 30Nm, plotted on the line of action rather than against roll angle. At other loads the delamination seemed to have relatively little influence, and the maximum wear was located in the mid-addendum rather than higher up the tooth. See Figure 5-6.

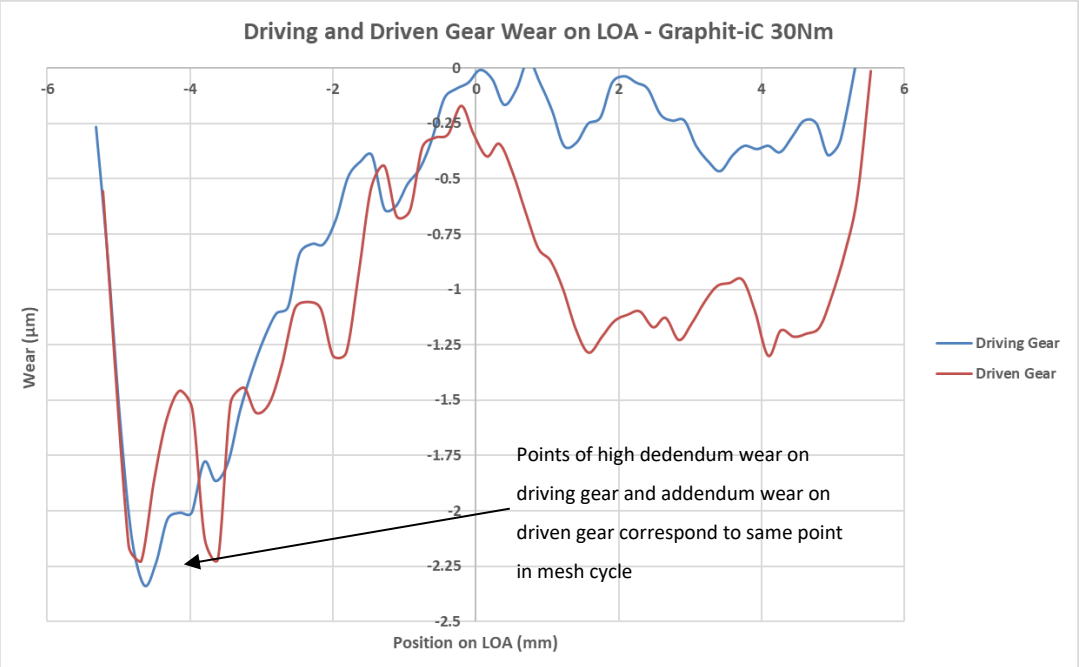

Figure 5-5: Wear Distribution for Graphit-iC Coated Tooth Pair from Test at 30Nm

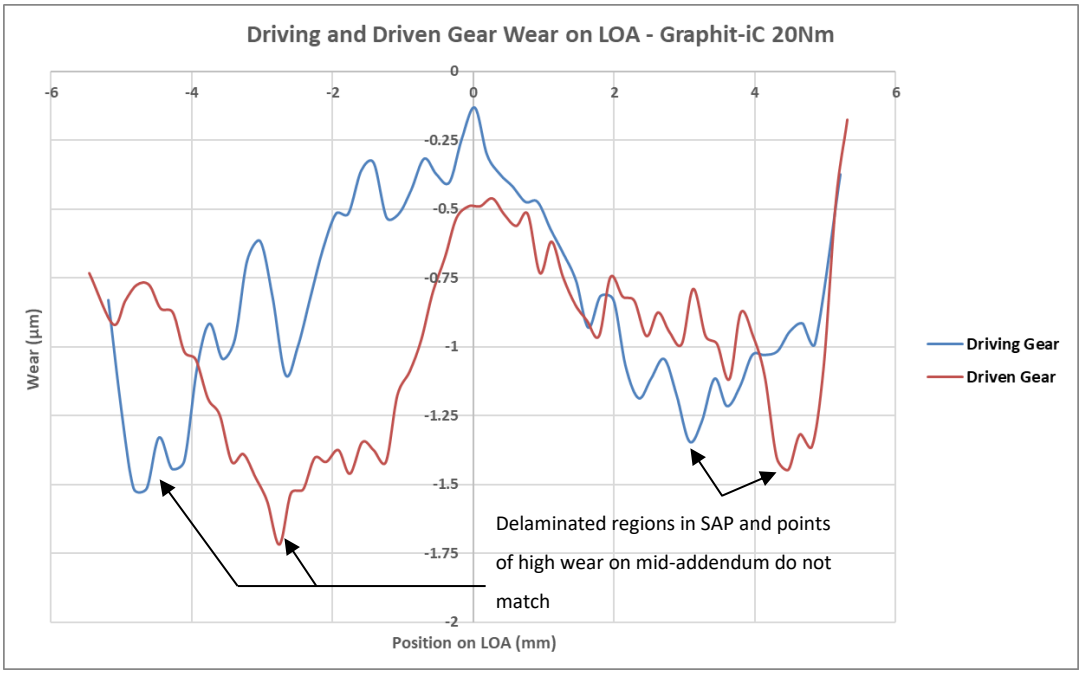

Figure 5-6: Wear Distribution for Graphit-iC Coated Tooth Pair from Test at 20Nm

The regions of high wear on the on the mid-addendum appear to be caused by a process of sliding wear, as evidenced by their gradual development (Figure 4-39), the orientation of the jagged features at the upper and lower boundaries in the direction of sliding, and the blending between the failure boundaries and the surrounding worn coating (Figure 4-42). However, the causes of such a high wear rate in these locations is currently not understood. The model developed does make several simplifications to the contact problem as previously described. Most notably in this instance is that the load distribution is effectively assumed to be static, and the variations in the load across the line action stemming from stiffness and inertia-induced effects are not considered. As shown in Figure 2-28 the actual load distribution may differ when dynamic effects are significant. The “rippled” nature of the wear depth evident when examining the teeth (see Figure 4-41) appears to bear no correlation to the tooth topography, and therefore may be an indication of a high frequency variation in tooth loads during the mesh cycle.

The Raman spectra for the as deposited and partially worn coating showed many similarities to that for WSC over the 800cm^{-1} to 1800cm^{-1} range, in addition to tests on other carbon based coatings in the literature (e.g. Figure 2-62). The broad response from the as-deposited coating separated more clearly into to peaks around the G and D band positions for the worn surfaces, and the G band showed a small shift to a higher wavenumber, indicating the development of an sp^2 rich lubricious surface. This is in line with the expected behaviour of the coating. The Raman spectra indicated presence of iron oxides even where the substrate was not exposed, though this

may be due to wear debris from the failed regions and contamination from cycling performed after the substrate was exposed in some areas.

The prospects for use of this coating in real-world actuation applications is clearly greater than that for either MoST or WSC, though it is clear Graphit-iC still lacks sufficient durability for a civil high lift gearbox such as the one used in testing. Civil passenger aircraft are heavily utilised and achieving a target of 120,000 cycles at 20Nm, compared to the 8,500 achieved, requires an order of magnitude improvement in performance. There are potential aerospace actuation applications outside of civil high lift, however. High lift applications for military transport aircraft typically have significantly lower cycle requirements and greater opportunities for scheduled overhaul of equipment to replace worn parts. Additionally other opportunities exist in low cycle geared actuation systems on military aircraft, such as payload bay doors. Further improvements durability would be required, but a satisfactory life could be achieved with a four to five fold improvement. This might be achieved though increases to coating thickness, adhesion, or modifications to the gear design. The implementation of a running-in procedure at low torque loads may help to reduce problems with delamination by developing the transfer film to lower friction at the SAP and reduce stresses on the coating interface during subsequent cycling.

5.2 Influence of Manufacturing Errors and Design Parameters on Predicted Wear

The comparison between the model outputs with nominal and measured geometries highlights the significant influence of profile errors and tip geometry on the contact conditions for the teeth, particularly around areas of tooth engagement and disengagement. Additionally, as shown in Figure 4-58, the relatively low levels of acceptable wear and high stiffness of the teeth mean that little redistribution of load can occur during the life of the gears. Consequently, whilst a running-in process may aid durability by allowing initial transfer film development, it is unlikely to improve the load profile over the line of action if the initial tooth geometry is poor.

The study of the influence of basic design parameters provides a useful indication of how gear designs may be adapted and optimised for the use of self-lubricating coatings. Increasing the pressure angle was found to reduce the predicted wear at the limits of the line of action by reducing its length. This lowered both sliding and contact stress at these points in the mesh cycle. An overall reduction in contact stress was also observed for regions of single and double tooth pair loading. High pressure angle designs (>20°) are a relatively common feature of actuation system designs where the beneficial effect on tooth strength and the ability to utilise gears with

fewer teeth without undercutting are favoured. Adopting high pressure angles in gears designed for the use of coatings therefore seems promising. The primary drawback of this approach is a reduction in contact ratio, and consequently a widening of the zone of single tooth contact around the pitch circle. Whilst the greater noise that results from higher pressure angles is typically not a concern for actuation designs, during the wear tests performed in the study there was a consistent observation of high wear on the mid-addenda of the teeth. A widening of the zone of single tooth contact, if sufficient to impinge on the mid-addendum, could result in worsening of this phenomena.

An increase in the number of teeth on each gear, whilst maintaining the distance between centres and overall ratio, was found to have a similar effect to the higher pressure angle on the contact conditions at the limits of the line of action. The length of the line of action is reduced, and hence the more severe sliding velocities and contact geometries associated with increasing distance from the pitch circle are not encountered. Contact stresses over the remaining length of action remained similar to those from the unmodified design but the contact ratio was slightly increased, resulting in a proportional reduction in the width of the zone of single tooth loading. Consequently, adopting finer gear pitches should offer an improvement in coating durability.

However, smaller teeth will also result in a reduction in strength and bending fatigue resistance for the teeth. As these parameters are often prime design drivers when sizing gears for actuation applications, it is somewhat at odds with typical practice. Manufacturing tolerances would also need to be appropriately scaled, with the potential for increases in cost. The coating thickness would also occupy an increasingly large proportion of the manufacturing tolerances, and at a certain point it may become necessary to modify the pre-coated profile to ensure the finished gear dimensions conform.

Modifying the tooth proportions, unlike the other parameters studied, does not result in a common reduction in predicted wear to both gears. It instead results in a rebalancing of the wear between the driving and driven members, accomplished by a shifting of the line of action. The high sliding and contact stresses at one end of the line of action can be reduced at the expense of an increase at the opposite end. The maximum wear prediction for an unmodified gear pair was found to be at the SAP of the smaller gear due to higher contact stress and sliding, in addition to suffering a greater number of tooth engagements. Hence modifying the tooth proportions would appear to be most beneficial when, for a speed reducing pair, applying a positive modification coefficient to increase the amount of recess action whilst reducing the length of approach. The opposite would be true for a speed increasing pair.

Modifying tooth proportions is also relatively common in RGAs due to the use of planet gears with low numbers of teeth, where it is required to avoid undercutting. However, a similar caution to increases in pressure angle has to be exercised when considering the observations from testing and the deviations in the model. Whilst the width of the zone of single tooth contact is not changed, it shifts along the line of action and is no longer centred on the pitch circle. Hence an increase in contact stress on the mid-addendum of the driven gear could result if such a change were implemented. Considering the prevalence of high wear on the mid-addendum during the tests performed in this study, there is the potential for such changes to result in more rapid failure.

The application of tip relief to the basic gear design results in the most significant improvement to the predicted wear of the gear pair. A correctly sized tip relief provides a significant reduction in contact at the ends of the line of action. Consequently, the areas of the teeth with the highest sliding velocities also suffer the lowest contact stresses, which has the effect of shifting the point of maximum predicted wear onto the middle of the addenda and dedenda. This would also be likely to reduce the tendency for delamination at the SAP. The application of tip relief in actuation designs varies by company and is far from universal. However, there would appear to be few drawbacks to implementing tip relief for a gearbox using coated gears, other than the need to use slightly modified tooling.

The results from the model when adopting all proposed improvements highlights that there is significant potential to optimise gear design for the use of self-lubricating coatings. None of the proposed changes would result in an increase in volume of the gears, and hence could fit within existing designs. However, it also highlights the need to understand the causes of high wear on the mid-addendum. Many of the improvements proposed have the potential to worsen the contact conditions at the locations often seen to suffer maximum wear during test, and hence there is a risk that the predicted reduction in wear might not be obtained.

5.3 Efficiency Testing

When comparing the performance of the coated gears and common fluid lubricants at room temperature, the zero-load losses were very similar. At low temperature, however, the anticipated reduction in zero-load losses was realised. An interesting aspect of the results is that the lower zero-load losses for the coated gears are somewhat negated by higher load-dependent losses. Whilst the Graphit-iC coated gears achieved the target of $\mu<0.06$, achieving a comparable level of load dependent losses to the fluid lubricants tested would appear to be unlikely,

particularly at low temperature. Hence the trade-off in different types of losses needs to be considered. This behaviour effectively creates a range of torque loads and temperature conditions over which the coated gears offer improved efficiency. Other conditions that increase zero-load losses in fluid lubricated gearboxes, such as increased speed, would lead to even greater benefits from adopting a dry-running approach. Within a high-lift system this points to transmission and PDU gearboxes as being the most likely candidates to utilise self-lubricating coatings. By comparison the highly loaded, slow moving gears of an RGA would likely exhibit a reduced benefit.

In some respects, the extent of the increase in zero-load losses for the coated gears at low temperature was surprising. Whilst zero-load losses were significantly lower than for the fluid-lubricated gears, the losses still increased at low temperature. With the test method used it was not possible to further isolate the sources of these losses, but these are likely to be attributable to stiffening of the grease within the bearings and changes to friction from the gearbox seals. The glass-fibre-filled PTFE seal material will have a greater coefficient of thermal expansion ($60x10^{-6}$ to $160x10^{-6}$ per C° [275]) than the steel shaft ($10 x10^{-6}$ to $11x10^{-6}$ per C° [276]), and hence the shaft seal will experience higher normal forces at low temperature.

In spite of the above caveats, low temperature efficiency, particularly following start-up, remains a key sizing case for many aerospace actuations systems and in that respect the coated gears outperformed the fluid lubricated gears over the entire torque range. The initially higher zero-load losses have a significant impact on system performance when the typical operating profile is one of short movements with long rest times between cycles. The comparatively high overall efficiency of the coated gears at this key sizing case demonstrates that replacing fluid lubricants with coatings, even if limited to specific gearboxes, could reduce peak power consumption, peak operating torque, and therefore weight, for a high-lift system.

The calculated coefficients of tooth friction for the coated gears compare well to those obtained by pin-on-disc tests in literature. The gears exhibited coefficients of friction in the range 0.051 to 0.055 during efficiency testing at 20°C, compared with the values of 0.06 to 0.09 obtained by Yang during the aforementioned pin-on-disc tests [250], and the value of 0.06 obtained using the coupon samples from deposition of the coating onto the gears (see Table 4-4).

The average coefficient of friction was found to increase to 0.059 to 0.063 when testing at -40°C. Little data for comparison is available for friction coefficients in a-C coatings at sub-zero temperatures. Ye et. al [277] performed a series of ball-on-disc tests on a Cr/Cr-W/W-DLC/DLC multilayer coating across a temperature range of -100°C to 25°C and provided Raman spectra of the as-deposited coating and wear tracks from the tests at each temperature. The top DLC layer

consisted of a-C:H. The friction forces at -50°C were more than double those measured at 25°C. The Raman spectra from tests at 25°C showed an increase in I_D/I_G ratio compared with the as-deposited coating, which indicated the successful formation of a sp^2-rich transfer film. The spectra from tests at -50°C, showed no such change and the conclusion was drawn that the degradation in frictional properties at lower temperatures was due to inhibition of transfer film formation, as the flash temperatures required to induce graphitization could not be achieved. Additionally, the effects of adsorbed water from ice layers formed during the cold soak period being drawn into the contact by capillary action may result in additional viscous drag.

The change in friction coefficient in the efficiency tests in this study were significantly less pronounced, which can be attributed to differences in the coating composition and test procedure. The I_D/I_G ratio of 0.848 for the a-C:H based coating used in Ye's study indicates a sp^3/sp^2 ratio of approximately 0.5 [278]. The coating therefore had significant sp^3 content and would have been highly reliant on high flash temperatures and graphitization in order to form the transfer film necessary for low friction. The non-hydrogenated a-C in Graphit-iC on the other hand is already highly graphic with little sp^3 content and would therefore be less dependent on graphitization to form a lubricious transfer film. Additionally, the running-in cycles and efficiency tests performed at 20° prior to the -40°C tests may have provided a period of operation in which the flash temperatures were high enough to allow initial graphitization to take place.

The limited extent of the increase in friction coefficient exhibited during tests at -40°C can therefore be viewed as a promising result, and an indication that low sp^3 graphitic a-C coatings are a preferable choice when compared to higher sp^3 a-C:H.

Chapter 6 Future Work and Conclusions

6.1 Future Work

As the wear tests reported in this study identified Graphit-iC as the most durable coating by a considerable margin, it seems relatively unlikely that further studies of either MoST or WSC for use on dry running would yield useful results. As the failure of the WSC coating appears to have been related to inconsistent adhesion and possible issues with substrate cleanliness, if these process failures could be addressed then perhaps further testing might produce more promising results. Nevertheless, the three coatings examined still represent a relatively narrow selection, given the range of coating types and potential variations to structure and depositions that are available. Expanding the range of tested coatings, particularly those incorporating carbon, to include films with wider range of sp^3/sp^2 ratios, H contents, and dopants may yet identify more suitable candidates. As the results in this study correlate well to pin-on-disc results in literature, the comparison of existing pin-on-disc data or a laboratory based screening process may help to narrow the field.

Aside from expanding the range of coatings, the most obvious potential for extensions to the results reported in this study relate to observations of unexpectedly high wear or delamination. The pattern of unexpectedly high wear occurring on the mid-addenda of the teeth is not aligned with the model predictions. This indicates either a locally higher wear rate, or inaccuracies in the loads or sliding distance calculated. As the model simplifies several aspects of the contact, refining the model to eliminate these known simplifications may result in a more accurate prediction, or at least eliminate them as a potential root cause for the discrepancy. These simplifications are:

- Assumption of constant average contact stress across the contact width.
- Assumption of constant radius of curvature across the contact width.
- Lack of consideration for the effects of friction in hertzian contact mechanics.
- Omission of the effects of dynamically induced load variations.
- Effect of half-width limitations at the SAP are not considered
- Errors in pitch and runout are neglected.

In particular the works of Andersson [63] on the effects of involute geometry, Flodin's [61] use of a Winkler surface mattress model, and Wu and Cheng's [67] examination of dynamic load variations should be considered.

The issue of delamination to the SAP is better understood according to the theory. Whilst the effects or likelihood of delamination cannot be readily considered within the rolling/sliding cylinder model, which only considers sliding wear, rather than focussing on simulating this failure it would largely be preferable to improve coating properties or gear design in order to prevent it. It is likely that the application of a controlled tip relief to ease the loads at the ends of the line of action could help to reduce contact stress and reduce the potential for delamination failure. This could be combined with a lightly loaded running in procedure to allow initial transfer film formation, lower friction, and smoothen surfaces to reduce the number and intensity of micro stress cycles prior to operating at higher torques. Further improvements to the strength of substrate adhesion may be possible through the use of a dedicated linear ion source to clean the substrate prior to deposition.

A greater range of test conditions also needs to be studied in order to better to have confidence in coating capability across the wide range of speeds and torques that are present in a high-lift actuation system. Whilst the effects of changes in torque load have been studied in this report, this needs to be further expanded to include changes in other operating parameters. The effect of speed would seems to be the highest priority, given the observation of critical speeds in other studies of PVD coatings. During efficiency testing, low temperature conditions were found to cause a small but significant impact on the friction coefficient of Graphit-iC. It seems likely therefore that a similar effect may be observed with respect to wear rate. Whilst long-term endurance testing at very low temperatures is usually considered impractical in aerospace system qualification, it is inevitable that any potential sensitivity will need to be quantified before fielding equipment with solid lubricated gears.

As most solid lubricant coatings, including those examined in this study, exhibit some degree of sensitivity with respect to humidity it remains to be seen how this effect translates to the target application. Whilst gearboxes in high-lift systems are sealed to prevent contaminant ingress, pressure and temperature cycling often results in the ingestion of some quantity of water. A combined temperature, altitude, and humidity test such as that defined in RTCA-DO160 [12] , performed in conjunction with endurance cycling may provide the best indicator, aside from genuine field experience.

More generally the wear and friction of dry-running coated gears forms one part of a larger problem. Whilst the coated gears exhibited a clear improvement in overall efficiency at low

temperature, there was still a significant increase in zero-load losses when compared with the room temperature values. Zero-load losses from the bearings and seals remained significant, and future studies need consider the how the losses from these other components might be reduced.

6.2 Conclusions

This research aimed to determine whether self-lubricating coatings could replace fluid lubricants in a high-lift systems in order to improve system efficiency at low temperature. The tests performed in this study clearly highlight that coating durability, as expected, is the most significant obstacle. Whilst the wear rates achieved by Graphit-iC on gears were very low at $2.34x10^{-11}$ to $4.25x10^{-11}$ $mm^3/N.mm$, a significant improvement in coating life would be required. As the approximate design life for the test gears is 120,000 cycles at 19Nm, the 8,500 cycles achieved at 20Nm is clearly insufficient. However, the tests were performed on gears manufactured according to typical design practice, and the coatings were deposited according to standard process parameters. Given the scope for application specific improvements to design of the coating and the gears, there remains some cause for optimism.

Testing has shown that Ti-doped MoS_2 coatings do not currently appear to be a promising candidate for further study . Whilst MoST displayed good adhesion properties, suffering no delamination during initial cycling, it wore rapidly, yielding wear rates in the range of $2.57x10^{-10}$ $mm^3/N.mm$ to $5.73x10^{-10}$ $mm^3/N.mm$. This rapid wear seems to be at least partially driven by substrate oxidation to Fe_3O_4. Even if coating thickness could be increased the wear rate remains an order of magnitude higher than for Graphit-iC.

Drawing firm conclusions regarding the suitability of self-adaptive W-S-C coatings is more difficult as the failure is linked to inconsistent adhesion, probably stemming from issues with pre-deposition cleanliness. In some respects, this may be a consequence of the relative immaturity of the deposition process when compared to a fully industrialised, commercially available coating. The coating may prove to be worth further study if these processing issues can be addressed.

Graphit-iC proved to be the most durable of the coatings tested. When comparing the results at 20Nm torque load it achieved a maximum wear rate of $2.98x10^{-11}mm^3/N.mm$, compared with $5.73x10^{-10}mm^3/N.mm$ for MoST and $1.30x10^{-10}mm^3/N.mm$ for WSC. It also completed the highest number of test cycles at 8,500, compared with 500 for MoST and 1500 for WSC. The wear rates were also found to be more consistent between individual teeth, refer to Figure 4-49 . Additionally, the results of efficiency testing show relatively little sensitivity to low temperatures,

with the coefficient of friction increasing by only 16-19%, allowing the significant reduction of zero-load losses in the flight environment whilst retaining sufficiently low friction to reduce overall power loss. Early SAP delamination, particularly at higher loads, remains an obstacle to fielding this technology. As this phenomenon can be understood from the combination of high contact stress and negative sliding, it may be possible to modify future gear designs to eliminate it.

The rolling/sliding cylinder model has been shown to be a useful tool to derive wear rates and predict wear distribution to the tooth surfaces. The correlation between wear rates reported in literature for standard pin-on-disc tests and the wear rates calculated for the tested gears suggests that it may be possible to estimate the useful life of other candidate coatings. This would aid in identifying which coatings may be worthwhile trialling for new designs. However clear discrepancies in the predicted distributions are still evident, most notably in extent of wear to the mid-addenda on the Graphit-iC coated gears. This requires greater understanding before the model could be fully utilised in this way.

The results of efficiency testing show that the anticipated benefits to performance can be realised, with the starting losses at 20Nm being reduced by 33% at -40°C. Hence the necessary improvements to durability are worth pursuing. Achieving a comparable level of tooth friction when compared to a fluid lubricant is evidently challenging, but coatings such as Graphit-iC are sufficiently competitive in this regard, with a coefficient of friction of 0.059-0.063 at -40°C. This ensures that the reduction in zero-load losses at low temperature sufficiently compensates for increased load-dependent losses. This, however, will depend on the balance of zero-load and load-dependent losses for a given gearbox. Consequently, a dry-running gearbox may offer improved performance in some instances, but not in others.

This research was initiated with a very specific application in mind, but the conclusions can of course be translated to others. Even if the discussion is limited to applications within the aerospace industry, a vast number of actuations systems similarly suffer from the same problem of high or inconsistent zero-load losses at low temperature. Military applications in particular tend to feature fewer actuation cycles per life, and a greater tolerance for scheduled maintenance and overhaul where worn components can be replaced. The prospects for this approach to gearbox lubrication therefore may be even greater outside of the realm of civil aviation.

List of References

[1] N. Kluga, "A Study of Flap Management, an Analysis of the Consequence of Flap Management, and a Search for Possible Causes*", Journal of Aviation/Aerospace Education and Research*, Vol. 1, pp 10-25, 1991.

[2] P. K. C. Rudolph, "High Lift Systems on Commercial Subsonic Airliners", *NASA Contractor Report 4746*, 1996.

[3] M. Recksiek, "Advanced High-Lift System Architecture with Distributed Electrical Flap Actuation", *Workshop on Aviation System Technology*, 2009.

[4] M. Pfennig, U. B. Carl, F. Thielecke, "Recent Advances Towards an Integrated and Optimized Design of High Lift Actuation Systems", *SAE International Journal of Aerospace*, Vol. 3, pp 55-64, 2009.

[5] T. A. Talay, "Introduction to the Aerodynamics of Flight", *NASA Report SP-367*, 1975.

[6] T. Ford, "Actuation Systems Development", *Aircraft Engineering and Aerospace Technology*, Vol. 70, Iss 4, pp 265-270, 1998.

[7] A. Wang, S. Gitnes. L. El-Bayoumy, "The Instantaneous Efficiency of Epicyclic Gears in Flight Control Systems", *Journal of Mechanical Design*, Vol. 133, 2011.

[8] L. Borello, G. Villero, M. Dalla Vedova, "Flap failure and aircraft controllability: Developments in asymmetry monitoring techniques", *Journal of Mechanical Science and Technology*, Vol. 28, 2014

[9] A. Wang, S. Gitnes, L. El-Bayoumy, J. Davies, "Gear Failure Analysis and Lessons Learned in Aircraft High-Lift Actuation", *Gear Solutions*, 2014.

[10] M. Pfennig, F. Thielecke, "A Knowledge-based Approach for Design and Modelling of High-Lift Actuation Systems", *Proceedings of the Institution of Mechanical Engineers*, Vol. 225, pp 302-311, 2010.

[11] "Rocol Aerospec 100 Semi-Fluid Grease", *Aircraft Engineering and Aerospace Technology*, pp 34-35, 1995.

[12] RTCA DO-160F "Environmental Conditions and Test Procedures for Airborne Equipment", 2007.

[13] "Aerospec 100 – Low Temperature, Semi-Fluid Aerospace Grease", *Rocol Technical Data Sheet*, 2012.

[14] B. Höhn, K. Michaelis, M. Hinterstoißer, "Influence Factors on Gearbox Power Loss", *Industrial Lubrication and Tribology*, Vol 63, pp 46-55, 2011.

[15] P.M.T. Marques, C.M.C.G. Fernandes, R.C. Martins, J.H.O. Seabra, "Power Losses at Low Speed in a gearbox Lubricated with Wind Turbine Gear Oils with Special Focus on Churning Losses", *Tribology International*, Vol 62, pp 186-197, 2013

[16] A.S. Terekhov, "Hydraulic Losses in Gearboxes with Oil Immersion", *Vestnic Mashinostroeniya*, Vol 55, pp 13-15, 1975.

[17] J. Phillips, "General Spatial Involute Gearing", *Springer*, 2003.

[18] G. Maitra, "Handbook of Gear Design", *Tata McGraw-Hill*, 2008

[19] J.R. Davis, "Gear Materials, Properties, and Manufacture", *ASM International*, 2005.

[20] S. Radzevich "Dudley's Handbook of Practical Gear Design and Manufacture", *CRC Press*, 2012

[21] J. D. Smith, "Gear Noise and Vibration", *Marcel-Dekker*, 2003

[22] E. Fatourehchi, M. Mohammadpour, P.D. King, H. Rahnejat, "Microgeometrical tooth profile modification influencing efficiency of planetary hub gears", *International Journal of Power Trains,* Vol. 7, pp 162-179, 2018.

[23] R. Errichello, "Friction, Lubrication, and Wear of Gears", *Lubrication Engineering*, pp. 18-22, Jan/Apr, 1990.

[24] P.J.L Fernandes, C. McDuling, "Surface Contact Fatigue Failures in Gears", *Engineering Failure Analysis*, Vol.4, pp 99-107, 1997.

[25] R. Errichello, J. Muller, "How to Analyse Gear Failures", *Power Transmission Design*, Vol. 36, pp 35-40, 1994.

[26] R.L. Errichello, “Morphology of Micropitting”, *Gear Technology*, pp 74-81, Nov/Dec 2012.

[27] “Gears – Wear and Damage to Gear Teeth – Terminology”, *BS 7848: 1996*, British Standards, 1996.

[28] T.L. Krantz, M.P. Alanou, H.P. Evans, R.W. Snidle “Surface Fatigue Lives of Case-Carburized Gears with an Improved Surface Finish”, *NASA/TM-2000-210044,* 2000.

[29] H. Winter, T. Weiss, “Some Factors Influencing Pitting, Micropitting (Frosted Areas), and Slow Speed Wear of Surface Hardened Gears”, *Journal of Mechanical Design*, Vol. 103, pp 499-505, 1981.

[30] W.E. Littmann, R.L. Widner, “Propagation of Contact Fatigue from Surface and Subsurface Origins”, *Journal of Basic Engineering*, pp 624-635, September 1966.

[31] D.P. Townsend, E.V. Zaretsky, “Effect of Shot Peening on Surface Fatigue Life of Carburized and Hardened AISI 9310 Spur Gears”, *NASA Technical Paper 2047*, 1982.

[32] T. L. Krantz, “On the Correlation of Specific Film Thickness and Gear Pitting Life”, *AMGA Technical Paper 14FTM21*, 2014.

[33] K.C. Ludema, “Sliding and Adhesive Wear”, *ASM Handbook*, Vol. 18, pp 236-241, 1992.

[34] E.J. Wellauer, G.A. Holloway, “Application of EHD Oil Film Theory to Industrial Oil Drives”, *Journal of Engineering for Industry*, Vol. 98, pp 626-631, 1976.

[35] M.R. Sari, A. Haiahem, L. Flamand, “Effect of Lubricant Contamination on Gear Wear”, *Tribology Letters*, Vol. 27, pp 119-126, 2007.

[36] J.H. Tylczak, “Abrasive Wear”, *ASM Handbook*, Vol. 18, pp 185-190, 1992.

[37] A. Dyson, “Scuffing – A Review”, *Tribology International*, Vol. 8, pp 77-87, 1975.

[38] K.C. Ludema, “A Review of Scuffing and Running-In of Lubricated Surfaces, with Asperities and Oxides in Perspective”, *Wear,* Vol. 10, pp 315-331, 1984.

[39] W.F. Bowman, G.W. Stachowiak, “A Review of Scuffing Models”, *Tribology Letters*, Vol. 2, pp 113-131, 1996.

[40] A. Dyson, *Proceedings of the Institution of Mechanical Engineers,* Vol. 190, pp 52-76, 1976.

[41] W.J. Bartz, J. Ehlert, “Relationship between Calculated Film Thickness and Wear in Elastohydrodynamic Contacts of Gears”, *Tribology International*, Vol. 8, pp 241-246, 1975.

[42] H.E. Staph, P.M. Ku, H.J. Carper, “Effect of Surface Roughness and Surface Texture on Scuffing”, *Mechanism and Machine Theory*, Vol. 8, pp 197-208, 1973.

[43] I.F. Bishop, R.W. Snidle, “Come Experimental Aspects of Running-in and Scuffing Failure of Steel Discs Operating under Elastohydrodynamic Conditions”, *The Running-In Process in Tribology: Proceedings of the 8th Leeds-Lyon Symposium on Tribology*, pp 62-77, 1981.

[44] J. Han, Q. Zou, “Effect of Surface Roughness and Lubricant on Scuffing Initiation”, *Proceedings of the ASME/STLE 2012 International Joint Tribology Conference*, 2012.

[45] E.S. Forbes, “Antiwear and Extreme Pressure Additives for Lubricants”, *Tribology*, Volume 3, pp 145-152, 1970.

[46] B.R. Höhn, K. Michaelis, “Influence of Oil Temperature on Gear Failures”, *Tribology International*, Vol. 37, pp 103-109, 2004.

[47] C. Naruse, S. Haizuka, R. Nemoto, H. Takahashi, “Influences of Tooth Profiles upon Limiting Load for Scoring and Frictional Loss of Spur Gear”, *Bulletin of the Japan Society of Mechanical Engineers*, Vol 27, pp 576-583, 1984.

[48] Y. Terauchi, H. Nadano, “Effect of Tooth Profile Modification on the Scoring Resistance of Spur Gears”, *Wear*, Vol. 80, pp 27-41, 1982.

[49] M.P. Alanou, H.P. Evans, R.W. Snidle, “Effect of different surface treatments and coatings on the scuffing performance of hardened steel discs at very high sliding speeds”, *Tribology International*, Vol. 37, pp 93-102, 2004.

[50] L. Faure, “Classification of Types of Gear Tooth Wear”, *Gear Technology*, November/December 1993.

[51] D. Walton, A.J. Goodwin, “The Wear of Unlubricated Metallic Spur Gears”, *Wear*, Vol 222, pp. 103-113, 1998.

[52] F.E. Kennedy, D.A. Voss, K.C. Glaeser, S.K. Rhee, “Wear of Materials”, *ASME*, pp 89–96, 1979.

[53] J.K. Lancaster, “The Formation of Surface Films at the Transition between Mild and Severe Metallic Wear”, *Proceedings of the Royal Society*, Vol. 273, pp 466-483, 1963.

[54] R.F. Handschuh, J. Polly, W. Morales, “Gear Mesh Loss-of-Lubrication Experiments and Analytical Simulation”, *NASA Technical Memorandum 2001-217107*, 2011.

[55] M. Petrik, R.W. Titel, H. Thomsen, P. Kaestner, J.P. Kropp, “Beschichtungen für Zahnräder”, *Vakuum in Forschung und Praxis*, Vol 20, pp 6-12, 2008

[56] S. Way, “Pitting due to Rolling Contact”, ASME Journal of Applied Mechanics, Vol. 57, pp A49-A114, 1935.

[57] S. Dhanasekaran, R. Gnanamoorthy, “Gear tooth wear in sintered spur gears under dry running conditions”, *Wear*, Vol. 265, pp 81-87, 2007.

[58] H. Blok, “Les Temperatures de Surface Dans des Conditions de Graissage Sous Pression Conditions”, *Proceedings of Second World Petroleum Congress (Paris)*, pp 151– 182, 1937.

[59] “Effect of Lubrication on Gear Surface Distress”, AGMA 925-A03, 2003.

[60] J.F. Archard, “Contact and Rubbing of Flat Surfaces”, *Journal of Applied Physics*, Vol. 24, pp 981-988, 1953.

[61] S. Andersson, A. Flodin, “Simulation of Mild Wear in Spur Gears”, *Wear*, Vol. 207, pp 16-23, 1997

[62] S. Andersson, “Wear Simulation with a Focus on Mild Wear in Rolling and Sliding Contacts”, *Friction, Wear, and Wear Protection*, pp 3-20, 2008.

[63] S. Andersson, “Partial EHD Theory and Initial Wear of Gears”, *Doctoral Thesis – Royal Institute of Technology, Stockholm*, 1975.

[64] S. Andersson, B. Eriksson, “Prediction of the Sliding Wear of Spur Gears”, *Proc. Nordtrib ’90*, 1990.

[65] S. Andersson, P. Põdra, “Wear Simulation with the Winkler Surface Model”, *Wear*, Vol. 207, pp 79-85, 1997

[66] K. Wang, H. Cheng, “A Numerical Solution to the Dynamic Load, Film Thickness and Surface Temperature in Spur Gears, Part I – Analysis”, *ASME J. Mech. Design*, Vol. 103, pp 177-187, 1980.

[67] S. Wu, H.S. Cheng, “Sliding Wear Calculation in Spur Gears”, *Journal of Tribology*, Vol 115, pp 493-500, 1993.

[68] D. Park, M. Kolivand, A. Kahraman, “An Approximate Method to Predict Surface Wear of Hypoid Gears Using Surface Interpolation”, *Mechanism and Machine Theory*, Vol. 71, pp 64-78, 2014.

[69] D. Park, M. Kolivand, A. Kahraman, “Prediction of Surface Wear of Hypoid Gears using a Semi-analytical Contact Model”, *Mechanism and Machine Theory*, Vol. 52, pp 180-194, 2012.

[70] D. Park, A. Kahraman, “A Surface Wear Model for Hypoid Gears”, *Wear*, Vol. 267, pp 1595-1604, 2009.

[71] M. Kolivand, A. Kahraman, “A Load Distribution Model for Hypoid Gears Using Ease-Off Topography and Shell Theory,” *Mechanism and Machine Theory*, Vol. 44, pp 1848-1865, 2009.

[72] B. Bajpai, A. Kahraman, N.E. Anderson, “A Surface Wear Prediction Methodology for Parallel-Axis Gear Pairs”, *Journal of Tribology*, Vol. 126, pp 597-605, 2004.

[73] S. Vijayakar, “A Combined Surface Integral and Finite Element Solution for a Three-Dimensional Contact Problem”, *International Journal for Numerical Methods in Engineering*, Vol. 31, pp. 525-545, 1991.

[74] A. Baumann, B. Bertsche, Coefficient of friction behaviour of gear oils and significance for the meshing process of spur gears, *Forsch Ingenieurwes*, Vol. 86, pp 795–805, 2022.

[75] H. Ohlendorf, "Verlustleistung und Erwärmung von Stirnrädern", *Dissertation*, TU München, 1958

[76] E. Buckingham, "Analytical mechanics of gears", *Dover Publications*, 1963

[77] G. Niemann, H. Winter, "Maschinenelemente: Band 2: Getriebe Allgemein, Zahnradgetriebe – Grundlagen, Stirnradgetriebe", Springer, 1989.

[78] P. Velex, F. Ville, "An analytical approach to tooth friction losses in spur and helical gears-influence of profile modifications", *Journal of Mechanical Design*, Vol 131, pp 1–10, 2009.

[79] A.P. Arun, A.P. Senthil Kumar, B. Giriraj, A. Faizur Rahaman, "Gear Test Rig – A Review", *International Journal of Mechanical and Mechatronics Engineering,* Vol. 14, pp 16-26, 2014.

[80] E. Allam, I. Ahmed, S. Abouel-Seoud, "An Experimental Investigation of Noise Emission from a Vehicle Gearbox System", *Journal of Mechanical Engineering Research*, Vol. 3, pp 75-84, 2011.

[81] S. Han Kim, M. Chul Shin, J. Won Byun, K. Hwan O, C. Nam Chu, "Efficiency Prediction of Worm Gear with Plastic Worm Wheel", *International Journal of Worm Gear with Plastic Worm Wheel*, Vol. 13, No. 2, pp 167-174, 2012.

[82] S. Senthilvelan, R. Gnanamoorthy, "Effect Of Rotational Speed On The Performance Of Unreinforced And Glass Fibre Reinforced Nylon 6 Spur Gears", *Materials and Design*, Vol. 28, pp 765-772, 2007.

[83] H. Ozturk, I. Yesilyurt, M. Sabuncu, "Detection and Advancement Monitoring of Distributed Pitting Failure in Gears", *Journal of Nondestructive Evaluation*, Vol. 29, pp 63-73, 2010.

[84] J.R. Davis, "Mechanical Testing", *Gear Materials, Properties, and Manufacture,* Chapter 15, 2005.

[85] W. Tuszynski, R. Michalczewski, M. Szczerek, M. Kalbarczyk, "A New Scuffing Shock Test Method For The Determination Of The Resistance To Scuffing Of Coated Gears", *Archives of Civil and Mechanical Engineering*, Vol. 12, Iss. 4, pp 436-445, 2012.

[86] Q. Zhang, J. Zhang, C. Wu, Z. Xu, S. Lyu, The Evaluation of Contact Fatigue Strength for 20MnCr5 Carburized Gear, "*International Journal Of Precision Engineering And Manufacturing"*, Vol. 15, No. 1, pp. 117-121, 2014.

[87] T. Takemasu, T. Koide, S. Sugimoto, S. Nishida, "Load Bearing Capacity of Sintered Steel Gears made of Completely Prealloy Powder for Automotive Power Transmission", *International Gear Conference 2014*, Session 12, pp 387-395, 2014.

[88] T. T. Petry-Johnson, A. Kahraman, N.E. Anderson, D. R. Chase, "An Experimental Investigation of Spur Gear Efficiency", *Journal of Mechanical Design,* Vol. 130, 2008.

[89] S. Li, "Experimental investigation and FEM analysis of resonance frequency behaviour of three-dimensional, thin-walled spur gears with a power-circulating test rig", *Mechanism and Machine Theory*, Vol. 43, Iss. 8, pp 934-963, 2008.

[90] R. Yakut, H. Düzcükoğlu, M.T. Demirci, "The load capacity of PC/ABS spur gears and investigation of gear damage", *Archives of Materials Science and Engineering,* Vol. 40, Iss. 1, pp 41-46, 2009.

[91] K. Mao, "A New Approach for Polymer Composite Gear Design", *Wear,* Volume 262, Iss. 3-4, pp 432-441, 2007.

[92] B.-R. Hoehn, P. Oster, T. Tobie, K. Michaelis, "Test Methods for Gear Lubricants", *Goriva I Maziva*, Vol 47, pp 129-152, 2008.

[93] ISO DIS 14635-1: FZG Test Procedure for Relative Scuffing Load Capacity of Oils, Part 1: Test Method A/8.3/90

[94] DGMK Information Sheet No. 377 "Method to Assess the Wear Characteristics of Lubricants in the FZG Gear Test Rig", Technical University of Munich, 1996.

[95] FVA Information Sheet No. 54/I-IV "Test procedure for the investigation of the micro-pitting capacity of gear lubricants", Technical University of Munich, 1993.

[96] FVA Information Sheet No. 2/IV "Influence of Lubricant on the Pitting Capacity of Case Carburized Gears in Load-Spectra and Single-Stage-Investigations", Technical University of Munich, 1997.

[97] V. Manoj, K. Gopinath, G. Muthuveerappan, "Development of a Power Re-Circulating Gear Test Rig", *Proceedings of 11th National Conference on Machines and Mechanisms*, 2003.

[98] T. Krantz, A. Kahraman, "An Experimental Investigation of the Influence of the Lubricant Viscosity and Additives on Gear Wear", *NASA/TM—2005-213956*, 2005.

[99] T. L. Krantz, F. B. Oswald, "Spur Gear Wear Investigated in Support of Space Shuttle Return-To-Flight Efforts", *Research and Technology 2004*, pp 149-151, 2004.

[100] B. Chen, Q. Bi, J. Yang, Y, Xia, J. Hao, "Tribological Properties Of Solid Lubricants (Graphite, h-BN) For Cu-Based P/M Friction Composites", *Tribology International*, Vol 41, pp 1145-1152, 2008.

[101] F.L. Koethen, "The Role of Graphite in Lubrication", *Industrial and Engineering Chemistry*, Vol 18, No 5, pp 497-499, 1926.

[102] R.R. Paxton, "Manufactured Carbon: A Self-Lubricating Material for Mechanical Devices", 1979.

[103] H.E. Sliney, "Solid Lubricants", *NASA Technical Memorandum 103803*, 1991.

[104] R.R.M. Johnston, A.J.W. Moore, "The Burnishing of Molybdenum Disulphide on to Metal Surfaces", *Wear,* Vol 7, pp 498-512, 1964.

[105] J. Gänsheimer, R. Holinksi, "A Study of Solid Lubricants in Oils and grease under Boundary Conditions", *Wear,* Vol 19, pp 439-449, 1972.

[106] C. Donnet, A. Erdemir, "Historical Developments and New Trends in Tribological and Solid Lubricant Coatings", *Surface and Coatings Technology*, Vol 180-181, pp 76-84, 2004.

[107] B. Chen, Q. Bi, J. Yang, Y, Xia, J. Hao, "Tribological Properties Of Solid Lubricants (Graphite, h-BN) For Cu-Based P/M Friction Composites", *Tribology International*, Vol 41, pp 1145-1152, 2008.

[108] A. Erdemir, "Solid Lubricants and Self-Lubricating Films", *Modern Tribology Handbook*, Chapter 22, 2001.

[109] J.J. Hu, R. Wheeler, J.S. Zabinski, P.A. Shade, A. Shiveley, A.A. Voevodin, "Transmission Electron Microscopy Analysis of Mo–W–S–Se Film Sliding Contact Obtained by Using Focused Ion Beam Microscope and In Situ Microtribometer", *Tribology Letters*, Vol 32, pp 49-57, 2008.

[110] A.R. Lansdown, "Molybdenum Disulphide Lubrication", Tribology Series, Vol 35, pp 13-165.

[111] T. Polcar, A. Cavaleiro, "Review on Self-Lubricant Transition Metal Dichalcogenide Nanocomposite Coatings Alloyed with Carbon", *Surface and Coatings Technology*, Vol 206, pp 686-695, 2011.

[112] I.L. Singer, "Solid Lubrication Processes", *Fundamentals of Friction: Macroscopic and Microscopic Processes*, pp 237-261, 1992.

[113] L.K. Ives, M.B. Peterson, "Models of Solid Lubrication", *Proceedings of Workshop on Fundamentals of High-Temperature Friction and Wear with Emphasis on Solid Lubrication for Heat Engines*, pp 43, 1984.

[114] H.E. Sliney, "Dynamics of Solid Lubrication as Observed by Optical Microscopy", *NASA Technical Memorandum 71880*, 1976.

[115] R.L. Fusaro, "A Comparison of The Lubricating Mechanisms of Graphite Fluoride and Molybdenum Disulphide Films", *NASA Technical Memorandum 71897*, 1978.

[116] R.L. Fusaro, "Mechanisms of Graphite Fluoride [(CFx)n] Lubrication", *Wear*, Vol 53, pp 303-323, 1979.

[117] S.V. Prasad, J.S. Zabinski, "Tribology Of Tungsten Disulphide (WS2): Characterization of Wear-Induced Transfer Films", *Journal of Materials Science Letters*, Vol 12, pp 1413-1415, 1993.

[118] J.M. Marton, "Superlubricity of Molybdenum Disulfide", *Superlubricity*, Chapter 13, pp 207-225, 2007.

[119] M.D. Kanakia, "Literature Review of Solid Lubrication Mechanisms", *Interim Report BFLRF No. 213*, 1987.

[120] P.W. Bridgman, "Shearing Phenomena at High Pressure, Particularly in Organic Compounds", *Proceedings of the American Academy of Arts and Sciences*, Vol 71, pp 387-460, 1937.

[121] F.P. Bowden, D. Tabor, "The Lubrication by Thin Metallic Films and the Action of Bearing Metals", *Journal of Applied Physics*, Vol 14, pp 141-151, 1943.

[122] D. Ramadanoff, S.W. Glass, "High Altitude Brush Problem", *Electrical Engineering*, Vol. 63, pp. 825-829, 1944.

[123] G.W. Rowe, "Some Observations on the Frictional Behaviour of Boron Nitride and of graphite", *Wear*, Vol 3, pp 274-285, 1960.

[124] R.F. Deacon, J.F. Goodman, "Lubrication by Lamellar Solids", *Proceedings of the Royal Society*, Vol 243, pp 464-482, 1958,

[125] B. K. Yen, B. E. Schwickert, M. F. Toney, "Origin of Low-Friction Behaviour in Graphite Investigated by Surface X-ray Diffraction", *Applied Physics Letters,* Vol 84, pp 4702-4704, 2004.

[126] J.K. Lancaster, "A Review of the Influence of Environmental Humidity and Water on Friction Lubrication and Wear", *Tribology International*, Vol 23, pp 371-389, 1990

[127] R.L Fusaro, H.E. Sliney, "Graphite Fluoride (CFx)n – A New Solid Lubricant", *ASLE Transactions*, Vol 13, pp 56-65, 1970.

[128] M.B. Peterson, R.L. Johnson, "Friction and Wear Investigation of Molybdenum Disulfide I – Effect of Moisture", *National Advisory Committee for Aeronautics Technical note 3055*, 1953.

[129] T. Kubart, T. Polcar, L. Kopecký, R. Novák, D. Nováková, "Temperature Dependence of Tribological Properties of MoS2 and MoSe2 Coatings", *Surface and Coatings Technology*, Vol 193, pp 230-233, 2005.

[130] S. Ross, A. Sussman, "Surface Oxidation of Molybdenum Disulfide", *Journal of Physics and Chemistry*, Vol 59, pp 889-892, 1955.

[131] J. Gänsheimer, R. Holinksi, "A Study of the Lubricating Mechanism of Molybdenum Disulfide", *Wear,* Vol 19, pp 329-342, 1972.

[132] E. Serpini, A. Rota, A. Ballestrazi, D. Marchetto, E. Gualtieri, S. Valeri, "The Role of Humidity and Oxygen on MoS_2 Thin Films Deposited by RF PVD Magnetron Sputtering", *Surface and Coating Technology,* Vol 319, pp 345-352, 2017.

[133] C. Chiu, "Hardness and indentation-induced damage of SiC-coated graphite", *Journal of Materials Science*, Vol 27, pp 3353-3358 , 1992.

[134] H.E. Sliney, "Solid Lubricant Materials for High Temperatures – A Review", *Tribology International*, Vol 15, pp 303-315, 1982.

[135] Z. Liu, Y. Ging, W. Zhou, L. Ma, J. Yu, J.C. Idrobo, J. Jung, A.H. MacDonald, R. Vajtai, J. Lou, P.M. Ajayan, "Ultrathin High-Temperature Oxidation-Resistant Coatings of Hexagonal Boron Nitride", *Nature Communications* 4:2541, 2013.

[136] M. Muralidhar Singh, G. Vijaya, M.S. Krupashankara, B.K. Srindhara, "Studies on Nanostructure Aluminium Thin Fil Coatings Deposited using DC Magnetron Sputtering Process", *IOP Conference Series: Materials Science and Engineering,* Vol 149, 2016.

[137] P.J. Kelly, R.D. Arnell, "Magnetron Sputtering: A Review of Recent Developments and Applications", *Vacuum,* Vol 56, pp 159-172, 2000.

[138] N.M. Renevier, V.C. Fox, D.G. Teer, J. Hampshire, "Coating Characteristics and Tribological Properties of Sputter-Deposited MoS_2/Metal Composite Coatings Deposited by Closed Field Unbalanced Magnetron Sputter Ion Plating", *Surface and Coatings Technology*, Vol 127, pp 24-37, 2000.

[139] T.W. Scharf, A. Rajendran, R. Banerjee, F. Sequeda, "Growth, Structure and Friction Behaviour of Titanium Doped Tungsten Disulphide (Ti-WS_2) Nanocomposite Thin Films", *Thin Solid Films*, Vol 517, pp 5667-5675, 2009.

[140] D.G. Teer, "New Solid Lubricant Coatings", *Wear*, Vol 251, pp 1068-1074, 2001.

[141] W. Lauwerens, J. Wang, J. Navratil, E. Wieërs, J. D'haen, L.M. Stals, J.P. Celis, Y. Bruynseraede, "Humidity Resistant MoS_x, Films Prepared by Pulsed Magnetron Sputtering", *Surface and Coatings Technology,* Vol 131, pp 216-221, 2000.

[142] E.W. Roberts, "Thin Solid Lubricant Films in Space", *Tribology International*, Vol 23, pp 95-104, 1990.

[143] P. Niederhäuser, H.E. Hintermann, M. Maillat, "Moisture-Resistant MoS2-based Composite Lubricant Coatings", *Thin Solid Films*, Vol 108, pp 209-218, 1983.

[144] B.C. Stupp, "Synergistic Effects of Metals Co-sputtered with MoS_2", *Thin Solid Films*, Vol 84, pp 257-266, 1981.

[145] N.M. Renevier, J. Hampshire, V.C. Fox, J. Witts, T. Allen, D.G. Teer, "Advantages of Using Self-Lubricating, Hard, Wear-Resistant MoS_2-based Coatings", *Surface and Coatings Technology*, Vol 142-144, pp 67-77, 2001.

[146] Z. Hui, Z. Jun, W. Qing-Ping, W. Zhi-hua, S. Rui-Peng, "The Effect of Ti Content on the Structural and Mechanical Properties of MoS_2-Ti Composite Coatings Deposited by Unbalanced Magnetron Sputtering System", *Physics Procedia*, Vol 18, pp 234-239, 2011.

[147] M.C. Simmonds, A. Savan, E. Pflüger, H. Van Swygenhoven, "Mechanical and Tribological Performance of MoS_2 Co-sputtered Composites", *Surface and Coatings Technology,* Vol 126, pp 15-24, 2000.

[148] Y.L. Su, W.H. Kao, "Tribological behaviour and Wear Mechanism of MoS_2-Cr Coatings Sliding against Various Counterbody", *Tribology International,* Vol 36, pp 11-23, 2000.

[149] G. Weise, A. Teresiak, I. Bächer, P. Markschläger, G. Kampschulte, "Influence of Magnetron Sputtering Process Parameters on Wear Properties of Steel/Cr_3Si or Cr/MoS_x", *Surface and Coatings Technology,* Vol 76-77, pp 382-392, 1995.

[150] X.-Z., Ding, X.T. Zeng, X.Y. He, Z. Chen, "Tribological Properties of Cr and Ti-doped MoS_2 Composite Coatings under Different Humidity Atmosphere", *Surface and Coatings Technology,* Vol 205, p 224-231, 2010

[151] J.D. Holbery, E. Pflueger, A. Savan, Y. Gerbig, Q. Luo, D.B. Lewis, W.D. Munz, "Alloying MoS_2, with Al and Au, Structure and Tribological Performance", *Surface and Coatings Technology,* Vol 169-170, pp 716-720, 2003.

[152] K.J. Wahl, D.N. Dunn, I.L. Singer, "Wear Behaviour of Pb-Mo-S Solid Lubricant Coatings", *Wear*, Vol 230, pp 175-183, 1999.

[153] Z. Wang, Z.-B. Cai, Y. Sun, J.-F. Peng, M.-H. Zhu, "Low Velocity Impact Wear Behaviour of MoS_2/Pb Nanocomposite Coating under Controlled Kinetic Energy", *Surface and Coatings Technology*, Vol 326, pp 53-62, 2017.

[154] J. S. Zabinski , M. S. Donley , S. D. Walck , T. R. Schneider & N. T. McDevitt, "The Effects of Dopants on the Chemistry and Tribology of Sputter-Deposited MoS2 Films", *Tribology Transactions"*, Vol 38, pp 894-904, 1995.

[155] S. Xu, X. Gao, M. Hu, D. Wang, D. Jiang, J. Sun, F. Zhou, L. Weng, W. Liu, "Microstructure Evolution and Enhanced Tribological Properties of Cu-Doped WS_2 Films", *Tribology Letters,* Vol 55, pp 1-13, 2014.

[156] S.-S. Xu, L.-J. Weng, Y.-Z. Liu, K.-H. Kang, C.-L Kim, D.-E. Kim, "Microstructure Evolution and Enhanced Tribological Properties of Ni-Doped WS_2 Films", *Surface and Coatings Technology,* Vol 325, pp 81-88, 2014.

[157] S. Wu, X. Gao, M. Hu, J. Sun, D. Wang, F. Zhou, L. Weng, W. Liu, "Morphology Evolution of Ag alloyed WS_2 Film and the Significantly Enhanced Mechanical and Tribological Properties", *Surface and Coatings Technology,* Vol 238, pp 197-206, 2014.

[158] S.P. Rodrigues, M. Evaristo, S. Carvalho, A. Cavaleiro, "Fluorine-Carbon Doping of WS-Based Coatings Deposited by Reactive Magnetron Sputtering for Low Friction Purposes", *Applied Surface Science,* Vol 445, pp 575-585, 2018.

[159] R. Gilmore, M.A. Baker, P.N. Gibson, W. Gissler, M. Soiber, P. Losbichler, C. Mitterer, "Low-Friction TiN- MoS_2 Coatings Produced by DC Magnetron Co-Deposition", *Surface and Coatings Technology,* Vol 108-109, pp 345-351, 1998.

[160] J. S. Zabinski , M. S. Donley , S. D. Walck , T. R. Schneider & N. T. McDevitt, "The Effects of Dopants on the Chemistry and Tribology of Sputter-Deposited MoS2 Films", *Tribology Transactions"*, Vol 38, pp 894-904, 1995.

[161] G.H. Kinner, J.S. Pippet, I.B. Atkinson, ""A Laboratory Study of the Performance and Behaviour of Solid Film Lubricants based on MoS_2 and Graphite Fluoride", *RAE Tech Report 76026,* 1976.

[162] K. Jousten, Handbook of Vacuum Technology, 2008.

[163] P.W. Centers, “The Role of Bulk Additions in Solid Lubricant Contacts”, *Air Force Wright Aeronautical Laboratories Report AFWAL-TR-86-2125*, 1987.

[164] P.J. John, S.V. Prasad, A.A. Voevodin, J.S. Zabinski, “Calcium Sulfate as a High-Temperature Solid Lubricant”, *Wear,* Vol 219, pp 155-161, 1998

[165] P.J. John, J.S. Zabinski, “Sulfate Based Coatings for use as High Temperature Lubricants”, *Tribology Letters,* Vol 7 pp 31-37, 1999.

[166] S.D. Walck, J.S. Zabinsky, N.T. McDevitt, J.E. Bultman, “Characterization of Air-Annealed, Pulsed Laser Deposited ZnO-WS_2 Solid Film Lubricants by Transmission Electron Microscopy”, *Thin Solid Films*, Vol 305, pp 130-143, 1997.

[167] S.V. Prasad, N.T. McDevitt, J.S. Zabinski, “Tribology of Tungsten Disulfide-Nanocrystalline Zinc Oxide Adaptive Lubricant Films from Ambient to 500^{o}C”, *Wear,* Vol 237, pp 186-196, 2000.

[168] H.P.P Schmellenmeier, “Die Beeinflussung von festen Oberflächen durch eine ionisierte Gasatmosphäre”, *Experimentelle Technik der Physik,* Vol 1, pp 49-68, 1953.

[169] S. Aisenberg, R. Chabot, “Ion-Beam Deposition of Thin Films of Diamondlike Carbon”, *Journal of Applied Physics,* Vol 42, pp 2953-2958, 1971.

[170] K. Bewwilogua, D. Hofmann, “History of diamond-like carbon films — From first experiments to worldwide applications”, *Surface and Coatings Technology,* Vol 242, pp 214-225, 2014.

[171] S. Craig, G.L. Harding, “Structure, Optical Properties, and Decomposition Kinetics of Sputtered Hydrogenated Carbon”, *Thin Solid Films*, Vol 97, pp 345-361, 1982.

[172] K. Bewwilogua, D. Hofmann, “History of diamond-like carbon films — From first experiments to worldwide applications”, *Surface and Coatings Technology,* Vol 242, pp 214-225, 2014.

[173] W. Jacob, W. Möller, “On the Structure of Thin Hydrocarbon Films”, *Applied Physics Letters*, Vol 63, pp 1771-1773, 1993.

[174] C. Casiraghi, A. C. Ferrari, J. Robertson, “Raman spectroscopy of hydrogenated amorphous carbons”, *Physical Review B*, Vol 72, 2005.

[175] A. Erdemir, C. Donnet, “Tribology of Diamond, Diamond-Like Carbon, and Related Films”, *Modern Tribology Handbook*, Chapter 24, 2001.

[176] D.C. Sutton, G. Limbert, D. Stewart, R.J.K. Wood, “The Friction of Diamond-Like Carbon Coatings in a Water Environment”, *Friction*, Vol 1,pp 210-221, 2013.

[177] J. Robertson, “Diamond-Like Amorphous Carbon”, *Materials Science and Engineering,* Vol 37, pp 129-281, 2002.

[178] J.W. Zou, K. Schmidt, K. Reichelt, B. Dischler, “The Properties of a-C:H Films Deposited by Bias Sputtering of Carbon”, *Journal of Applied Physics*, Vol 68, pp 1558-1562, 1990.

[179] Y. Lifshitz, S.R. Kasi, J.W. Rabalais, “Subplantation Model for Film Growth from Hypothermal Species: Application to Diamond”, *Physical Review Letters,* Vol 62, pp 1290-1293, 1989.

[180] J. Robertson, “Deposition Mechanisms for Promoting sp3 Bonding in Diamond-Like Carbon”, *Diamond and Related Materials*, Vol 2, pp 984-989, 1993.

[181] A. von Keudell, M. Meier, C. Hopf, “Growth Mechanism of Amorphous Hydrogenated Carbon”, *Diamond and Related Materials,* Vol 11, pp 969-975, 2002.

[182] Y. Pauleau, “Generation and Evolution of Residual Stresses in Physical Vapour-Deposited Thin Films”, *Vacuum*, Vol 61, pp 175-181, 2001.

[183] Y. Pauleau, “Residual Stresses in DLC Films and Adhesion to Various Substrates”, *Tribology of Diamond-Like Carbon Films: Fundamentals and Applications*, 2008.

[184] A. Grill, “Review of the Tribology of Diamond-Like Carbon”, *Wear*, Vol 168, pp 143-153, 1993.

[185] C. Donnet, A. Grill, “Friction Control of Diamond-Like Carbon Coatings”, *Surface and Coatings Technology*, Vol 94-95, pp 456-462, 1997.

[186] A. Erdemir, C. Bindal, J. Pagan, P. Wilbur, “Characterization of Transfer Layers on Steel Surfaces Sliding against Diamond-Like Hydrocarbon Films in Dry Nitrogen”, *Surface and Coating Technology,* Vol 76-77, pp 559-563, 1995.

[187] B. Racine, M. Benlahsen, K. Zellama, M. Zarrabian, J. P. Villain, G. Turban, A. Grosman, “Hydrogen Stability in Diamond-Like Carbon Films During Wear Tests”, *Applied Physics Letters*, Vol 75, pp 3479-3481, 1999.

[188] Y. Liu, A. Erdemir, E.I. Meletis, “A Study of the Wear Mechanism of Diamond-Like Carbon Films”, *Surface and Coatings Technology,* Vol 82, pp 48-56, 1996.

[189] A.A. Voevodin, A.W. Phelps, J.S. Zabinski, M.S. Donley, “Friction Induced Phase Transformation of Pulsed Laser Deposited Diamond-Like Carbon”, *Diamond and Related Materials,* Vol 5, pp 1264-1269, 1996.

[190] K. Enke, H. Dimigen, H. Hübschm, “Frictional Properties of Diamond-Like Carbon Layers”, *Applied Physics Letters*, Vol 36, pp 291-292, 1980.

[191] C. Donnet, T. Le Mogne, L. Ponsonnet, M. Belin, A. Grill, V. Patel, C. Jahnes, “The Respective Role of Oxygen and Water Vapour on the Tribology of Hydrogenated Diamond-Like Carbon Coatings”, *Tribology Letters,* Vol 4, pp 259-265, 1998.

[192] H. Li, T. Xu, C. Wang, J. Chen, H. Zhou, H. Liu, “Tribochemical Effects on the Friction and Wear Behaviours of Diamond-Like Carbon Film under High Relative Humidity Condition”, *Tribology Letters,* Vol 19, pp 231-238, 2004.

[193] A.A. Voevodin, M.S. Donley, J.S. Zabinski, J.E. Bultman, “Mechanical and Tribological Properties of Diamond-Like Carbon Coatings Prepared by Pulsed Laser Deposition”, *Surface and Coatings Technology,* Vol 76-77, pp 534-539, 1995.

[194] A. Grill, V. Patel, “Tribological Properties of Diamond-Like Carbon and Related Materials”, *Diamond and Related Materials,* Vol 2, pp 597-605, 1993.

[195] C. Chen, C. Hong, “Interfacial Studies for Improving the Adhesion of Diamond-Like Carbon Films on Steel”, Applied Surface Science, Vol. 243, pp 296-303, 2005.

[196] X.-M. He, W.-Z. Li, H.-D. Li, “Ion Beam Assisted Deposition of Diamond-Like Carbon onto Steel Materials Preparation and Advantages”, *Surface and Coatings Technology,* Vol 84, pp 414-419, 1996.

[197] A. Grill, B. Meyerson, V. Patel, “Interface Modifications for Improving the Adhesion of a-C:H Films to Metals”, *Journal of Materials Research,* Vol 3, pp 214-217, 1988.

[198] P. Wang, X. Wang, T. Xu, W. Liu, J. Zhang, “Comparing Internal Stress in Diamond-Like Carbon Films with Different Structure”, *Thin Solid Films,* Vol 515, pp 6899-6903, 2007.

[199] C. Wang, D. Wang, “Microstructure and Adhesion Characteristics of Diamond-Like Carbon Films Deposited on Steel Structures”, Diamond and Related Materials, Vol. 10, pp 1528-1534, 2000.

[200] H. Dimigen, H. Huebsch, “Applying Low-Friction Wear-Resistant Thin Solid Films by Physical Vapour Deposition”, *Phillips Technical Review*, Vol 41, pp 186-197, 1983

[201] B. Feng, D.M. Cao, W.J. Meng, J. Xu, R.C. Tittsworth, L.E. Rehn, P.M. Baldo, G.L. Doll, “Characterization of Microstructure and Mechanical Behaviour of Sputter Deposited Ti-containing Amorphous Carbon Coatings” *Surface and Coatings Technology*, Vol 148, pp 153-162, 2001.

[202] P.V. Bharathy, D. Nataraj, P.K. Chu, H. Wang, Q. Yang, M.S.R.N. Kiran, J. Silvestre-Albero, D. Mangalaraj, “Effect of Titanium Incorporation on the Structural, Mechanical and Biocompatible Properties of DLC Thin Film Prepared by Reactive- Biased Target Ion Beam Deposition Method”, *Applied Surface Science,* Vol 257, Vol 257, pp 143-150, 2010.

[203] V.Y. Kulikovsky, F. Fendrych, L. Jastrabik , D. Chvostova, “Study of Formation and some Properties of Ti-C:H Films Prepared by D.C. Magnetron Sputtering”, *Surface and Coatings Technology*, Vol 91, pp 122-130, 1997.

[204] Q. Wei, R.J. Narayan, A.K. Sharma, J. Sankar, “Preparation and Mechanical Properties of Composite Diamond-Like Carbon Thin Films”, *Journal of Vacuum Science and Technology*, Vol 17, pp 3406-3414, 1999.

[205] B. Yang, Z.H. Huang, C.S. Liu, Z.Y. Zeng, X.J. Fan, D.J. Fu, “Characterization and Properties of Ti-Containing Amorphous Carbon Nanocomposite Coatings Prepared by Middle Frequency Magnetron Sputtering”, *Surface and Coatings Technology,* Vol 200, pp 5812-5818, 2006.

[206] A.A. Voevodin, J.S. Zabinski, “Load-Adaptive Crystalline-Amorphous Nanocomposites”, *Journal of Materials Science,* Vol 33, pp 319-327, 1998.

[207] K. Bewilogua, R. Wittorf, H. Thomsen, M. Weber, “DLC Based Coatings Prepared by Reactive D.C. Magnetron Sputtering”, *Thin Solid Films,* Vol 447-448, pp 142-147, 2004.

[208] P. Mutafov, J. Lanigan, A. Neville, A. Cavaleiro, T. Polcar, “DLC-W Coatings Tested in Combustion Engine – Frictional and Wear Analysis”, *Surface and Coatings technology,* Vol 260, pp 284-289, 2014.

[209] J. Veverkova, S.V. Hainsworth, “Effect of Temperature and Counterface on the Tribological Performance of W-DLC on a Steel Substrate”, *Wear,* Vol 264, pp 518-525, 2008.

[210] A. Czyżniewski, W. Precht, “Deposition and some Properties of Nanocrystalline, Nanocomposite and Amorphous Carbon-Based Coatings for Tribological Applications”, *Journal of Materials Processing Technology*, Vol 157-158, pp 274-283, 2004.

[211] O. R. Monteiro, M-.P. Delplancke-Ogletree, I. G. Brown, “Tungsten-Containing Amorphous Carbon Films Deposited by Pulsed Vacuum Arc”, *Thin Solid Films,* Vol 342, pp 100-107, 1999.

[212] A. Voevodin, S. Walck, J. Zabinski, “Architecture of Multilayer Nanocomposite Coatings with Super-Hard Diamond-like Carbon Layers for Wear Protection at High Contact Loads”, Wear, Vol. 203-203, pp 516-527, 1997.

[213] K. Holmberg, A. Matthews, H. Ronkainen, “Coatings Tribology – Contact Mechanisms and Surface Design”, *Tribology International,* Vol. 31, pp 107-120, 1998.

[214] A.A. Voevodin, J.M. Schneider, C. Rebholz, A. Matthews, “Multilayer Composite Ceramic-Metal-DLC Coatings for Sliding Wear Applications”, *Tribology International,* Vol 29, pp 559-570, 1996.

[215] K.L. Choy, E. Felix, “Functionally Graded Diamond-Like Carbon Coatings on Metallic Substrates”, *Materials Science and Engineering,* Vol 228, pp162-169, 2000.

[216] X. Chen, Z. Peng, Z. Fu, S. Wu, W. Yue, C. Wang, “Microstructural, Mechanical and Tribological Properties of Tungsten-Gradually Doped Diamond-Like Carbon Films with Functionally Graded Interlayers”, *Surface and Coatings Technology*, Vol. 205, pp 3631-3638, 2011.

[217] J. Jiang, W. Meng, A. Evans, C. Cooper, “Structure and Mechanics of W-DLC Coated Spur Gears”, Surface and Coatings Technology, Vol. 176, pp 50-56, 2003.

[218] J. Stallard, D.G. Teer, “A Study of the tribological Behaviour of CrN, Graphit-iC and Dymon-iC Coatings under Oil Lubrication”, *Surface and Coatings Technology*, Vol 188-189, pp 252-529, 2004.

[219] A.A. Voevodin, T.A. Fitz, J.J. Hu, J.S. Zabinski, “Nanocomposite Tribological Coatings with “Chameleon” Surface Adaptation”, *Journal of Vacuum Science and Technology*, Vol 20, pp 1434-1444, 2002.

[220] T. Polcar, A. Cavaleiro, “Review on Self-Lubricant Transition Metal Dichalcogenide Nanocomposite Coatings Alloyed with Carbon”, *Surface and Coatings Technology,* Vol 206, pp 686-695, 2011.

[221] F. Joachim, N. Kurz, B. Glatthaar, “Influence of Coatings and Surface Improvements on the Lifetime of Gears”, Gear Technology, pp 50-56, July/August 2004.

[222] Y. Xiao, W. Shi, J. Luo, Y. Liao, "The Tribological Performance of TiN, WC/C and DLC Coatings Measured by the Four-Ball Test", *Ceramics International*, Vol. 40, pp 6919-6925, 2013.

[223] H. Singh, G. Ramirez, O. Eryilmaz, A. Greco, G. Doll, A. Erdemir, "Fatigue Resistant Carbon Coatings for Rolling/Sliding Contacts", *Tribology International*, Vol. 98, pp 172-178, 2016.

[224] M. Fujii, M. Seki, A. Yoshida, "Surface Durability of WC/C-Coated Case-Hardened Steel Gear", *Journal of Mechanical Science and Technology*, Vol. 24, pp 103-106, 2010.

[225] B. Kržan, M. Kalin, J. Vižintin, "The Lubrication of DLC Coated Gears with Environmentally Adapted Ester-Based Oil", *Gear Technology*, July/August, pp 36-40, 2006.

[226] C. Mercer, A.G. Evans, N. Yao, S. Allameh, C.V. Cooper, "Material Removal on Lubricated Steel Gears with W-DLC –Coated Surfaces", *Surface and Coating Technology*, Vol. 173, pp 122-129, 2003.

[227] V. Moorthy, B. Shaw, "Contact Fatigue Performance of Helical Gears with Surface Coatings", *Wear*, Vol. 276-277, pp 130-140, 2012.

[228] V. Moorthy, B. Shaw, "Effect of As-Ground Surface and the BALINIT C® and Nb-S Coatings on Contact Fatigue Damage in Gears", *Tribology International* ,Vol 51, pp 61-70, 2012.

[229] B. Kržan, "Load Carrying Capacity of WC/C-Coated Gears Lubricated with a Low-Viscosity Oil", *Lubrication Science,* Vol 28, pp 127-139, 2015.

[230] M. Kalin, J. Vižintin, "The Tribological Performance of DLC-Coated Gears Lubricated with Biodegradable Oil in Various Pinion/Gear Material Combinations", Wear, Vol. 259, pp 1270-1280, 2005.

[231] M. Weck, O. Hurasky-Schönwerth, C. Bugiel, "Service Behaviour of PVD-Coated Gearing Lubricated with Biodegradable Synthetic Ester Oils", *Proceedings of the International Conference on Gears*, 2002.

[232] S. Emmert, G. Schönnenbeck, "Standard Micropitting Test GT" *FVA Information Sheet on Research Project No.54/I-IV*, Forschungsvereinigung Antriebstechnik, 1997

[233] R. Michalczewski, W. Piekoszewski, M. Szczerek, W. Tuszynski, "The Lubricant-Coating Interaction in Rolling and Sliding Contacts", Tribology International, Vol. 42, pp 554-560, 2009.

[234] R.I. Amaro, R.C. Martins, J.O. Seabra, S. Yang, D.G. Teer, N.M, Renevier, "Carbon/Chromium Low Friction Surface Coating for Gears Application", *Industrial Lubrication and Tribology,* Vol 57, Iss 6, pp 233-242, 2005.

[235] R.I. Amaro, R.C. Martins, J.O. Seabra, D.G. Teer, N.M, Renevier, "Molybdenum Disulphide/Titanium Low Friction Coating for Gears Application", *Tribology International,* Vol 38, pp 423-434, 2005.

[236] R.C. Martins, P. S. Moura, J. O. Seabra, "MoS_2/Ti Low-Friction Coating for Gears", *Tribology International,* Vol 39, pp 1686-1697, 2006.

[237] R. Martins, R. Amaro, J. Seabra, "Influence of Low Friction Coatings on the Scuffing Load Capacity and Efficiency of Gears", Tribology International, Vol. 41, pp 234-243, 2007.

[238] "Thermal Rating of Gear Drives Balance Between Power Loss and Heat Dissipation", *AGMA Technical Paper 96FTM8*, 1996.

[239] P.D. Fleischauer, "Fundamental Aspects of the Electronic Structure, Materials Properties, and Lubricant Performance of Sputtered MoS_2 Films", *Thin Solid Films,* Vol 154, pp 309-322, 1987.

[240] "Gear Classification and Inspection Handbook - Tolerances and Measuring Methods for Unassembled Spur and Helical Gears (Including Metric Equivalents)", *American National Standard ANSI/AGMA 200-A88,* 1988.

[241] J.E. Shigley, J.J. Uicker, "Theory of Machines and Mechanisms", 2nd edition, 1995.

[242] M. Fujii, M. A. Kumar, A. Yoshida, "Influence of DLC Coating Thickness on Tribological Characteristics under Sliding Rolling Contact Condition", *Tribology International,* Vol 44, pp 1289-1295, 2011.

[243] J. Farley, L. C. Wrobel, K. Mao, "Performance Evaluation of Multilayer Thin Film Coatings under Mixed Rolling-Sliding Dry Contact Conditions", *Wear,* Vol 268, pp 269-276, 2010.

[244] M. Murakawa, T. Komori, S. Takeuchi, K. Miyoshi, "Performance of a Rotating Gear Pair Coated with an Amorphous Carbon Film under a Loss-of-Lubrication Condition", *Surface and Coatings Technology,* Vol 120-121, pp 646-652, 1999.

[245] K. Holmberg, A. Matthews, "Coatings Tribology", *Tribology and Interface Engineering Series*, No. 56, 1994.

[246] B. Rebbechi, F. B. Oswald, D. P. Townsend, "Measurement of Gear Tooth Dynamic Friction", *Proceedings of the Seventh International Power Transmission and Gearing Conference*, 1996.

[247] M. Björling, J. Miettinen, P. Marklund, A. Lehtovaara, R. Larsson, "The Correlation between Gear Contact Friction and Ball on Disc Friction Measurements", *Tribology International*, Vol 83, pp 114-119, 2015.

[248] C. Fernandes, P. Marques, R. Martins, J. Seabra, "Gearbox Power Loss. Part II: Friction Losses in Gears", *Tribology International,* Vol 88, pp 309-316, 2015.

[249] S. Yang, D. Camino, N. Renevier, A. Jones, and D. Teer, "Deposition and tribological behavior of sputtered carbon hard coatings", *Surface and Coatings Technology*, Vol. 124, 2000.

[250] S. Yang, X. Li, N. Renevier, and D. Teer. "Tribological Properties and Wear Mechanism of Sputtered C/Cr coating", *Surface and Coatings Technology*, Vol. 142, 2001

[251] M. Evaristo, T. Polcar, A. Cavaleiro, "Tribological Behaviour of C-alloyed Transition Metal Dichalcogenides (TMD) Coatings in different Environments", International Journal of Mechanics and Materials in Design, Vol 4, pp 137–143,2008.

[252] T. Polcar, M. Evaristo, A. Cavaleiro, "Friction of Self-Lubricating W-S-C Sputtered Coatings Sliding Under Increasing Load", *Plasma, Processes and Polymers*, Vol 4, pp S541–S546, 2007.

[253] T. Polcar, A. Nossa, M. Evaristo and A. Cavaleiro, "Nanocomposite Coatings of Carbon-Based and Transition Metal Dichalcogenides Phases: A Review", *Reviews on Advanced Material Science*, Vol 15, pp 118-126, 2007.

[254] T. Vuchkov, M. Evaristo, T. bin Yaqub, T. Polcar, A. Cavaleiro, "Tribological Behaviour in Diverse Testing Environments of a Self-lubricant W-S-C Coating Deposited by CFUBMS", *Proceedings of 46th Leeds-Lyon Symposium on Tribology*, 2019.

[255] T. Vuchkov, M. Evaristo, T. bin Yaqub, T. Polcar, Albano Cavaleiro, "Synthesis, microstructure and mechanical properties of W-S-C self-lubricant thin films deposited by magnetron sputtering", Tribology International, Vol 150, pp 1-14, 2020

[256] SKF Group, "The SKF model for calculating the frictional moment", *SKF Rolling Bearings Catalogue*, 2018

[257] B.R. Höhn, K. Michaelis, A. Wimmer, "Low Loss Gears", *Gear Technology,* Vol 24, pp 28-35, 2007.

[258] M. Lerch, F. Thielecke, "Concepts for a Safety Device in Conventional Track-Linkage Kinematics to Prevent Skew in a Single Flap System", *Deutscher Luft- und Raumfahrtkongress*, 2017.

[259] ESDU International, "Specification S162 – Bar, Forgings", Metallic Materials Data Handbook, Section 11, 2002.

[260] D. Chicot, J. Mendoza, A. Zaoui , G. Louis, V. Lepingle, F. Roudet, J. Lesage, "Mechanical properties of magnetite (Fe_3O_4), hematite (α -Fe_2O_3) and goethite (α-FeO·OH) by instrumented indentation and molecular dynamics analysis", *Materials Chemistry and Physics*, Vol 129, pp 862-870, 2011.

[261] K. Gołasa, M. Grzeszczyk, K.P. Korona, R. Bożek, J. Binder, J. Szczytko, A. Wysmołek, A. Babiński, "Optical Properties of Molybdenum Disulfide (MoS2)", *Acta Physica Polonica A*, Vol. 124, pp 849-851, 2013.

[262] E. Serpini, T. Vitu, A. Rota, T. Polcar, and S. Valeri, "Friction-Induced Chemical and Structural Modifications of Molybdenum Disulphide Thin Films", *Journal of Materials Engineering and Performance*, Vol 30, pp 4177-4125, 2021.

[263] M. Hanesch, "Raman spectroscopy of iron oxides and (oxy)hydroxides at low laser power and possible applications in environmental magnetic studies", *Geophysical Journal International*, Vol 177, pp 941–948, 2009.

[264] M. Dieterle, G. Weinberg and G. Mestl, “Raman spectroscopy of molybdenum oxides”, *Physical Chemistry Chemical Physics*, Vol 4, pp 812–821, 2002.

[265] S. Challagulla, K. Tarafder, R. Ganesan, S. Roy, “Structure sensitive photocatalytic reduction of nitroarenes over TiO_2”, *Scientific Reports*, Vol 7, pp 1-11, 2017.

[266] A.N. Barbosa, N.S. Figueroa, M. Giarola, G. Mariotto, F.L. Freire Jr., “Straightforward identification of monolayer WS2 structures by Raman spectroscopy”, *Materials Chemistry and Physics*, Vol 243, 2020.

[267] A.C. Ferrari, J. Robertson, “Interpretation of Raman spectra of disordered and amorphous carbon”, *Physical Review B*, Vol 21, 1999.

[268] L. Mazzetti, P. J. Thistlethwaite, “Raman spectra and thermal transformations of ferrihydrite and schwertmannite”, *Journal of Raman Spectroscopy*, Vol 33, pp 104–111, 2002.

[269] G. Ketteler, W. Weiss, W. Ranke, R. Schlögl, “Bulk and Surface phases of iron oxides in an oxygen and water atmosphere at low pressure”, *Physical Chemistry Chemical Physics*, Vol 3, pp 1114-1122, 2001.

[270] F.H. Stott, “The role of oxidation in the wear of alloys”, *Tribology International*, Vol 31, pp 61–71, 1998

[271] A.F. Bower, “The Influence of Crack Face Friction and Trapped Fluid on Surface Initiated Rolling Contact Fatigue Cracks”, *Journal of Tribology*. Vol 110, pp 704-711, 1988.

[272] Y. Murakami, M. Kaneta, H Yatsuka, “Analysis of Surface Crack Propagation in Lubricated Rolling Contact”, *Tribology Transactions*, Vol 28, pp 60-68, 1985.

[273] P. Rycerz, A. Kadiric, “The Influence of Slide–Roll Ratio on the Extent of Micropitting Damage in Rolling–Sliding Contacts Pertinent to Gear Applications”, Tribology Letters, Vol 67, Article number 63, 2019.

[274] R. Errichello, “Gear Sliding”, *Encyclopaedia of Tribology*, 2013.

[275] Z.Xi, O.R. Ghita, K.E. Evans, “The unusual thermal expansion behaviour of PTFE/GF composites incorporating PTFE/GF recyclate”, *Composites Part A: Applied Science and Manufacturing*, Vol 43, pp 1999-2006, 2012.

[276] R. Kandrotaitė Janutienė, “Investigation of hardening and tempering deformations of carburized low alloy steel”, *Mechanika*, Vol 19, pp 236-242, 2013

[277] T. Ye, J. Ma, Z. Jia, T. Li, W. Liu, W. Yu, ,”Microstructure, Mechanical Properties and Low-Temperature Tribological Behavior of Cr/Cr-W/W-DLC/DLC Multilayer Coatings on 5A06 Al alloy”, *Journal of Materials Research and Technology*, Vol. 18, pp. 810-819, 2022.

[278] G. Irmer, A. Dorner-Reisel, “Micro-Raman Studies of DLC Coatings”, *Advanced Engineering Materials*, Vol 7, pp 694-705, 2005.